Broj: 02/1-1633/2
Datum: 26.10.2018

UNIVERZITET CRNE GORE

- Centru za doktorske studije -

- Senatu -

O V D J E

U prilogu dostavljamo Odluku Vijeća Elektrotehničkog fakulteta sa sjednice od 26.10.2018. godine i **obrazac D2,** sa pratećom dokumentacijom, za kandidata mr **Miloša Brajovića,** na dalji postupak.

D E K A N,

Prof. dr Zoran Veljović

ISPUNJENOST USLOVA DOKTORANDA

OPŠTI PODACI O DOKTORANDU	
Titula, ime, ime roditelja, prezime	MSc Miloš Željko Brajović
Fakultet	Elektrotehnički fakultet
Studijski program	Doktorske studije elektrotehnike
Broj indeksa	2/13

NAZIV DOKTORSKE DISERTACIJE	
Na službenom jeziku	Analiza algoritama za rekonstrukciju signala rijetkih u Hermitskom i Furijeovom transformacionom domenu
Na engleskom jeziku	On Reconstruction Algorithms for Signals Sparse in Hermite and Fourier Domains
Naučna oblast	Elektrotehnika / Obrada signala

MENTOR/MENTORI			
Prvi mentor	Prof. dr Miloš Daković	Elektrotehnički fakultet, Univerzitet Crne Gore, Podgorica, Crna Gora	Elektrotehnika/ Obrada signala

KOMISIJA ZA PREGLED I OCJENU DOKTORSKE DISERTACIJE		
Prof. dr Ljubiša Stanković	Elektrotehnički fakultet, Univerzitet Crne Gore, Podgorica, Crna Gora	Elektrotehnika/ Obrada signala
Prof. dr Miloš Daković	Elektrotehnički fakultet, Univerzitet Crne Gore, Podgorica, Crna Gora	Elektrotehnika/ Obrada signala
Prof. dr Danilo Mandić	Department of Electrical and Electronic Engineering, Faculty of Engineering, Imperial College London, London, UK	Elektrotehnika/ Obrada signala

Datum značajni za ocjenu doktorske disertacije	
Sjednica Senata na kojoj je data saglasnost na ocjenu teme i kandidata	23.06.2016.
Dostavljanja doktorske disertacije organizacionoj jedinici i saglasanost mentora	18.10.2018. 18.10.2018.
Sjednica Vijeća organizacione jedinice na kojoj je dat prijedlog za imenovanje komisija za pregled i ocjenu doktorske disertacije	26.10.2018.

ISPUNJENOST USLOVA DOKTORANDA
U skladu sa članom 38 pravila doktorskih studija kandidat je dio sopstvenih istraživanja vezanih za doktorsku disertaciju publikovao u časopisu sa **(SCI/SCIE)** liste kao prvi autor.
Spisak radova doktoranda iz oblasti doktorskih studija koje je publikovao u časopisima

sa (upisati odgovarajuću listu)

Spisak radova iz oblasti doktorskih studija koje je kandidat publikovao u časopisima sa SCI/SCIE liste:

[1] LJ. Stanković, and M. Brajović, "Analysis of the Reconstruction of Sparse Signals in the DCT Domain Applied to Audio Signals," IEEE/ACM Transactions on Audio, Speech, and Language Processing, vol. 26, no.7, July 2018, pp.1216-1231, DOI: 10.1109/TASLP.2018.2819819
Link na rad: https://ieeexplore.ieee.org/document/8327444
Informacija o IMPACT faktoru časopisa:
https://ieeexplore.ieee.org/xpl/RecentIssue.jsp?punumber=6570655

[2] M. Brajović, I. Orović, M. Daković, and S. Stanković, "Compressive Sensing of Sparse Signals in the Hermite Transform Basis," IEEE Transactions on Aerospace and Electronic Systems, Volume: 54, Issue: 2, April 2018, pp. 950 - 967, DOI: 10.1109/TAES.2017.2768938
Link na rad: https://ieeexplore.ieee.org/document/8093654
Informacija o IMPACT faktoru časopisa:
https://ieeexplore.ieee.org/xpl/RecentIssue.jsp?punumber=7

[3] M. Brajović, S. Stanković, and I. Orović, "Analysis of noisy coefficients in the discrete Hermite transform domain with application in signal denoising and sparse signal reconstruction," Signal Processing, vol. 150, September 2018, https://doi.org/10.1016/j.sigpro.2018.04.007
Link na rad:
https://www.sciencedirect.com/science/article/pii/S0165168418301348
Informacija o IMPACT faktoru časopisa:
https://www.journals.elsevier.com/signal-processing

[4] M. Brajović, I. Stanković, M. Daković, C. Ioana, and LJ. Stanković, "Error in the Reconstruction of Nonsparse Images," Mathematical Problems in Engineering, Volume 2018 (2018), Article ID 4314527, 10 pages https://doi.org/10.1155/2018/4314527
Link na rad: https://www.hindawi.com/journals/mpe/2018/4314527/
Informacija o IMPACT faktoru časopisa:
https://www.hindawi.com/journals/mpe/

[5] LJ. Stanković, D. Mandic, M. Daković, and M. Brajović, "Time-frequency decomposition of multivariate multicomponent signals," Signal Processing, Volume 142, January 2018, pp. 468-479, http://dx.doi.org/10.1016/j.sigpro.2017.08.001
Link na rad:
https://www.sciencedirect.com/science/article/pii/S0165168417302839
Informacija o IMPACT faktoru časopisa:
https://www.journals.elsevier.com/signal-processing

[6] M. Brajović, V. Popović-Bugarin, I. Djurović, and S. Djukanović, "Post-processing of Time-Frequency Representations in Instantaneous Frequency Estimation Based on Ant Colony Optimization," Signal Processing, Vol. 138, September 2017, pp. 195–210, http://dx.doi.org/10.1016/j.sigpro.2017.03.022.
Link na rad:
https://www.sciencedirect.com/science/article/pii/S0165168417301160
https://www.journals.elsevier.com/signal-processing

Informacija o IMPACT faktoru časopisa:

[7] M. Brajović, I. Orović, M. Daković, and S. Stanković, "On the Parameterization of Hermite Transform with Application to the Compression of QRS Complexes," Signal Processing, vol. 131, pp. 113-119, February 2017.
Link na rad:
https://www.sciencedirect.com/science/article/pii/S0165168416301931
Informacija o IMPACT faktoru časopisa:
https://www.journals.elsevier.com/signal-processing

[8] M. Brajović, I. Orović, M. Daković, and S. Stanković, "Gradient-based signal reconstruction algorithm in the Hermite transform domain," Electronics Letters, Volume 52, Issue 1, pp.41-43, 2016.
Link na rad: https://ieeexplore.ieee.org/document/7374834
Informacija o IMPACT faktoru časopisa:
http://digital-library.theiet.org/content/journals/el

Radovi publikovani u drugim časopisima:

[9] M. Brajović, A. Draganić, I. Orović, and S. Stanković, "Sparse Representation of FHSS Signals in the Hermite Transform Domain," Telfor Journal, Vol. 9, No. 2, 2017.

[10] M. Brajović, LJ. Stanković, and M. Daković, "Reconstruction of non-stationary signals with missing samples using S-method and a gradient-based reconstruction algorithm," ETF Journal of Electrical Engineering, Vol. 21, No. 1, 2015.

Međunarodne konferencije (indeksirane u bazi SCOPUS):

[11] M. Brajović, I. Stanković, C. Ioana, M. Daković, and LJ. Stanković, "Reconstruction of Rigid Body with Noncompensated Acceleration After Micro-Doppler Removal," *5th International Workshop on Compressed Sensing applied to Radar, Multimodal Sensing, and Imaging (CoSeRa)*, Siegen, Germany, September 2018.

[12] LJ. Stanković, M. Brajović, I. Stanković, C. Ioana, and M. Daković, "Analysis of Initial Estimate Noise in the Sparse Randomly Sampled ISAR Signals," *5th International Workshop on Compressed Sensing applied to Radar, Multimodal Sensing, and Imaging (CoSeRa)*, Siegen, Germany, September 2018.

[13] I. Stanković, M. Brajović, M. Daković, and C. Ioana, "Effect of Random Sampling on Noisy Nonsparse Signals in Time-Frequency Analysis," *26th European Signal Processing Conference EUSIPCO 2018*, Rome, Italy, September 2018.

[14] M. Brajović, LJ. Stanković, M. Daković, and D. Mandic, "Additive Noise Influence on the Bivariate Two-Component Signal Decomposition," 7th Mediterranean Conference on Embedded Computing, MECO 2018, Budva, Montenegro, June 2018.

[15] M. Brajović, LJ. Stanković, and M. Daković, "Micro-Doppler removal in radar imaging in the case of non-compensated rigid body acceleration," 2018 23rd International Scientific-Professional Conference on Information Technology (IT), Zabljak, Montenegro, 2018, pp. 1-4, February 19-24, doi: 10.1109/SPIT.2018.8350451

[16] M. Brajović, S. Vujović, I. Orović, and S. Stanković, "Coefficient Tresholding in the Gradient Reconstruction Algorithm for Signals Sparse in the Hermite Transform Basis," Applications of Intelligent Systems 2018 (APPIS 2018), Las Palmas De Gran Canaria, 8-12 January 2018

[17] Z. Vulaj, M. Brajović, A. Draganić, and I. Orović, "Detection of Irregular QRS

Complexes using Hermite Transform and Support Vector Machine," 59th International Symposium ELMAR-2017, Zadar, Croatia, 2017

[18] LJ. Stanković, M. Brajović, M. Daković, and D. Mandic, "Two-component Bivariate Signal Decomposition Based on Time-Frequency Analysis," 22nd International Conference on Digital Signal Processing IEEE DSP 2017, August 23-25, London, United Kingdom

[19] M. Brajović, I. Orović, M. Daković, and S. Stanković, "The Reconstruction of 2D Sparse Signals by Exploiting Transform Coefficients Variances," 17th IEEE Int. Conference on Smart Technologies, IEEE EUROCON 2017

[20] Z. Vulaj, A. Draganić, M. Brajović, and I. Orović, "A tool for ECG signal analysis using standard and optimized Hermite transform," 6th Mediterranean Conference on Embedded Computing, MECO 2017, Bar, Montenegro

[21] M. Daković, I. Stanković, M. Brajović, and LJ. Stanković, "Sparse Signal Reconstruction Based on Random Search Procedure," 40th International Convention on Information and Communication Technology, Electronics and Microelectronics MIPRO, Opatija, Croatia, May 2017

[22] M. Daković, T. Ružić, T. Rogač, M. Brajović, and B. Lutovac, "Neural Networks Application to Neretva Basin Hydro-meteorological Data," 13th Symposium on Neural Networks and Applications NEUREL 2016, November 2016, Belgrade, Serbia

[23] M. Brajović, I. Orović, and S. Stanković, "The Optimization of the Hermite transform: Application Perspectives and 2D Generalization," 24th Telecommunications Forum TELFOR 2016, November 2016, Belgrade, Serbia.

[24] M. Brajović, B. Lutovac, I. Orović, M. Daković, and S. Stanković, "Sparse Signal Recovery Based on Concentration Measures and Genetic Algorithm," 13th Symposium on Neural Networks and Applications NEUREL 2016, Belgrade, Serbia, November 2016

[25] M. Brajović, A. Draganić, I. Orović, and S. Stanković, "FHSS signal sparsification in the Hermite transform domain," 24th Telecommunications Forum TELFOR 2016, November 2016, Belgrade, Serbia

[26] I. Stančić, M. Brajović, I. Orović, and J. Musić, "Compressive sensing for reconstruction of 3D point clouds in smart systems," 24th International Conference on Software, Telecommunications and Computer Networks (SoftCOM 2016), Split, Croatia, September 2016

[27] M. Brajović, I. Orović, M. Daković, and S. Stanković, "Representation of Uniformly Sampled Signals in the Hermite Transform Domain," 58th International Symposium ELMAR-2016, Zadar, Croatia, Sept. 2016.

[28] M. Brajović, I. Orović, M. Daković, and S. Stanković, "Compressive Sensing of Signals Sparse in 2D Hermite Transform Domain," 58th International Symposium ELMAR-2016, Zadar, Croatia, Sept. 2016

[29] M. Brajović, M. Daković, and LJ. Stanković, "Convexity of the l1-norm based Sparsity Measure with Respect to the Missing Samples as Variables," 5th Mediterranean Conference on Embedded Computing, MECO 2016, Bar, June 2016

[30] M. Brajović, I. Orović, M. Daković, and S. Stanković, "The Analysis of Missing Samples in Signals Sparse in the Hermite Transform Domain," 23rd Telecommunications Forum TELFOR, Belgrade, 2015

[31] A. Draganić, M. Brajović, I. Orović, and S. Stanković, "A Software Tool for Compressive

Sensing based Time-Frequency Analysis," 57th International Symposium ELMAR-2015, Zadar, Croatia

[32] M. Brajović, and V. Popović-Bugarin, "Instantaneous Frequency Estimation Using Ant Colony Optimization and Wigner Distribution," 4th Mediterranean Conference on Embedded Computing, MECO 2015, Budva, Montenegro, June 2015.

Radovi izloženi na regionalnim i nacionalnim konferencijama

[33] M. Brajović, LJ. Stanković, and M. Daković, "Reconstruction of non-stationary signals with missing samples using S-method and a gradient-based reconstruction algorithm," Informacione Tehnologije - IT 2015, Žabljak, Montenegro, February 2015

Obrazloženje mentora o korišćenju doktorske disertacije u publikovanim radovima

Doktorand MSc Miloš Brajović je većinu svojih istraživanja na kojima je zasnovana doktorska disertacija prezentovao kroz 8 radova, koji su publikovani u renomiranim međunarodnim časopisima sa SCI/SCIE liste, sa **kumulativnim IMPACT Factor-om 21.27**. Na 6 radova, kandidat je **prvi** autor. Dio rezultata je objavljen i u radovima (njih ukupno **22**) koji su izloženi na međunarodnim konferencijama koje su indeksirane u bazi SCOPUS, zatim kroz dva rada u drugim časopisima i kroz jedan rad publikovan na lokalnoj/regionalnoj konferenciji. Treba istaći da je doktorand autor i drugih radova mimo oblasti disertacije, što se može vidjeti iz bibliografije koja je data u prilogu ovog obrasca. U nastavku slijedi obrazloženje ključnih rezultata publikovanih kroz 8 radova u renomiranim međunarodnim časopisima, koji predstavljaju i temelj predmetne doktorske disertacije.

Naučni rad *"Analysis of the Reconstruction of Sparse Signals in the DCT Domain Applied to Audio Signals"* publikovan je u renomiranom časopisu IEEE/ACM Transactions on Audio, Speech, and Language Processing sa IMPACT Factor-om **2.95** i u njemu je predstavljena originalna analiza uticaja nedostajućih odbiraka na rekonstrukciju signala rijetkih u domenu Diskretne kosinusne transformacije (DCT), kao i analiza performansi različitih algoritama za rekonstrukciju signala na osnovu redukovanog skupa dostupnih odbiraka (mjerenja). Diskretna kosinusna transformacija je direktno povezana sa Diskretnom Furijeovom transformacijom. Rad sadrži opsežne numeričke rezultate, uključujući i razmatranje aspekata primjene u rekonstrukciji realnih audio signala koji su oštećeni impulsnim smetnjama. Sadržaj rada je obrađen u trećoj glavi disertacije.

U naučnom radu *"Analysis of noisy coefficients in the discrete Hermite transform domain with application in signal denoising and sparse signal reconstruction"*, koji je publikovan u renomiranom časopisu IEEE Transactions on Aerospace and Electronic Systems sa IMPACT Factor-om **2.063,** razmatrano je kompresivno odabiranje u domenu Hermitske transformacije, koje uključuje detaljnu teorijsku analizu uticaja nedostajućih odbiraka na Hermitske transformacione koeficijente, probabilističku analizu procesa rekonstrukcije ali i analizu performansi novopredloženih pristupa za rekonstrukciju signala koji imaju rijetku reprezentaciju u Hermitskom domenu. Rezultati su, pored velikog broja opsežnih numeričkih eksperimenata, verifikovani i kroz rekonstrukciju realnih UWB komunikacionih/radarskih signala. Sadržaj rada je obrađen u drugoj glavi disertacije.

U naučnom radu *"Analysis of noisy coefficients in the discrete Hermite transform domain with application in signal denoising and sparse signal reconstruction"*, publikovanom u renomiranom naučnom časopisu Signal Processing, sa IMPACT Factor-om **3.47**, analizira se uticaj aditivnog šuma na koeficijente

diskretne Hermitske transformacije. U radu je predložen pristup za uklanjanje aditivnog šuma, uz posebno razmatranje primjena u kontekstu realnih biomedicinskih EKG signala i komunikacionih UWB signala. Analiza je inkorporirana u algoritam za rekonstrukciju signala iz konteksta kompresivnog odabiranja. Sadržaj rada pokriven je u drugoj glavi doktorske disertacije.

Rad *"Error in the Reconstruction of Nonsparse Images"* publikovan u renomiranom časopisu Mathematical problems in Engineering, sa IMPACT Factor-om **1.145**, sadrži analizu kompresivnog odabiranja u domenu dvodimenzione DCT. U radu je izveden egzaktan izraz za energiju greške u rekonstrukciji signala koji nijesu rijetki u ovom domenu, a rekonstruisani su uz pretpostavku o rijetkosti. Posebno razmatran kontekst primjene odnosi se na digitalne slike. Sadržaj rada je obrađen u trećoj glavi disertacije.

Dekompozicija multivarijantnih multikomponentnih signala koja je zasnovana na mjerama koncentraicije iz konteksta kompresivnog odabiranja, razmatrana je u radu „*Time-frequency decomposition of multivariate multicomponent signals*", koji je publikovan u renomiranom časopisu Signal Processing, sa IMPACT Factor-om **3.47**. Predloženi pristup omogućava izdvajanje nestacionarnih komponenti signala uprkos njihovom preklapanju u vremensko-frekvencijskoj ravni, što predstavlja veoma značajan prilog rješavanju problema koji je odavno poznat u vremensko-frekvencijskoj analizi. Sadržaj rada je obrađen u četvrtoj glavi doktorske disertacije.

U radu *"Post-processing of Time-Frequency Representations in Instantaneous Frequency Estimation Based on Ant Colony Optimization"* koji je publikovan u renomiranom časopisu Signal Processing, sa IMPACT Factor-om **3.47**, predložen je novi algoritam za estimaciju trenutne frekvencije u uslovima izloženosti signala jakom aditivnom šumu. Algoritam je zasnovan na vremensko-frekvencijskoj reprezentaciji koja je poznata pod nazivom Wigner-ova distribucija, i optimizacionom pristupu poznatom pod nazivom Optimizacija mravlje kolonije. Wigner-ova distribucija predstavlja Furijeovu transformaciju specifično definisane autokorelacione funkcije. Najbitniji aspekti ovog rada obrađeni su u četvrtoj glavi doktorske disertacije.

Koncept mjera koncentracije iz konteksta kompesivnog odabiranja je u radu *"On the Parameterization of Hermite Transform with Application to the Compression of QRS Complexes"* primijenjen na optimizaciju parametara diskretne Hermitske tranformacije, konkretno, faktora skaliranja vremenske ose i faktora pomjeraja po vremenskoj osi baznih funkcija ove transformacije. Rad je publikovan u časopisu Signal Processing, sa IMPACT Factor-om **3.47.** Posebno važan doprinos u radu jeste razmatranje kompresije QRS kompleksa, specifičnih djelova EKG signala sa bitnom primjenom u medicinskoj dijagnostici i liječenju. Rad je obrađen u drugoj glavi disertacije.

Konačno, u radu *"Gradient-based signal reconstruction algorithm in the Hermite transform domain"* predstavljen je gradijentni pristup za rekonstrukciju signala koji su rijetki u Hermitskom domenu. Rad je publikovan u renomiranom časopisu Electronics Letters izdavača IET, sa IMPACT Factor-om **1.232**. U radu je posebno razmatrana primjena na kompresivno odabiranje QRS kompleksa. Problematika razmatrana u radu pokrivena je u drugoj glavi disertacije.

Jedan dio rezultata kandidata publikovan je i kroz 22 rada izložena na renomiranim međunarodnim konferencijama koje su indeksirane u bazi SCOPUS, uključujući i konferenciju EUSIPCO, koja je široko poznata kao jedna od najznačajnih konferencija u svijetu u oblasti

obrade signala, zatim konferencije MECO, CoSeRa, DSP i brojne druge konferencije veoma prepoznatljivog međunarodnog renomea.
Datum i ovjera (pečat i potpis odgovorne osobe)
U Podgorici, 26.10.2018.

Prilog dokumenta sadrži:

1. Potvrdu o predaji doktorske disertacije organizacionoj jedinici
2. Odluku o imenovanju komisije za pregled i ocjenu doktorske disertacije
3. Kopiju rada publikovanog u časopisu sa odgovarajuće liste
4. Biografiju i bibliografiju kandidata
5. Biografiju i bibliografiju članova komisije za pregled i ocjenu doktorske disertacije sa potvrdom o izboru u odgovarajuće akademsko zvanje i potvrdom da barem jedan član komisije nije u radnom odnosu na Univerzitetu Crne Gore

Broj: 02/1- 1633

Datum: 26. 10. 2018.

Na osnovu službene evidencije i dokumentacije Elektrotehničkog fakulteta u Podgorici, izdaje se

POTVRDA

Mr Miloš Brajović, student doktorskih studija na Elektrotehničkom fakultetu u Podgorici, dana 19.10.2018. godine dostavio je ovom Fakultetu doktorsku disertaciju pod nazivom: „Analiza algoritama za rekonstrukciju signala rijetkih u Hermitskom i Furijeovom transformacionom domenu", na dalji postupak.

D E K A N,

Prof. dr Zoran Veljović

Univerzitet Crne Gore
ELEKTROTEHNIČKI FAKULTET

81000 Podgorica, Dž. Vašingtona bb, tel. (020) 245 839, fax: (020) 245 873
Ž.R. 510-255-51, **PIB:** 02016702 302, **PDV:** 30/31-03951-6

Broj: 02/1-1633/1

Datum: 26.10. 2018

Na osnovu člana 64 Statuta Univerziteta Crne Gore, u vezi sa članom 41 Pravila doktorskih studija, na predlog Komisije za doktorske studije, Vijeće Elektrotehničkog fakulteta u Podgorici, na sjednici od 26.10.2018. godine, donijelo je

ODLUKU

I Utvrđuje se da su ispunjeni uslovi iz Pravila doktorskih studija za dalji rad na doktorskoj disertaciji „**Analiza algoritama za rekonstrukciju signala rijetkih u Hermitskom i Furijeovom transformacionom domenu**" kandidata mr **Miloša Brajovića.**

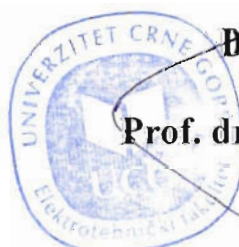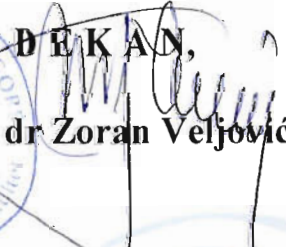**II Predlaže se Komisija za ocjenu navedene doktorske disertacije, u sastavu:**

1. Dr Ljubiša Stanković, redovni profesor Elektrotehničkog fakulteta Univerziteta Crne Gore,
2. Dr Miloš Daković, redovni profesor Elektrotehničkog fakulteta Univerziteta Crne Gore,
3. Prof. dr Danilo Mandić, Department of Electrical and Electronic Engineering, Imperial College London, London, UK.

Komisija iz tačke II ove Odluke podnijeće Izvještaj Vijeću Fakulteta u roku od 45 dana od dana imenovanja.

-VIJEĆE ELEKTROTEHNIČKOG FAKULTETA-

DEKAN,

Prof. dr Zoran Veljović

Dostavljeno:
- Senatu,
- Centru za doktorske studije,
- u dosije,
- a/a.

SPISAK RADOVA KOJI SADRŽE REZULTATE DOKTORSKE DISERTACIJE

Radovi iz vodećih časopisa (SCI/SCIE list)

[1] LJ. Stanković, and M. Brajović, "Analysis of the Reconstruction of Sparse Signals in the DCT Domain Applied to Audio Signals," IEEE/ACM Transactions on Audio, Speech, and Language Processing, vol. 26, no.7, July 2018, pp.1216-1231, DOI: 10.1109/TASLP.2018.2819819

[2] M. Brajović, I. Orović, M. Daković, and S. Stanković, "Compressive Sensing of Sparse Signals in the Hermite Transform Basis," IEEE Transactions on Aerospace and Electronic Systems, Volume: 54, Issue: 2, April 2018, pp. 950 - 967, DOI: 10.1109/TAES.2017.2768938

[3] M. Brajović, S. Stanković, and I. Orović, "Analysis of noisy coefficients in the discrete Hermite transform domain with application in signal denoising and sparse signal reconstruction," Signal Processing, vol. 150, September 2018, https://doi.org/10.1016/j.sigpro.2018.04.007

[4] M. Brajović, I. Stanković, M. Daković, C. Ioana, and LJ. Stanković, "Error in the Reconstruction of Nonsparse Images," Mathematical Problems in Engineering, Volume 2018 (2018), Article ID 4314527, 10 pages https://doi.org/10.1155/2018/4314527

[5] LJ. Stanković, D. Mandic, M. Daković, and M. Brajović, "Time-frequency decomposition of multivariate multicomponent signals," Signal Processing, Volume 142, January 2018, pp. 468-479, http://dx.doi.org/10.1016/j.sigpro.2017.08.001

[6] M. Brajović, V. Popović-Bugarin, I. Djurović, and S. Djukanović, "Post-processing of Time-Frequency Representations in Instantaneous Frequency Estimation Based on Ant Colony Optimization," Signal Processing, Vol. 138, September 2017, pp. 195–210, http://dx.doi.org/10.1016/j.sigpro.2017.03.022.

[7] M. Brajović, I. Orović, M. Daković, and S. Stanković, "On the Parameterization of Hermite Transform with Application to the Compression of QRS Complexes," Signal Processing, vol. 131, pp. 113-119, February 2017.

[8] M. Brajović, I. Orović, M. Daković, and S. Stanković, "Gradient-based signal reconstruction algorithm in the Hermite transform domain," Electronics Letters, Volume 52, Issue 1, pp.41-43, 2016

Radovi publikovani u drugim časopisima:

[9] M. Brajović, A. Draganić, I. Orović, and S. Stanković, "Sparse Representation of FHSS Signals in the Hermite Transform Domain," Telfor Journal, Vol. 9, No. 2, 2017.

[10] M. Brajović, LJ. Stanković, and M. Daković, "Reconstruction of non-stationary signals with missing samples using S-method and a gradient-based reconstruction algorithm," ETF Journal of Electrical Engineering, Vol. 21, No. 1, 2015.

Međunarodne konferencije (indeksirane u bazi SCOPUS):

[11] M. Brajović, I. Stanković, C. Ioana, M. Daković, and LJ. Stanković, "Reconstruction of Rigid Body with Noncompensated Acceleration After Micro-Doppler Removal," *5th International Workshop on Compressed Sensing applied to Radar, Multimodal Sensing, and Imaging (CoSeRa)*, Siegen, Germany, September 2018.

[12] LJ. Stanković, M. Brajović, I. Stanković, C. Ioana, and M. Daković, "Analysis of Initial Estimate Noise in the Sparse Randomly Sampled ISAR Signals," *5th International Workshop on Compressed Sensing applied to Radar, Multimodal Sensing, and Imaging (CoSeRa)*, Siegen, Germany, September 2018.

[13] I. Stanković, M. Brajović, M. Daković, and C. Ioana, "Effect of Random Sampling on Noisy Nonsparse Signals in Time-Frequency Analysis," *26th European Signal Processing Conference EUSIPCO 2018*, Rome, Italy, September 2018.

[14] M. Brajović, LJ. Stanković, M. Daković, and D. Mandic, "Additive Noise Influence on the Bivariate Two-Component Signal Decomposition," 7th Mediterranean Conference on Embedded Computing, MECO 2018, Budva, Montenegro, June 2018.

[15] M. Brajović, LJ. Stanković, and M. Daković, "Micro-Doppler removal in radar imaging in the case of non-compensated rigid body acceleration," 2018 23rd International Scientific-Professional Conference on Information Technology (IT), Zabljak, Montenegro, 2018, pp. 1-4, February 19-24, doi: 10.1109/SPIT.2018.8350451

[16] M. Brajović, S. Vujović, I. Orović, and S. Stanković, "Coefficient Tresholding in the Gradient Reconstruction Algorithm for Signals Sparse in the Hermite Transform Basis," Applications of Intelligent Systems 2018 (APPIS 2018), Las Palmas De Gran Canaria, 8-12 January 2018

[17] Z. Vulaj, M. Brajović, A. Draganić, and I. Orović, "Detection of Irregular QRS Complexes using Hermite Transform and Support Vector Machine," 59th International Symposium ELMAR-2017, Zadar, Croatia, 2017

[18] LJ. Stanković, M. Brajović, M. Daković, and D. Mandic, "Two-component Bivariate Signal Decomposition Based on Time-Frequency Analysis," 22nd International Conference on Digital Signal Processing IEEE DSP 2017, August 23-25, London, United Kingdom

[19] M. Brajović, I. Orović, M. Daković, and S. Stanković, "The Reconstruction of 2D Sparse Signals by Exploiting Transform Coefficients Variances," 17th IEEE Int. Conference on Smart Technologies, IEEE EUROCON 2017

[20] Z. Vulaj, A. Draganić, M. Brajović, and I. Orović, "A tool for ECG signal analysis using standard and optimized Hermite transform," 6th Mediterranean Conference on Embedded Computing, MECO 2017, Bar, Montenegro

[21] M. Daković, I. Stanković, M. Brajović, and LJ. Stanković, "Sparse Signal Reconstruction Based on Random Search Procedure," 40th International Convention on Information and Communication Technology, Electronics and Microelectronics MIPRO, Opatija, Croatia, May 2017

[22] M. Daković, T. Ružić, T. Rogač, M. Brajović, and B. Lutovac, "Neural Networks Application to Neretva Basin Hydro-meteorological Data," 13th Symposium on Neural Networks and Applications NEUREL 2016, November 2016, Belgrade, Serbia

[23] M. Brajović, I. Orović, and S. Stanković, "The Optimization of the Hermite transform: Application Perspectives and 2D Generalization," 24th Telecommunications Forum TELFOR 2016, November 2016, Belgrade, Serbia.

[24] M. Brajović, B. Lutovac, I. Orović, M. Daković, and S. Stanković, "Sparse Signal Recovery Based on Concentration Measures and Genetic Algorithm," 13th Symposium on Neural Networks and Applications NEUREL 2016, Belgrade, Serbia, November 2016

[25] M. Brajović, A. Draganić, I. Orović, and S. Stanković, "FHSS signal sparsification in the Hermite transform domain," 24th Telecommunications Forum TELFOR 2016, November 2016, Belgrade, Serbia

[26] I. Stančić, M. Brajović, I. Orović, and J. Musić, "Compressive sensing for reconstruction of 3D point clouds in smart systems," 24th International Conference on

Software, Telecommunications and Computer Networks (SoftCOM 2016), Split, Croatia, September 2016

[27] M. Brajović, I. Orović, M. Daković, and S. Stanković, "Representation of Uniformly Sampled Signals in the Hermite Transform Domain," 58th International Symposium ELMAR-2016, Zadar, Croatia, Sept. 2016.

[28] M. Brajović, I. Orović, M. Daković, and S. Stanković, "Compressive Sensing of Signals Sparse in 2D Hermite Transform Domain," 58th International Symposium ELMAR-2016, Zadar, Croatia, Sept. 2016

[29] M. Brajović, M. Daković, and LJ. Stanković, "Convexity of the l1-norm based Sparsity Measure with Respect to the Missing Samples as Variables," 5th Mediterranean Conference on Embedded Computing, MECO 2016, Bar, June 2016

[30] M. Brajović, I. Orović, M. Daković, and S. Stanković, "The Analysis of Missing Samples in Signals Sparse in the Hermite Transform Domain," 23rd Telecommunications Forum TELFOR, Belgrade, 2015

[31] A. Draganić, M. Brajović, I. Orović, and S. Stanković, "A Software Tool for Compressive Sensing based Time-Frequency Analysis," 57th International Symposium ELMAR-2015, Zadar, Croatia

[32] M. Brajović, and V. Popović-Bugarin, "Instantaneous Frequency Estimation Using Ant Colony Optimization and Wigner Distribution," 4th Mediterranean Conference on Embedded Computing, MECO 2015, Budva, Montenegro, June 2015.

Radovi izloženi na regionalnim i nacionalnim konferencijama

[33] M. Brajović, LJ. Stanković, and M. Daković, "Reconstruction of non-stationary signals with missing samples using S-method and a gradient-based reconstruction algorithm," Informacione Tehnologije - IT 2015, Žabljak, Montenegro, February 2015

Compressive Sensing of Sparse Signals in the Hermite Transform Basis

MILOŠ BRAJOVIĆ, Student Member, IEEE
IRENA OROVIĆ, Member, IEEE
MILOŠ DAKOVIĆ, Member, IEEE
SRDJAN STANKOVIĆ, Senior Member, IEEE
University of Montenegro, Podgorica, Montenegro

An analysis of the influence of missing samples in signals exhibiting sparsity in the Hermite transform domain is presented. Based on the statistical properties derived for the Hermite coefficients of randomly undersampled signal, the probability of success in detection of signal components support is determined and a threshold for the detection of signal components is provided. It is a crucial step in a simple noniterative and iterative matching pursuit (MP)-based algorithm for compressive sensing signal reconstruction.

I. INTRODUCTION

The Hermite transform (HT) of signals has drawn significant research attention during the last decades, since it exhibits some important properties and high suitability for several signal processing applications [1]–[10]. Namely, the HT, referred to as the Hermite expansion, is a signal representation with promising applicability in different research fields, due to specific waveforms of its basis functions. The Hermite functions (HF) have been recognized as a suitable basis for the representation and compression of QRS complexes in ECG signals [1]–[3]. Other important applications include: image processing, [4], [5], computed tomography, analysis of protein structure, optics [7], and radar signals [9]. As the ultra-wideband (UWB) signal waveforms are closely related to Gaussian function and its derivatives, these signals can be sparsely represented in the HT domain [10]–[16], in contrary to the standard discrete Fourier transform (DFT) domain, where these signals have a wide frequency band. The sparsity of UWB signals has been explored in recent works [17], [18]. Interesting mathematical properties of the HT have led to fast computation algorithms, which are important in state-of-the-art research in biomedicine and biology [1]. Their good localization properties have found some important applications in time-frequency signal analysis, radar signal processing, and processing of video signals [9], [12].

A small number of nonzero coefficients in a transform domain is the basic assumption for successful application of compressive sensing (CS) algorithms in the reconstruction of signals with missing samples [25]–[57]. This useful property of a transform to represent the analyzed signals with small number of nonzero coefficients is identified as sparsity and measured by ℓ_0-norm of the transform coefficients. When considering the HT, this assumption is valid for many of the mentioned types of signals, for instance the QRS complexes [1]–[3] or UWB signals [10], [17], [18].

The CS of UWB signals has been recently studied [17]–[19]. The research on the sparsification of these signals was done [18]. CS and sparse signal theory have many important applications in radar signals and systems: channel estimation, waveform design, radar imaging [19]–[20], [22]. CS and sparse signal processing are done in numerous transform domains, where usually the concrete application and signal nature dictate the domain amenability for the signal representation and processing [34]–[49]. The theory presented in this paper could be also developed for other transform domains.

The reduced set of observations in CS is usually a consequence of a sampling strategy, but signal samples can be also intentionally omitted using robust signal processing due to a high noise corruption [23], [24]. Therefore, our basic motivation is to analyze the influence of missing samples on the HT and signal reconstruction possibilities. The signal reconstruction is based on finding the solution of an undetermined system of equations, having the sparsest transform representation. Direct solution using minimization of ℓ_0-norm is an NP-hard problem. In order to apply

iterative minimization algorithms for finding the solution, e.g., linear programming approaches and methods, the reconstruction constraint is relaxed, and ℓ_1-norm is used as a measure of sparsity [26]–[28]. The solution can be obtained by using ℓ_1-norm minimization via convex optimization algorithms, for example, primal-dual interior point methods. Other approaches are iterative procedures such as orthogonal matching pursuit (OMP), gradient pursuit, CoSaMP [25]–[27], etc. An interesting iterative reconstruction algorithm which uses a steepest descent based procedure to achieve the minimization of the ℓ_1-norm is used in [3]. However, this type of algorithm suffers from slow convergence, as it starts to oscillate when approaching the solution [33]. Additionally, with a large number of missing samples (unknowns), it may take a significant number of iterations for the algorithm to converge, requiring significant calculation time. Therefore, in this paper we consider alternative reconstruction approaches.

Noniterative approach for signal reconstruction that avoids the constraint relaxation is presented in [32]. It is based on the comprehensive analysis of the missing samples influence to the sparse transform, namely, the DFT [23]. However, due to the specific form and different properties of the HT, a direct generalization of the mentioned reconstruction approach to this sparsity domain is not possible. This fact led us to the theoretical contributions presented in this study. The presented results can be directly applied in an matching pursuit (MP)-based algorithm, where, in each iteration, blocks of detected signal components positions are exploited in the reconstruction. If component amplitudes have close values, then this type of MP becomes a single-iteration algorithm [32]. Besides the derivations modeling the missing samples influence on the HT basis, the relation with the coherence index condition is established. We analyze the influence of the additive Gaussian noise on the CS reconstruction, and the error in the reconstruction of nonsparse signals using the presented approaches with the sparsity assumption.

The paper is organized as follows. The HT and its placement into the CS framework is done in Section II. The detailed analysis of the missing samples influence on the HT is provided in Section III. The analysis of the additive noise influence and the nonsparse signal reconstruction with sparsity assumption is done in Section IV. The theory extension toward the simple reconstruction approach is done in Section V. Section VI provides numerical evaluation of the presented theory along with reconstruction example, and the concluding remarks are presented in the end of the paper.

II. THEORETICAL BACKGROUND

A. Discrete HT

The Hermite polynomial of order p, widely known among the orthogonal polynomials, can be defined as [1]–[8]

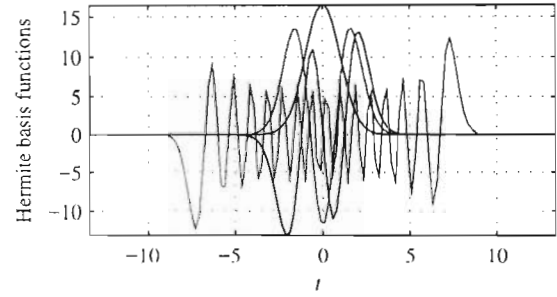$$H_p(t) = (-1)^p e^{t^2} \frac{d^p(e^{-t^2})}{dt^p}. \tag{1}$$

Fig. 1. Examples of Hermite basis functions: blue - $\psi_0(t_m)$, red - $\psi_2(t_m)$, black - $\psi_3(t_m)$, and mangenta - $\psi_{29}(t_m)$.

The pth order HF is related with the pth order Hermite polynomial as follows:

$$\psi_p(t, \sigma) = \left(\sigma 2^p p! \sqrt{\pi}\right)^{-1/2} e^{-t^2/(2\sigma^2)} H_p(t/\sigma) \tag{2}$$

where the constant σ is used to "stretch" and "compress" HFs, in order to provide a representation with desirable properties [1]. Few HFs are shown in Fig. 1. In further analysis, for the sake of simplicity, it will be assumed that this constant is $\sigma = 1$. The HFs can be calculated in a recursive manner, which is an advantage in applications [1], [6]. The orthogonality of the Hermite polynomials and the orthonormality of HFs, often makes them suitable as a basis for signal representation. The Hermite expansion or HT is given by [1]–[6]

$$f(t) = \sum_{p=0}^{N} c_p \psi_p(t, \sigma) \tag{3}$$

where c_p denotes the pth order Hermite coefficient

$$c_p = \int_{-\infty}^{\infty} f(t)\psi_p(t)dt, \quad p = 0, 1, \ldots, M - 1. \tag{4}$$

An infinite number $N \to \infty$ of HFs is needed for the exact representation of the continuous signal $f(t)$. However, in numerous applications, a finite number of M HFs can be used with a certain approximation error, e.g., [1], [2], [12]. For the numerical calculation of the integral (4) quadrature approximation techniques are used, [1], [8], [9] and usually interpreted as discrete form of the HT. Since it provides significant calculation advantages over other approximations, the Gauss–Hermite quadrature is considered

$$c_p = \frac{1}{M} \sum_{m=1}^{M} \frac{\psi_p(t_m)}{[\psi_{M-1}(t_m)]^2} f(t_m), \quad p = 0, 1, \ldots, M - 1 \tag{5}$$

where t_m is used to denote zeros of the Mth order Hermite polynomial. If continuous HFs are sampled at the zeros of the Mth order Hermite polynomial, then the summation (3) becomes a complete representation of the analyzed signal. For a signal of length M, the complete set of discrete HFs used for unique signal representation consists of exactly M functions [1], [3].

Note that the discrete HT satisfies the following properties [1], [3], [7]:

$$\frac{1}{M} \sum_{m=1}^{M} \frac{\psi_p(t_m)}{(\psi_{M-1}(t_m))^2} \psi_k(t_m) = \delta(p-k) \qquad (6)$$

and

$$\frac{1}{M} \sum_{p=0}^{M-1} \frac{\psi_p(t_m)}{(\psi_{M-1}(t_m))^2} \psi_p(t_n) = \delta(t_n - t_m) \qquad (7)$$

with m and n being the indices of Hermite polynomial roots t_m and t_n, respectively. In the further analysis, it will be assumed that the analyzed signal (of length M) and HFs are sampled at the roots t_m of the Mth order Hermite polynomial and the index m will be used to denote the discrete time index.

Having in mind previous definitions, the expansion using M HFs can be written in a matrix–vector notation. Let us introduce the vector $\mathbf{c} = [c_0, c_1, \ldots, c_{M-1}]^T$ consisted of Hermite coefficients c_p, and vector $\mathbf{f} = [f(1), f(2), \ldots, f(M)]^T$ consisted of M signal samples. Using the Gauss–Hermite approximation formula (5), we obtain the inverse transform matrix $\mathbf{\Psi}$ consisted of M HFs as

$$\mathbf{\Psi} = \begin{bmatrix} \psi_0(1) & \psi_1(1) & \ldots & \psi_{M-1}(1) \\ \psi_0(2) & \psi_1(2) & \cdots & \psi_{M-1}(2) \\ \vdots & \vdots & \ddots & \vdots \\ \psi_0(M) & \psi_1(M) & \cdots & \psi_{M-1}(M) \end{bmatrix}.$$

Based on previous matrix definition, the inverse HT for the case of discrete signals can be written as

$$\mathbf{f} = \mathbf{\Psi} \mathbf{c}. \qquad (8)$$

B. CS and HT

The CS procedure based on the randomly selected/acquired signal values can be modeled by using a random measurement matrix $\mathbf{\Phi}$

$$\mathbf{y}_{cs} = \mathbf{\Phi} \mathbf{f} = \mathbf{\Phi} \mathbf{\Psi} \mathbf{c} = \mathbf{A}_{cs} \mathbf{c}$$

where $\mathbf{y}_{cs}$ denotes the vector of available samples of the analyzed signal. The matrix $\mathbf{A}_{cs}$ is obtained from the inverse transform matrix $\mathbf{\Psi}$, in our case the inverse HT matrix, by omitting the rows corresponding to the positions of missing samples. The available samples have random positions denoted by

$$m \in \mathbf{M}_A = \{m_1, m_2, \ldots, m_{M_A}\} \subseteq \mathbf{M} = \{1, 2, \ldots, M\}. \qquad (9)$$

The index m on the discrete grid corresponds to the sampling point t_m. In order to obtain the reconstructed signal values, an undetermined system of M_A linear equations and M unknowns have to be solved. It is known that such systems may have infinitely many solutions, but the idea behind the CS is to find the sparsest one. The signal reconstruction problem is usually reduced to the problem of identifying signal support (positions and values of nonzero

coefficients in the sparsity domain). Here, we assume that the observed signal is sparse in the HT domain, i.e., $K \ll M$ and K being the number of nonzero Hermite coefficients. The nonzero coefficients have indices from the set

$$\mathbf{P} = \{p_1, p_2, \ldots, p_K\} \subseteq \mathbf{P}_M = \{0, 1, \ldots, M-1\}, K \ll M.$$

The problem of finding the sparsest solution corresponds to the minimization problem of the form

$$\min \|\mathbf{c}\|_0 \text{ subject to } \mathbf{y}_{cs} = \mathbf{A}_{cs} \mathbf{c}. \qquad (10)$$

It is known that the ℓ_0-norm cannot be used in the direct minimization, and thus (10) is usually reformulated using the ℓ_1-norm, making possible to apply linear programming or other efficient approaches. On the other hand, if the signal support is known or appropriately estimated within a set $\hat{\mathbf{P}}$ containing $K \leq \hat{K} \leq M$ elements such that $\mathbf{P} \subseteq \hat{\mathbf{P}}$, the reconstruction is achieved using the pseudoinversion

$$\mathbf{c}_K = \left(\mathbf{A}_{csK}^T \mathbf{A}_{csK}\right)^{-1} \mathbf{A}_{csK}^T \mathbf{y}_{cs} \qquad (11)$$

often exploited in standard matching pursuit approaches. The matrix $\mathbf{A}_{csK}$ is the submatrix of the matrix $\mathbf{A}_{cs}$ with omitted columns corresponding to positions $p \notin \hat{\mathbf{P}}$.

Our aim is to analyze the influence of missing samples of the compressed sensed signal to the Hermite domain representation. If we are able to model and characterize the effects caused in the sparsity domain as a consequence of compressive sampling, then we can develop efficient procedures to determine signal support in the transform domain, defined by a proper set $\hat{\mathbf{P}}$ suitable for the reconstruction.

III. ANALYSIS OF MISSING SAMPLES

Consider the HT of the signal $f(m)$ sampled at the points corresponding to the zeros of the Mth order Hermite polynomial. The coefficients of the Hermite expansion using M HFs are calculated by

$$c_p = \frac{1}{M} \sum_{m=1}^{M} \frac{\psi_p(m)}{(\psi_{M-1}(m))^2} f(m). \qquad (12)$$

The fact that the signal samples are placed on a grid corresponding to Hermite polynomials zeros allows a high accuracy level in the Gauss–Hermite quadrature calculation. We will assume that the analyzed signal $f(m)$ is sparse in the Hermite domain, so that it can be represented as

$$f(m) = \sum_{i=1}^{K} A_i \psi_{p_i}(m) \qquad (13)$$

with K being the number of signal components, A_i is used to denote amplitudes of signal component, and p_i denotes the order of the HF. For the multicomponent signal (13), the HT coefficients (12) are calculated as follows:

$$c_p = \sum_{m=1}^{M} \sum_{i=1}^{K} \frac{A_i}{M} \frac{\psi_p(m)\psi_{p_i}(m)}{(\psi_{M-1}(m))^2}, \ p = 0, \ldots, M-1. \qquad (14)$$

Normalized signal components are multiplied by the basis functions $\psi_p(m)/(\psi_{M-1}(m))^2$ to produce the signal

$y_p(m)$ defined as

$$y_p(m) = \frac{A_i}{M} \frac{\psi_p(m)\psi_{p_i}(m)}{(\psi_{M-1}(m))^2}, \quad i = 1, \ldots, K. \qquad (15)$$

Values of the signal denoted with $y_p(m)$ are from the set

$$\Omega = \left\{ \frac{A_i}{M} \frac{\psi_p(m)\psi_{p_i}(m)}{(\psi_{M-1}(m))^2}, m = 1, \ldots, M, i = 1, \ldots, K \right\}. \qquad (16)$$

Since property (6) holds, it is obvious that the members of Ω satisfy the relation

$$\sum_{m=1}^{M} y_p(m) = y_p(1) + y_p(2) + \cdots + y_p(M) = 0 \qquad (17)$$

for given $p \neq p_i$, $i = 1, 2 \ldots, K$.

In order to analyze the CS signal case, a subset consisted of $M_A \leq M$ randomly positioned available samples from the set Ω is considered

$$\Theta = \{y_p(m_1), y_p(m_2), \ldots, y_p(m_{M_A})\} \subseteq \Omega. \qquad (18)$$

Therefore, $M_Q = M - M_A$ samples are unavailable. Since the HT is a linear transform, and the inner products are performed between signal values and the basis functions, if some samples are omitted from the signal, it produces the same result as if these samples assume zero values. Consequently, a reduced number of signal samples can be considered as a complete set of samples, where some of them are affected by an additive noise modeled as

$$\eta(m) = \begin{cases} -y_p(m), & \text{for } m \in \mathbf{N} \backslash \mathbf{M_A} \\ 0, & \text{for } m \in \mathbf{M_A}. \end{cases}$$

Under this assumption, in the following sections we will derive the statistical properties of HT coefficients on the signal and nonsignal positions.

A. Monocomponent Signal Case

First the one-component signal case, with $K = 1$, $A_i = 1$, and $p_i = p_0$, will be considered. The HT over the set of available samples from Θ can be written in the following form:

$$Y_p = c_p \approx \sum_{i=1}^{M_A} y_p(m_i) = \sum_{m=1}^{M} [y_p(m) + \eta(m)]. \qquad (19)$$

It is a random variable, formed as a sum of M_A randomly positioned available samples. Here, the derivation of the mean value and the variance of the random variable Y_p in the Hermite domain will be conducted. As it will be shown, this variable has different statistical properties at the position $p = p_0$ corresponding to the signal component, and at other positions $p \neq p_0$ in the Hermite domain corresponding to the noise.

1) *Statistical Properties of the HT at the Nonsignal Positions:* For the nonsignal positions $p \neq p_0$, the random variable $Y_{p \neq p_0}$ corresponds to an additive transform domain noise [23]. Applying property (6) and using the fact that samples $y_p(m_i)$ from the set Θ have random positions, we

conclude that $E\{y_p(m_i)\} = E\{y_p(m)\} = 0$. Consequently, the random variable $Y_{p \neq p_0}$ has a zero mean value

$$\mu_N = E\{Y_{p \neq p_0}\} = E\left\{ \sum_{i=1}^{M_A} y_p(m_i) \right\} = \sum_{i=1}^{M_A} E\{y_p(m_i)\} = 0. \qquad (20)$$

The variance of the real-valued random variable $Y_{p \neq p_0}$ is defined as follows:

$$\sigma_N^2 = \text{var}\{Y_{p \neq p_0}\} = E\{|Y_{p \neq p_0}|^2\} = E\{(Y_{p \neq p_0})(Y_{p \neq p_0})^*\}$$

$$= E\left\{ \sum_{i=1}^{M_A} \sum_{j=1}^{M_A} y_p(m_i)y_p(m_j) \right\}$$

$$= \underbrace{E\left\{ \sum_{i=1}^{M_A} y_p^2(m_i) \right\}}_{S1} + \underbrace{E\left\{ \sum_{i=1}^{M_A} \sum_{\substack{j=1 \\ i \neq j}}^{M_A} y_p(m_i)y_p(m_j) \right\}}_{S2}. \qquad (21)$$

According to (17), we have

$$E\{y_p(m_i)(y_p(1) + y_p(2) + \cdots + y_p(M))\} = 0$$

$$\text{i.e., } E\{y_p(m_i)y_p(1)\} + E\{y_p(m_i)y_p(2)\}$$

$$+ \cdots + E\{y_p(m_i)y_p(M)\} = 0 \qquad (22)$$

for $i = 1, 2, \ldots, M$.

Terms $E\{y_p(m_i)y_p(m_j)\}$, for $i \neq j$ are equally distributed

$$E\{y_p(m_i)y_p(m_j)\} = B, \quad i \neq j. \qquad (23)$$

The expectation $E\{y_p(m_i)y_p(m_j)\}$ for $i \neq j$ can be derived from property (7), where $p \neq p_0$ is considered

$$E\{y_p(m_i)y_p(m_i)\}$$

$$= E\left\{ \frac{1}{M^2} \frac{\psi_p(m_i)\psi_p(m_i)}{(\psi_{M-1}(m_i))^2} \frac{\psi_{p_0}(m_i)\psi_{p_0}(m_i)}{(\psi_{M-1}(m_i))^2} \right\}$$

$$= E\left\{ \frac{1}{M} \frac{\psi_p(m_i)\psi_p(m_i)}{(\psi_{M-1}(m_i))^2} \right\} E\left\{ \frac{1}{M} \frac{\psi_{p_0}(m_i)\psi_{p_0}(m_i)}{(\psi_{M-1}(m_i))^2} \right\}.$$

The appearances of the HFs of orders p and p_0 (i.e., their values at instant m_i) are statistically independent events, and thus the expectations are separated. Due to property (7), we have

$$E\left\{ \frac{1}{M} \frac{\psi_p(m_i)\psi_p(m_i)}{(\psi_{M-1}(m_i))^2} \right\} = E\left\{ \frac{1}{M} \frac{\psi_{p_0}(m_i)\psi_{p_0}(m_i)}{(\psi_{M-1}(m_i))^2} \right\} = \frac{1}{M}. \qquad (24)$$

Thus, it can be easily concluded that

$$E\{y_p(m_i)y_p(m_i)\} = E\{y_p(m_i)\}E\{y_p(m_i)\} = 1/M^2. \qquad (25)$$

Since there are $M - 1$ terms given by (23) with the same expectation B for $i \neq j$ and one term with value (25) for $i = j$, (22) further produces $1/M^2 + (M-1)B = 0$.

The unknown B is therefore given by

$$E\{y_p(m_i)y_p(m_j)\} = B = \frac{-1}{M^2(M-1)}, \quad i \neq j. \qquad (26)$$

Since there are M_A terms in $S1$ summation in (21) and $M_A(M_A - 1)$ terms in $S2$ summation, we finally obtain the variance at the nonsignal positions (noise variance) as

$$\sigma_N^2 = \text{var}\{Y_{p \neq p_0}\} = \frac{M_A}{M^2} + M_A(M_A - 1)B = \frac{M_A M - M_A^2}{M^2(M - 1)}. \tag{27}$$

We can conclude that the variance of the noise at nonsignal positions $p \neq p_0$ in the Hermite domain depends only on the number of available samples M_A and the signal length M. According to the central limit theorem, the observed random variable $Y_{p \neq p_0}$ has the normal distribution.

2) *Statistical Properties of HT at the Signal Components Positions:* The statistics of the Hermite expansion coefficients of the CS signal for the case $p = p_0$ is quite different. Since that the product $\psi_{p_0}(m_i)\psi_{p_0}(m_i)$ in the considered case depends on the values of the specific HF $\psi_{p_0}(m_i)$, whose samples are missing at random positions, it can be concluded that $Y_{p = p_0}$ is also a random variable with normal distribution, according to the central limit theorem.

In the case of $y_{p=p_0}(m_i) = y_{p_0}(m_i)$ with M_A available randomly positioned samples from the set Θ, the expected (mean) value of the random variable $Y_{p=p_0}$ follows from (24)

$$\mu_s = E\{Y_{p=p_0}\} = \frac{1}{M} E\left\{ \sum_{i=1}^{M_A} \frac{\psi_{p_0}(m_i)\psi_{p_0}(m_i)}{(\psi_{M-1}(m_i))^2} \right\} = \frac{M_A}{M} \tag{28}$$

and all the values of the random variable $Y_{p=p_0}$ are equally distributed. Since the mean value is not equal to zero, variance is calculated as follows:

$$\sigma_s^2 = \text{var}\{Y_{p=p_0}\} = E\left\{|Y_{p=p_0} - \mu_s|^2\right\} = E\left\{Y_{p=p_0}^2\right\} - |\mu_s|^2. \tag{29}$$

Using the definition of the random variable $Y_{p=p_0}$, the variance σ_s^2 can be expanded in the form

$$\sigma_s^2 = E\left\{ \sum_{i=1}^{M_A} y_{p_0}^2(m_i) \right\} + E\left\{ \sum_{i=1}^{M_A} \sum_{\substack{j=1 \\ i \neq j}}^{M_A} y_{p_0}(m_i) y_{p_0}(m_j) \right\} - |\mu_s|^2. \tag{30}$$

The calculation of individual terms in (30) will differ from the previous case ($p \neq p_0$). Starting from the orthogonality property (7) for $p = p_0$

$$y_{p_0}(1) + y_{p_0}(2) + \cdots + y_{p_0}(M) = 1 \tag{31}$$

and multiplying left and right side by $y_{p_0}(m_i)$, $i \in \{1, \ldots, M\}$, the expectation is calculated as

$$E\left\{ y_{p_0}(m_i)y_{p_0}(1) + y_{p_0}(m_i)y_{p_0}(2) + \cdots + y_{p_0}(m_i)y_{p_0}(M) \right\}$$
$$= E\left\{ y_{p_0}(m_i) \right\} \tag{32}$$

i.e.. $\quad E\left\{ y_{p_0}(m_i)y_{p_0}(1) \right\} + \cdots + E\left\{ y_{p_0}(m_i)y_{p_0}(M) \right\}$
$$= 1/M. \tag{33}$$

In the case $i \neq j$, $M - 1$ terms are equally distributed and satisfy

$$E\{y_{p_0}(m_i)y_{p_0}(1)\} = \cdots = E\{y_{p_0}(m_i)y_{p_0}(M)\}$$
$$= E\{y_{p_0}(m_i)y_{p_0}(m_j)\} = D.$$

For $i = j$ the expectations $E\{y_{p_0}^2(m_i)\}$, $i = 1, \ldots M$ cannot be estimated as $E\{y_{p_0}(m_i)\}E\{y_{p_0}(m_i)\}$, because statistical independence requirement is not satisfied. Hence, in order to determine $E\{y_{p_0}^2(m_i)\}$ let us observe the summation

$$E\left\{ \sum_{i=1}^{M} y_{p_0}^2(m_i) \right\} = \frac{1}{M^2} \sum_{i=1}^{M} \left(\frac{\psi_{p_0}^2(m_i)}{(\psi_{M-1}(m_i))^2} \right)^2$$
$$= \frac{1}{M^2} \sum_{i=1}^{M} a(m_i, p_0, M) = \frac{1}{M^2} P_{p_0} \tag{34}$$

which corresponds to the energy of the monocomponent signal defined by the HF of order p_0. Note that the following notation is used:

$$\left(\frac{\psi_{p_0}^2(m_i)}{(\psi_{M-1}(m_i))^2} \right)^2 = a(m_i, p_0, M)$$

where $m_i \in \{m_1, m_2, \ldots, m_{M_A}\}$ are random positions of M_A available samples. It can be concluded that

$$E\{a(m_i, p_0, M)\} = E\{a(p_0, M)\} = P_{p_0}/M^3.$$

Now, (33) becomes

$$a(p_0, M) + (M - 1)D = 1/M$$

and then D can be expressed as

$$D = \frac{1 - Ma(p_0, M)}{M(M - 1)}. \tag{35}$$

The variance (30) of the considered random variable can be now written as

$$\sigma_s^2 = M_A a(p_0, M) + M_A(M_A - 1)D - \left(\frac{M_A}{M}\right)^2$$
$$- M_A a(p_0, M) + M_A(M_A - 1)\frac{1 - Ma(p_0, M)}{M(M - 1)}$$
$$- \left(\frac{M_A}{M}\right)^2. \tag{36}$$

After a simple rearrangement of the previous equation, the variance can be expressed as

$$\sigma_s^2 = \text{var}\{Y_{p=p_0}\} = \frac{MM_A - M_A^2}{M^2(M - 1)}\left(M^2 a(p_0, M) - 1\right)$$
$$= \sigma_N^2 \left(\frac{1}{M} \sum_{m=1}^{M} \left(\frac{\psi_{p_0}^2(m_i)}{(\psi_{M-1}(m_i))^2} \right)^2 - 1 \right)$$
$$= \sigma_N^2 \left(\frac{P_{p_0}}{M} - 1 \right). \tag{37}$$

The relation (37) describing how the variance depends on the Hermite coefficient order p_0 is evaluated also experimentally. The results are shown in Fig. 2, for the signal of length $M = 200$, with $M_A = 120$ available samples.
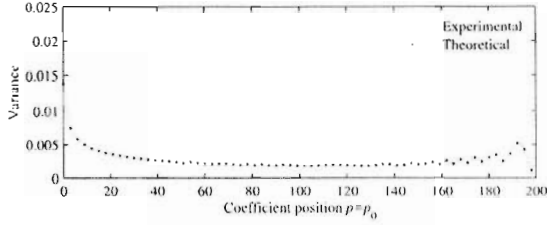
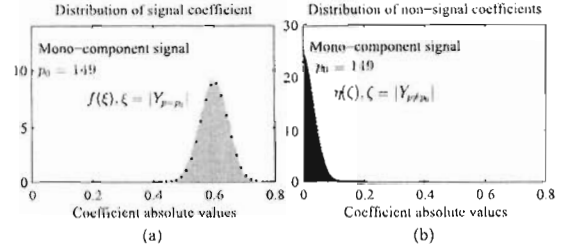Fig. 2. Variance at the position of the signal component as a function of the component position p_0.

Fig. 3. Histograms and pdfs for the absolute values of Hermite coefficients at: (a) signal and (b) nonsignal positions. Histograms [(a) gray surface for coefficient at signal position and (b) blue surface for coefficients at nonsignal positions] are simulated for signal with $M_A = 120$ out of $M = 200$ samples and amplitude $A_0 = 1$, based on 20 000 independent signal realizations with randomly positioned missing samples. Theoretical results (dots) are obtained using folded normal distribution (39) calculated with estimated value of variance (38) and half normal distribution (40) with variance (27).

The numerical calculation of the variance is obtained using 5000 independent realizations of the signal with randomly positioned missing samples.

When only M_A out of M samples are available, the known bias in the amplitude should be compensated by M / M_A, while P_{p_0} can be estimated from the available set of samples

$$\tilde{P}_{p_0} = \sum_{i=1}^{M_A} \left(\frac{\psi_{p_0}^2(m_i)}{(\psi_{M-1}(m_i))^2} \right)^2.$$

Consequently, the variance at the signal component positions $p = p_0$, for an incomplete set of samples, can be estimated as

$$\tilde{\sigma}_s^2 = \frac{M}{M_A} \sigma_N^2 \left(\frac{\tilde{P}_{p_0}}{M} - 1 \right). \tag{38}$$

B. Probabilistic Analysis of the Detection Error for Hermite Coefficient Corresponding to Signal Component

According to the central limit theorem, both random variables $Y_{p=p_0}$ and $Y_{p \neq p_0}$ behave as Gaussian variables with their own mean values and variances. The derived mean values and variances will be used to define a method to distinguish between HT components corresponding to signal from those corresponding to noise caused by missing samples. This approach refers to the signal component detection. In the sequel, we consider the absolute values of the random variables $Y_{p=p_0}$ and $Y_{p \neq p_0}$. Given a normally distributed random variable $Y_{p=p_0}$ corresponding to the signal component in the HT domain, with mean value μ_s and variance σ_s^2 [given by (28) and (38) respectively], the random variable $\xi = |Y_{p=p_0}|$ has the folded normal distribution as the probability density function (pdf)

$$f(\xi) = \frac{1}{\sigma_s \sqrt{2\pi}} \left(\exp\left(-\frac{(\xi - \mu_s)^2}{2\sigma_s^2} \right) + \exp\left(-\frac{(\xi + \mu_s)^2}{2\sigma_s^2} \right) \right) \tag{39}$$

see Fig. 3(a). The random variable which corresponds to the noise, $Y_{p \neq p_0}$, has also the normal pdf, while its absolute value, $\zeta = |Y_{p \neq p_0}|$ has the half normal distribution, since the mean value is zero

$$\eta(\zeta) = \frac{\sqrt{2}}{\sigma_N \sqrt{\pi}} \exp\left(-\frac{\zeta^2}{2\sigma_N^2} \right) \tag{40}$$

with variance given by (27). This distribution along with the experimentally obtained histogram is shown in Fig. 3(b).

The probability that the random variable $\zeta = |Y_{p \neq p_0}|$ is smaller than χ is

$$P_N(\chi) = \int_0^\chi \frac{\sqrt{2}}{\sigma_N \sqrt{\pi}} \exp\left(-\frac{\zeta^2}{2\sigma_N^2} \right) d\zeta = \text{erf}\left(\frac{\chi}{\sqrt{2}\sigma_N} \right). \tag{41}$$

The total number of noise-alone components is $M - 1$. Probability that $M - 1$ independent noise components are smaller than χ is

$$P_{NN}(\chi) = \text{erf}\left(\frac{\chi}{\sqrt{2}\sigma_N} \right)^{M-1}. \tag{42}$$

The probability that at least one noise component is larger than χ is $P_{NL}(\chi) = 1 - P_{NN}(\chi)$. In the standard detection theory terminology, null hypothesis $\mathcal{H}_0$ can be formulated as: c_p is a noise-only Hermite coefficient, that is, $\mathcal{H}_0 : c_p = Y_{p=p_0}$. The other hypothesis can be formulated as: c_p is the Hermite coefficient at the signal position, that is, $\mathcal{H}_1 : c_p = Y_{p \neq p_0}$.

If the signal value is within ξ and $\xi + d\xi$ with probability $f(\xi)d\xi$, it will be misdetected if at least one noise component is above ξ. This will occur with the probability $P_{NL}(\xi)f(\xi)d\xi = (1 - P_{NN}(\xi))f(\xi)d\xi$. Considering all possible values of ξ, the misdetection occurs with probability:

$$P_E = \int_0^\infty (1 - P_{NN}(\xi))f(\xi)d\xi = \frac{1}{\sigma_s \sqrt{2\pi}}$$
$$\times \int_0^\infty \left(1 - \text{erf}\left(\frac{\xi}{\sqrt{2}\sigma_N} \right)^{M-1} \right)$$
$$\times \left(\exp\left(-\frac{(\xi - \mu_s)^2}{2\sigma_s^2} \right) + \exp\left(-\frac{(\xi + \mu_s)^2}{2\sigma_s^2} \right) \right) d\xi. \tag{43}$$

Previous relation is the probability of error in the detection of signal component for a one component sparse signal. It can be approximated using the assumption that

the signal component is deterministic, and equal to its mean value $\mu_s = E\{Z_{p-p_s}\}$. A rough approximation of the error probability follows[1]:

$$P_E \approx 1 - \mathrm{erf}\left(\frac{\mu_s}{\sqrt{2}\sigma_N}\right)^{M-1}. \tag{44}$$

This approximation can be corrected with 1.5 standard deviation of the signal component if we use the fact that signal components in Hermite domain smaller than the mean value contribute more to the error than those above the mean value

$$P_E \approx 1 - \mathrm{erf}\left(\frac{\mu_s - 1.5\sigma_s}{\sqrt{2}\sigma_N}\right)^{M-1}. \tag{45}$$

In the case of signal with nonunit amplitude A_0, mean value is multiplied by the amplitude, while the signal variance is multiplied by A_0^2, for both analyzed cases.

The false alarm probability (probability that noise-only coefficients are above the threshold χ) is given by

$$P_{FA}(\chi) = 1 - P_{NN}(\chi) = 1 - \mathrm{erf}\left(\frac{\chi}{\sqrt{2}\sigma_N}\right)^{M-1}$$

whereas the true detection probability (probability that the signal component is above the threshold χ) can be calculated as

$$P_{TD}(\chi) = \int_\chi^\infty \left(\exp\left(-\frac{(\xi - \mu_s)^2}{2\sigma_s^2}\right) + \exp\left(-\frac{(\xi + \mu_s)^2}{2\sigma_s^2}\right)\right) d\xi$$

for given threshold χ. For given signal length M, these probabilities are functions of the number of available samples M_A, as they appear in both variances and mean values.

Based on $P_{FA}(\chi)$ and $P_{TD}(\chi)$ the receiver operating characteristic curve (ROC) can be calculated. Let us observe a one-component signal of length $M = 200$ with unity amplitude $A = 1$, vary the threshold $0 \leq \chi \leq 1$ and calculate ROC curves [showing $P_{TD}(\chi)$ versus $P_{FA}(\chi)$] for different numbers of available samples: $M_A \in \{10, 20, 40, 60\}$. The CS noise appears as a consequence of single signal component, and therefore, we expect that the signal-only coefficient can be detected with a small number of available samples. The results are shown in Fig. 4.

If we calculate the expression of P_E for the considered numbers of available samples, we obtain the following error probabilities: $P_E(M_A = 10) = 0.44$, $P_E(M_A = 20) = 0.16$, $P_E(M_A = 40) = 0.01$, and $P_E(M_A = 60) = 0.0$. It is in accordance with the results shown in Fig. 4.

C. Analysis of Multicomponent Signals

The previous analysis will be extended to the multicomponent signals. In the multicomponent signal case, analyzed

[1] The expected value and variance of a random variable with folded normal distribution are given as: $E\{\zeta\} = \sigma_s\sqrt{\frac{2}{\pi}}\exp(\frac{-\mu_s^2}{2\sigma_s^2}) - \mu_s\mathrm{erf}(\frac{-\mu_s}{\sqrt{2}\sigma_s}) \cong \mu_s$ and $\mathrm{var}\{\zeta\} = \mu_s^2 + \sigma_s^2 - \{\sigma_s\sqrt{\frac{2}{\pi}}\exp(\frac{-\mu_s^2}{2\sigma_s^2}) - \mu_s\mathrm{erf}(\frac{-\mu_s}{\sqrt{2}\sigma_s})\} \cong \sigma_s^2$.
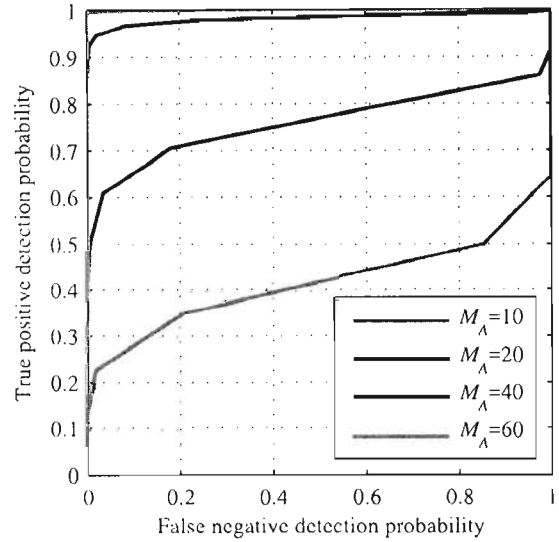
Fig. 4. ROC curves for the detection of single component, shown for various numbers of available samples.

signals $y_p(m) \in \Omega$ become

$$y_p(m) = \sum_{l=1}^K \frac{A_l}{M} \frac{\psi_p(t_m)\psi_{p_l}(t_m)}{(\psi_{M-1}(t_m))^2} \tag{46}$$

consisted of K components. Hermite coefficients calculated as

$$Y_p = c_p \approx \sum_{i=1}^{M_A} y_p(m_i) = \sum_{m=1}^M [y_p(m) + \eta(m)]$$

act as random variables. According to the previous results, in the case of K-component signal, the coefficients $Y_{p=p_i}$ at the signal position behave as a Gaussian variable, with mean value equal to

$$\mu_S = \sum_{l=1}^K A_l \frac{M_A}{M}\delta(p - p_l) \tag{47}$$

since the noise caused by missing samples is zero mean, as shown for the monocomponent case.

The variance at the points with no signal components is equal to

$$\sigma_N^2 = \mathrm{var}\{Y_{p \neq p_i}\} = \sum_{l=1}^K \sigma_{N,l}^2 = \frac{M_A M - M_A^2}{M^2(M-1)}\sum_{l=1}^K A_l^2 \tag{48}$$

since at the points $p \neq p_i$ the noise caused by missing samples from each signal component contributes, and these noisy components are uncorrelated and zero mean.

According to the presented monocomponent analysis, the ith signal component at the position $p = p_i$ has the variance equal to

$$\bar{\sigma}_{s_i}^2 \approx \frac{M_A M - M_A^2}{M^2(M-1)}\left(\frac{M}{M_A}A_i^2\left(\sum_{i=1}^{M_A}\left(\frac{\psi_{p_i}^2(m_i)}{(\psi_{M-1}(m_i))^2}\right)^2 - 1\right)\right)$$
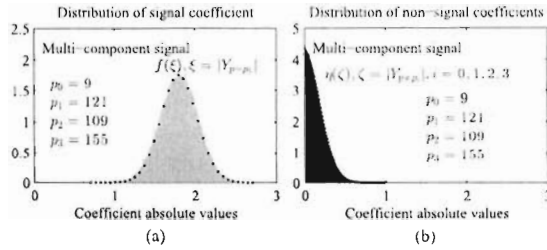
Fig. 5. Histograms and pdfs for the absolute values of Hermite coefficients at: (a) signal and (b) nonsignal positions. Histograms [(a) gray surface for coefficient at signal position and (b) blue surface for coefficients at nonsignal positions] are simulated for multicomponent signals with $M_A = 120$ out of $M = 200$ samples and amplitudes $A_0 = 1$, $A_1 = 3$, $A_2 = 4$, and $A_3 = 2$, based on 20 000 independent signal realizations with randomly positioned available samples. Theoretical results are obtained using folded normal distribution calculated with estimated value of variance (49), and half normal distribution with variance (48).

where the subscript s_i denotes that it originates from the ith signal component. Additionally, the noise caused by missing samples from other $K - 1$ components is also present at the position of the ith signal component. This means that, besides the random variable Y_{p-p_i}, the sum of $K - 1$ random variables $Y_{p \neq p_i}$ with $p \in \mathbf{P} = \{p_1, p_2, ..., p_K\}$ originating from other signal components also affects the ith signal position. Note that all random variables at the ith position are normally distributed. $K - 1$ random variables $Y_{p \neq p_i}$, $p \in \{p_1, p_2, ..., p_K\}$ are zero mean, while the random variable $Y_{p=p_i}$ has the mean value $\mu_{S,i} = A_i M_A / M$. The resulting variance at the ith signal position $p = p_i$ is finally

$$\sigma_i^2 = \tilde{\sigma}_{s_i}^2 + \sum_{\substack{l=1 \\ l \neq i}}^{K} \sigma_{N,l}^2 = \frac{M - M_A}{M(M-1)} \left(A_i^2 \left(\frac{\tilde{P}_{p_i}}{M} - 1 \right) \right.$$
$$\left. + \sum_{\substack{l=1 \\ l \neq i}}^{K} A_l^2 \right). \tag{49}$$

It can be concluded that the Hermite expansion coefficient at signal position $p = p_i$ will be modeled as the random variable $Y_{p=p_i}$ with normal distribution: $\mathcal{N}(M_A A_i / M, \sigma_i^2)$. Also, the coefficients corresponding to noise are modeled by the random variable $Y_{p \neq p_i}$ with normal distribution: $\mathcal{N}(0, \sigma_N^2)$ where σ_N^2 is given by (48).

As it is done for the monocomponent signal case, previous results can be used to derive the probability of error in the detection of signal components. The false signal component detection occurs when at least one noise component at positions $p \neq p_i$, $i \in \{1, 2, ..., K\}$ is above signal component at the position p_i. Recall that the absolute values of the random variables $Y_{p=p_i}$ and $Y_{p \neq p_i}$ have half normal and folded normal distributions, as shown on Fig. 5(a) and (b), respectively.

The random variable $\xi = |Y_{p=p_i}|$ has the pdf given by (39), with mean value equal to (47) and variance given

by (49). The random variable representing the noise $\zeta = |Y_{p \neq p_i}|$, is zero mean, with half normal pdf (40), where the variance is equal to (48). The probability that $M - K$ independent noise-alone points are smaller than χ is

$$P_{NN}(\chi) = \text{erf}\left(\frac{\chi}{\sqrt{2}\sigma_N} \right)^{M-K}. \tag{50}$$

Following the monocomponent signal case, the probability of error in the detection of the ith signal component in the multicomponent case has the form

$$P_{E_i} = \frac{1}{\sigma_i \sqrt{2\pi}} \int_0^\infty \left(1 - \text{erf}\left(\frac{\xi}{\sqrt{2}\sigma_N} \right)^{M-K} \right)$$
$$\times \left(\exp\left(-\frac{(\xi - \mu_{s_i})^2}{2\sigma_i^2} \right) + \exp\left(-\frac{(\xi + \mu_{s_i})^2}{2\sigma_i^2} \right) \right) d\xi. \tag{51}$$

Under the same assumptions as in the monocomponent signal case, this error can be approximated by

$$P_{E_i} \approx 1 - \text{erf}\left(\frac{\mu_{s_i} - 1.5\sigma_i}{\sqrt{2}\sigma_N} \right)^{M-K}. \tag{52}$$

D. Relation With the Coherence Index

Let us assume an OMP-based reconstruction [32]. In the worst case analysis, the maximal possible influence from other signal components on the detection of the strongest component occurs when all K components have equal (without loss of generality - unity) amplitudes. Assume that only M_A out of M randomly positioned samples are available. Mean value of each considered HT component is M_A / M.

The coherence factor for the matrix $\mathbf{A}_{cs}^T \mathbf{A}_{cs}$ is defined as follows:

$$\mu_{coh} = \max \left| \frac{M}{M_A} \sum_{\substack{m \\ l, p \neq p_i}}^{M_A} \frac{A_i}{M} \frac{\psi_p(m)\psi_{p_i}(m)}{(\psi_{M-1}(m))^2} \right|,$$
$$i = 1, 2, ..., K.$$

On the other side, the noise-only component at HT index p originating from the signal component p_i can be written in the following form:

$$n_p = \sum_{m=1, p \neq p_i}^{M_A} \frac{A_i}{M} \frac{\psi_p(m)\psi_{p_i}(m)}{(\psi_{M-1}(m))^2}.$$

It obviously can be related with the coherence index. If the noise originating from all signal components adds up at a nonsignal position $p \neq p_i$, then this noise-only coefficient has the maximal possible value

$$K \max |n_p| = K \frac{M_A}{M} \mu_{coh}.$$

Now let us observe the signal-only position $p = p_i$. The observed signal coefficient is corrupted by the CS noise originating from other $K - 1$ components. In the worst possible case, all these noise components add up in the direction opposite from the component mean value

(in this case M_A / M, in general, multiplied by the component's amplitude). Assuming the largest possible nose values $K \max |n_p|$, the resulting worst possible signal coefficient value is

$$\min \{c_{p_i}\} = \frac{M_A}{M} - (K - 1) \max |n_p| = \frac{M_A}{M}$$
$$- (K - 1) \frac{M_A}{M} \mu_{\text{coh}}.$$

The observed signal component can be detected if it is larger than the largest noise-only coefficient

$$\frac{M_A}{M} - (K - 1) \frac{M_A}{M} \mu_{\text{coh}} > K \frac{M_A}{M} \mu_{\text{coh}}$$

and this can be rearranged to the form of the well-known spark-based condition for the signal reconstruction

$$K < \frac{1}{2} \left(1 + \frac{1}{\mu_{\text{coh}}} \right). \tag{53}$$

This is a well-known and already established result in the CS theory.

IV. ADDITIVE NOISE INFLUENCE AND NONSPARSE SIGNAL RECONSTRUCTION

A. Additive Noise in Measurements

Previous analysis assumes measurements that are not affected by external noise. As noise is common in practical applications, previous analysis can be easily extended for noisy signal case. Assume that the measurements are affected by a white Gaussian noise with variance σ_ε^2. In this case, the total disturbance in the transform domain is caused by both the external noise and the noise caused by missing samples. It is easily shown that the additive white Gaussian noise has the following variance in the Hermite domain:

$$\sigma_{he}^2 = \frac{\sigma_\varepsilon^2}{M^2} \sum_{m=1}^{M} \frac{1}{\psi_{M-1}^2(t_m)}.$$

As these random variables are uncorrelated and Gaussian, for noise-only coefficients the total variance equals

$$\sigma_T^2 = \sigma_N^2 + \sigma_{he}^2 = \frac{M_A M - M_A^2}{M^2(M-1)} \sum_{l=1}^{K} A_l^2 + \sigma_{he}^2 \tag{54}$$

with constant $\sum_{m=1}^{M} \psi_{M-1}^{-2}(t_m)$ which is not dependent on measurements positions.

In order to keep the same probability $P_{\text{NN}}(T)$ that $M - K$ independent noise components are smaller than a threshold $\chi = T$, given in (50), the following condition should be satisfied [32]:

$$\frac{\frac{M_A(M - M_A)}{M^2(M-1)} \sum_{l=1}^{K} A_l^2}{\frac{M_A(M - M_A)}{M^2(M-1)} \sum_{l=1}^{K} A_l^2 + \sigma_{he}^2} = 1. \tag{55}$$

The approximation of the term $\sum_{l=1}^{K} A_l^2$ is easily obtained based on available measurements, using $\sum_{l=1}^{K} A_l^2 \approx$

$\frac{M}{M_A} \sum_{p=0}^{M-1} c_p^2$, thus, it can be considered as known. Therefore, for a given signal length M, number of available samples M_A and external noise variance σ_ε^2, we can determine M_i which represents the increased number of measurements required in the presence of noise, in order to keep the same probability of error as in the noiseless signal case.

The input SNR of signal with additive noise, when all samples are available is equal to

$$\text{SNR} = 10 \log \frac{\sum_{m=1}^{M} |f(t_m)|^2}{\sum_{m=1}^{M} |\varepsilon(t_m)|^2} = 10 \log \frac{E_f}{E_\varepsilon} \tag{56}$$

where $E_\varepsilon = M\sigma_\varepsilon^2$ and $E_f = \sum_{m=1}^{M} |f(t_m)|^2$. Signal components in the HT domain have mean value $\frac{M_A}{M} A_l$, $l \in \mathbf{P}$. In the reconstruction process, coefficients corresponding to signal components are amplified for a factor $\frac{M}{M_A}$. Assuming a successful CS reconstruction, a signal transform coefficient is equal to the coefficient of the original signal with all signal samples being used. If a small additive noise with variance σ_ε^2 exists in M_A measurements, then in one coefficient of the initial HT (calculated for the under sampled signal with zeros at missing samples positions) noise variance is multiplied with factor $\frac{M_A}{M}$.

The additive noise energy will be increased for $(\frac{M}{M_A})^2$ in each nonzero coefficient of the reconstructed signal. As the successful CS reconstruction provides exactly K nonzero Hermite coefficients corresponding to signal components, whereas other $M - K$ coefficients are equal to zero, the noise energy in the reconstructed signal remains within K nonzero coefficients.

The signal-to-noise ratio in the reconstructed signal is therefore

$$\text{SNR}_r = 10 \log \frac{\sum_{m=1}^{M} |f(t_m)|^2}{K \frac{M_A}{M} \left(\frac{M}{M_A} \right)^2 \sigma_\varepsilon^2} = 10 \log \frac{E_f}{\frac{K}{M_A} E_\varepsilon}.$$

This means that, in the reconstructed signal, initial SNR is increased for $-10 \log(K / M_A)$

$$\text{SNR}_r = \text{SNR} - 10 \log \left(\frac{K}{M_A} \right) \tag{57}$$

as $K < M_A$. Note that this result holds when the small additive noise is present in measurements, and the successful reconstruction of each K nonzero signal coefficients is possible. This also means that MP-based algorithms presented in the following section can be used to reduce additive noise, by intentionally reducing the number of available signal samples, and applying the reconstruction algorithm. Namely, if the smallest possible K is used, the residual additive noise will be, after the reconstruction, present in only K coefficients selected by the algorithm. The results are numerically verified in Section VI.

B. Nonsparse Signal Reconstruction

Let us observe a nonsparse signal with largest amplitudes $A_l, l = 1, 2, \dots, K$, having M_A out of M randomly positioned samples available. Assume that the signal is reconstructed as it was K sparse. Let $\mathbf{c}_K$ denotes the vector

having Hermite coefficients equal to A_l at the positions of signal components, $p = p_l$, $p_l \in \mathbf{P}$, $l = 1, \ldots, K$ and zeros at other positions, $p \neq p_l$ whereas $\mathbf{c}_R$ denotes HT coefficients vector of the reconstructed signal (with zeros at $p \neq p_l$), and $\mathbf{c}$ denotes the coefficients vector of the observed nonsparse signal, with all samples available. Vector $\mathbf{c}_K$ is therefore obtained by setting to zero all coefficients in the vector $\mathbf{c}$, at positions $p \neq p_l$

$$\mathbf{c}_K = \begin{cases} \mathbf{c}(p), & p \in \mathbf{P} \\ 0, & p \notin \mathbf{P}. \end{cases}$$

Each nonreconstructed component behaves as additive Gaussian noise with variance

$$\sigma_N^2 = \frac{M_A(M - M_A)}{M^2(M - 1)} A_l^2. \tag{58}$$

Therefore, all nonreconstructed components in transform domain will manifest as a noise with variance

$$\frac{M_A(M - M_A)}{M^2(M - 1)} \sum_{l=K+1}^{M} A_l^2.$$

After the reconstruction, the total noise energy, present in K reconstructed components as the consequence of the nonreconstructed components is equal to

$$\|\mathbf{c}_K - \mathbf{c}_R\|_2^2 = K \frac{M^2}{M_A^2} \frac{M_A(M - M_A)}{M^2(M - 1)} \sum_{l=K+1}^{M} A_l^2$$
$$= \frac{K(M - M_A)}{M_A(M - 1)} \sum_{l=K+1}^{M} A_l^2. \tag{59}$$

The energy of nonreconstructed components is equal to

$$\sum_{l=K+1}^{M} A_l^2 = \|\mathbf{c} - \mathbf{c}_K\|_2^2. \tag{60}$$

Therefore, the total error in the nonreconstructed components is

$$\|\mathbf{c}_K - \mathbf{c}_R\|_2^2 = \frac{K(M - M_A)}{M_A(M - 1)} \|\mathbf{c} - \mathbf{c}_K\|_2^2. \tag{61}$$

In the presence of additive Gaussian noise with variance σ_ε^2 whose values are below the level of reconstructed components, the total error becomes

$$\|\mathbf{c}_K - \mathbf{c}_R\|_2^2 = \frac{K(M - M_A)}{M_A(M - 1)} \|\mathbf{c} - \mathbf{c}_K\|_2^2 + K \frac{M}{M_A} \sigma_\varepsilon^2. \tag{62}$$

The results are numerically verified in Section VI.

V. DETECTION OF SIGNAL COMPONENTS AND SIGNAL RECONSTRUCTION ALGORITHM

A. Detection of Signal Component in the HT Domain

Due to its importance, we will consider in detail the probability that $M - K$ independent noise components are smaller than χ given by (50). This relation can give the threshold $\chi = T$ for the separation of signal components

and noise. Following (50) for $\chi = T$, the threshold value can be derived as follows:

$$T = \sqrt{2}\sigma_N \mathrm{erf}^{-1}\left((P_{NN}(T))^{\frac{1}{M-K}}\right) \approx \sqrt{2}\sigma_N$$
$$\times \mathrm{erf}^{-1}\left((P_{NN}(T))^{\frac{1}{M}}\right). \tag{63}$$

Note that K can be neglected in (63), since the number of components K is in general much lower than the number of samples M ($K \ll M$). The threshold is calculated for a given (desired) probability $P_{NN}(T)$, using the noise variance defined by (48). Furthermore, the function $\mathrm{erf}(x)$ can be approximated by [58], [59]

$$\mathrm{erf}(x) \approx \mathrm{sgn}(x)\sqrt{1 - \exp\left(-x^2 \frac{4/\pi + ax^2}{1 + ax^2}\right)} \tag{64}$$

with $a \approx 0.147$, and $x = T/(\sqrt{2}\sigma_N)$. Since $T \geq 0$ and $\sigma_N \geq 0$, and thus $x > 0$ we conclude that it always holds that $\mathrm{sgn}(x) = 1$. Then, according to (64), we have

$$(P_{NN}(T))^{\frac{1}{M}} = \sqrt{1 - \exp\left(-x^2 \frac{4/\pi + ax^2}{1 + ax^2}\right)}. \tag{65}$$

Taking the square and $\log(\cdot)$ on both sides of (65), we obtain

$$ax^4 + \left(\frac{4}{\pi} + a\log\left(1 - (P_{NN}(T))^{\frac{2}{M}}\right)\right)x^2$$
$$+ \log\left(1 - (P_{NN}(T))^{\frac{2}{M}}\right) = 0.$$

The previous equation can be solved by introducing the substitution $t = x^2$. There is only one positive solution (out of four) which represents the threshold value

$$T = \sigma_N \sqrt{\left(-4/\pi - aL + \sqrt{(4/\pi + aL)^2 - 4aL}\right)/a} \tag{66}$$

which is an approximation of the threshold (63) with $L = \log(1 - (P_{NN}(T))^{2/M})$ and $a \approx 0.147$ suitable for hardware realizations.

B. Threshold-Based Reconstruction Procedures

The previous analysis can be used to define a simple CS reconstruction procedure. The threshold T is used to determine the positions $\mathbf{P} = \{p_1, p_2, \ldots, p_K\}$ of signal components in the HT domain. If the estimated set of positions is such that $\mathbf{P} \subseteq \hat{\mathbf{P}}$ and $\mathrm{card}\{\hat{\mathbf{P}}\} \leq M_A$ with $K \ll M$, the reconstruction can be achieved using the pseudoinversion (11).

The reconstruction is performed using the procedures presented in Algorithm 1 and Algorithm 2.

Presented algorithms work in similar way as the OMP. In fact, the iterative form can be considered as a generalization of the OMP, reducing the number of iterations by setting the proper threshold levels for signal components detections. Let $\mathbf{e} = \mathbf{y}_{cs}$ at the beginning of the algorithm. Namely, in the OMP algorithm, the first element of the set $\hat{\mathbf{P}}$ is estimated as the position of the maximum in the vector

Algorithm 1: Single-iteration reconstruction.

Input:

Signal length M, number of available samples M_A, transform matrix $\boldsymbol{\Psi}$, available samples positions $\mathbf{M}_A = \{m_1, m_2, \ldots, m_{M_A}\}$, measurement vector $\mathbf{y}_{cs}$. Measurement matrix is: $\mathbf{A}_{cs} = \boldsymbol{\Psi}(\mathbf{M}_A)_r$, where $(\cdot)_r$ denotes that only rows $\mathbf{M}_A$ are used from $\boldsymbol{\Psi}$.

Calculations:

1. $P_{NN}(T) \leftarrow 0.99$
2. $\mathbf{c}_0 \leftarrow \mathbf{A}_{cs}^{-1}\mathbf{y}_{cs}$
3. $\sigma_N \leftarrow \sqrt{\frac{M_A M - M_A^2}{M^3(M-1)} \sum_{p=0}^{M-1} \frac{M}{M_A}|c_p|^2}$, $c_p \in \mathbf{c}_0$
4. $a \leftarrow 0.147$
5. $L \leftarrow \log(1 - (P_{NN}(T))^{2/M})$
6. $T \leftarrow$
   $\sigma_N \sqrt{(-4/\pi - aL + \sqrt{(4/\pi + aL)^2 - 4aL})/a}$
7. $\hat{\mathbf{P}} \leftarrow \arg\{|\mathbf{c}_0| > T\}$
8. $\mathbf{A}_{csK} \leftarrow \mathbf{A}_{cs}(\hat{\mathbf{P}})_k$, only columns with indexes $\hat{\mathbf{P}}$ are used
9. $\mathbf{c}_{KR} \leftarrow (\mathbf{A}_{csK}^T\mathbf{A}_{csK})^{-1}\mathbf{A}_{csK}^T\mathbf{y}_{cs}$

The reconstructed coefficient vector $\mathbf{c}_R$ contains values $\mathbf{c}_{KR}$ at positions $\hat{\mathbf{P}}$, and zeros at other positions.

Algorithm 2: Iterative reconstruction.

Input:

Signal length M, number of available samples M_A, transform matrix $\boldsymbol{\Psi}$, available samples positions $\mathbf{M}_A = \{m_1, m_2, \ldots, m_{M_A}\}$, measurement vector $\mathbf{y}_{cs}$ and required precision ε. Measurement matrix is: $\mathbf{A}_{cs} = \boldsymbol{\Psi}(\mathbf{M}_A)_r$, where $(\cdot)_r$ denotes that only rows $\mathbf{M}_A$ are used from $\boldsymbol{\Psi}$.

Calculations:

1. $\hat{\mathbf{P}} \leftarrow \emptyset$
2. $\mathbf{e} \leftarrow \mathbf{y}_{cs}$
3. $a \leftarrow 0.147$
4. $L \leftarrow \log(1 - (P_{NN}(T))^{2/M})$
While $\|\mathbf{e}\|_2^2 > \delta$ **do**
5. $\mathbf{c}_0 \leftarrow \mathbf{A}_{cs}^{-1}\mathbf{e}$
6. $\sigma_N \leftarrow$
   $\sqrt{\frac{M_A M - M_A^2}{M^2(M-1)} \sum_{p=0}^{M-1} \frac{M}{M_A}|c_p|^2}$, $c_p \in \mathbf{c}_0$
7. $T \leftarrow$
   $\sigma_N \sqrt{(-4/\pi - aL + \sqrt{(4/\pi + aL)^2 - 4aL})/a}$
8. $\hat{p} \leftarrow \arg\{|\mathbf{c}_0| > T\}$
9. $\hat{\mathbf{P}} \leftarrow \hat{\mathbf{P}} \cup \hat{p}$
10. $\mathbf{A}_{csK} \leftarrow \mathbf{A}_{cs}(\hat{\mathbf{P}})_k$
11. $\mathbf{c}_{KR} \leftarrow (\mathbf{A}_{csK}^T\mathbf{A}_{csK})^{-1}\mathbf{A}_{csK}^T\mathbf{y}_{cs}$
12. $\mathbf{y}_{\hat{p}} \leftarrow \mathbf{A}_{csK}\mathbf{c}_{KR}$
13. $\mathbf{e} \leftarrow \mathbf{y}_{cs} - \mathbf{y}_{\hat{p}}$
end while

The reconstructed coefficient vector $\mathbf{c}_R$ contains values $\mathbf{c}_{KR}$ at positions $\hat{\mathbf{P}}$, and zeros at other positions.

$\mathbf{c}_0 = \mathbf{A}_{cs}^{-1}\mathbf{e}$, which is in fact the HT of the signal whose missing samples assume zero values:

$$\hat{p}_1 \leftarrow \max\{|\mathbf{c}_0|\}.$$

This index is added in the empty set $\hat{\mathbf{P}} = \{\hat{p}_1\}$. Then, the partial sensing matrix $\mathbf{A}_1 = \mathbf{A}_{cs}(\hat{p}_1)_k$ is formed from the sensing matrix, using only column with index p_1. The first component is obtained by solving the system of measurement equations, using the well-known pseudoinversion

$$\mathbf{c}_1 = (\mathbf{A}_1^T\mathbf{A}_1)^{-1}\mathbf{A}_1^T\mathbf{y}_{cs}.$$

Then, the signal $\mathbf{y}_1 = \mathbf{A}_1\mathbf{c}_1$ is calculated. If $\mathbf{e} = \mathbf{y}_1$ holds, then the signal sparsity is 1, and the $\mathbf{c}_1$ is the problem solution. If this is not the case, then the estimated component is removed form $\mathbf{e}$, thus, forming the signal $\mathbf{e}_1 = \mathbf{e} - \mathbf{y}_1$. After this step, the second nonzero position is estimated. First, new $\mathbf{c}_0 = \mathbf{A}_{cs}^{-1}\mathbf{e}_1$ is calculated, and

$$\hat{p}_2 \leftarrow \max\{|\mathbf{c}_0|\}$$

is found. Then, the new set of component positions $\hat{\mathbf{P}} = \{\hat{p}_1, \hat{p}_2\}$ is formed. Pseudoinversion

$$\mathbf{c}_2 = (\mathbf{A}_2^T\mathbf{A}_2)^{-1}\mathbf{A}_2^T\mathbf{y}_{cs}$$

is calculated for the new partial sensing matrix $\mathbf{A}_2 = \mathbf{A}_{cs}(\hat{\mathbf{P}})_k$ now having two columns corresponding to the detected component positions. Vector $\mathbf{e}_2 = \mathbf{e} - \mathbf{y}_2$ is formed. If it is a zero vector the solution is found $\mathbf{y} = \mathbf{y}_2$. If not, the process is iteratively continued, until zero, or acceptable error is achieved.

Previous principle of the OMP algorithm is also used in Algorithm 1 and Algorithm 2. Our theoretical analysis enables us to change the criterion for the component detection. Namely, by detecting the set components, the number of iterations of the OMP can be significantly reduced. The number of OMP algorithm iterations equals the number of detected components. If the component amplitudes have close values, then Algorithm 1 can be used to reconstruct the signal in a single iteration, as the threshold T used in the criterion $\hat{\mathbf{P}} \leftarrow \arg\{|\mathbf{c}_0| > T\}$ will result in the set $\hat{\mathbf{P}}$ containing positions of all components. However, if this is not possible, as some components may have significantly lower values than the others, then Algorithm 2 can be used. Namely, it enables the detection of component positions blocks (all components above the threshold will be detected simultaneously). Therefore, we may say that the presented reconstruction procedures are greedy algorithms, completely analogous to the OMP, but with a reduced number of iterations.

VI. EXAMPLES

In order to validate the accuracy of variances derived in Section III, statistical analysis was performed with respect to the number of available samples, order of Hermite coefficients and signal length. Probabilities of detection error and their respective approximations are verified by experimental examples. The performance of reconstruction algorithm based on the derived threshold is demonstrated in the last example.
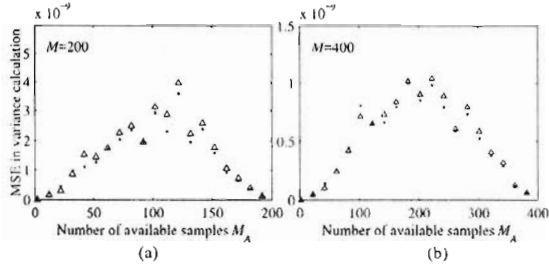
Fig. 6. MSE of the variance calculation using (37) and (38) for the Hermite coefficient at the signal position p_0, for the different number of available samples. For given M_A MSE is calculated for all possible signal coefficient positions p_0. Signals of length (a) $M = 200$ and (b) $M = 400$ are considered. For every position p_0 numerical variance values are calculated based on 7000 different realizations with randomly positioned samples.

EXAMPLE 1 Consider the case of monocomponent signal with unit amplitude that is sparse in the HT domain

$$s(m) = \psi_{p_0}(m). \tag{67}$$

The signal has M_A out of M available samples. The HF order p_0 is changed between

1) 0 and 199 for signal of length $M = 200$;
2) 0 and 399 for signal of length $M = 400$.

For every given value p_0, 7000 independent realizations of the signal are performed, with M_A available samples at random positions different in each realization, and the experimental value of the variance $\bar{\sigma}_s^2$ at the position p_0 is calculated.

The experimentally obtained variance is compared with the theoretical variance σ_s^2 given by (37) and its approximation (estimated value from available samples averaged over 7000 realizations) given by (38), based on the mean squared error (MSE) calculation. The results are shown in Fig. 6(a) and (b). The comparison is performed for different numbers of available samples: (a) between 2 and 200 with step 2, and (b) between 4 and 400 with step 4. Dotted line represents the MSE between the experimental results and theoretical model (37), while triangle line represents the MSE between experimental results and approximate model (38) with the assumption of known p_0. It can be seen that for both cases, the achieved MSE is of order 10^{-9}, which confirms the accuracy of the derived theoretical variances. Note that the error shape corresponds to the shape of the estimated variances.

EXAMPLE 2 The monocomponent signal of the form (67) is considered, for three Hermite coefficient positions (a) $p_0 = 1$, (b) $p_0 = 266$, and (c) $p_0 = 390$. The signal length is $M = 400$. The number of available samples M_A is changed between 1 and M. For every given M_A, the variance of random variable $Y_{p=p_0}$ is calculated experimentally based on 5000 independent realizations of signal, with random missing samples positions. The variance $\bar{\sigma}_s^2$ corresponding to signal position is calculated by (38) for every realization of signal. The results are averaged over 5000
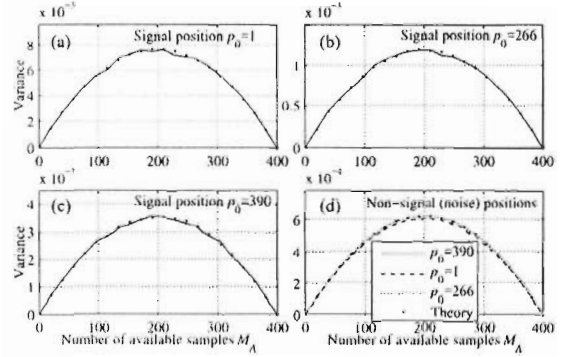

Fig. 7. Variance of the Hermite coefficient at signal component position as a function of available samples M_A: different signal component positions are considered (a)–(c); numerical result is denoted by black line, theoretical variance (38) is denoted by dots; (d) shows the numerically obtained variance of the nonsignal Hermite coefficients $p \neq p_0$ for p_0 as in: (a) denoted with dashed line, (b) dotted line, and (c) thick gray line, as well as the theoretically calculated variance (27) of nonsignal coefficients (dots).
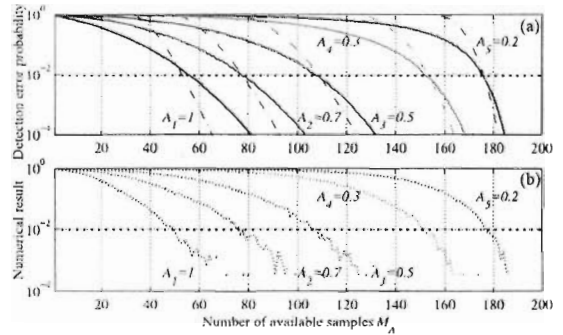

Fig. 8. Probability of components misdetection, presented as a function of the number of available samples: (a) exact probability calculated by (51) (solid line) and approximation (52); (b) experimental results.

realizations, for every given M_A. The results for the variances of $Y_{p=p_0}$ are presented in Fig. 7, for (a) $p_0 = 1$, (b) $p_0 = 266$, and (c) $p_0 = 390$. A significant matching of theoretical and experimental results is achieved for all signal positions p_0. Moreover, the variance of the nonsignal coefficients is also statistically evaluated for all three monocomponents signals, based on the same signal realizations. Experimental results along with theoretical variance σ_N^2 [given by (27)] are shown in Fig. 7(d), confirming the fact that the variance σ_N^2 is independent of p_0.

EXAMPLE 3 The derived statistical parameters along with the error probability (51) and its approximation (52) are verified experimentally in this example. The signal with $M = 200$ samples and $K = 5$ components is given by

$$s(m) = \sum_{i=1}^{K} A_i \psi_{p_i}(m) \tag{68}$$

with $A_i = \{1, 0.7, 0.5, 0.3, 0.2\}$ and $p_i = \{20, 54, 94, 162, 192\}$ for $i = 1, \dots, K$. Fig. 8(a) shows the probability of misdetection for each component separately, calculated

using (51). The probability approximation (52) is calculated as well. The number of available samples M_A is varied between 1 and 200. Horizontal dotted line denotes the error probability equal to $P = 10^{-2}$. It can be concluded that the exact and approximate probabilities almost match for the given probability $P = 10^{-2}$.

Note that, Fig. 8(a) specifies the number of available samples needed for successful detection of observed signal component with given probability. For example, 80 available samples are sufficient to detect the component with amplitude $A_1 = 0.1$ error probability close to 0, and the component with amplitude $A_2 = 0.7$ with error probability equal to $P = 10^{-2}$. We can also conclude that about 176 available samples are needed for detection of all signal components with a given probability.

The probabilities are further experimentally evaluated. For every number of available samples M_A between 1 and 200, the randomly positioned available signal samples were selected in 3000 realizations. In every realization, and for every signal component, the component misdetection events are counted. The misdetection of the ith signal component occurs if at least one nonsignal Hermite coefficient at position $p \neq p_i$, $i = 1, ..., 5$ has equal or higher amplitude than the amplitude of the ith signal component at $p = p_i$. The number of misdetection events is then divided by the number of signal realizations. The experiment is repeated for every M_A. Results are shown in Fig. 8(b). Note that numerically obtained results highly match the theoretical ones in Fig. 8(a).

EXAMPLE 4 Considered is the signal with missing samples from Example 3. Observed are different numbers of available samples used to calculate the expected probabilities of detection error (see Fig. 8).

The first considered case is

(a) $M_A = 56$ which enables detection of the signal components with the following probabilities of detection error: $P_1 = 0$, $P_2 = 0.0086$, $P_3 = 0.8679$, $P_4 = 1$, and $P_5 = 1$, for five considered signal components. This means that the first and the second component will be detected with probability higher than 0.99, the third component will be detected with probability ~ 0.13, while the fourth and the fifth component almost certainly will not be detected.
Similar discussion holds for

(b) $M_A = 108$ where probabilities of detection error for different components are: $P_1 = 0$, $P_2 = 0$, $P_3 = 0.0109$, $P_4 = 1$, and $P_5 = 1$;

(c) $M_A = 154$ with detection error probabilities $P_1 = 0$, $P_2 = 0$, $P_3 = 0$, $P_4 = 0.0073$, and $P_5 = 0.9944$;

(d) $M_A = 176$, with corresponding detection error probabilities $P_1 = 0$, $P_2 = 0$, $P_3 = 0$, $P_4 = 0$, and P_5
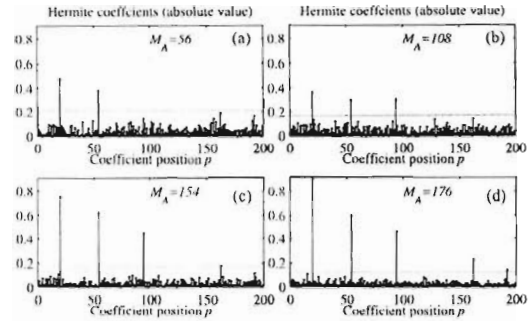

Fig. 9. Illustration of the automated threshold setting based on the number of available samples M_A. (a) $M_A = 56$. (b) $M_A = 108$. (c) $M_A = 154$. (d) $M_A = 176$.

0.0106. In this case, in about 99% of signal realizations all signal components will be above the threshold. The HT coefficients and probabilistic threshold (66) are shown in Fig. 9(a)–(d) for single signal realizations with different number of available samples.

EXAMPLE 5 The efficiency of the introduced threshold is checked on a real UWB signal transmitted in an indoor environment, obtained in the experiment described in [14] and available online [15], with bandwidth 1.3 GHz. First $M = 165$ samples of the signal "ACW7FD45.dat" from the database are considered. The signal has been resampled at roots of the Mth order Hermite polynomial using sinc interpolation and adequate scaling factor [10]. Then, the scenario with only $M_A = 55$ (33.33%) randomly positioned available samples is considered (see Fig. 10). Based on approximation (52), the given number of missing samples is sufficient for successful detection of all signal components with error probability lower than 10^{-2}. Reconstruction results are shown in Fig. 11.

The reconstruction was performed using Algorithm 2. The complete signal recovery is achieved after only four iterations of the algorithm as the proposed thresholds enabled the detection of signal coefficients positions blocks in each iteration. The MSE of the reconstructed signal is $2.1451 \cdot 10^{-27}$ (-266.66 dB). The computational time needed for the reconstruction was tested on a laptop with Intel(R) Core(TM) i7-6700HQ CPU @2.60 GHz processor and 8 GB of RAM. The algorithm is executed on MATLAB R2015a. The execution time is 0.0156 s.

EXAMPLE 6 Signal sparse in HT domain is observed, having $K = 3$ components

$$s(m) = \sum_{i=1}^{K} A_i \psi_{p_i}(m) + \varepsilon(m)$$

with $A_1 = 1$, $A_2 = 0.9$, and $A_3 = 0.6$. Component positions p_i are selected randomly, with uniform distribution, from the set of possible positions $0 \leq p_i \leq M - 1$. Additive noise variance is $\sigma_\varepsilon^2 = 0.1$ and the SNR for all available samples is SNR $= 7.67$ dB.
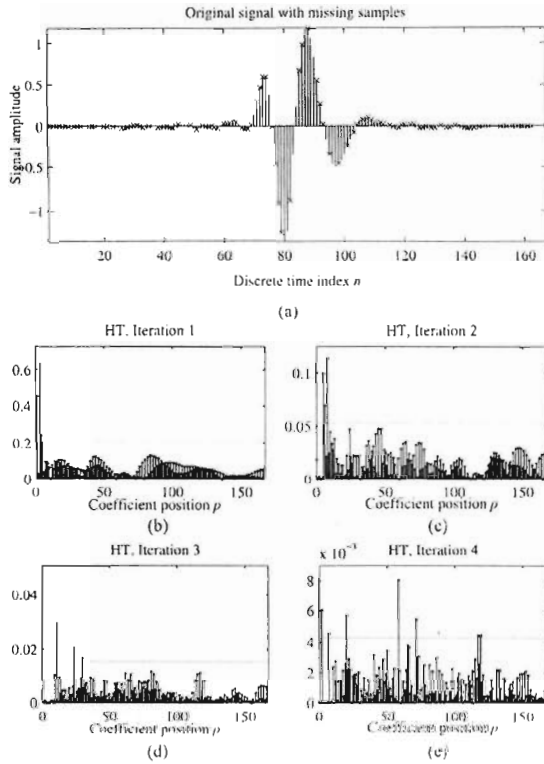
Fig. 10. (a) Original UWB signal with missing samples denoted with crosses. Hermite coefficients detected using the threshold: (b) in the first iteration, (c) in the second iteration, (d) in the third iteration, and (e) in the fourth iteration.
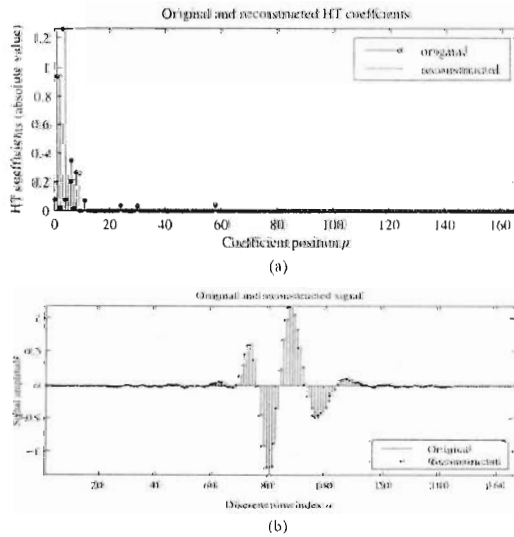

Fig. 11. (a) Reconstructed transform and (b) reconstructed UWB signal.

For a random set of M samples, the SNR_r after the reconstruction is calculated, based on 500 realizations of available samples positions, noise $\varepsilon(m)$, and component positions p_i. The results are summarized in Table I for a different number of available samples M_A, and with high agreement of the theory and the statistics. SNR_{Rt} denotes the theoretical result using (57), whereas SNR_{Rs} denotes the numerically obtained result.

TABLE I
SNR: In the Input Signal (SNR), Obtained
by Theory (SNR_{Rt}) and by statistics
(SNR_{rs}) for Various M_A

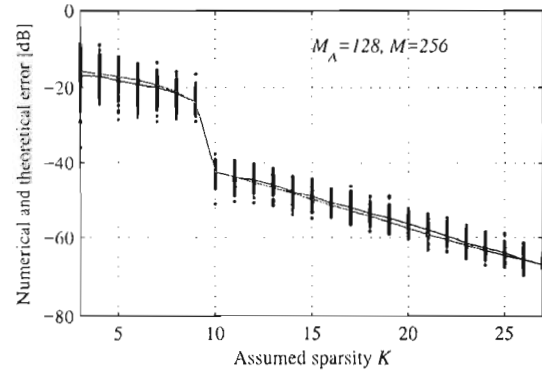| M_A	60	120	180	240
SNR	7.82	7.45	7.48	7.27
SNR_{Rt}	20.83	23.47	25.26	26.31
SNR_{RS}	20.13	23.28	25.12	26.59

Fig. 12. Error energy in the reconstruction of noisy nonsparse signal—calculated numerically and according to the presented theory.

EXAMPLE 7 Let us consider a nonsparse signal

$$s(m) = \sum_{l=1}^{M} A_l \psi_{p_l}(m) + \varepsilon(m)$$

with amplitudes $A_l = 1$ for $l < S$ and $A_l = 0.5e^{-2l/(S+1)}$ for $S + 1 \leq l \leq M$, and $S = 10$. HFs indexes p_l are selected randomly, and $0 \leq p_l \leq M - 1$. This signal is approximately S sparse. Only $M_A = 128$ out of $M = 256$ randomly positioned samples are available. The signal is embedded in weak additive, white Gaussian noise with mean value equal to zero, and standard deviation equal to $\sigma_t = 0.1/N$. The reconstruction of missing samples is performed using the Algorithm 2, assuming various sparsities $3 \leq K \leq 27$. Mean squared reconstruction errors are calculated based on 100 independent realizations of noisy signal with randomly positioned missing samples and noise realizations. Obtained results are compared with the theoretical one (62). Normalization to the assumed sparsity is done for both numerical and theoretical results

$$E_{\mathrm{num}} = 10 \log \left(\frac{1}{K} \| \mathbf{c}_K - \mathbf{c}_R \|_2^2 \right)$$

and

$$E_{\mathrm{theory}} = 10 \log \left(\frac{(M - M_A)}{M_A(M - 1)} \| \mathbf{c} - \mathbf{c}_K \|_2^2 + \frac{M}{M_A} \sigma_r^2 \right).$$

The results are shown in Fig. 12. Red line is the theoretical result. Blue dots indicate the numerical result, which is averaged to obtain the blue line. It can be observed that theoretical and averaged numerical curves highly match, confirming the expression for the reconstruction error (62) as well as the theory regarding the additive noise influence.

TABLE II

Reconstruction MSE Obtained Using Algorithm 2 (MSE_1) and OMP (MSE_2) in the UWB Signal Reconstruction, for Various MA

M_A	30	50	70	90	110	130
MSE_1	10.02	3.63	−5.18	−21.08	−268.80	−270.09
MSE_2	9.05	3.38	−5.35	−12.81	−31.65	−270.83

TABLE III

Average Computational Time of the Reconstruction Based on Algorithm 2 (CT 1) and OMP (CT 2) With Various MA

M_A	30	50	70	90	110	130
CT 1	0.007	0.008	0.003	0.001	0.0016	0.0017
CT 2	0.006	0.015	0.008	0.003	0.0018	0.0019

TABLE IV

Average Number of Iterations in the Reconstruction Based on Algorithm 2 (IT 1) and OMP (IT 1) with Various MA

M_A	30	50	70	90	110	130
IT 1	48.49	27.10	9.31	4.70	4.08	3.68
IT 2	29.83	40.91	22.77	14.61	12.15	12.00

EXAMPLE 8 Let us consider the experimental UWB data from Example 5. This signal is sparse in the HT domain, however, having a number of small, nearly zero-valued coefficients. Different numbers of randomly positioned available measurements are considered $M_A = \{30, 50, 70, 90, 110, 130\}$. Signal length is $M = 165$. Signal was reconstructed using Algorithm 2 and the OMP, and the result are compared in Tables II–IV (the experiment is done at the same computer as in Example 5). The precision $\delta = 10^{-13}$ was set in both algorithms as the stopping criterion. The number of iterations was limited to 50 in case when the required precision was not achievable. Reconstruction MSE, computation time and the number of iterations are obtained by averaging results in 500 independent reconstructions randomly positioned available measurements realizations. Clearly reduced number of iterations and computation are obtained with Algorithm 2, when the signal reconstruction with meaningful results is possible (for $M_A \geq 50$ in this example).

VII. CONCLUSION

The paper analyzes the influence of missing samples of the compressed sensed signal to the Hermite domain representation. The effects of compressed sensing are statistically modeled in the Hermite sparsity domain using two independent random variables located at the signal and nonsignal positions. Being able to characterize these variables allows us to develop a method to distinguish between them, and consequently, to easily determine the true signal support in the transform domain. Also, it was shown that depending on the percent of available samples and signal component amplitudes, we can calculate the probability of exact signal support detection. Furthermore, very simple methods for signal reconstruction are proposed based on the derived theoretical concepts. The crucial segments of presented theory are verified using a large number of statistical tests. Also, the efficiency of the proposed algorithms is proved on the examples.

REFERENCES

[1] A. Sandryhaila, S. Saba, M. Puschel, and J. Kovacevic
Efficient compression of QRS complexes using Hermite expansion
IEEE Trans. Signal Process., vol. 60, no. 2, pp. 947–955, Feb. 2012.

[2] A. Sandryhaila, J. Kovacevic, and M. Püschel
Compression of QRS complexes using Hermite expansion
In Proc. IEEE Int. Conf. Acoust., Speech, Signal Process., Prague, Czech Republic, May 22–27, 2011, pp. 581–584.

[3] M. Brajović, I. Orović, M. Daković, and S. Stanković
Gradient-based signal reconstruction algorithm in the Hermite transform domain
Electron. Lett., vol. 52, no. 1, pp. 41–43, 2016.

[4] J.-B. Martens
The Hermite transform—applications
IEEE Trans. Acoust., Speech, Signal Process., vol. 38, no. 9, pp. 1607–1618, Sep. 1990.

[5] D. Kortchagine and A. Krylov
Image database retrieval by fast hermite projection method
In Int. Conf. Graphicon, Novosibirsk, Russia, Jun. 20–24, 2005, pp. 308–311.

[6] A. Krylov and D. Korchagin
Fast Hermite projection method
In Int. Conf. Image Anal. Recognit., Póvoa de Varzim, Portugal, Sep. 18–20, 2006, pp. 329–338.

[7] P. Lazaridis, G. Deharge, and P. Gallion
Discrete orthogonal Gauss–Hermite transform for optical pulse propagation analysis
J. Opt. Soc. Amer. B, vol. 20, pp. 1508–1513, 2003.

[8] S. Thangavelu
Lectures on Hermite and Laguerre Expansions. Princeton, NJ, USA: Princeton Univ. Press, 1993.

[9] S. Stanković, I. Orović, and A. Krylov
The two-dimensional Hermite S-method for high resolution inverse synthetic aperture radar imaging applications
IET Signal Process., vol. 4, no. 4, pp. 352–362, 2010.

[10] M. Brajović, I. Orović, M. Daković, and S. Stanković
On the parameterization of Hermite transform with application to the compression of QRS complexes
Signal Process., vol. 131, pp. 113–119, Feb. 2017.

[11] M. Brajović, I. Orović, M. Daković, and S. Stanković
The analysis of missing samples in signals sparse in the Hermite transform domain
In Proc. 23rd Telecommun. Forum TELFOR, Belgrade, Serbia, Nov. 24–25, 2015.

[12] S. Stanković, I. Orović, and A. Krylov
Video frames reconstruction based on time-frequency analysis and Hermite projection method
EURASIP J. Adv. Signal Process., Spec. Issue Time-Freq. Anal. Appl. Multimedia Signals, vol. 2010, 2010, Art. no. 970105.

[13] M. Ghavami, L. B. Michael, and R. Kohno
Ultra Wideband Signals and Systems in Communication Engineering. 2nd ed. Hoboken, NJ, USA: Wiley, 2007.

[14] R. J. M. Cramer, R. A. Scholtz, and M. Z. Win
Evaluation of an ultra-wide band propagation channel
IEEE Trans. Antennas Propag., vol. 50, no. 5, pp. 561–570,
May 2002.

[15] UltRa Lab UWB data. [Online]. Available: http://ultra.usc.
edu/uwb_database/tdcindoor.htm. Accessed on: May 2017.

[16] H. Zhang, X. Cui, and T. A. Gulliver
Remotely-sensed TOA interpretation of synthetic UWB based
on neural networks
EURASIP J. Adv. Signal Process., vol. 2012, 2012, Art. no. 185.

[17] M. C. Shastry, R. M. Narayanan, and M. Rangaswamy
Sparsity-based signal processing for noise radar imaging
IEEE Trans. Aerosp. Electron. Syst., vol. 51, no. 1, pp. 314–325,
Jan. 2015.

[18] L. H. Nguyen, T. Tran, and T. Do
Sparse models and sparse recovery for ultra-wideband SAR
applications
IEEE Trans. Aerosp. Electron. Syst., vol. 50, no. 2, pp. 940–958,
Apr. 2014.

[19] J. L. Paredes, G. R. Arce, and Z. Wang
Ultra-wideband compressed sensing: Channel estimation
IEEE J. Sel. Topics Signal Process., vol. 1, no. 3, pp. 383–395,
Oct. 2007.

[20] M. J. Lindenfeld
Sparse frequency transmit-and-receive waveform design
IEEE Trans. Aerosp. Electron. Syst., vol. 40, no. 3, pp. 851–861,
Jul. 2004.

[21] M. C. Shastry, R. M. Narayanan, and M. Rangaswamy
Sparsity-based signal processing for noise radar imaging
IEEE Trans. Aerosp. Electron. Syst., vol. 51, no. 1, pp. 314–325,
Jan. 2015.

[22] L. J. Stanković, I. Stanković, and M. Daković
Nonsparsity influence on the ISAR recovery from reduced data
IEEE Trans. Aerosp. Electron. Syst., vol. 52, no. 6, pp. 3065–
3070, Dec. 2016.

[23] L. J. Stanković, S. Stanković, and M. Amin
Missing samples analysis in signals for applications to l-
estimation and compressive sensing
Signal Process., vol. 94, pp. 401–408, Jan. 2014.

[24] L. J. Stanković, I. Orović, S. Stanković, and M. Amin
Compressive sensing based separation of non-stationary and
stationary signals overlapping in time-frequency
IEEE Trans. Signal Process., vol. 61, no. 18, pp. 4562–4572,
Sep. 2013.

[25] D. Donoho
Compressed sensing
IEEE Trans. Inf. Theory, vol. 52, no. 4, pp. 1289–1306,
Apr. 2006.

[26] R. Baraniuk
Compressive sensing
IEEE Signal Process. Mag., vol. 24, no. 4, pp. 118–121,
Jul. 2007.

[27] M. Elad
*Sparse and Redundant Representations: From Theory to Ap-
plications in Signal and Image Processing.* Berlin, Germany:
Springer, 2010.

[28] S. Stanković, I. Orović, and E. Sejdić
Multimedia Signals and Systems. Berlin, Germany: Springer-
Verlag, 2012.

[29] E. Candes, J. Romberg, and T. Tao
Robust uncertainty principles: Exact signal reconstruction from
highly incomplete frequency information
IEEE Trans. Inf. Theory, vol. 52, no. 2, pp. 489–509, Feb.
2006.

[30] E. Sejdić, M. A. Rothfuss, M. L. Gimbel, and M. H. Mickle
Comparative analysis of compressive sensing approaches for
recovery of missing samples in an implantable wireless doppler
device
IET Signal Process., vol. 8, no. 3, pp. 230–238, May 2014.

[31] L. Zhao, G. Bi, L. Wang, and H. Zhang
An improved auto-calibration algorithm based on sparse
bayesian learning framework
IEEE Signal Proc. Lett., vol. 20, no. 9, pp. 889–892,
Sep. 2013.

[32] S. Stanković, I. Orović, and L. J. Stanković
An automated signal reconstruction method based
on analysis of compressive sensed signals in noisy
environment
Signal Process., vol. 104, pp. 43–50, 2014.

[33] L. J. Stanković, M. Daković, and S. Vujović
Adaptive variable step algorithm for missing samples recovery
in sparse signals
IET Signal Process., vol. 8, no. 3, pp. 246–256, 2014.

[34] N. Anselmi, G. Oliveri, M. Salucci, and A. Massa
Wavelet-based compressive imaging of sparse targets
IEEE Trans. Antennas Propag., vol. 63, no. 11, pp. 4889–4900,
Nov. 2015.

[35] N. Anselmi, G. Oliveri, M. A. Hannan, M. Salucci, and A. Massa
Color compressive sensing imaging of arbitrary shaped scatter-
ers
IEEE Trans. Microw. Theory Techn., vol. 65, no. 6, pp. 1986–
1999, Jun. 2017.

[36] A. Massa, P. Rocca, and G. Oliveri
Compressive sensing in electromagnetics–A review
IEEE Antennas Propag. Mag., vol. 57, no. 1, pp. 224–238,
Feb. 2015.

[37] A. Massa, P. Rocca, and G. Oliveri
Compressive sensing as a new paradigm in wave scattering and
propagation
In *Proc. IEEE Int. Symp. Antennas Propag.*, Fajardo, Puerto
Rico, Jun. 2016, pp. 1525–1526.

[38] A. Massa, G. Oliveri, N. Anselmi, L. Poli, and L. Tenuti
CS-based computational imaging at microwave frequencies
In *Proc. IEEE Int. Symp. Antennas Propag.*, Fajardo, Puerto
Rico, Jun. 2016, pp. 1061–1062.

[39] A. Massa, G. Oliveri, N. Anselmi, and L. Poli
Compressive sensing as applied to electromagnetics—
Challenges, solutions, and future trends
In *Proc. 10th Eur. Conf. Antennas Propag.*, Davos, Switzerland,
Apr. 2016, pp. 1–4.

[40] L. C. Potter, E. Ertin, J. T. Parker, and M. Cetin
Sparsity and compressed sensing in radar imaging
Proc. IEEE, vol. 98, no. 6, pp. 1006–1020, Jun. 2010.

[41] Q. Huang, L. Qu, and F. Guangyou
UWB through-wall imaging based on compressive sensing
IEEE Trans. Geosci. Remote Sens., vol. 48, no. 3, pp. 1408–
1415, Mar. 2010.

[42] E. Lagunas, M. G. Amin, F. Ahmad, and M. Najar
Joint wall mitigation and compressive sensing for indoor image
reconstruction
IEEE Trans. Geosci. Remote Sens., vol. 51, no. 2, pp. 891–906,
Feb. 2013.

[43] P. R. Oliveri and A. Massa
A Bayesian compressive sampling-based inversion for imaging
sparse scatterers
IEEE Trans. Geosci. Remote Sens., vol. 49, no. 10, pp. 3993–
4006, Oct. 2011.

[44] G. Oliveri, N. Anselmi, and A. Massa
Compressive sensing imaging of non-sparse 2D scatterers by a
total-variation approach within the Born approximation
IEEE Trans. Antennas Propag., vol. 62, no. 10, pp. 5157–5170,
Oct. 2014.

[45] E. A. Marengo, R. D. Hernandez, Y. R. Citron, F. K. Gruber, M.
Zambrano, and H. Lev-Ari
Compressive sensing for inverse scattering
In *Proc. XXIX URSI Gen. Assem.*, Chicago, IL,USA,
Aug. 7–16, 2008. [Online]. Available: http://www.
ursi.org/proceedings/procGA08/papers/B03p7.pdf

[46] Fannjiang and H.-C. Tseng
Compressive radar with off-grid targets: A perturbation approach
Inverse Problems, vol. 29, no. 5 pp. 1–23, May 2013, Art. no. 054008.

[47] D. Malioutov, M. Cetin, and A. S. Willsky
A sparse signal reconstruction perspective for source localization with sensor arrays
IEEE Trans. Signal Process., vol. 53, no. 8, pp. 3010–3022. Aug. 2005.

[48] M. D. Migliore
A compressed sensing approach for array diagnosis from a small set of near-field measurements
IEEE Tran. Antennas Propag., vol. 59, no. 6, pp. 2127–2133. Jun. 2011.

[49] V. M. Patel, G. R. Easley, D. M. Healy, and R. Chellappa
Compressed synthetic aperture radar
IEEE J. Sel. Topics Signal Process., vol. 4, no. 2, pp. 244–254. Apr. 2010.

[50] E. Sejdic and L. Chaparro
Time-frequency representations based on compressive samples
In *Proc. 21st Eur. Signal Process. Conf.*, 2013, pp. 1–4.

[51] X. Li and G. Bi
Image reconstruction based on the improved compressive sensing algorithm
In *Proc. IEEE Int. Conf. Digital Signal Process.*, Singapore, 2015, pp. 357–360.

[52] H. Rauhut and R. Ward
Sparse Legendre expansions via l1-minimization
J. Approx. Theory, vol. 164, no. 5, pp. 517–533, 2012.

[53] H. Rauhut
Stability results for random sampling of sparse trigonometric polynomials
IEEE Trans. Inf. Theory, vol. 54, no. 12, pp. 5661–5670, Dec. 2008.

[54] M. Davenport, M. Duarte, Y. Eldar, and G. Kutyniok
Introduction to compressed sensing
In *Compressed Sensing: Theory and Applications*, Eldar, Y., Ed. Cambridge, U.K.: Cambridge Univ. Press, 2012.

[55] I. Candel, C. Ioana, and B. Reeb
Robust sparse representation for adaptive sensing of turbulent phenomena
IET Signal Process., vol. 8, no. 3, pp. 285–290, 2014.

[56] S. Stankovic, L. J. Stankovic, and I. Orovic
A Relationship between the robust statistics theory and sparse compressive sensed signals reconstruction
IET Signal Process., vol. 8, no. 3, pp. 223–229, May 2014.

[57] L. J. Stankovic, M. Dakovic, and T. Thayaparan
Time-Frequency Signal Analysis With Applications. Boston, MA, USA: Artech House, Mar. 2013.

[58] S. Winitzki
Uniform approximations for transcendental functions
In *Computational Science and Its Applications—ICCSA 2003* (LNCS 2667/2003), Berlin, Germany:Springer, 2003, pp. 962–962.

[59] S. Winitzki
A handy approximation for the error function and its inverse
Lecture Note, 2008, [Online]. Available: http://www.scribd.com/document/82414963/Winitzki-Approximation-to-Error-Function.

Miloš Brajović (S'12) was born in Podgorica, Montenegro, in 1988. He received the B.S. and M.Sc. degrees in electrical engineering from the University of Montenegro, Podgorica, Montenegro, in 2011 and 2013, respectively. He is currently working toward the Ph.D. degree is signal processing (more precisely, analysis of compressive sensing reconstruction algorithms for signals sparse in Fourier and Hermite transform domains, as well as the time-frequency decomposition of multivariate signals).
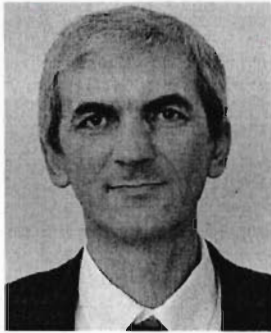
He is currently working as a teaching assistant at the University of Montenegro. He is a member of the Time-Frequency Signal Analysis Group, University of Montenegro, where he is involved in several research projects. His research interests include signal processing, time-frequency signal analysis, and compressive sensing. He has published several papers in these areas.

Irena Orović (M'10) was born in Montenegro, in 1983. She received the B.Sc., M.Sc., and Ph.D. degrees in electrical engineering from the University of Montenegro (UoM), Podgorica, Montenegro, in 2005, 2006, and 2010, respectively.

From 2005 to 2010, she was a TA with the UoM. In the period 2010–2015, she was an Assistant Professor with the Faculty of Electrical Engineering, UoM, where she has been an Associate Professor since 2015. She has published about 50 journal papers and coauthored several books and book chapters. Her research interests include compressive sensing, multimedia signals and systems, and time-frequency analysis with applications.

Dr. Orović received the Award for the best Ph.D. thesis in 2010 by the TRIMO Award Slovenia and award for the Best Woman Scientist in Montenegro in 2012 by the Ministry of Science of Montenegro. She was the Vice President of the Council for Scientific Research Activity in Montenegro. She is currently the President of the Scientific Board at the University of Montenegro.

Miloš Daković (M'07) was born in Nikšić, Montenegro, in 1970. He received the B.S. degree in 1996, the M.Sc. degree in 2001, and the Ph.D. degree in 2005, all in electrical engineering from the University of Montenegro, Podgorica, Montenegro.

He is a Professor at the University of Montenegro. His research interests are in signal processing, time-frequency signal analysis, compressive sensing, and radar signal processing. He is a member of the Time-Frequency Signal Analysis Group, University of Montenegro, where he was involved in several research projects supported by Volkswagen foundation, Montenegrin Ministry of Science and Canadian Government (DRDC).

Srdjan Stanković (SM'08–M'94) was born in Montenegro, in 1964. He received the B.S. (Hons.) degree in electrical engineering from the University of Montenegro, Podgorica, Montenegro, in 1988, the M.S. degree in electrical engineering from the University of Zagreb, Zagreb, Croatia, in 1991, and the Ph.D. degree in electrical engineering from the University of Montenegro, in 1993.

From 1988 to 1992, he worked in the Aluminum Plant of Podgorica as a Research Assistant. In 1992, he joined the Faculty of Electrical Engineering, University of Montenegro, where he is currently a Full Professor. From 2007 to 2013, he was the Dean of the Faculty of Electrical Engineering, University of Montenegro. During the winter semester 2014/2015, he was the Vice Rector of the University of Montenegro. He is the President of the Board of Directors in Montenegrin Broadcasting Company. As the Alexander von Humboldt Fellow, he spent one year at the Darmstadt University of Technology and four months at the University of Applied Sciences Bonn-Rhein-Sieg. He spent one year as a Visiting Professor at the Villanova University, PA, USA. He has published more than 100 journal papers in the areas of signal and image processing. He is a coauthor of the book *Multimedia Signals and Systems* (Springer-Verlag, in two editions in 2012 and 2015).

Dr. Stanković was serving as an Associate Editor for the IEEE TRANSACTIONS ON IMAGE PROCESSING from 2005 to 2009.

Analysis of the Reconstruction of Sparse Signals in the DCT Domain Applied to Audio Signals

Ljubiša Stanković , *Fellow, IEEE*, and Miloš Brajović , *Student Member, IEEE*

Abstract—Sparse signals can be reconstructed from a reduced set of signal samples using compressive sensing (CS) methods. The discrete cosine transform (DCT) can provide highly concentrated representations of audio signals. This property implies the DCT as a good sparsity domain for the audio signals. In this paper, the DCT is studied within the context of sparse audio signal processing using the CS theory and methods. The DCT coefficients of a sparse signal, calculated with a reduced set of available samples, can be modeled as random variables. It has been shown that the statistical properties of these variables are closely related to the unique reconstruction conditions. The main result of this paper is in an exact formula for the mean-square reconstruction error in the case of approximately sparse and nonsparse noisy signals reconstructed under the sparsity assumption. Based on the presented analysis, a simple and computationally efficient reconstruction algorithm is proposed. The presented theoretical concepts and the efficiency of the reconstruction algorithm are verified numerically, including examples with synthetic and recorded audio signals with unavailable or corrupted samples. Random disturbances and disturbances simulating clicks or inpainting in audio signals are considered. Statistical verification is done on a dataset with experimental signals. Results are compared with some classical and recent methods used in similar signal and disturbance scenarios.

Index Terms—Audio signals, digital signal processing, compressed sensing, discrete cosine transform, sparse signal processing.

I. INTRODUCTION

SPARSE signals are characterized by a small number of nonzero coefficients in one of their transformation domains [1]–[22]. These signals can be reconstructed from a reduced set of measurements [1]–[15], [21]. Measurements are linear combinations of the sparsity domain coefficients. Signal samples can be considered as measurements in the case of linear signal transforms. In certain applications reduced sets of measurements/samples result as a consequence of their physical unavailability, whereas in other applications they are a result of a particular interest to reduce the number of measurements while preserving the whole information (data compression) [1],

[2]. The unavailability of signal samples may also arise in the cases when some samples are intentionally omitted due to a high noise or corruption [4]. The last scenario may happen in highly corrupted audio signals.

In signal processing, the most common transformation domain is the Fourier domain [4], [14], with the discrete-time domain of signal samples as the measurements [1], [2]. Corresponding measurement matrices are the partial Discrete Fourier transform (DFT) matrix and the partial random Fourier transform matrix [1], [2]. The influence of a reduced set of samples on the analysis and signal reconstruction/synthesis with the partial Fourier transform matrices is studied in [4].

The discrete cosine transform (DCT) is one important and commonly used tool in audio signal processing [14]. The main reason is that the audio signals can be represented in a more compact form in the DCT domain than in the Fourier domain. This is the reason why many signal compression algorithms exploit the DCT [14], [23]–[25]. This particular transform was also used in speech enhancement applications based on compressive sensing due to its superior compressibility [7]. Therefore, this transform can play an important role in the audio signal representation with a reduced set of samples. The measurement matrices obtained from the DCT transform matrices are the topic of this paper. Like in the case of the DCT itself, many specific properties of DCT partial measurement matrices make their analysis different from the analysis of the Fourier transform based partial matrices.

The initial idea for this analysis comes from our previous correspondence on the two-dimensional DFT and radar signals [15]. However, the DCT sparsity domain exhibits many properties different from the two-dimensional DFT, starting from the fact that the ℓ_2-norms of the partial DCT matrix columns are random variables. The ℓ_2-norms of the partial DFT matrix columns are constant.

Commonly, audio signals are subject to localized time-domain distortions, including impulsive noises and clicks [26], [27], [28]–[41], clipping [26], packet loss during the signal transmission [42]–[50], and CD scratching [26], [27]. Significant research efforts have been focused on the removal and reconstruction/synthesis of the audio signals with this kind of disturbances [27], [35], [37]–[41], [51]–[55]. Corruption of audio signals by clicks in old recordings, scratched CDs, or the typed keystrokes [51], [56], assumes corrupted samples or intervals of corrupted samples occurring at random locations. Many different approaches have been proposed to recover the corrupted samples, including the median and low-pass filtering, autoregressive modeling [37], [38], and the Bayesian estimation [41]. Recently, the emerging area of CS provided new approaches for restoration of corrupted samples [7], [8], [26], [52]. Spectrogram as a domain of sparsity, in conjunction with solving a

regularized ℓ_1-norm least squares problem, has been considered in [52] for treating a speech recognition problem. It has been shown that the problem of corrupted/unavailable samples can be efficiently solved using the matching pursuit (MP) approaches [8], [26] with the DCT acting as a domain of the audio signal sparsity. Audio inpainting concept, introduced in [26], assumes the reconstruction of audio signal portions distorted by disturbances such as impulsive noise, clicks, or audio clipping, using the orthogonal MP algorithms. A variant of the reconstruction algorithms from this class, particularly adapted to the time-domain noise (Tdn-CoSaMP), has been recently introduced in [8] for speech enhancement. Therein, a random sampling matrix is included in the sensing scheme. Substantial efforts have been made to derive the reconstruction error upper bounds for this CS reconstruction algorithm.

In the CS theory, only upper bounds of the mean square reconstruction error are derived [3]. The upper bounds introduced in [8] are similar to these bounds in the general CS theory. The main contribution of this paper is in the exact relation for the mean squared error (MSE) in audio signals reconstructed from a reduced set of signal samples when the DCT is used as the sparsity domain.

The exact reconstruction error relation is the final result of a comprehensive analysis of the influence of unavailable/corrupted samples to the DCT, presented in the paper. This analysis shed a new light on some other important relations in the CS theory. A simple derivation of the coherence-based condition for unique reconstruction is presented and explained for the partial DCT measurement matrices. The presented reconstruction error analysis has also resulted in a simple and computationally efficient method for sparse signal reconstruction, with a data-driven threshold. This algorithm belongs to the class of MP algorithms. The results for additive noise influence are derived and related to the results obtained by using the Bayesian-based approach to the reconstruction of noisy signals sparse in the DCT domain [12]. The analysis of additive noise influence is combined with the derived initial CS noise properties, to get the main result that consists in the exact expression for the MSE in the reconstructed signal. The presented theory is illustrated and verified numerically on various audio signals.

The paper is organized as follows. In Section II the basic DCT definitions are given. Starting from the reduced set of observations framework and the partial DCT matrix, in Section III we present the theorem describing statistical properties of the DCT coefficients of randomly under-sampled data, the reconstruction based on missing samples analysis as well as the coherence reconstruction relation. In Section IV additive noise influence on the reconstruction result is analyzed, whereas the nonsparse signal reconstruction scenario is analyzed in Section V. The application of the presented theory to audio signals is illustrated in Section VI. Validation of the theory in the audio signal processing context is done in Section VII.

II. BASIC DEFINITIONS

The DCT (DCT-II) of a discrete-time signal $x(n)$ is defined by

$$X^C(k) = \sum_{n=0}^{N-1} a_k x(n) \cos\left(\frac{\pi(2n+1)}{2N}k\right), \quad (1)$$

with $k = 0, ..., N-1$, while the corresponding inverse transform has the form

$$x(n) = \sum_{k=0}^{N-1} a_k X^C(k) \cos\left(\frac{\pi(2n+1)}{2N}k\right), \quad (2)$$

$n = 0, ..., N-1$, where $a_k = \sqrt{1/N}$ for $k = 0$ and $a_k = \sqrt{2/N}$ for $k \neq 0$. The DCT transform can be written in a matrix form

$$\mathbf{X}^C = (\mathbf{C}_N)\mathbf{x}, \quad (3)$$

where $\mathbf{X}^C$, $(\mathbf{C}_N)$, and $\mathbf{x}$ are the DCT coefficients vector, DCT transformation matrix and the signal vector, respectively. For the inverse DCT the relation $\mathbf{x} = (\mathbf{C}_N)^{-1}\mathbf{X}^C$ holds. Note that for this DCT matrix relation $(\mathbf{C}_N)^{-1} = (\mathbf{C}_N)^T$ holds [57]. Since we will use the DCT-II form in this paper, index II will be omitted.

A signal of the form:

$$x(n) = \sum_{l=1}^{K} a_{k_l} A_l \cos\left(\frac{\pi(2n+1)}{2N}k_l\right) \quad (4)$$

is sparse in the DCT domain if the number of components (nonzero DCT coefficients) K is much smaller than the number of signal samples N, $K \ll N$. Component amplitudes are denoted by A_l, $l = 1, 2, ..., K$. Positions $k_1, k_2, ..., k_K$ will be referred to as signal coefficient positions while the remaining positions will be referred to as nonsignal coefficient positions.

The DCT of signal (4) reads:

$$X^C(k) = \sum_{n=0}^{N-1}\sum_{l=1}^{K} A_l a_k a_{k_l} \cos\left(\frac{\pi(2n+1)}{2N}k_l\right)\cos\left(\frac{\pi(2n+1)}{2N}k\right) \quad (5)$$

where $k = 0, ..., N-1$. Signal components of the form $A_l \cos(\pi k_l(2n+1)/(2N))$ are multiplied with DCT basis functions, producing in (5) the terms of the form:

$$z(k_l, k, n) = A_l a_k a_{k_l} \cos\left(\frac{\pi(2n+1)}{2N}k_l\right)\cos\left(\frac{\pi(2n+1)}{2N}k\right). \quad (6)$$

If all signal samples are available, then the corresponding DCT equals $X^C(k) = \sum_{l=1}^{K} A_l \delta(k - k_l)$.

III. REDUCED SET OF OBSERVATIONS

Assume that only $M \leq N$ randomly positioned signal samples at $n_i \in \mathbf{M} = \{n_1, n_2, ..., n_M\} \subseteq \mathbf{N} = \{0, 1, ..., N-1\}$ are available,

$$\mathbf{y} = \{x(n_1), x(n_2), ..., x(n_M)\} \subseteq \mathbf{x}$$

with

$$x(n_i) = \sum_{k=0}^{N-1} a_k X^C(k) \cos\left(\frac{\pi(2n_i+1)}{2N}k\right), \quad i = 1, ..., M.$$

A matrix form of the available samples is

$$\mathbf{y} = \mathbf{A}_{MN}\mathbf{X}^C,$$

with $\mathbf{A}_{MN}$ representing an $M \times N$ matrix of observations (measurements matrix). It is defined as the partial inverse DCT

matrix, with rows being equal to the rows of $(\mathbf{C}_N^{-1})$, corresponding to the available samples positions n_i:

$$\mathbf{A}_{MN} = \frac{\sqrt{2}}{\sqrt{N}} \begin{bmatrix} \frac{\sqrt{2}}{2} & \cos\left(\frac{\pi(2n_1+1)}{2N}\right) & \cdots & \cos\left(\frac{\pi(2n_1+1)(N-1)}{2N}\right) \\ \frac{\sqrt{2}}{2} & \cos\left(\frac{\pi(2n_2+1)}{2N}\right) & \cdots & \cos\left(\frac{\pi(2n_2+1)(N-1)}{2N}\right) \\ \vdots & \vdots & \ddots & \vdots \\ \frac{\sqrt{2}}{2} & \cos\left(\frac{\pi(2n_M+1)}{2N}\right) & \cdots & \cos\left(\frac{\pi(2n_M+1)(N-1)}{2N}\right) \end{bmatrix}.$$

In compressive sensing, it is common to normalize the column mean value energies (diagonal elements of matrix $\mathbf{A}_{MN}^T \mathbf{A}_{MN}$). In this case, the factor $\sqrt{M/2}$ would be used instead of $\sqrt{N/2}$.

The initial (norm-two based) DCT estimation uses the available samples only

$$X_0^C(k) = \sum_{n \in \mathbf{M}} a_k x(n) \cos\left(\frac{\pi(2n+1)}{2N}k\right)$$
$$= \sum_{i=1}^{M} \sum_{l=1}^{K} z(k_l, k, n_i), \qquad (7)$$

where $k = 0, 1, ..., N - 1$. It produces the same result as if the missing (unavailable) samples assume zero values [4]. In a matrix form we can write

$$\mathbf{X}_0^C = \mathbf{A}_{MN}^T \mathbf{y}.$$

Note that the terms $z(k_l, k, n_i)$ belong to the set

$$\Theta = \{z(k_l, k, n_1), z(k_l, k, n_2), ..., z(k_l, k, n_M)\}.$$

that is a subset of complete set of samples

$$\left\{ A_l a_k a_{k_l} \cos\left(\frac{\pi(2n+1)}{2N}k_l\right) \cos\left(\frac{\pi(2n+1)}{2N}k\right), \right.$$
$$\left. n, k = 0, ..., N-1, l = 1, ..., K \right\}.$$

Consequently, the set of missing samples Q can be considered as a subset of the complete set of samples, $\mathbf{Q} = \mathbf{N} \backslash \mathbf{M}$. Original signal samples at the positions defined by Q are affected by a noise [4]:

$$\eta(k_l, k, n) = \begin{cases} -z(k_l, k, n), & n \in \mathbf{Q} \\ 0, & n \in \mathbf{M}, \end{cases} \qquad (8)$$

for $k = 0, ..., N-1, l = 1, ..., K$. The DCT coefficients

$$X_0^C(k) = \sum_{i=1}^{M} \sum_{l=1}^{K} z(k_l, k, n_i)$$
$$= \sum_{n=0}^{N-1} \sum_{l=1}^{K} [z(k_l, k, n) + \eta(k, k_l, n)] \qquad (9)$$

with randomly positioned available samples and $1 \ll M \ll N$ may be considered as random variables. Here we will analyze the statistical properties of coefficients $X_0^C(k)$.

Theorem 1: Assume a sparse signal with K nonzero coefficients in the DCT domain at random positions k_l with amplitudes $A_l, l = 1, 2, ..., K$. Assume that out of the total number of N samples only M samples, $1 \ll M \ll N$, are available. The DCT coefficients $X_0^C(k)$ calculated using the available samples are random, approximately Gaussian distributed variables.

Their mean-value and variance are

$$\mu_{X_0^C(k)} = \frac{M}{N} \sum_{l=1}^{K} A_l \delta(k - k_l) \qquad (10)$$

and

$$\sigma_{X_0^C(k)}^2 = \frac{M(N-M)}{N^2(N-1)} \sum_{l=1}^{K} A_l^2 \left[1 - \frac{1}{2}\delta(k - (N - k_l)) \right. $$
$$\left. - \frac{1}{2}[1 + \delta(k_l)]\delta(k - k_l) \right], \qquad (11)$$

respectively, where a_k are the DCT constants.

The proof is given in Appendix. The theorem result will be numerically checked next.

Example 1: A sparse monocomponent randomly undersampled signal of form (4) is considered, with $K = 1, k_1 = 12$, and $N = 129$. The number of randomly positioned available samples M is varied from 0 to $N - 1$. For each number of available samples M, the variance of the DCT coefficient $X_0^C(k_1)$ at the signal component position is calculated and averaged in 30000 independent realizations with randomly positioned missing samples. The result is compared with the theoretical variance (11). The results are shown in Fig. 1(a).

The same experiment is performed for the DCT coefficients corresponding to the nonsignal positions $k \neq k_1$ (and for $k \neq N - k_1$). Since we now have $N - 2 = 127$ non-signal (noise) coefficients in one realization, we reduce the set of random realizations to 200 (with the total number of observed nonsignal coefficients in all realizations being 25400). The average variance is compared with the theoretical result (11) in Fig. 1(b). To emphasize the difference between variances at the signal coefficient and the nonsignal coefficients positions, the variances of all DCT coefficients of the signal (for $M = 64$ available samples) are calculated based on 10000 independent realizations and shown in Fig. 1(c). Finally, the signal component position k_1 is varied from 0 to $N - 1$ with $M = 50$ available samples. Based on 10000 independent realizations of randomly positioned missing samples, the variance of $X_0^C(k_1)$ is calculated and compared with the theoretical result (11). As expected, a position independent variance value is obtained, except for $k_1 = 0$ when the variance is zero (as expected). The results are shown in Fig. 1(d).

Example 2: A multicomponent signal of form (4), with $K = 5$, is considered here. The complete signal length is $N = 155$. Signal components are positioned at $k_l = \{22, 49, 47, 89, 100\}$, with corresponding amplitudes $A_l = \{5, 3.5, 1.5, 2.5, 1\}$. In order to check the distribution of random variables $X_0^C(k)$, 60000 independent realizations of signal with randomly positioned $M = 90$ samples are considered. The histograms of the signal component coefficient $X_0^C(22)$ and the nonsignal coefficient $X_0^C(130)$ are shown in Fig. 2. Histograms are scaled with the number of realizations. The histogram of coefficient $C(22)$ is compared with the Gaussian distribution (in dots) having the mean value $\mu_{X_0^C(22)} = A_1 M/N \approx 2.90$ and the variance $\sigma_{X_0^C(22)}^2 = 0.0542$, calculated according to (11). The result is presented in Fig. 2 (right). Similarly, the nonsignal coefficient $X_0^C(130)$ histogram is compared with the zero-mean Gaussian distribution, whose variance is equal to $\sigma_{X_0^C(130)}^2 = 0.0739$, according to (11). The result is shown in Fig. 2 (left).
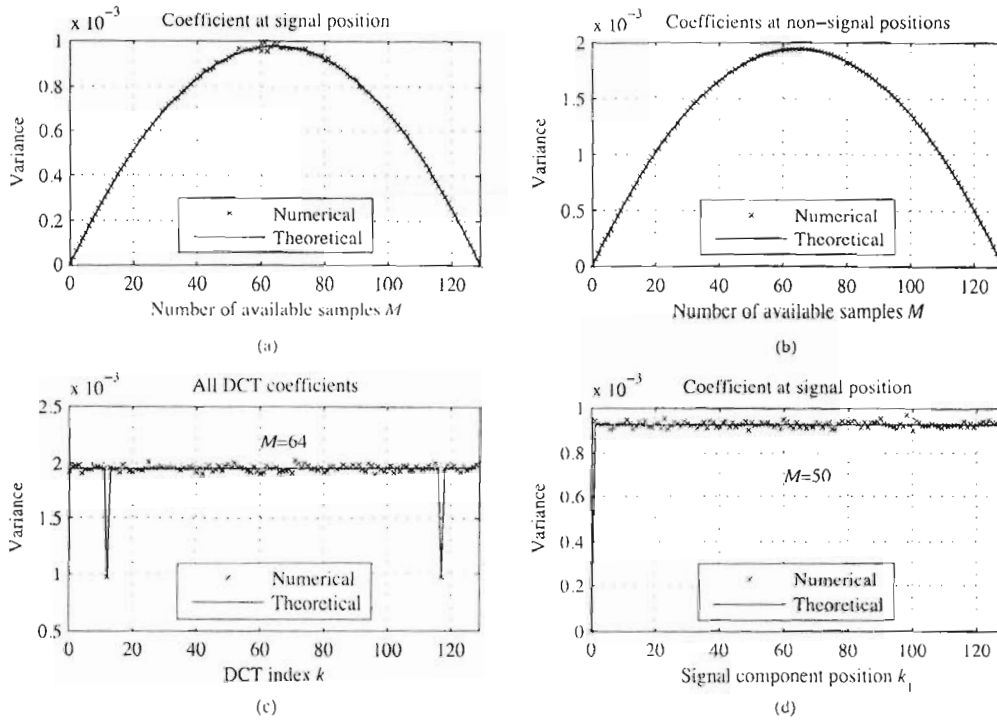
Fig. 1. Numerical check of the derived variance: (a) the variance of the DCT coefficient at the signal position $k = k_1$ as a function of the number of available samples, (b) the average variance of the DCT coefficients at noise only positions $k \neq k_1$ shown as a function of the number of available samples, (c) the variance of all DCT coefficients of a sparse mono-component signal with $k_1 = 12$ and with $M = 64$ available samples, (d) the variance of the DCT coefficient $X_0^C(k = k_1)$ as a function of k_1, calculated for signals with $M = 50$ available samples.
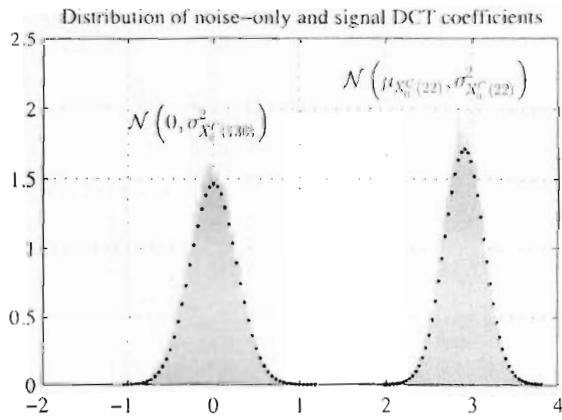

Fig. 2. Scaled histograms of DCT coefficients and the corresponding pdfs: at the non-signal position (left) and at the signal position (right). Dots denote the theoretical result.

A. The Reconstruction Based on the Missing Sample Analysis

The variance of noise only components, using the result of Theorem (11) can be expressed as:

$$\sigma_{X_0^C(k)}^2 = \frac{M(N - M)}{N^2(N - 1)} \sum_{l=1}^{K} A_l^2 \left[1 - \frac{1}{2}\delta(k - (N - k_l)) \right],$$

where $k \neq k_l$. The coefficients at positions $k = N - k_l$, $l = 1, \dots, K$ have the variance reduced for $A_l^2/2$ when compared to the other coefficients at nonsignal positions. We may assume that

the variance for noise-only coefficients is position independent and equal to:

$$\sigma_{csN}^2 = \frac{M(N - M)}{N^2(N - 1)} \sum_{l=1}^{K} A_l^2. \tag{12}$$

It is overestimated at positions $k = N - k_l$. The variance (12) depends on the total signal power, that can be easily estimated using the available samples, as

$$\sum_{l=1}^{K} A_l^2 = E_s \cong \frac{N}{M} \sum_{n \in M} s^2(n).$$

If we set a threshold, for example at $4\sigma_{csN}$, then (according to the four-sigma rule) we know that less than 1 noise-only (nonsignal) coefficient in 15,000 coefficients will be above this level. Coefficients above the threshold may be considered as signal components and reconstructed after their positions are detected. If a noise component is included, then it will produce a zero coefficient value in the final result. In the case when small signal coefficients exist, within the level of the noise produced by missing samples, the reconstruction procedure can be repeated after the strongest components are detected, reconstructed and subtracted from the available samples values.

Example 3: A three-component signal with $N = 256$ is observed. Component positions and amplitudes are $k_1 = 14$, $k_2 = 162$, $k_3 = 203$ and $A_1 = 1$, $A_2 = 1/\sqrt{2}$, $A_3 = 1/2$, respectively. Only $M = 128$ of its randomly positioned samples are available. In order to reconstruct the signal, we calculate the initial estimation $X_0^C(k)$. Then we define a threshold based on the variance due to the missing samples, whose value is
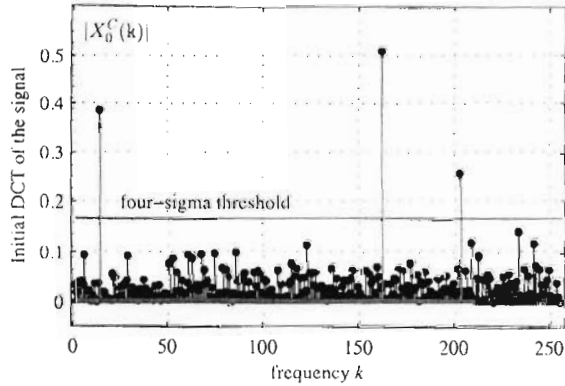
Fig. 3. The DCT of a three-component sparse signal, with the four-sigma threshold (horizontal line): crosses - DCT coefficients of the full-length signal, dots - DCT coefficients of the signal with missing samples.

$\sigma^2_{csN} = \frac{128(256-128)}{256^2(256-1)}(1 + 1/2 + 1/4) = 0.0017$. A threshold at $4 \times \sqrt{0.0017} = 0.1657$ is used, Fig. 3. The weakest component mean value $1/4$ is well above this threshold.

This kind of analysis can be generalized to a K component signal. In the worst case, we should be able to detect at least the strongest component (the detection of other components would follow after the reconstruction and subtraction of this strongest component). The worst case for the strongest component detection would be the case when other components are equally strong, $A_1 = A_2 = \cdots = A_K = 1$. In the worst case of a K-sparse signal with equal components, the four-sigma threshold would be

$$ T = 4\sqrt{\frac{M(N-M)}{N^2(N-1)}K}. $$

We may conclude that the mean value of a signal-only coefficient is above the threshold (with a probability defined by the four-sigma rule) if $\frac{M}{N} > 4\sqrt{\frac{M(N-M)}{N^2(N-1)}}K$ holds. It produces the upper bound for sparsity K

$$ K < \frac{M(N-1)}{16(N-M)}. \tag{13} $$

For $N = 256$ and $M = 128$ we get $K < 15.94$ or $K \leq 15$. If we allowed the three-sigma rule, then $K \leq 28$ would be obtained. Note that few noise components, that are wrongly detected as the signal components, will not influence the reconstruction as far as the reconstruction conditions are met. The algorithm will produce zero values as the result for such coefficients.

After the component positions are detected, the measurement equation becomes

$$ \mathbf{y} = \mathbf{A}_{MK}\mathbf{X}^C_K, $$

where $\mathbf{X}^C_K$ is the vector of K unknown coefficients at the detected positions. The measurement matrix is reduced to a $M \times K$ matrix by omitting columns corresponding to the zero-valued coefficients. Since $K < M$, the equation can be solved in the mean-square sense. The result is a vector with K elements

$$ \mathbf{X}^C_K = (\mathbf{A}^T_{MK}\mathbf{A}_{MK})^{-1}\mathbf{A}^T_{MK}\mathbf{y}. \tag{14} $$

If the obtained coefficients are such that $\mathbf{e} = \mathbf{y} - \mathbf{A}_{MK}\mathbf{X}^C_K$ is zero (or within the acceptable bounds), then we have found the solution. If the error is not small, then some of non-zero

coefficients have not been detected and included into $\mathbf{X}^C_K$. The calculation should be repeated with $\mathbf{e}$ now acting as a signal. The candidates for nonzero coefficient positions should be detected based on the initial DCT of this new signal and added to the previous set $\mathbf{K}$ of nonzero coefficient positions. Calculation of $\mathbf{X}^C_K$ should be repeated with this new (updated) set of positions, until an acceptable (zero) error level is achieved.

Next, the exact analysis of the signal-only and noise-only (non-signal) coefficients will be presented, in order to better position the threshold for the signal components detection.

Let us observe a K-sparse signal of the form (4). The noise-only DCT coefficient is a random variable described by approximative Gaussian distribution, $\mathcal{N}(0, \sigma^2_{csN})$ with zero mean and variance σ^2_{csN} defined by (12). The l-th signal DCT coefficient is also a random variable described by approximative Gaussian distribution $\mathcal{N}(\frac{M}{N}A_l, \sigma^2_{X^C_0(k_l)})$, $l = 1, 2, ..., K$, with mean value $\mu_{X^C_0(k_l)} = \frac{M}{N}A_l$ and variance $\sigma^2_{X^C_0(k_l)}$ defined by (11). The absolute DCT coefficient values at the position of the l-th signal component have the folded normal distribution

$$ p(\xi) = \frac{1}{\sigma_{X^C_0(k_l)}\sqrt{2\pi}}\left[\exp\left(-\frac{(\xi - \frac{M}{N}A_l)^2}{2\sigma^2_{X^C_0(k_l)}}\right) + \exp\left(-\frac{(\xi + \frac{M}{N}A_l)^2}{2\sigma^2_{X^C_0(k_l)}}\right)\right]. \tag{15} $$

The probability density function for the absolute values of noise-only DCT coefficients is the half normal distribution

$$ q(\xi) = \frac{\sqrt{2}}{\sigma_N\sqrt{\pi}}\exp\left(-\frac{\xi^2}{2\sigma^2_{csN}}\right). $$

The DCT coefficient at a noise-only position takes a value lower than Ξ, with probability

$$ Q(\Xi) = \int_0^{\Xi}\frac{\sqrt{2}}{\sigma_N\sqrt{\pi}}\exp\left(-\frac{\xi^2}{2\sigma^2_{csN}}\right)d\xi = \text{erf}\left(\frac{\Xi}{\sqrt{2}\sigma_{csN}}\right). \tag{16} $$

The total number of noise-only coefficients is $N - K$. The probability that $N - K$ independent DCT noise-only coefficients are lower than Ξ is $Q(\Xi)^{N-K}$. Probability that at least one of $N - K$ DCT noise-only coefficients is greater than Ξ is $G(\Xi) = 1 - Q(\Xi)^{N-K}$. When a noise-alone DCT value surpasses the DCT coefficient at a signal position, then an error in the signal component detection occurs. To calculate this error probability, consider the absolute DCT value of a signal component at and around ξ. The DCT coefficient at the signal position has a value within ξ and $\xi + d\xi$ with the probability $p(\xi)d\xi$, where $p(\xi)$ is defined by (15). The probability that at least one of $N - K$ DCT noise-alone coefficients is above ξ is $G(\xi) = 1 - Q(\xi)^{N-K}$. Consequently, the probability that the absolute value of a DCT signal-only coefficient is within ξ and $\xi + d\xi$ and that at least one of the absolute DCT noise-alone values outside the DCT signal value exceeds the DCT signal value is $G(\xi)p(\xi)d\xi$. Considering all possible values of ξ, it follows that the probability of the wrong detection of the l-th

signal component is

$$P_E = \frac{1}{\sigma_{X_0^C(k_l)}\sqrt{2\pi}} \int_0^\infty \left(1 - \text{erf}\left(\frac{\xi}{\sqrt{2}\sigma_{c*N}}\right)^{N-K}\right)$$

$$\times \left[\exp\left(-\frac{(\xi - \frac{M}{N}A_l)^2}{2\sigma_{X_0^C(k_l)}^2}\right) + \exp\left(-\frac{(\xi + \frac{M}{N}A_l)^2}{2\sigma_{X_0^C(k_l)}^2}\right)\right] d\xi.$$

A simple approximation of this expression can be obtained following the steps for the DFT analysis presented in [4].

B. Coherence Reconstruction Relation

For the worst case analysis, assume the maximal possible influence from other signal components to the strongest signal component detection. The maximal influence of signal components to each other occurs when all K components are with equal (unity) amplitudes.

For M available samples, the mean value of a component (DCT coefficient at a signal position) is M/N. The noise component at the frequency index k, that originates from the component at k_l, is equal to

$$Q(k, k_l) = \sum_{n \in \mathbf{M}, k \neq k_l} a_k a_{k_l} \cos\left(\frac{\pi(2n+1)}{2N}k_l\right)$$

$$\times \cos\left(\frac{\pi(2n+1)}{2N}k\right). \quad (17)$$

It can be related to the coherence factor of $\mathbf{A}_{MN}^T \mathbf{A}_{MN}$, defined by

$$\mu = \max\left|\frac{N}{M} \sum_{n \in \mathbf{M}, k \neq k_l} a_k a_{k_l} \cos\left(\frac{\pi(2n+1)}{2N}k_l\right)\right.$$

$$\left. \times \cos\left(\frac{\pi(2n+1)}{2N}k\right)\right|. \quad (18)$$

If the noise originating from all signal components is such that it adds up in phase at the nonsignal coefficient positioned at k, assuming maximal possible value for μ, then the maximal nonsignal coefficient value is

$$K \max|Q(k, k_l)| = K\mu\frac{M}{N}.$$

At the same time, if at a signal coefficient position all noise factors that originate from other $K-1$ components add up in phase in the negative direction from the component mean value, assuming again their maximal possible absolute values μ, then the resulting worst signal component amplitude will be

$$\min\{X_0^C(k_l)\} = \frac{M}{N} - (K-1)\max|Q(k, k_l)|.$$

The detection of the signal component is still possible if

$$\min\{X_0^C(k_l)\} > K \max|Q(k, k_l)|, \quad \text{or}$$

$$\frac{M}{N} - (K-1)\frac{M}{N}\mu > K\mu\frac{M}{N}.$$

The condition $1 - (K-1)\mu > K\mu$ is equivalent to the well known spark-based condition for the signal reconstruction [58]

$$K < \frac{1}{2}\left(1 + \frac{1}{\mu}\right).$$

From the derivation we can see that this is an extremely pessimistic reconstruction condition.

If we are in position to make a sampling positions strategy, then it should be done in such a way to minimize the value of μ. The minimal value is defined by the Welch bound $\mu \geq \sqrt{\frac{(N-M)}{M(N-1)}}$, [59]. Equality holds for a quite specific form of transforms and measurement matrices (equiangular tight frames - ETF). The DCT does not satisfy the properties of the ETF. Even if it were an ETF, then for $N = 256$ and $M = 128$ condition $\mu \geq \sqrt{(256-128)/128/255} = 0.0626$ holds, according to the Welch bound. The minimal possible value of μ guarantees the recovery for $K < 8.5$. However, as stated before, this is extremely pessimistic for real cases. With $N = 256$ and $M = 128$ we conclude from our numerical analysis that we are able to reconstruct signals with much higher sparsity values. For example, in the worst case of the signal amplitudes and a pessimistic three-sigma rule, we concluded that a full reconstruction with K up to 28 is possible.

IV. ADDITIVE NOISE INFLUENCE

Since the signal components have a mean value $\mu_{X_0^C(k_l)} = A_l\frac{M}{N}$, in the reconstruction process they are amplified for N/M in order to produce the correct signal amplitude A_l. Therefore, if there is a small additive noise with variance σ_ε^2 in the signal, its variance will be amplified for $(N/M)^2$ in an initial DCT coefficient estimate

$$\sigma_{X_0^C(k)}^2 = \sum_{n \in \mathbf{M}} \sum_{m \in \mathbf{M}} a_k^2 E\left\{\varepsilon(n)\varepsilon(m) \cos\left(\frac{\pi(2n+1)}{2N}k\right)\right.$$

$$\left. \times \cos\left(\frac{\pi(2m+1)}{2N}k\right)\right\} = \frac{M}{N}\sigma_\varepsilon^2.$$

Thus, the variance in one estimated coefficient is

$$\sigma_{X_0^C(k)}^2 = \frac{N}{M}\sigma_\varepsilon^2. \quad (19)$$

The reconstructed noise energy in K components, will be

$$E_{\varepsilon R} = \frac{M}{N}\sigma_\varepsilon^2 K \left(\frac{N}{M}\right)^2 = \frac{K}{M}\sigma_\varepsilon^2 N.$$

The signal to noise ratio is

$$SNR = 10\log\left(\frac{E_s}{E_{\varepsilon R}}\right) = 10\log\left(\frac{E_s}{\frac{K}{M}\sigma_\varepsilon^2 N}\right)$$

$$= 10\log\left(\frac{E_s}{\frac{K}{M}E_\varepsilon}\right) = SNR_i - 10\log\left(\frac{K}{M}\right),$$

where $SNR_i = 10\log(E_s/E_\varepsilon)$ is the input signal to noise ratio in all signal samples.

This result, obtained through a quite simple derivation, will be compared with the one that can be obtained using the Bayesian compressive sensing approach [12]. The covariance matrix in the estimated coefficients, according to the Bayesian reconstruction approach, is $\Sigma = (\mathbf{A}_{MN}^T \mathbf{A}_{MN}/\sigma_\varepsilon^2 + \mathbf{D})^{-1}$, where $\mathbf{D}$ is a diagonal matrix of hyperparameters. After the positions of nonzero coefficients are found, using an iterative procedure in the Bayesian approach, coefficients with large hyperparameters are excluded along with the corresponding elements of matrix $\mathbf{D}$ and columns of $\mathbf{A}_{MN}$. For our measurement matrix

the variance in the estimated coefficients is equal to the diagonal elements of $\mathbf{A}_{MN}^T \mathbf{A}_{MN}$, since the hyperparameters for the nonzero coefficients are zero. Mean value of the diagonal elements of $\mathbf{A}_{MN}^T \mathbf{A}_{MN}$ is M/N. It does not change by omitting columns of the measurement matrix. Therefore, the diagonal elements of the covariance matrix in the final iteration of the Bayesian based reconstruction are $\sigma_\varepsilon^2 N/M$, producing (19).

The presented result for the additive noise influence will be used (and numerically checked) in the analysis of nonsparse signal reconstruction.

V. NONSPARSE SIGNAL RECONSTRUCTION

Theorem 2: Assume a nonsparse signal with largest amplitudes A_l, $l = 1, 2, ..., K$. Assume that out of total number of N samples only M samples, $1 \ll M \ll N$, are available. Assume that the signal is reconstructed under the assumption as it were K-sparse. The energy of error in the K reconstructed coefficients $\|\mathbf{X}_K^C - \mathbf{X}_T^C\|_2^2$ is related to the energy of nonreconstructed components $\|\mathbf{X}_{T_s}^C - \mathbf{X}^C\|_2^2$ as

$$\|\mathbf{X}_K^C - \mathbf{X}_T^C\|_2^2 = \frac{K(N-M)}{M(N-1)} \|\mathbf{X}_{T_s}^C - \mathbf{X}^C\|_2^2, \quad (20)$$

where $\mathbf{X}_K^C$ is a $K \times 1$ vector with the reconstructed coefficients, $\mathbf{X}_T^C$ is a $K \times 1$ vector with the true coefficient values at the reconstructed coefficient positions, $\mathbf{X}^C$ is a $N \times 1$ vector with all true coefficients, and $\mathbf{X}_{T_s}^C$ is a $N \times 1$ vector with K true coefficients at the reconstructed positions and zeros at the remaining $N - K$ positions.

Proof: A nonreconstructed component in the signal behaves as a Gaussian input noise with variance

$$\sigma_{csN}^2 = A_l^2 \frac{M(N-M)}{N^2(N-1)}. \quad (21)$$

All nonreconstructed components will behave as a noise with variance

$$\sigma_T^2 = \sum_{l=K+1}^{N} A_l^2 \frac{M(N-M)}{N^2(N-1)}. \quad (22)$$

After the reconstruction, the total noise energy from the nonreconstructed components (in K reconstructed components) will be

$$\|\mathbf{X}_K^C - \mathbf{X}_T^C\|_2^2 = E_{\varepsilon R} = K \frac{N^2}{M^2} \sigma_T^2 = \frac{K(N-M)}{M(N-1)} \sum_{l=K+1}^{N} A_l^2.$$

The noise of nonreconstructed components can easily be related to the energy of the nonreconstructed components

$$\|\mathbf{X}_{T_s}^C - \mathbf{X}^C\|_2^2 = \sum_{l=K+1}^{N} A_l^2.$$

It means that the total error in the reconstructed components is

$$\|\mathbf{X}_K^C - \mathbf{X}_T^C\|_2^2 = \frac{K(N-M)}{M(N-1)} \|\mathbf{X}_{T_s}^C - \mathbf{X}^C\|_2^2.$$

This completes the proof.

The previous result can easily be generalized to the noisy signal case. If the input signal contains an input noise whose values
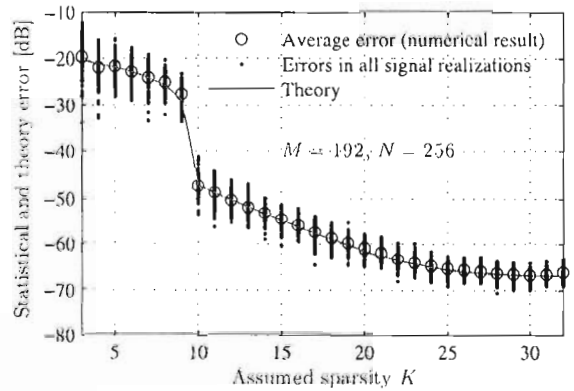

Fig. 4. Error energy in the reconstruction of noisy non-sparse signal calculated numerically and according to the presented theory. Error is shown for various assumed sparsity.

are bellow the level of the reconstructed component values in the transformation domain, then

$$\|\mathbf{X}_K^C - \mathbf{X}_T^C\|_2^2 = \frac{K(N-M)}{M(N-1)} \|\mathbf{X}_{T_s}^C - \mathbf{X}^C\|_2^2 + \frac{K}{M}\sigma_\varepsilon^2 N. \quad (23)$$

Example 4: Consider a non-sparse signal:

$$x(n) = \sum_{l=1}^{N} a_{k_l} A_l \cos\left(\frac{\pi(2n+1)}{2N} k_l\right) + \varepsilon(n),$$

with $A_l = 1$ for $l \leq S$ and $A_l = 0.5e^{-2l/(S+1)}$ for $S+1 \leq l \leq N$, all at random DCT indexes $0 \leq k_l < N$. Only $M = 192$ out of $N = 256$ signal samples are available at random positions. Corresponding DCT normalization constants are denoted by a_{k_l}. This signal is approximately S-sparse, with $S = 10$. It is embedded in additive, white, zero-mean Gaussian noise with standard deviation $\sigma_\varepsilon = 0.11/N$. Signal was reconstructed using the presented procedure,[1] with various assumed sparsity $3 \leq K \leq 32$. Based on 200 realizations of the signal with random DCT indexes, positions of available samples and random noise realizations, the MSE is calculated and compared with the theoretical result. The error (23) is calculated assuming the normalization to the assumed sparsity. The errors are calculated as follows $E_{\text{numerical}} = 10 \log\left(\frac{1}{K}\|\mathbf{X}_K^C - \mathbf{X}_T^C\|_2^2\right)$ and $E_{\text{theory}} = 10 \log\left(\frac{N-M}{M(N-1)} \|\mathbf{X}_{T_s}^C - \mathbf{X}^C\|_2^2 + \frac{1}{M}\sigma_\varepsilon^2 N\right)$.

The results are presented in Fig. 4. The line represents the theoretical MSE, whereas dots represent the numerical data, whose averaging produces the values indicated by black circles, highly matching the theoretical result.

VI. APPLICATION TO AUDIO SIGNALS

The DCT is well known for its applicability in the processing of various signal types: radar, biomedical (ECG, EEG etc.), audio signals, and digital images [14], [23]–[25]. For the context of this paper, especially interesting are the DCT-based algorithms developed for the compression of ECG signals and digital images [14], and for audio signal processing (compression, speech enhancement, denoising, inpainting) [7], [24]–[26], [60], indicating the potential for audio signal representation in the DCT

---

[1]Code is available at http://www.tfsa.ac.me/Open_source_codes.html

transformation domain with a reduced number of nonzero co-efficients. This fact indicates the applicability of sparse signal reconstruction algorithms when the signal samples are missing due to compressive sensing or unavailability, as already confirmed in several recent works [7], [26].

Audio signals are nonstationary with changing spectral content in time. In general they are not sparse [24]. The sparsity can be improved considering localized segments of audio signals [7], [24], [25]. These kind of signals can be then considered as approximately sparse. In order to improve the sparsity of audio signals, a windowed form of the DCT is used, as in the case of MDCT [61]. This form is widely employed in compression procedures involved in modern audio formats [23]. Long duration audio signals $x(n)$ are analyzed with the DCT applied on consecutive blocks of windowed signals

$$x_i(n) = w(n)x(n + iN/2),$$

where $w(n)$ is a windowing function within $0 \leq n \leq N - 1$. The subsequent blocks are overlapped such that the second half of one block coincides with the first half of the next block. It is important to note that such a block-based approach in the analysis and processing of audio signals is also important for the presented sparse signal reconstruction algorithms (since it reduces the dimensionality of the partial DCT matrices pseudo-inversion). Note that the block approach is used in the DCT based image analysis as well. If the windowing function form satisfies the condition $w(n) + w(n + N/2) = 1$ within the overlapping interval, $N/2 \leq n \leq N - 1$, then the reconstruction of the whole signal is quite simple from the reconstructed windowed signal segments $x_i(n)$ as

$$\hat{x}(n) = \sum_i \hat{x}_i(n - iN/2).$$

Many windowing function forms satisfy this condition [14]. The most commonly used windowing function among them is the Hann windowing function $w(n) = 0.5(1 + \cos(\frac{2\pi}{N}(n + \frac{N}{2}))) = \sin^2(\frac{\pi}{N}n)$. In our example the windowing function is used on the analysis side only.

Next, we will assume that a reduced set of distrurbance-free signal samples is available, within a block, at positions $n \in M - \{n_1, n_2, ..., n_M\}$. Various circumstances may cause the unavailability of audio signal samples. One illustrative example includes clicks and pops present in the old recordings [24]–[27], [41] highly corrupting certain percent of samples at $n \in Q$. The set Q can be considered as a time-domain support function of the localized disturbance. After impulsive disturbances removal, these randomly positioned samples at $n \in Q$ can are considered as unavailable. They are reconstructed using the presented CS-based method. This issue is illustrated in Examples 5 and 6. Within compressive sensing framework, a reduced set of randomly positioned samples can be initially acquired. This kind of signal is illustrated in Example 7. Nevertheless, both cases, with highly corrupted and omitted randomly positioned signal samples at $n \in Q$ or with randomly sensed signal samples at $n \in M$, can be processed in the same way in the reconstruction based on compressive sensing approaches.

Example 5: Embedded MATLAB test signal 'mtlb.mat' is considered, being a low-quality audio recording of a female voice saying the word "matlab", with sampling frequency 7418 Hz. Its form is shown in Fig. 5(a). Signal is corrupted with impulsive noise in 15% of randomly positioned samples, Fig. 5(b). Positions of the noise impulses can be easily detected
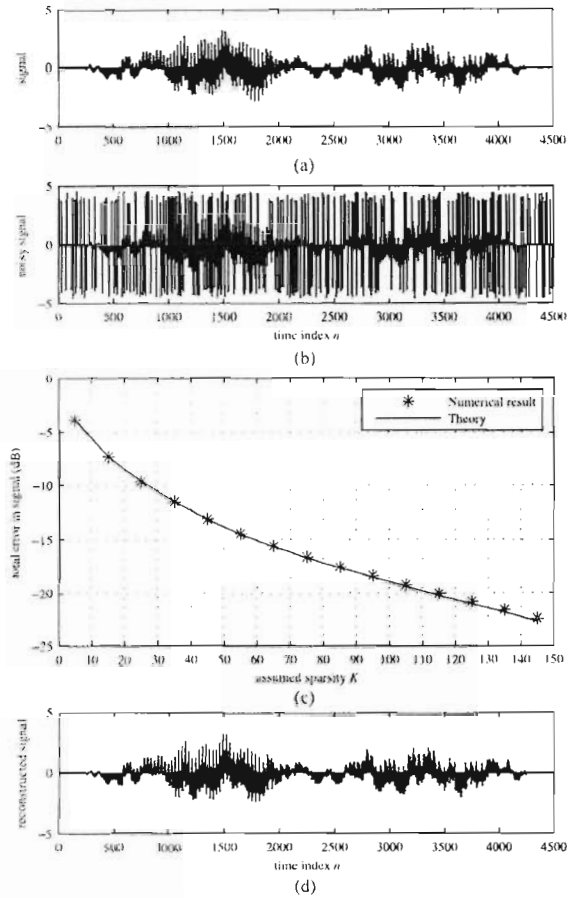

Fig. 5. Reconstruction of audio signal 'mtlb.mat' after impulsive noise removal: (a) original signal, (b) signal corrupted with impulsive disturbances, (c) total error energy after the reconstruction with various assumed sparsity, (d) reconstructed signal.

using a limiter (a method for detection of the more complex impulsive noise having amplitudes within the signal values range can be found in [62]). The signal samples at the positions of strong noise are considered as unavailable, and the reconstruction of signal is performed using the rest of samples on blocks, with a Hann windowing function of the length $N = 500$, with overlapping on the half of windowing function length. Reconstruction is preformed using the presented algorithm with various assumed sparsities K. The estimated error in the signal is calculated along with the one presented in Theorem 2. The estimated error is presented by '*' and the one expected by theory is presented by a solid line in Fig. 5(c). The agreement is high. The reconstructed signal segments are added up and the final reconstructed signal is presented in Fig 5(d) for the case of assumed sparsity $K = 150$. RMSE between signals presented in Fig. 5(a) and (d) is 0.0738.

Example 6: A recorded signal representing word 'Hallelujah' is considered in this example. Signal is recorded on a MacBook computer using MATLAB with sampling frequency 11025 Hz. Again we assumed that 20% of arbitrary signal samples are corrupted by a high impulsive noise. These samples are omitted and the signal is reconstructed using the remaining samples only. The result of the reconstruction procedure as in the previous example is presented in Fig 6, where a zoomed signal is also shown for visual clarity of the results.
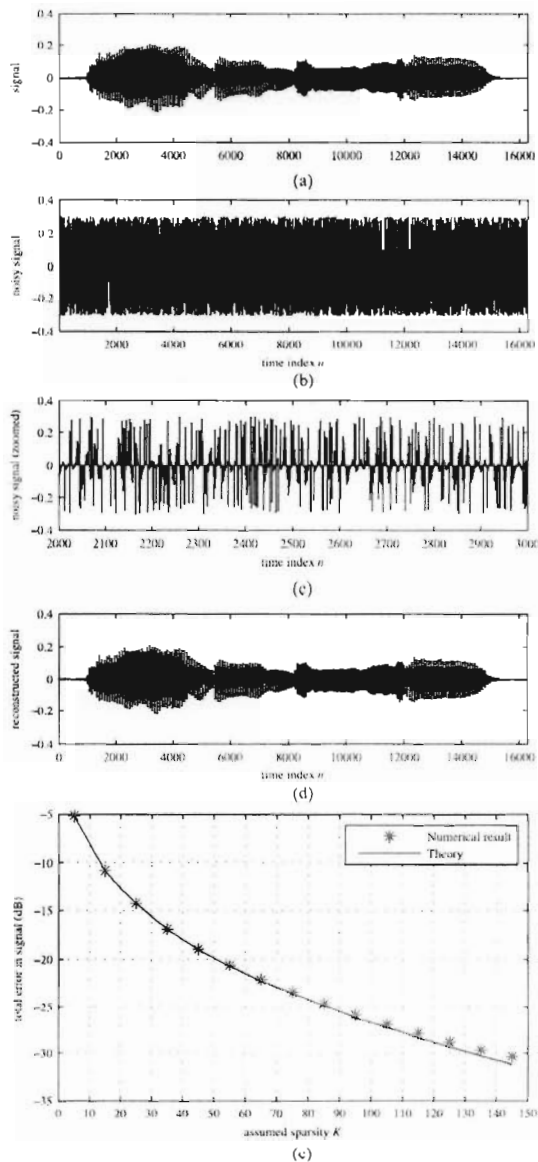
Fig. 6.   Reconstruction of a recorded audio signal after impulsive noise removal: (a) original signal, (b) signal corrupted with impulsive disturbances, (c) zoomed 1000 samples of the corrupted signal, (d) reconstructed signal, (e) total error energy after the reconstruction with various assumed sparsities.
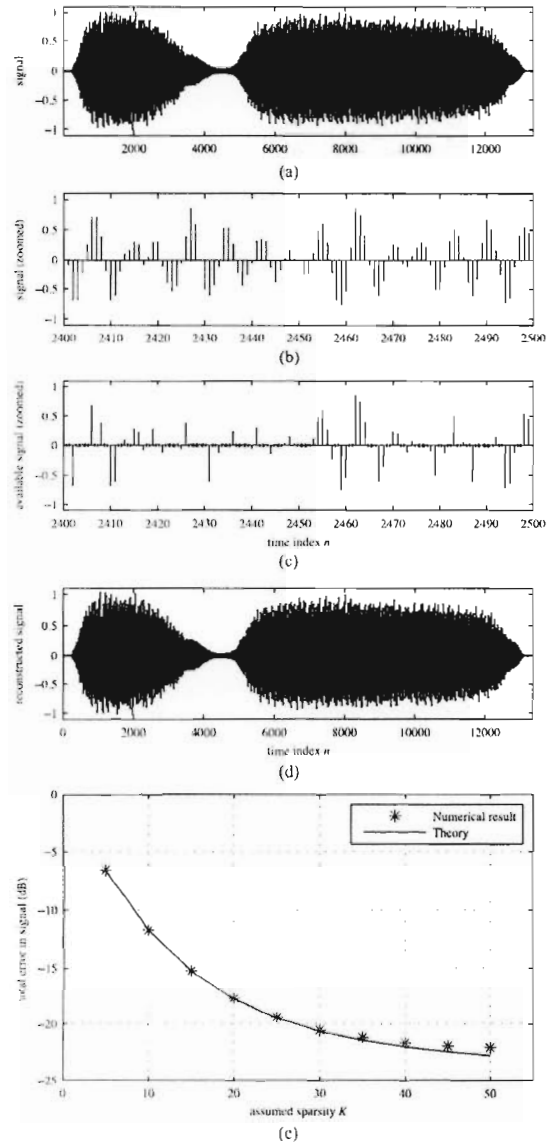

Fig. 7.   Reconstruction of compressive sensed audio signal having 50% of randomly positioned available samples: (a) original signal, (b) zoomed part of the signal, (c) zoomed part of the signal with crosses at the missing sample positions, (d) reconstructed signal, (e) total error energy after the reconstruction with various assumed sparsities.

Example 7: MATLAB signal 'train.mat' is considered in this example, shown in Fig. 7(a). It is an audio recording of a train whistle, sampled at 8192 Hz. It has been assumed that the signal is sensed in a compressive way and only 50% of randomly positioned samples are available [as presented in zoomed images in Fig. 7(b) and (c)]. The signal is reconstruct assuming various sparsities and the total reconstruction error, is presented in Fig. 7(e). The reconstructed signal with $K = 50$ is shown in Fig. 7(d).

VII. EXPERIMENTAL EVALUATION ON AUDIO SIGNALS

Three datasets from [26] are used in the experimental evaluation of the presented theory. Each dataset consists of 10 signals of length 5 s from the 2008 Signal Separation Evaluation Campaign [63], [64]. The datasets from this database are:

- Music @ 16 kHz: a set of 10 music signals sampled at 16 kHz,
- Speech @ 16 kHz: consisted of 10 male and female speech signals sampled at 16 kHz,
- Speech @ 8 kHz: consisted of speech signals sampled at 8 kHz, representing a phone quality speech. These signals are obtained by downsampling the signals from the second dataset.

The signals are carefully chosen in order to include a large diversity of audio mixtures and sources. They include both male and female speech from different speakers, singing voice, and pitched and percussive musical instruments [26].

Disturbances are simulated with two possible scenarios. In the first case, it has been assumed that the audio signals are corrupted at random positions. In the second case, the corrupted samples are grouped into random blocks to simulate click/inpainting

scenario [41]. In both scenarios the signals are reconstructed and the accuracy of the presented MSE relation is statistically tested.

The presented algorithm is compared with other audio restoration techniques: median and low-pass filtering, then with two widely used model-based audio restoration methods, and with an ℓ_1-norm optimization based reconstruction from the CS framework. The median filters of length 3 and length 5 and low-pass filters of Butterworth type with two cut-off frequences, set in accordance with signals spectrum, are considered. The model-based audio restoration methods are representative examples of the autoregressive (AR) model-based interpolation [27],[36], [66]. Herein we have considered the least-squares AR interpolator (LSAR), originally introduced for the concealment of uncorrectable errors in the CD systems [27],[36], along with the implementation provided in the Audio Inpainting Toolbox [26]. The AR model order is set to 30, and the interpolation is performed in blocks of 500 samples, as in the proposed approach. The second considered algorithm is from the class of AR + basis function representation [27], [66]. In our comparative analysis we have used the implementation with sinusoids as basis functions (LSAR+SIN), [66], which has been recently tested in [37], [39]. This algorithm is used with the default settings. The AR model is of order $P = 31$, the number of basis functions is $Q = 31$, and the block size of 1024 samples is used, in accordance with the experimental results presented in [37] and [66]. In all algorithms the reconstruction performance highly depends on the accuracy of the detection of the disturbed sample positions. In order to provide a fair comparison, we have turned off the impulsive disturbances detection in all algorithms, assuming that the disturbed sample positions are correctly detected. In this way, we have been able to test and compare the reconstruction capabilities of these algorithms.

The LASSO-ISTA (Iterative Shrinkage Thresholding Algorithm for LASSO problem) is used as a representative of the base-line ℓ_1-norm minimization reconstruction algorithms [14], [19]. The regularization constant was set to $\lambda = 0.01$.

In the second considered scenario, in addition to these standard methods, two recent approaches that are highly adapted for the removal and reconstruction of clicks in audio signals are also considered [37], [38]. In these two approaches, the reconstruction was performed along with their inherent clicks detection algorithms. However, for the very large number of impulses/blocks in both considered cases, the algorithms failed to perform successful detections. These algorithms (codes) have been used with default settings.

A. Randomly Positioned Disturbances

In the first experiment, signals from each of the three considered datasets are corrupted with a strong impulsive noise in $p\%$ of randomly positioned samples, as illustrated in Example 5 and Fig. 5. These signals are well concentrated in the DCT domain, analyzed in blocks whose length is $N = 500$ samples, weighted with the Hann windowing function. However, they are only approximately sparse. Positions of strong disturbances could easily be detected by using a limiter. More advanced detection methods are described in [27], [37], [38], [41], [62]. Any of them can be used for the detection of corrupted signal samples. Within the CS framework formulation the detected corrupted samples at positions $n \in Q$ are considered as unavailable measurements. The reconstruction is performed based on the remaining samples in these blocks, considered as the CS measurements at $n \in M$. Blocks are overlapped by a half of the

TABLE I
MSE AVERAGED OVER SIGNALS FROM THREE CONSIDERED DATABASES, FOR RANDOMLY POSITIONED IMPULSIVE DISTURBANCES

	Music@16kHz	Speech@8kHz	Speech@16kHz
Noisy	-12.40dB	-25.85dB	-25.60dB
Med3	-27.42dB	-44.04dB	-44.16dB
Med5	-27.41dB	-43.52dB	-44.20dB
LPF1	-26.92dB	-42.42dB	-43.24dB
LPF2	-26.89dB	-42.55B	-43.37dB
LSAR	-36.22dB	-52.58dB	-51.31dB
LSAR+SIN	-37.48dB	-53.59dB	-52.44dB
LASSO	-40.69dB	-49.80dB	-51.15dB
MP	-41.33dB	-55.28dB	-59.02dB

windowing function length. Reconstruction is done using the presented algorithm with various assumed sparsities K.

1) Theoretical Error: First, accuracy of the proposed MSE expression is evaluated. The case with $p = 30\%$ is considered. For the i-th block, the numerical error is calculated as:

$$E_{numerical}^{(i)} = 10 \log \left(\frac{1}{K} \| \mathbf{X}_K^C - \mathbf{X}_T^C \|_2^2 \right) \qquad (24)$$

whereas the theoretical one is given by

$$E_{theory}^{(i)} = 10 \log \left(\frac{N-M}{M(N-1)} \| \mathbf{X}_{T_i}^C - \mathbf{X}^C \|_2^2 \right). \qquad (25)$$

The squared errors are averaged over blocks, and compared in Fig. 9 as functions of assumed sparsity K, for each signal from each dataset. Solid lines represent the theoretical MSE values whereas the asterisks indicate the numerical results. The agreement of the results is high, confirming the main result of this paper.

2) Comparison With Respect to the MSE: The reconstruction results using the considered CS algorithm with sparsity $K = 80$ are compared with the standard approaches for signal filtering and smoothing, then with two standard model-based audio restoration techniques, as well as with an ℓ_1-norm minimization based CS reconstruction with a least absolute shrinkage and selection operator (LASSO) approach [19]–[21]. In this part of the experiment the number of impulses was set to $p = 40\%$.

The results are presented in Table I. The comparison is done with respect to the MSE and objective perceptual quality metrics. These results will be discussed in more details next.

We start the comparison of the presented CS based reconstruction results with a classical method for the impulsive noise reconstruction based on the median filter. The considered filter lengths are 3 and 5. For all three datasets, the median filter of length 3 reduced the MSE for 17.26 dB on average, whereas the median filter of length 5 performed similarly (rows denoted as med3 and med5 in Table I).

Next, the low-pass Butterworth filter, as a representative example of a low-pass filtering based smoothing techniques, is considered. Two cutoff frequencies are used on datasets Music @ 16 kHz and Speech @ 16 kHz. The cutoff frequencies are determined based on the analysis of the signals spectrum. The first filter (row denoted as LPF1) was designed with the normalized cutoff frequency 0.375 and the second one (row LPF2) with 0.625. For the dataset Speech @ 8 kHz normalized cutoff frequencies were 0.5, for the first, and 0.7 for the second low-pass filter. Both filters produced similar results, with an
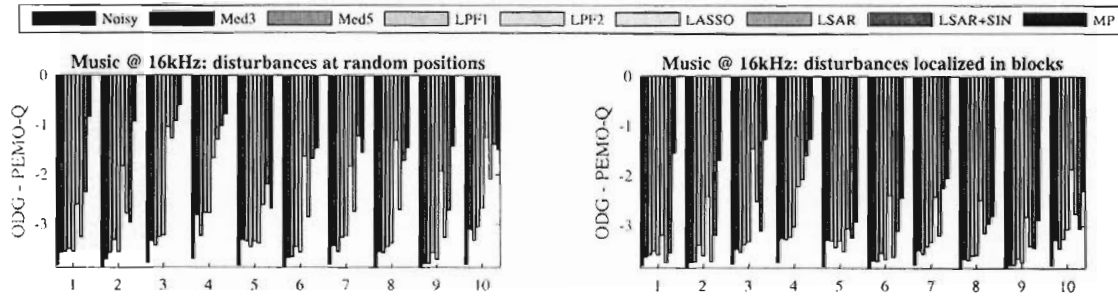
Fig. 8.   Perceptual evaluation of signals from Music @ 16 kHz dataset, using the PEMO-Q ODG metrics. Left figure shows PEMO-Q ODG scores for noisy signal and reconstructed signals in the scenario with randomly positioned impulsive disturbances, corresponding to the MSE results in Table I. Right figure shows results for impulsive disturbances localized in time-domain blocks, with corresponding MSE results shown in Table II.
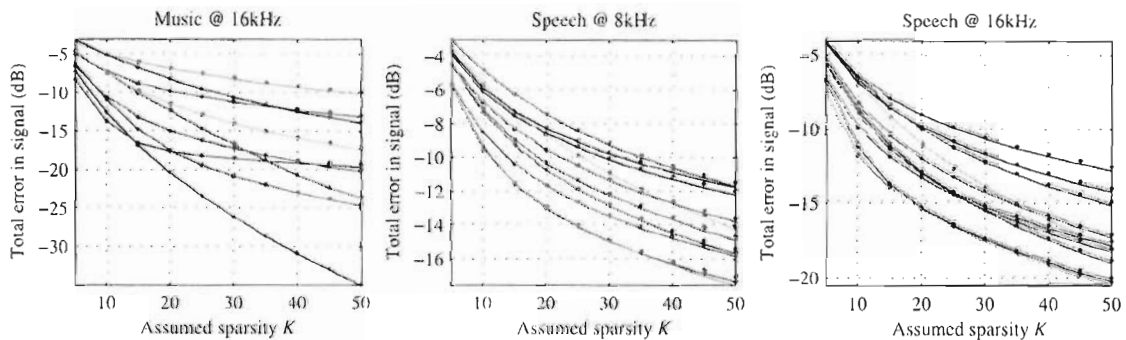

Fig. 9.   Error energy in the reconstruction of noisy non-sparse signal - calculated numerically (stars) and according to the presented theory (solid lines) for the randomly positioned disturbances. Errors are shown for various assumed sparsities K. First subplot shows the results for 10 music signals sampled at 16 kHz, second subplot shows the errors for 10 speech signals sampled at 8 kHz whereas the third one shows the errors for 10 different speech signals sampled at 16 kHz.
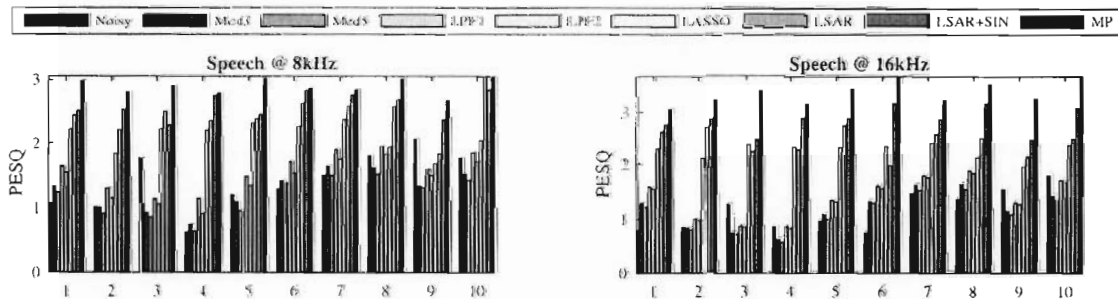

Fig. 10.   Perceptual evaluation of speech signals using the PESQ metrics, shown for the scenario with randomly positioned disturbances. Signals corrupted with impulsive noise and signals reconstructed using median filters of length 3 and 5, low-pass filters with two cut-off frequencies, LSAR and LSAR+SIN teqniques, LASSO-ISTA CS method and presented MP reconstruction are compared with original non-corrupted signals. The figure is related with the results presented in Table I.

MSE drop of 16.25 dB on average (as compared to the MSE for the corrupted signal).

The results produced by the state-of-the-art LSAR and LSAR+SIN algorithms were significantly better as compared to the results using the previous classical filtering methods. The average MSE improvement was 25.12 dB for the LSAR technique, and 26.55 dB for the LSAR+SIN. It is important to note that in the considered scenario, the LSAR implementation [26] suffered from several breakdowns producing high-valued peaks, most likely when the algorithm was not able to track the AR model due to a large number of corrupted/missing values. This hypothesis is confirmed as those breakdowns did not appear in the tests with smaller number of corrupted/missing samples, when the MSE was almost the same as in the LSAR+SIN.

The presented CS method outperfomed the LSAR+SIN for 4 dB on average, and the LSAR for about 5 dB on average. It is interesting to observe that the improvement was the smallest

for the undersampled dataset Speech@8 kHz - only 1.69 dB. A reason for this could be in the reduced sparsity in the considered domain, arising as a consequence of the signals undersampling.

The ℓ_1-norm minimization based CS reconstruction (the LASSO-ISTA approach) produces results worse than the ones obtained with the presented CS method. These results are worse for about 0.5 dB on average than the LSAR results.

3) *Comparison With Respect to the Objective Perceptual Quality Measures:* The results presented in Table I are evaluated from the perceptual quality perspective as well. For an objective assessment and prediction of perceived audio quality of signals from Music @ 16 kHz dataset, the PEMO-Q method is engaged [67]. We used a freely available online implementation included in the software companion of [68], [69]. We mapped the output of the algorithm, that is, the perceptual similarity measure (PSM_t), to the corresponding objective difference grade (ODG) scale using the procedure described in [67]. The

scale has values in the range of −4 (very annoying impairment) to 0 (imperceptible impairment). The PEMO-Q ODG results are calculated for the corrupted signals and for all reconstructed signals, considered in Section VII-A2, for Music @ 16 kHz dataset. The results shown in Fig. 8 (first subplot) indicate that the presented CS algorithm outperforms other methods, on average, having an average score of −1.32, compared to the LSAR+SIN score −1.81, and the LASSO-ISTA score −1.85. However, for the 5th and 7th signal the presented method is slightly overperfomed by the LSAR-SIN, and for the 8th and 10th signals it is very slightly outperformed by the LASSO-ISTA algorithm.

For the perceptual quality comparison of reconstruction results in the speech signals case, the PESQ [65] is used as a quality measure. It is commonly applied in the evaluation of speech quality in the CS-based speech enhancement in various noisy environments [7], [8] with the DCT of windowed audio signal frames as the sparsity domain [7]. Results for the PESQ-based perceptual evaluation obtained for datasets Speech @ 8 kHz and Speech @ 16 kHz are shown in Fig. 10. The PESQ score is calculated for corrupted signals and for all reconstructed signals considered in Section VII-A2. For Speech @ 8 kHz dataset, the PESQ score for the proposed method was 2.89. It is larger than the average LSAR+SIN score 2.59, the LSAR score 2.45, and the LASSO-ISTA score 2.1.

All these algorithms have significantly improved the perceptual quality in comparison to the corrupted signals. The improvement in reconstruction for Speech @ 16 kHz dataset is even more evident. In this case the average score of the presented CS method was 3.37. The other considered methods produced following scores: the LSAR+SIN 2.87, the LSAR 2.44, and the LASSO-ISTA 2.27. The improvement is higher than in the case of Speech @ 8 kHz dataset.

B. Disturbances Localized in the Time-Domain Blocks

In this experiment, impulsive disturbances are located in blocks of subsequent samples. All signals from each of three considered datasets were corrupted with a noise located in randomly positioned blocks having random lengths between 1 and 5, such that in average $p\%$ of samples are affected by the noise. Such impulsive noise is considered in order to simulate the reconstruction potential/performance and theoretical error accuracy in cases when localized time-domain audio signal distortions exist (clicks, CD scratches, clipping etc.), [26], [38], [41]. The reconstruction was performed as in the first experiment, considering half-overlapped signal frames of length $N = 500$, weighted by the Hann windowing function. Corrupted samples are detected and considered as unavailable. They are reconstructed using the presented algorithm with various assumed sparsities.

1) Theoretical MSE: Numerically obtained MSE (24) highly matches the theoretical expression (25) in this case as well, as shown in Fig. 11. Results are shown for all signals in all three considered datasets, for the case when the average percent of corrupted samples is $p = 10\%$. Solid lines represent the theoretical error curves, whereas the numerical results are presented using asterisks. The accuracy of the proposed theoretical MSE is expected as long as the conditions for a full CS-based reconstruction are met, even in the cases when the corruption (unavailability) occurs in blocks of successive samples.

2) Comparison With Respect to the MSE: The reconstruction results using the presented CS method are compared with the results obtained using the median filters, the low-pass Butterworth filters (with the same parameters as de-

	Music@16kHz	Speech@8kHz	Speech@16kHz
Noisy	-11.33dB	-23.55dB	-24.53dB
Med3	-26.15dB	-42.70dB	-42.83dB
Med5	-25.96dB	-42.25dB	-42.68dB
LPF1	-25.72dB	-41.62dB	-42.21dB
LPF2	-25.77dB	-41.72dB	-42.31dB
FTR	-26.24dB	-42.92dB	-42.91dB
BDR	-26.66dB	-42.93dB	-42.95dB
LSAR	-32.52dB	-45.48dB	-46.58dB
LSAR+SIN	-34.17dB	-48.61dB	-50.20dB
LASSO	-37.64dB	-48.41dB	-49.65dB
MP	-37.80dB	-50.58dB	-53.17dB

scribed in Section VII-A2 for the first experimental setup), the LSAR and the LSAR+SIN audio restoration algorithms, and the LASSO-ISTA, with respect to the MSE. The results are presented in Table II, for the case when the average percent of corrupted samples is $p = 50\%$. Additionally, in this scenario the reconstruction MSE is given for a recent method for impulsive noise/clicks detection and removal (AR-based reconstruction) presented in [37], [38]. The detection and the AR-model based reconstruction are done using authors' algorithms, codes and parameters (semi-causal with decision-feedback scheme) [38]. The row denoted by FTR contains the results for the forward-time approach and the row indicated by BDR shows the results with a bidirectional signal processing, originally introduced in [37]. These algorithms are highly adapted for the clicks removal application. For these algorithms the corrupted samples detection was performed using embedded detection procedures. A large number of corrupted samples in this example significantly reduced algorithms' reconstruction efficiency. As in the previous experiment, the considered CS reconstruction techniques, the LSAR, and the LSAR+SIN produced, in average, better results than the other considered methods.

The average MSE improvement with median filters was approximately 17.5 dB. It is similar for both filter lengths. The low-pass filtering produced an average improvement of 16.7 dB, similar for both considered filters as well. Improvement in the FTR and BDR algorithms was significantly lower for the considered experiment with 50% missing samples than in the case when this percent is lower (e.g. when $p = 10\%$ or 15%). The improvement was on average 17.6 dB. The ℓ_1-norm minimization based CS reconstruction (LASSO-ISTA) produced in this experiment better average results, with 25.43 dB of MSE improvement, as compared to the LSAR and the LSAR-SIN, producing improvements of 21.72 dB and 24.52 dB, respectively. The LASSO-ISTA outperformed, on average, the LSAR-SIN due to a significant MSE improvement in the Music @ 16 kHz dataset case. The presented CS method produced 1.95 dB better result, on average, than the LASSO-ISTA reconstruction. The largest difference in the results occurs for the Speech @ 16 kHz dataset.

3) Comparison With Respect to the Objective Perceptual Quality Measures: For perceptual quality evaluation, the PEMO-Q and PESQ metrics are again used as objective measures. The results for the Music @ 16 kHz dataset are shown in Fig. 8 (second subplot). The perceptual evaluation results for
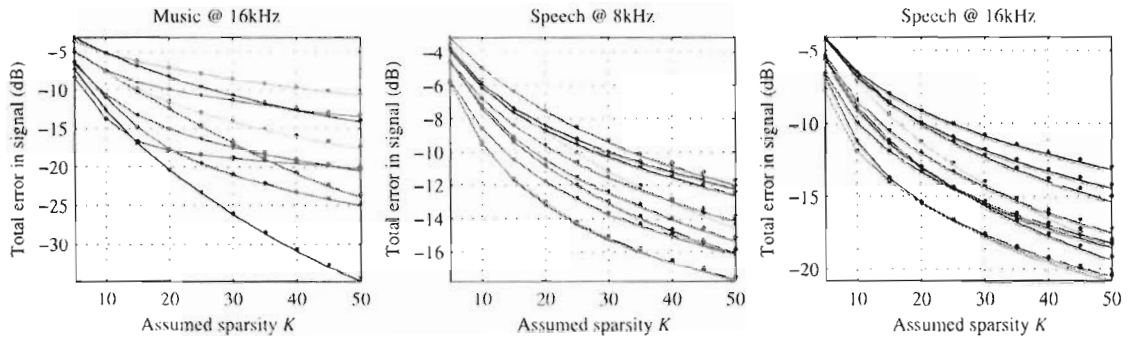
Fig. 11.   Error energy in the reconstruction of noisy non-sparse signal - calculated numerically (stars) and according to the presented theory (solid lines), when the impulsive noise occurs in the time-domain blocks of varying length. Error is shown for various assumed sparsity.
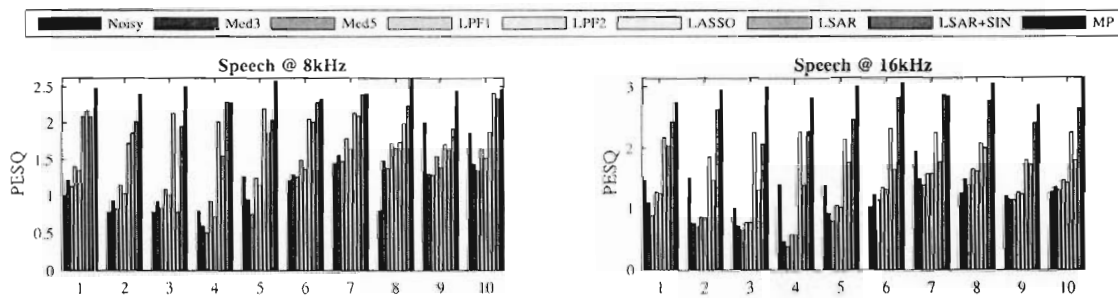

Fig. 12.   Perceptual evaluation of speech signals using the PESQ metrics shown for the scenario with disturbances localized in the time-domain blocks. Impulsive noise appears in blocks of length varying from 1 to 5 samples. Signals corrupted with impulsive noise and signals reconstructed using median filters of length 3 and 5, low-pass filters with two cut-off frequencies, LSAR and LSAR+SIN teqniques, LASSO-ISTA CS method and presented MP reconstruction are compared with original non-corrupted signals. The figure is related with the results presented in Table II.

the Speech @ 8 kHz and Speech @ 16 kHz are presented in Fig. 12.

From the PEMO-Q scores in Fig. 8 (second subplot) we may conclude that the presented CS reconstruction, having the average score of -2.12 outperforms the LASSO-ISTA (-2.48), the LSAR+SIN (-2.95), and the LSAR (-3.13). However, for some signals the LASSO-ISTA outperformed the presented CS method. In accordance with the MSE results from Table II, the LASSO-ISTA outperformed the LSAR and the LSAR+SIN in this experiment.

The PESQ scores, shown in Fig. 12, match the results presented in Table II. For Speech @ 8 kHz dataset, the average PESQ score for the presented CS reconstruction is 2.44, outperforming the LSAR+SIN (2.15), the LASSO-ISTA (1.96) and the LSAR (1.83). For Speech @ 16 kHz dataset the average scores are: the presented CS reconstruction (2.93), the LSAR+SIN (2.53), the LASSO-ISTA (2.13), and the LSAR (1.68). As indicated in the previous scenario, the perceptual quality improvement is larger for the dataset Speech @ 16 kHz.

VIII. CONCLUSION

As one of the most significant signal transforms, incorporated in many compression algorithms, DCT is analyzed here within the framework of a reduced set of observations. As it exhibits many specific properties, the analysis of the DCT is different from the corresponding Fourier analysis. The properties of partial DCT matrix acting as measurement matrix in the considered framework, place it in the middle position between the commonly analyzed partial DFT and Gaussian based measurement matrices. Based on the analysis of the DCT coefficients corresponding to the under-sampled signal, the coherence-based reconstruction condition is derived, with less

conservative theoretical bounds guaranteeing successful reconstruction. Additive noise influence on the reconstruction of signals sparse in this particular domain is also analyzed. Assuming that a nonsparse noisy signal is reconstructed under the sparsity assumption, an explicit analytic expression of the reconstruction error is provided in this paper. A reconstruction algorithm inspired by the presented analysis is proposed. Numerical examples on audio signals confirm the accuracy of the presented theory and efficiency of the reconstruction algorithm as compared to other base-line algorithms for the audio signal reconstructions.

APPENDIX A
PROOF OF THE THEOREM 1

Monocomponent signals: Let us observe a mono-component signal case, $K = 1$, $k_l = k_1$. Without loss of generality, the amplitude $A_1 = 1$ is assumed. Starting from the theorem assumptions, the initial DCT of a signal with M available samples can be calculated as:

$$X_0^C(k) = \sum_{i=1}^{M} z(k_1, k, n_i).$$ (26)

where $z(k_1, k, n_i)$ is defined by (6) with $A_1 = 1$. As the signal and basis functions are orthogonal, it can be written

$$\sum_{n=0}^{N-1} z(k_1, k, n) = \delta(k - k_1).$$ (27)

The case for $k = k_1$: For analysis simplicity let us first consider $k = k_1$ and analyze the corresponding DCT coefficient $X_0^C(k_1)$. It is a random variable. According to (27), and due to

the fact that all values $z(k_1, k_1, n_i)$ are equally distributed with expected values $1/N$, it can be easily concluded that the mean value of $X_0^C(k_1)$ equals:

$$\mu_{X_0^C(k_1)} = E\left\{X_0^C(k_1)\right\} = \frac{M}{N}. \qquad (28)$$

For $A_1 \neq 1$ the mean value (28) is multiplied by A_1. Next, we derive the variance of this random variable. It is given by

$$\sigma^2_{X_0^C(k_1)} = E\left\{\sum_{i=1}^{M} z^2(k_1, k_1, n_i) \right. $$
$$\left. + \sum_{i=1}^{M}\sum_{\substack{j=1 \\ i \neq j}}^{M} z(k_1, k_1, n_i)z(k_1, k_1, n_j)\right\} - \mu^2_{X_0^C(k_1)}.$$

Starting from (27) for $k = k_1$, by multiplying the left and the right side with $z(k_1, k_1, n)$, and taking the expectation of both sides we get:

$$E\left\{z(k_1, k_1, 0)z(n, k_1, k_1) + \ldots + z(k_1, k_1, N-1)z(k_1, k_1, n)\right\}$$
$$= E\left\{z(k_1, k_1, n)\right\} = \frac{1}{N}. \qquad (29)$$

Values $z(k_1, k_1, n)$ are equally distributed. Therefore, expectations $E\{z(k_1, k_1, m)z(k_1, k_1, q)\}$ for $m \neq q$, $m, q \in \mathbf{N}$ are the same and equal to a constant B. We may write:

$$(N-1)B + E\left\{z^2(k_1, k_1, m)\right\} = \frac{1}{N} \qquad (30)$$

The variance can be now expressed as follows:

$$\sigma^2_{X_0^C(k_1)} = ME\left\{z^2(k_1, k_1, m)\right\} + M(M-1)B - \frac{M^2}{N^2}, \qquad (31)$$

with $m \in \mathbf{M} \subseteq \mathbf{N}$. The expectation appearing in the first term of (31) equals $E\left\{z^2(k_1, k_1, m)\right\} = \frac{a_{k_1}^4}{4} + \frac{a_{k_1}^2}{4N}$ for $k_1 \neq 0$. For $k_1 = 0$ it is equal to $a_{k_1}^4$. Incorporating this result into (31) with B expressed from (30), then multiplying the variance expression with A_1^2 and replacing the values of a_{k_1} we get the result as in Theorem 1:

$$\sigma^2_{X_0^C(k_1)} = \frac{M(N-M)}{N^2(N-1)}\left[1 - \frac{1}{2}(1 + \delta(k_1))\right]A_1^2. \qquad (32)$$

The case $k \neq k_1$: The DCT at non-signal (noisy) positions, $X_0^C(k)$, $k \neq k_1$ is a random variable with statistical properties different from the previously analyzed case. Namely, due to (27) and the fact that all values $z(k_1, k, n_i)$ are equally distributed, it can be concluded that its mean-value is equal to zero, i.e.:

$$\mu_{X_0^C(k)} = E\left\{X_0^C(k)\right\} = 0, \quad k \neq k_1. \qquad (33)$$

For the zero-mean random variable, the variance reads:

$$\sigma^2_{X_0^C(k)} = E\left\{\sum_{i=1}^{M} z^2(k_1, k, n_i) \right.$$
$$\left. + \sum_{i=1}^{M}\sum_{\substack{j=1 \\ i \neq j}}^{M} z(k_1, k, n_i)z(k_1, k, n_j)\right\}, \quad k \neq k_1.$$

Now, starting from (27), multiplying the left and right side by $z(k_1, k, n)$, and taking the expectation of both sides we get similar result as (29) with right side equal to zero. As in the previous case, we may assume that the values of $z(k_1, k, n)$ are equally distributed, and that the expectations $E\{z(k_1, k, m)z(k_1, k, q)\}$ for $m \neq q$, $m, q = 0, 1, \ldots, N-1$ are the same, and equal to a constant D leading to

$$(N-1)D + E\left\{z^2(k_1, k, m)\right\} = 0 \qquad (34)$$

Since $k \neq k_1$, then the unknown term $E\left\{z^2(k_1, k, m)\right\}$, assuming that $k \neq N - k_1$, can be expressed as

$$E\left\{z^2(k_1, k, m)\right\} = E\left\{z(k_1, k_1, m)\right\}E\left\{z(k, k, m)\right\} = \frac{1}{N^2},$$

$m = 0, \ldots, N-1$. According to (27), all values of $z(k_1, k_1, m)$ i.e. $z(k, k, m)$ are equally distributed. It can be easily shown that $E\{z(k_1, k_1, m)\}$, $E\{z(k, k, m)\} = 1/N$. For $k = N - k_1$ unknown expectation becomes previously calculated

$$E\left\{z^2(k_1, N-k_1, m)\right\} = E\left\{z^2(k_1, k_1, m)\right\} = \frac{a_{k_1}^4}{4} + \frac{a_{k_1}^2}{4N},$$

$m = 0, \ldots, N-1$, for $k_1 \neq 0$ and $E\left\{z^2(k_1, N-k_1, m)\right\} = a_{k_1}^4$, for $k_1 = 0$. It can be concluded that for the coefficient at the position $k = N - k_1$, the variance expression (32) holds.

Starting from (35), that is $\sigma^2_{X_0^C(k)} = ME\left\{z^2(k, k_1, n_i)\right\} + M(M-1)D$, $k \neq k_1$ and following the previous conclusions and incorporating the non-zero amplitude $A_1 \neq 1$ we get

$$\sigma^2_{X_0^C(k)} = \frac{M(N-M)}{N^2(N-1)}A_1^2\left[1 - \frac{1}{2}\delta(k - (N-k_1))\right], \qquad (35)$$

where $k \neq k_1$, leading to the result of Theorem 1.

Gaussian distribution: Consider the distribution of $X_0^C(k_1) = \sum_{i=1}^{M} z(k_1, k, n_i)$ for large M and $k_1 \neq k$. The probability density function of a normalized zero-mean random variable $c = X_0^C(k_1)/\sigma_{X_0^C(k_1)}$, according to the Edgeworth expression [70], is

$$f(c) = \phi(c) + \frac{1}{4!M}\left[\frac{\kappa_4}{\sigma^4}\phi^{(4)}(c) + \frac{\kappa_3^2}{3\sigma^6}\phi^{(6)}(c)\right] + O\left(\frac{1}{M^2}\right)(c).$$

The first term is the Gaussian distribution $\phi(c) = e^{-c^2/2}/\sqrt{2\pi}$, while the remaining terms are the deviations from this distribution. The variance, third, and fourth order moments of $z(k_1, k, n_i)$ are denoted by σ^2, κ_3, and κ_4, respectively. In our case, for a large M, we have $\sigma^2 \to 1/N^2$, $\kappa_3 \to 0$, and $\kappa_4 \to 9/(4N^4)$. Therefore $\kappa_4/(4!M\sigma^4) \to 3/(32M) \to 0$ and $f(c) \to \phi(c)$.

Multicomponent signals: The analysis provided for monocomponent signals is extended to the case of multicomponent signals next. The analyzed random variable (26) is now:

$$X_0^C(k) = \sum_{i=1}^{M}\sum_{l=1}^{K} a_k^2 A_l \cos\left(\frac{\pi(2n_i + 1)}{2N}k_l\right)$$
$$\times \cos\left(\frac{\pi(2n_i + 1)}{2N}k\right). \qquad (36)$$

According to the previously presented results, for the case of multi-component signals the DCT coefficients at the l-th signal position $X_0^C(k)$, $k = k_l$ behave as random Gaussian vari-

ables with non-zero mean values equal to $\mu_{X_0^C(k)} = A_l \frac{M}{N}$, $l = 1, 2, ..., K$ whereas the DCT coefficients at non-signal positions, $X_0^C(k)$, $k \neq k_l$ also behave as Gaussian variables, with mean-values equal to zero, since the noise caused by missing samples is zero-mean. These conclusions follow from the classical central limit theorem [71], and from the fact that the summation of Gaussian variables produces a new Gaussian variable. The DCT coefficients mean-value for a multicomponent signal can be written as: $\mu_{X_0^C(k)} = \frac{M}{N} \sum_{l=1}^{K} A_l \delta(k - k_l)$.

The variance of the DCT coefficients $X_0^C(k)$ at nonsignal positions $k \neq k_l$ equals:

$$\sigma^2_{X_0^C(k)} = \frac{M(N-M)}{N^2(N-1)} \sum_{l=1}^{K} A_l^2 \left[1 - \frac{1}{2}\delta(k - (N - k_l)) \right]. \quad (37)$$

This expression is easily obtained, as at the positions $k \neq k_l$ the missing samples in every signal component contribute to the noise, and the noises from each component are Gaussian, uncorrelated and zero-mean, with variances $A_l^2 \frac{M(N-M)}{N^2(N-1)} \left[1 - \frac{1}{2}\delta(k - (N - k_l)) \right]$, $l = 1, ..., K$, for the noise that originates from the l-th signal component. Note that the result (37) holds in the sense of an average variance of the DCT coefficients at nonsignal positions, as the statistical independence of the random variables is assumed. However, strictly speaking, components of signal multiplied with basis functions may cause a coupling effect if they are placed at positions satisfying certain conditions. For example, in a two-component sparse signal with DCT coefficients at positions k_1 and k_2 if the condition $k_1 + k_2 = 2k$ is satisfied, the coupling effect causes the increase of variances at positions $k_{c1} = (k_1 + k_2)/2$ and $k_{c2} = (k_2 - k_1)/2$. However, at positions $N - k_{c1}$ and $N - k_{c2}$ the variance is decreased for the same values. Consequently, the average variance of DCT coefficients at nonsignal positions $k \neq k_l$ remains the same and equal to (37).

According to the presented analysis for the mono-component signal case, the K-th signal component at the position $k = k_p$, $p \in \{1, 2, ..., K\}$ has variance $A_p^2 \frac{M(N-M)}{N^2(N-1)} \left[1 - \frac{1}{2}(1 + \delta(k_p)) \right]$ and mean value $\mu_{X_0^C(k_p)} = A_p^2 M/N$. Additionally, at the position $k = k_p$ the noise caused by missing samples in the remaining $K - 1$ components is also present. This means that the sum of random variables originating from other signal components at positions k_l, $l = \{1, 2, ..., K\}$, $l \neq p$ is added at the position k_p. These $K - 1$ random variables are Gaussian, zero mean, mutually uncorrelated, with variances $A_l^2 \frac{M(N-M)}{N^2(N-1)} \left[1 - \frac{1}{2}\delta(k - (N - k_l)) \right]$ and $l \neq p$, with $l = 1, ..., K$, $p = 1, ..., K$. The resulting random variable is also Gaussian, with the mean-value $\mu_{X_0^C(k_p)} = A_p^2 M/N$ and the variance equal to:

$$\sigma^2_{X_0^C(k_p)} = \frac{M(N-M)}{N^2(N-1)} \left\{ A_p^2 \left[1 - \frac{1}{2}(1 + \delta(k_p)) \right] \right.$$
$$\left. + \sum_{\substack{l=1 \\ l \neq p}}^{K} A_l^2 \left[1 - \frac{1}{2}\delta(k - (N - k_l)) \right] \right\}. \quad (38)$$

Unification of the results given by (37) and (38) leads to Theorem 1 statement for the variance.

REFERENCES

[1] D. Donoho, "Compressed sensing," *IEEE Trans. Inf. Theory*, vol. 52, no. 4, pp. 1289–1306, Apr. 2006.

[2] R. Baraniuk, "Compressive sensing," *IEEE Signal Process. Mag.*, vol. 24, no. 4, pp. 118–121, Jul. 2007.

[3] E. J. Candès and M. B. Wakin, "An introduction to compressive sampling," *IEEE Signal Process. Mag.*, vol. 25, no. 2, pp. 21–30, Mar. 2008.

[4] L. Stanković, S. Stanković, and M. Amin, "Missing samples analysis in signals for applications to L-estimation and compressive sensing," *Signal Process.*, vol. 94, pp. 401–408, Jan. 2014.

[5] M. Elad, *Sparse and Redudant Representations: From Theory to Applications in Signal and Image Processing*. New York, NY, USA: Springer, 2010.

[6] H. Rauhut, "Stability results for random sampling of sparse trigonometric polynomials," *IEEE Trans. Inf. Theory*, vol. 54, no. 12, pp. 5661–5670, Dec. 2008.

[7] D. Wu, W. P. Zhu, and M. N. S. Swamy, "The theory of compressive sensing matching pursuit considering time-domain noise with application to speech enhancement," *IEEE/ACM Trans. Audio, Speech, Lang. Process.*, vol. 22, no. 3, pp. 682–696, Mar. 2014.

[8] J. C. Wang, Y. S. Lee, C. H. Lin, S. F. Wang, C. H. Shih, and C. H. Wu, "Compressive sensing-based speech enhancement," *IEEE/ACM Trans. Audio, Speech, Lang. Process.*, vol. 24, no. 11, pp. 2122–2131, Nov. 2016.

[9] R. E. Carrillo, K. E. Barner, and T. C. Aysal, "Robust sampling and reconstruction methods for sparse signals in the presence of impulsive noise," *IEEE J. Sel. Topics Signal Process.*, vol. 4, no. 2, pp. 392–408, Apr. 2010.

[10] E. Sejdić, M. A. Rothfuss, M. L. Gimbel, and M. H. Mickle, "Comparative analysis of compressive sensing approaches for recovery of missing samples in an implantable wireless Doppler device." *IET Signal Process.*, vol. 8, no. 3, pp. 230–238, May 2014.

[11] Z. Zhang, Y. Xu, J. Yang, X. Li, and D. Zhang, "A survey of sparse representation: Algorithms and applications," *IEEE Access*, vol. 3, pp. 490–530, 2015.

[12] S. Ji, Y. Xue, and L. Carin, " Bayesian compressive sensing," *IEEE Trans. Signal Process.*, vol. 56, no. 6, pp. 2346–2356, Jun. 2008.

[13] S. Stanković, I. Orović, and L. Stanković, "An automated signal reconstruction method based on analysis of compressive sensed signals in noisy environment," *Signal Process.*, vol. 104, pp. 43–50, Nov. 2014.

[14] L. Stanković, *Digital Signal Processing With Selected Topics*. North Charleston, South Carolina, USA: CreateSpace Independent Publishing Platform, Nov. 2015.

[15] L. Stanković, I. Stanković, and M. Daković, "Nonsparsity influence on the ISAR recovery from reduced data," *IEEE Trans. Aerosp. Electron. Syst.*, vol. 52, no. 6, pp. 3065–3070, Dec. 2016.

[16] G. Bi, S. K. Mitra, and S. Li, "Sampling rate conversion based on DFT and DCT," *Signal Process.*, vol. 93, no. 2, pp. 476–486, Feb. 2013.

[17] L. Zhao, G. Bi, L. Wang, and H. Zhang, "An improved auto-calibration algorithm based on sparse Bayesian learning framework," *IEEE Signal Process. Lett.*, vol. 20, no. 9, pp. 889–892, Sep. 2013.

[18] G. Davis, S. Mallat, and M. Avellaneda, "Greedy adaptive approximation," *J. Construct. Approx.*, vol. 12, pp. 57–98, 1997.

[19] R. J. Tibshirani, "Regression shrinkage and selection via the lasso: A retrospective," *J. Roy. Statist. Soc. Ser. B*, vol. 73, pp. 273–282, 2011.

[20] A. Beck and M. Teboulle, "A fast iterative shrinkage-thresholding algorithm for linear inverse problems," *SIAM J. Imag. Sci.*, vol. 1, no. 2, pp. 183–202, 2009.

[21] L. Stanković and M. Daković, "On a gradient-based algorithm for sparse signal reconstruction in the signal/measurements domain," *Math. Probl. Eng.*, vol. 2016, 2016, Art. no. 6212674, doi:10.1155/2016/6212674

[22] M. G. Christensen, J. Østergaard, and S. H. Jensen, "On compressed sensing and its application to speech and audio signals," in *Proc. Conf. Rec. 43rd Asilomar Conf. Signals, Syst. Comput.*, Pacific Grove, CA, USA, 2009, pp. 356–360.

[23] V. Britanak and K. R. Rao, "An efficient implementation of the forward and inverse MDCT in MPEG audio coding," *IEEE Signal Process. Lett.*, vol. 8, no. 2, pp. 48–51, Feb. 2001.

[24] P. Maechler *et al.*, "VLSI design of approximate message passing for signal restoration and compressive sensing," *IEEE J. Emerg. Sel. Topics Circuits Syst.*, vol. 2, no. 3, pp. 579–590, Sep. 2012.

[25] D. Bellasi, P. Maechler, A. Burg, N. Felber, H. Kaeslin, and C. Studer, "Live demonstration: Real-time audio restoration using sparse signal recovery," in *Proc. IEEE Int. Symp. Circuits Syst.*, Beijing, China, 2013, pp. 659–659.

[26] A. Adler, V. Emiya, M. G. Jafari, M. Elad, R. Gribonval, and M. D. Plumbley, "Audio inpainting," *IEEE Trans. Audio, Speech, Lang. Process.*, vol. 20, no. 3, pp. 922–932, Mar. 2012, doi: 10.1109/TASL.2011.2168211.

[27] S. J. Godsill and P. J. W. Rayner, *Digital Audio Restoration–A Statistical Model-Based Approach*. Berlin, Germany: Springer-Verlag, 1998.

[28] W. Etter, "Restoration of a discrete-time signal segment by interpolation based on the left-sided and right-sided autoregressive parameters," *IEEE Trans. Signal Process.*, vol. 44, no. 5, pp. 1124–1135, May 1996.

[29] H. Lin and S. Godsill, "The multi-channel AR model for real-time audio restoration," in *Proc. IEEE Workshop Appl. Signal Process. Audio Acoust.*, New Paltz, NY, USA, 2005, pp. 335–338.

[30] P. J. W. Rayner and S. J. Godsill, "The detection and correction of artefacts in degraded gramophone recordings," in *Proc. IEEE ASSP Workshop Appl. Signal Process. Audio Acoust., Final Prog. Paper Summaries*, New Paltz, NY, USA, 1991, pp. 151–152.

[31] S. J. Godsill and P. J. W. Rayner, "A Bayesian approach to the restoration of degraded audio signals," *IEEE Trans. Speech Audio Process.*, vol. 3, no. 4, pp. 267–278, Jul. 1995.

[32] S. J. Godsill and C. H. Tan, "Removal of low frequency transient noise from old recordings using model-based signal separation techniques," in *Proc. Workshop Appl. Signal Process. Audio Acoust.*, New Paltz, NY, USA, 1997.

[33] S. J. Godsill and P. J. W. Rayner, "Robust noise modelling with application to audio restoration," in *Proc. Workshop Appl. Signal Process. Audio Acoust.*, New Paltz, NY, USA, 1995, pp. 143–146.

[34] C. M. Hicks and S. J. Godsill, "A two-channel approach to the removal of impulsive noise from archived recordings," in *Proc. Int. Conf. Acoust., Speech, Signal Process.*, Adelaide, SA, Australia, 1994, vol. 2, pp. II/213–II/216.

[35] S. J. Godsill, P. J. Wolfe, and W. N. W. Fong, "Statistical model-based approaches to audio restoration and analysis," *J. New Music Res.*, vol. 30, no. 4, pp. 323–328, 2001.

[36] A. Janssen, R. Veldhuis, and L. Vries, "Adaptive interpolation of discrete-time signals that can be modeled as autoregressive processes," *IEEE Trans. Acoust., Speech, Signal Process.*, vol. ASSP-34, no. 2, pp. 317–330, Apr. 1986.

[37] M. Niedźwiecki and M. Ciołek, "Elimination of impulsive disturbances from archive audio signals using bidirectional processing," *IEEE Trans. Audio, Speech, Lang. Process.*, vol. 21, no. 5, pp. 1046–1059, May 2013.

[38] M. Ciołek and M. Niedźwiecki, "Detection of impulsive disturbances in archive audio signals," in *Proc. IEEE Int. Conf. Acoust., Speech, Signal Process.*, New Orleans, LA, USA, 2017, pp. 671–675.

[39] M. Ruhland, J. Bitzer, M. Brandt, and S. Goetze, "Reduction of Gaussian, supergaussian, and impulsive noise by interpolation of the binary mask residual," *IEEE/ACM Trans. Audio, Speech, Lang. Process.*, vol. 23, no. 10, pp. 1680–1691, Oct. 2015.

[40] M. Siu and A. Chan, "A robust viterbi algorithm against impulsive noise with application to speech recognition," *IEEE Trans. Audio, Speech, Lang. Process.*, vol. 14, no. 6, pp. 2122–2133, Nov. 2006, doi: 10.1109/TASL.2006.872592.

[41] F. R. Avila and L. W. P. Biscainho, "Bayesian restoration of audio signals degraded by impulsive noise modeled as individual pulses," *IEEE Trans. Audio, Speech, Lang. Process.*, vol. 20, no. 9, pp. 2470–2481, Nov. 2012, doi: 10.1109/TASL.2012.2203811.

[42] J. K. Nielsen, M. G. Christensen, A. T. Cemgil, S. J. Godsill, and S. H. Jensen, "Bayesian interpolation in a dynamic sinusoidal model with application to packet-loss concealment," in *Proc. 18th Eur. Signal Process. Conf.*, Aalborg, Denmark, 2010, pp. 239–243.

[43] H. Ofir, D. Malah, and I. Cohen, "Audio packet loss concealment in a combined MDCT-MDST domain," *IEEE Signal Process. Lett.*, vol. 14, no. 12, pp. 1032–1035, Dec. 2007.

[44] H. Ofir and D. Malah, "Packet loss concealment for audio streaming based on the GAPES and MAPES algorithms," in *Proc. IEEE 24th Conv. Elect. Electron. Eng. Israel*, Eilat, Israel, 2006, pp. 280–284.

[45] C. Perkins, O. Hodson, and V. Hardman, "A survey of packet loss recovery techniques for streaming audio," *IEEE Netw.*, vol. 12, no. 5, pp. 40–48, Sep./Oct. 1998.

[46] D. Goodman, G. Lockhart, O. Wasem, and Wai-Choong Wong, "Waveform substitution techniques for recovering missing speech segments in packet voice communications," *IEEE Trans. Acoust., Speech, Signal Process.*, vol. ASSP-34, no. 6, pp. 1440–1448, Dec. 1986.

[47] B. K. Lee and J. H. Chang, "Packet loss concealment based on deep neural networks for digital speech transmission," *IEEE/ACM Trans. Audio, Speech, Lang. Process.*, vol. 24, no. 2, pp. 378–387, Feb. 2016.

[48] A. Stenger, K. Ben Younes, R. Reng, and B. Girod, "A new error concealment technique for audio transmission with packet loss," in *Proc. 8th Eur. Signal Process. Conf.*, Trieste, Italy, 1996, pp. 1–4.

[49] B. W. Wah, X. Su, and D. Lin, "A survey of error-concealment schemes for real-time audio and video transmissions over the Internet," in *Proc. Int. Symp. Multimedia Softw. Eng.*, Taipei, Taiwan, 2000, pp. 17–24.

[50] C. A. Rodbro, M. G. Christensen, S. V. Andersen, and S. H. Jensen, "Compressed domain packet loss concealment of sinusoidally coded speech," in *Proc. Int. Conf. Acoust., Speech, Signal Process.*, 2003, vol. 1, pp. I-104–I-107.

[51] A. Subramanya, M. L. Seltzer, and A. Acero, "Automatic removal of typed keystrokes," *IEEE Signal Process. Lett.*, vol. 14, no. 5, pp. 363–366, May 2007.

[52] J. Gemmeke, H. Van Hamme, B. Cranen, and L. Boves, "Compressive sensing for missing data imputation in noise robust speech recognition," *IEEE J. Sel. Topics Signal Process.*, vol. 4, no. 2, pp. 272–287, Aug. 2010.

[53] O. Cappé, "Elimination of the musical noise phenomenon with the Ephraim and Malah noise suppressor," *IEEE Trans. Speech Audio Process.*, vol. 2, no. 2, pp. 345–349, Apr. 1994.

[54] O. Cappé and J. Laroche, "Evaluation of short-time spectral attenuation techniques for the restoration of musical recordings," *IEEE Trans. Speech Audio Process.*, vol. 3, no. 1, pp. 84–93, Jan. 1995.

[55] S. Canazza, G. De Poli, and G. A. Mian, "Restoration of audio documents by means of extended Kalman filter, " *IEEE Trans. Audio, Speech, Lang. Process.*, vol. 18, no. 6, pp. 1107–1115, Aug. 2010, doi: 10.1109/TASL.2009.2030005.

[56] H. Buchner, J. Skoglund, and S. Godsill, "An acoustic keystroke transient canceler for speech communication terminals using a semi-blind adaptive filter model," in *Proc. IEEE Int. Conf. Acoust., Speech, Signal Process.*, Shanghai, China, 2016, pp. 614–618.

[57] V. Britanak, P. C. Yip, and K. R. Rao, *Discrete Cosine and Sine Transforms: General Properties, Fast Algorithms and Integer Approximations*. New York, NY, USA: Elsevier, 2007.

[58] D. Donoho and M. Elad, "Optimally sparse representation in general (nonorthogonal) dictionaries via ℓ_1 minimization," *Proc. Nat. Acad. Sci.*, vol. 100, no. 5, pp. 2197–2202, 2003.

[59] L. Welch, "Lower bounds on the maximum cross correlation of signals," *IEEE Trans. Inf. Theory*, vol. IT-20, no. 3, pp. 397–399, May 1974.

[60] J. Huang and Y. Zhao, "A DCT-based fast signal subspace technique for robust speech recognition," *IEEE Trans. Speech Audio Process.*, vol. 8, no. 6, pp. 747–751, Nov. 2000.

[61] H. S. Malvar. *Signal Processing With Lapped Transforms*. Boston, MA, USA: Artech House, 1992.

[62] L. Stanković, M. Daković, and S. Vujović, "Reconstruction of sparse signals in impulsive disturbance environments," *Circuits, Syst., Signal Process.*, vol. 36, no. 2, pp. 767–794, 2017, doi: 10.1007/s00034-016-0334-3.

[63] E. Vincent, S. Araki, and P. Bofill, *The 2008 Signal Separation Evaluation Campaign: A Community-Based Approach to Large-Scale Evaluation*. Paraty, Brazil: Springer, Mar. 2009.

[64] Audio signals database. Online. Available: http://small-project.eu/ software-data. Accessed on: Sep. 15, 2017

[65] A. W. Rix, J. G. Beerends, M. P. Hollier, and A. P. Hekstra, "Perceptual evaluation of speech quality (PESQ)-a new method for speech quality assessment of telephone networks and codecs," in *Proc. IEEE Int. Conf. Acoust., Speech, Signal Process.*, 2001, vol. 2, pp. 749–752.

[66] J. Nuzman, "Audio restoration: An investigation of digital methods for click removal and hiss reduction," Inst. Adv. Comput. Stud., Univ. Maryland, College Park, MD, USA, 2004. Online. Available: www.github.com/ jnuzman/audio-restoration-2004, Accessed on: Dec. 2017.

[67] R. Huber and B. Kollmeier, "PEMO-Q–A new method for objective audio quality assessment using a model of auditory perception," *IEEE Trans. Audio, Speech, Lang. Process.*, vol. 14, no. 6, pp. 1902–1911, Nov. 2006.

[68] V. Emiya, E. Vincent, N. Harlander, and V. Hohmann, "Subjective and objective quality assessment of audio source separation," *IEEE Trans. Audio, Speech, Lang. Process.*, vol. 19, no. 7, pp. 2046–2057, Sep. 2011.

[69] E. Vincent, "Improved perceptual metrics for the evaluation of audio source separation," *Proc. 10th Int. Conf. Latent Variable Anal. Signal Separation*, 2012, pp. 430–437.

[70] M. Hazewinkel, Ed., *Encyclopedia of Mathematics* (Edgeworth series). New York, NY, USA: Springer, 2001.

[71] P. Billingsley, *Probability and Measure*. 3rd ed. Hoboken, NJ, USA: Wiley, 1995.

Authors' photographs and biographies not available at the time of publication.

Analysis of noisy coefficients in the discrete Hermite transform domain with application in signal denoising and sparse signal reconstruction

Miloš Brajović*, Srdjan Stanković, Irena Orović

University of Montenegro, Faculty of Electrical Engineering, Podgorica 20 000, Montenegro

ARTICLE INFO

ABSTRACT

The influence of an additive Gaussian noise on the discrete Hermite transform based signal representation is analyzed. The Hermite coefficients of noisy signals are random Gaussian variables. Based on the derived respective mean values and the variances, an efficient nonlinear threshold for a simple signal denoising approach is introduced, suitable for signals well concentrated in this transform domain. Moreover, the results are easily incorporated into a coefficient thresholding based compressed sensing algorithm for the reconstruction of noisy signals with missing samples. These approaches and the theory behind are motivated by the signals concentrated in the Hermite transform domain, such as the QRS complexes and UWB signals. Numerical examples validate the presented theory.

© 2018 Elsevier B.V. All rights reserved.

1. Introduction

Recently, the Hermite transform (HT), in both continuous and discrete forms, has drawn a significant research interest in various practical applications [1–9], showing a better performance compared to the commonly used Fourier-based approaches. For instance, the HT is extensively applied in the processing and compression of ECG signals, as well as in the automatic recognition and classification of QRS complexes [1–9]. Other important applications include biomedicine [4,5], image processing and computer tomography [2,9], molecular biology [2], radar signal processing [10], etc. In the light of popular compressive sensing scenarios, the HT was also considered as a domain of signal sparsity [11,12]. Therein, it has been shown that signals, exhibiting sparsity in the HT domain, can be efficiently reconstructed from a small set of random measurements. Besides many application examples, Hermite functions (HF) have been the subject of extensive research in the context of the discrete fractional Fourier transform [13–30]. These Hermite–Gaussian like functions, being closed-form Discrete Fourier Transform (DFT) eigenvectors used to define the discrete fractional Fourier transform, can be also used to define the HT. Various approaches have been reported in this context [13]: methods based on nearly tridiagonal matrices [14–23], methods based

on orthogonal projections [24–29] as well as methods based on closed-form vectors, [9,30].

An interesting example of signals with suitable representation in the HT domain can be found in communications and remote sensing applications, namely, the ultra-wideband (UWB) signals received at antennas. Signals from this class typically have the Gaussian waveforms, such as Gaussian doublets or other shapes resembling the derivatives of the Gaussian function [31–34], that exhibit a compact support in the HT domain. The UWB signals are characterized by an inherent fine resolution in time as well as by good penetration into many common materials and therefore, these signals are widely used in the remote sensing applications [33–37]. However, the presence of noise, that is common in real scenarios, often leads to the performance degradation of algorithms dealing with UWB signals [35,36], thus making the denoising techniques especially important. Having in mind the waveform similarity between the UWB signals and the Hermite basis, the UWB applications, including the denoising, may benefit from the HT [33]. The HT has been continuously related to QRS complexes, particularly important parts of ECG signals. Recently, it was shown that the compressed sensing based reconstruction of these signals is possible exploiting the Hermite transform [11]. Moreover, HT based compression of QRS complexes has been a widely studied topic, and the literature suggests the amenability of this particular transform [1,8]. However, neither the HT based compression nor the compressed sensing has been previously studied for signals affected by common white Gaussian noise.

* Corresponding author.
E-mail address: milosb@ac.me (M. Brajović).

In this paper, the influence of an additive white Gaussian noise (AWGN) on the discrete HT is considered. This is particularly important, as the discrete HT form ordinarily assumes the Gauss–Hermite quadrature applied in the accurate numerical calculation of integrals defining Hermite coefficients, which inevitably leads to a different behavior of this transform in noisy environments when compared with common linear transforms [2,10,11]. We also discuss an alternative form of discrete Hermite transform, recently studied in [5,6,32]. The influence of AWGN is modeled through the expressions for the mean value and variance of noisy Hermite coefficients. Based on these expressions, a nonlinear threshold which separates signal components from the noise is derived. It enables an efficient signal denoising. Moreover, we incorporate the results into a compressed sensing algorithm based on the detection of signal support ([38,39]), leading to the successful reconstruction of noisy signals with missing samples.

The paper is organized as follows. A basic theoretical background about Hermite expansion method using the Gauss–Hermite quadrature is presented in Section 2. The matrix form of the discrete Hermite transform is presented in Section 3. The influence of AWGN on the HT domain is analyzed in Section 4, while the thresholding method and denoising applications are presented in Section 5. The presented theory is put into the compressive sensing and sparse signal processing context in Section 6. The concluding remarks are provided in Section 7.

2. Hermite expansion

The pth order Hermite function is defined as:

$$\psi_p(t,\sigma) = \left(\sigma 2^p p! \sqrt{\pi}\right)^{-\frac{1}{2}} e^{\frac{-t^2}{2\sigma^2}} H_p(t/\sigma)$$

$$= \left(\sigma 2^p p! \sqrt{\pi}\right)^{-\frac{1}{2}} e^{\frac{-t^2}{2\sigma^2}} (-1)^p e^{\frac{t^2}{\sigma^2}} t \frac{d^p(e^{\frac{-t^2}{\sigma^2}})}{dt^p}. \tag{1}$$

with $H_p(t)$ being the pth order Hermite polynomial (HP). A scaling factor σ which stretches or compresses HFs is often used in the definition (1) in order to match the analyzed signal [1,5,31]. Without loss of generality, it is assumed that it has a value $\sigma = 1$ [1,11], and can be omitted in further notations. Hermite basis functions can be recursively calculated [1–3]:

$$\psi_0(t) = \frac{1}{\sqrt[4]{\pi}} e^{-t^2/2}, \qquad \psi_1(t) = \frac{\sqrt{2}t}{\sqrt[4]{\pi}} e^{-t^2/2},$$

$$\psi_p(t) = t\sqrt{\frac{2}{p}}\, \psi_{p-1}(t) - \sqrt{\frac{p-1}{p}}\, \psi_{p-2}(t). \tag{2}$$

The signal representation using the Hermite basis is referenced as the Hermite expansion:

$$s(t) = \sum_{p=0}^{\infty} C(p)\psi_p(t). \tag{3}$$

For a continuous signal $s(t)$, an infinite number $M \to \infty$ of HFs is needed for an accurate signal representation. Otherwise, (3) is just an approximation of the analyzed signal. The pth order Hermite coefficient $C(p)$ is calculated by:

$$C(p) = \int_{-\infty}^{\infty} s(t)\psi_p(t)dt. \tag{4}$$

2.1. Discrete Hermite transform based on the Gauss–Hermite quadrature approximation

The discrete Hermite transform can be considered as a discretized version of the continuous-time Hermite expansion (3). Namely, if HFs are sampled at zeros of the Mth order HP, then the summation (3) becomes the inverse form of the Hermite transform, [1]. In that case, any discrete signal of length M can be

uniquely represented by expansion (3), with a complete set of M discrete basis functions. The integral of the form (4) can be accurately calculated by the Gauss–Hermite (GH) quadrature [3,8,10]:

$$C(p) = \frac{1}{M} \sum_{m=1}^{M} \frac{\psi_p(t_m)}{[\psi_{M-1}(t_m)]^2} s(t_m), \tag{5}$$

where t_m, $1 \le m \le M$ is used to denote zeros of the Mth order HP [1–11]. Functions $\psi_p(t_m)$, $1 \le m \le M$, $0 \le p \le M - 1$ obtained by sampling the continuous HFs at points t_m are orthogonal [1]. When the sampling points are proportional to t_m, the transform (5) is a complete signal representation [1,2,11]. This form of the discrete Hermite transform will be further denoted as DGHmT.

Note that a proper calculation of (5) requires a specific form of sampling. However, as indicated in our previous research [8], when the continuous signal $s(t)$, with assumption of a compact time support, $s(t) = 0$ for $t \notin [-T, T]$, is sampled uniformly to obtain the corresponding finite duration discrete-time signal $s(n) = s(n\Delta t)$, then the discrete signal values at desired points t_m (or at proportional points λt_m where constant λ is directly related with the scaling factor σ (dilation parameter)), are obtained applying a re-sampling procedure. Without loss of generality, assume an odd signal length $M = 2K + 1$, $n = -K,..., K$, with Δt being the sampling period. The continuous-time signal can be reconstructed and resampled at the desired points λt_1, λt_2,..., λt_M using [8]:

$$s(\lambda t_m) \approx \sum_{n=-K}^{K} s(n\Delta t) \frac{\sin(\pi(\lambda t_m - n\Delta t)/\Delta t)}{\pi(\lambda t_m - n\Delta t)/\Delta t}, \tag{6}$$

where $m = 1,..., M$, $n = -K,..., K$.

The truncation error [40,41] using sinc interpolation is largest for time instants near the edges of the considered discrete grid. However, in the case of compact time-support signals, the truncation error will be significantly reduced. Finite signals interpolation problem is additionally discussed from the perspective of FIR filter-based sinc interpolation in [40], where it is emphasized that the truncation effects could be alleviated by multiplying the interpolation kernel $\sin(\pi(t - n\Delta t)/\Delta t)/(\pi(t - n\Delta t)/\Delta t)$ with a window function. The interpolation error has been derived in [42]. Recently, it has been confirmed that this error is negligible for signals with finite-time support, [8].

2.2. Discrete Hermite transform based on symmetric tridiagonal matrix that commutes with a centered Fourier matrix

The previous form of the discrete Hermite transform has been considered in many different application contexts [8,10–12]. Recently, it has been successfully applied in the compression of QRS complexes [8], and in the reconstruction of compressively sensed UWB signals [51]. The highly successful applicability is related to the strong resemblance of these basis functions with analyzed signals. However, as it will be shown in next Section, the DGHmT matrix based on (5) is not orthogonal. As it is generally known that the sampling of continuous HFs does not lead to a compatible discrete orthogonal basis, significant research efforts have been made to determine other approaches for discrete Hermite functions definition [5,6,32]. For example, it has been shown that discrete HFs can be generated as eigenvectors of a centered or shifted Fourier matrix [5,6]. These alternative HFs will be further denoted as $\hat{\psi}_p(n,\sigma)$ when $\sigma = 1$ and $\tilde{\psi}_p(n)$ in the case when time-axis scaling factor $\sigma \ge 1$ (dilation parameter) is assumed. Note that n denotes discrete time index at a uniform time grid related with the sampling theorem. Other alternative approaches for the discrete HFs calculation can be also found in [13–30].

Observe a discrete-time signal $s(n)$ of length N, sampled according to the sampling theorem, with $0 \le n \le M - 1$. For such signal, there exist a set of orthogonal digital functions $\hat{\psi}_p(n,\sigma)$, $p =$
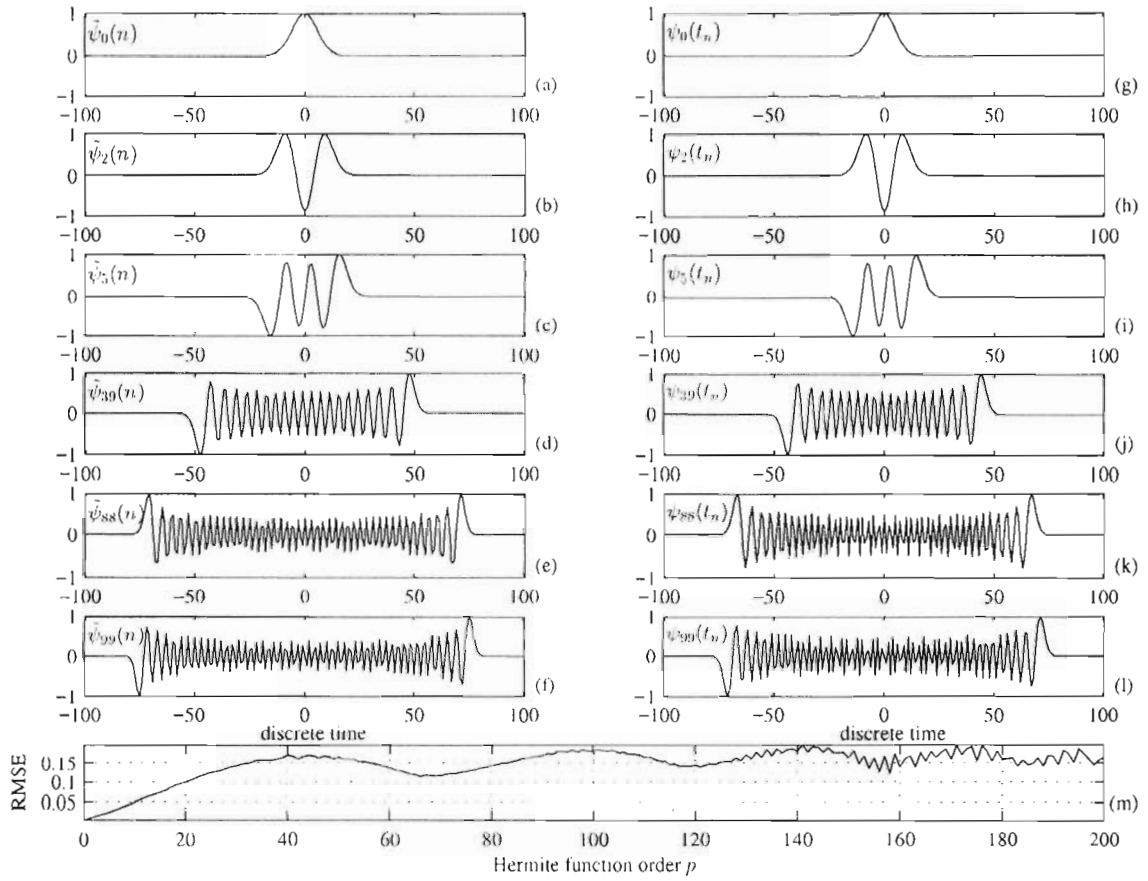
Fig. 1. Examples of: (a)–(f) DHmT and (g)–(l) DGHmT basis functions for $M = 201$; (m) RMSE between functions.

0, ..., $M - 1$, being strongly related to continuous HFs $\psi_p(t)$. It was recently shown that such functions are obtained as eigenvectors of the centered Fourier matrix $\mathbf{F}_C$ [5], satisfying

$$\mathbf{F}_C \tilde{\psi}_p(n, \sigma) = j^n \tilde{\psi}_p(n, \sigma),$$

where $j = \sqrt{-1}$. The set of functions is obtained based on eigenvalue decomposition

$$\mathbf{F}_C = \mathbf{Q}\mathbf{\Lambda}\mathbf{Q}^T \qquad (7)$$

as columns of matrix $\mathbf{Q} = [\ \tilde{\psi}_0, \quad \tilde{\psi}_1, \quad \dots \quad \tilde{\psi}_M\ ]$. Column vectors $\tilde{\psi}_p$, $p = 0, \dots, M - 1$ contain values of discrete HFs $\tilde{\psi}_p(n, \sigma)$, $n = 0, \dots, M - 1$ and $\mathbf{\Lambda}$ is a diagonal matrix containing eigenvalues of matrix $\mathbf{F}_C$. It was shown that these discrete HFs can be generated in an computationally efficient manner as the set of eigenvectors of a symmetric sparse tridiagonal matrix defined by [5,6,32]:

$$\mathbf{T} = \begin{bmatrix} \varphi_0(0) & \varphi_1(1) & 0 & \cdots & 0 \\ \varphi_1(1) & \varphi_0(1) & \varphi_1(2) & \cdots & 0 \\ 0 & \varphi_1(2) & \varphi_0(2) & \ddots & 0 \\ \vdots & \vdots & \ddots & \ddots & \varphi_1(M-1) \\ 0 & 0 & 0 & \varphi_1(M-1) & \varphi_0(M-1) \end{bmatrix}. \qquad (8)$$

with

$$\varphi_0(n) = -2\cos\left(\frac{\pi}{\sigma^2}\right)\sin\left(\frac{\pi n}{M\sigma^2}\right)\sin\left(\frac{\pi}{M\sigma^2}(M - 1 - n)\right),$$

for $0 \le n \le M - 1$, and

$$\varphi_1(n) = \sin\left(\frac{\pi n}{M\sigma^2}\right)\sin\left(\frac{\pi}{M\sigma^2}(M - n)\right).$$

for $0 \le n \le M - 1$. Eigenvalue decomposition of the form

$$\mathbf{T} = \mathbf{Q}\mathbf{\Lambda}\mathbf{Q}^T. \qquad (9)$$

leads to the same matrix of eigenvectors as in (7), in a computationally efficient manner [5]. Functions $\{\tilde{\psi}_0(n, \sigma), \tilde{\psi}_1(n, \sigma), \dots, \tilde{\psi}_{M-1}(n, \sigma)\}$ form an M-dimensional basis of the alternative discrete Hermite transform, further denoted as DHmT. Discrete HFs obtained in this manner are visually very similar to the continuous-time analogous functions. Similar to the continuous case, these functions are non-zero valued near the interval of the definition, and they are odd or even depending on the value of index p (which also counts the number of zero-crossings of the signal), just as in the continuous case [5]. As previously noted [6], the difference between the continuous-time and discrete HFs produced by the presented method increases as the index p (order of the HF) increases.

This issue is illustrated in Fig. 1, where some of the DHmT basis functions (left column) are compared with corresponding basis functions of DGHmT (right column), obtained by sampling the continuous HFs at the roots of the Hermite polynomial of order $M = 201$. For the better comparability, functions are normalized with respect to their maximal amplitudes. For functions with $p = 0$, 2 and 5 there is a high similarity between $\tilde{\psi}_p(n)$ and $\psi_p(n)$, as presented in Fig. 1, first and second rows. For $p = 39$, the difference becomes more obvious (third row), and it increases, as illustrated for $p = 88$ and $p = 99$ (fourth and fifth rows). Fig. 1 emphasizes the DGHmT relevancy for applications requiring a strong similarity with continuous HFs. The RMSE between DGHmT and DHmT basis functions is shown in Fig. 1(m), versus HF order p. It is important to note that calculation of the DHmT is numerically more efficient

than the calculation of the DGHmT. For example, when $M = 201$, the average computation time needed for generation of the set of DHmT basis functions is 0.0025 s, compared to 0.0060 s needed to generate the set of DGHmT basis functions (tested on the same computer with Intel(R) Core(TM) i7-6700HQ CPU @ 2.60 GHz and 8GB of RAM). For $M = 500$, these computation times are 0.012 s in the first case, and 0.016 s in the DGHmT case. However, it should be also noted that DGHmT requires an additional computational burden if the analyzed signal needs to be resampled, according to (6), as well as for the Hermite coefficients calculation based on (5). The accuracy of DHmT basis with respect to continuous-time HFs can be improved by producing a larger set of functions and properly adapting the dilation (time-axis scaling) parameter, [5].

3. Discrete Hermite transforms in matrix forms

The direct and the inverse DGHmT, given by (5) and (3), respectively, can be written in a matrix form. First, we define HT matrix $\mathbf{T}_H$:

$$\mathbf{T}_H = \frac{1}{M} \begin{bmatrix} \frac{\psi_0(t_1)}{(\psi_{M-1}(t_1))^2} & \frac{\psi_0(t_2)}{(\psi_{M-1}(t_2))^2} & \cdots & \frac{\psi_0(t_M)}{(\psi_{M-1}(t_M))^2} \\ \frac{\psi_1(t_1)}{(\psi_{M-1}(t_1))^2} & \frac{\psi_1(t_2)}{(\psi_{M-1}(t_2))^2} & \cdots & \frac{\psi_1(t_M)}{(\psi_{M-1}(t_M))^2} \\ \vdots & \vdots & \ddots & \vdots \\ \frac{\psi_{M-1}(t_1)}{(\psi_{M-1}(t_1))^2} & \frac{\psi_{M-1}(t_2)}{(\psi_{M-1}(t_2))^2} & \cdots & \frac{\psi_{M-1}(t_M)}{(\psi_{M-1}(t_M))^2} \end{bmatrix}. \tag{10}$$

and the corresponding inverse DGHmT matrix $\mathbf{T}_H^{-1}$ (of size $M \times M$)

$$\mathbf{T}_H^{-1} = \begin{bmatrix} \psi_0(t_1) & \psi_1(t_1) & \cdots & \psi_{M-1}(t_1) \\ \psi_0(t_2) & \psi_1(t_2) & \cdots & \psi_{M-1}(t_2) \\ \vdots & \vdots & \ddots & \vdots \\ \psi_0(t_M) & \psi_1(t_M) & \cdots & \psi_{M-1}(t_M) \end{bmatrix}. \tag{11}$$

If $\mathbf{C} = [C(0), C(1), \ldots, C(M-1)]^T$ denotes the vector of Hermite coefficients and $\mathbf{s} = [s(t_1), s(t_2), \ldots, s(t_M)]^T$ is a vector of M signal samples, then:

$$\mathbf{C} = \mathbf{T}_H \mathbf{s}, \tag{12}$$

represents the matrix form of the DGHmT. The inverse discrete DGHmT has the following matrix form:

$$\mathbf{s} = \mathbf{T}_H^{-1} \mathbf{C}. \tag{13}$$

The inverse DGHmT matrix can be written as a product

$$\mathbf{T}_H^{-1} = \mathbf{T}_H^T \mathbf{D}, \tag{14}$$

where the matrix $\mathbf{D}$ is a diagonal matrix whose form is presented in [1], confirming that the discrete HT matrix is not orthogonal. The standard QR decomposition of the DGHmT matrix $\mathbf{T}_H$ leads to the product $\mathbf{T}_H = \mathbf{QR}$ with $\mathbf{Q}$ being the orthogonal matrix, satisfying $\mathbf{QQ}^T = \mathbf{I}$, with $\mathbf{I}$ being the identity matrix and the matrix $\mathbf{R}$ being a diagonal matrix with elements:

$$d_m = (-1)^{m-1} \left[\sqrt{M} \psi_{M-1}(t_m) \right]^{-1}, \quad m = 1, 2, \ldots, M. \tag{15}$$

Orthogonal matrix $\mathbf{Q}$, taking into account (10) has the following form:

$$\mathbf{Q} = \frac{1}{\sqrt{M}} \begin{bmatrix} \frac{\psi_0(t_1)}{\psi_{M-1}(t_1)} & \frac{\psi_0(t_2)}{\psi_{M-1}(t_2)} & \cdots & \frac{\psi_0(t_M)}{\psi_{M-1}(t_M)} \\ \frac{\psi_1(t_1)}{\psi_{M-1}(t_1)} & \frac{\psi_1(t_2)}{\psi_{M-1}(t_2)} & \cdots & \frac{\psi_1(t_M)}{\psi_{M-1}(t_M)} \\ \vdots & \vdots & \ddots & \vdots \\ \frac{\psi_{M-1}(t_1)}{\psi_{M-1}(t_1)} & \frac{\psi_{M-1}(t_2)}{\psi_{M-1}(t_2)} & \cdots & \frac{\psi_{M-1}(t_M)}{\psi_{M-1}(t_M)} \end{bmatrix} \tag{16}$$

Due to the form of (14) and (15) where $d_m = 1$ does not hold for every $m = 1, 2, \ldots, M$, we may expect that the common AWGN will influence the DGHmT in a different manner, compared to standard orthogonal transforms, e.g. DFT.

In the case of DHmT, the transform matrix has the following form

$$\tilde{\mathbf{T}}_H = \begin{bmatrix} \tilde{\psi}_0(1) & \tilde{\psi}_0(2) & \cdots & \tilde{\psi}_0(M) \\ \tilde{\psi}_1(1) & \tilde{\psi}_1(2) & \cdots & \tilde{\psi}_1(M) \\ \vdots & \vdots & \ddots & \vdots \\ \tilde{\psi}_{M-1}(1) & \tilde{\psi}_{M-1}(2) & \cdots & \tilde{\psi}_{M-1}(M) \end{bmatrix}, \tag{17}$$

Let us denote with $\tilde{\mathbf{C}} = [\tilde{C}(0), \tilde{C}(1), \ldots, \tilde{C}(M-1)]^T$ the vector of DHmT coefficients and with $\mathbf{s} = [s(0), s(1), \ldots, s(M-1)]^T$ a vector of M signal samples obtained according to the sampling theorem. The DHmT can be written as

$$\tilde{\mathbf{C}} = \tilde{\mathbf{T}}_H \mathbf{s}. \tag{18}$$

As it is formed based on eigenvectors of symmetric matrix (9), matrix $\tilde{\mathbf{T}}_H$ is orthogonal, implying that $\tilde{\mathbf{T}}_H^{-1} = \tilde{\mathbf{T}}_H^T$ and $\tilde{\mathbf{T}}_H \tilde{\mathbf{T}}_H^T = \mathbf{I}$. The inverse DHmT has the following form

$$\mathbf{s} = \tilde{\mathbf{T}}_H^T \tilde{\mathbf{C}}. \tag{19}$$

4. Additive Gaussian noise influence

Observe the DGHmT of zero-mean AWGN vector η. Without loss of generality, it is inherently assumed that the signal and noise samples are available at the discrete points t_m, $m = 1, \ldots, M$ corresponding to the roots of the Mth order HP. The discrete DGHmT of noise reads:

$$\Xi = \mathbf{T}_H \eta = \mathbf{QR}\eta = \mathbf{Q} \begin{bmatrix} d_1\eta(t_1) & 0 & \cdots & 0 \\ 0 & d_2\eta(t_2) & \cdots & 0 \\ \vdots & \vdots & \ddots & 0 \\ 0 & 0 & \cdots & d_M\eta(t_M) \end{bmatrix}. \tag{20}$$

Thus, scaled noise samples $d_m\eta(t_m)$, $m = 1, 2, \ldots, M$ are expanded on the orthogonal vector space basis consisted of rows of matrix $\mathbf{Q}$. Note that in the case of DFT matrix, non-scaled noise samples $\eta(t_m)$ appear in $\mathbf{R}\eta$, which means that AWGN differently influences the HT compared to the DFT.

Next, we derive the statistical properties of HT coefficients corresponding to the signal $s(t_m)$ affected by AWGN $\eta(t_m)$:

$$x(t_m) = s(t_m) + \eta(t_m). \tag{21}$$

Since the HT is linear, (21) leads to $X(p) = S(p) + \Xi(p)$, with $S(p)$ and $\Xi(p)$ being the DGHmT of the signal $s(t_m)$ and noise $\eta(t_m)$, respectively. Since the noise $\eta(t_m)$ is a random Gaussian process, due to the central limit theorem and the definition (5), it can be concluded that $\Xi(p)$ and $X(p)$ are also Gaussian random variables. We further analyze statistical properties of the random variable $X(p)$. The mean value can be expressed as:

$$\mu_X(p) = E\{X(p)\} = S(p) + E\{\Xi(p)\}. \tag{22}$$

For a zero-mean additive noise $E\{\eta(n)\} = 0$ we have:

$$\mu_X(p) = S(p) + \frac{1}{M} \sum_{m=1}^{M} \frac{\psi_p(t_m)}{[\psi_{M-1}(t_m)]^2} E\{\eta(t_m)\} = S(p). \tag{23}$$
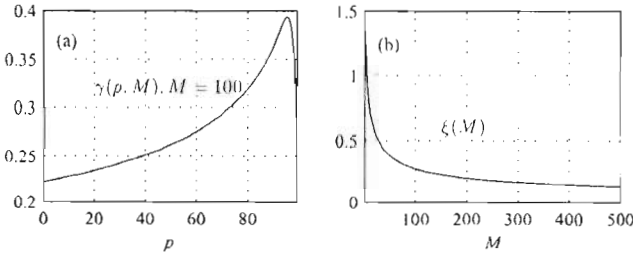
Fig. 2. Functions appearing in variance definitions: (a) $\gamma(p, M)$. (b) $\xi(M)$.

Let us now calculate the variance of the random variable $X(p)$ with the assumption that the $\eta(t_m)$ is a zero-mean noise:

$$\sigma_X^2(p) = E\left\{|X(p) - \mu_X(p)|^2\right\} = E\left\{|S(p) + \Xi(p)|^2\right\} - \mu_X^2(p)$$

$$= \frac{1}{M^2}\sum_{m_1=1}^{M}\sum_{m_2=1}^{M}\frac{\psi_p(t_{m_1})}{[\psi_{M-1}(t_{m_1})]^2}\frac{\psi_p(t_{m_2})}{[\psi_{M-1}(t_{m_2})]^2}E\{\eta(t_{m_1})\eta(t_{m_2})\}.$$

For a white noise with variance σ_η^2 the autocorrelation function is: $r_{\eta\eta}(t_{m_1}, t_{m_2}) = E\{\eta(t_{m_1})\eta(t_{m_2})\} = \sigma_\eta^2(t_{m_1} - t_{m_2})$. Hence, $\sigma_X^2(p)$ can be further written in the form:

$$\sigma_X^2(p) = \frac{\sigma_\eta^2}{M^2}\sum_{m=1}^{M}\frac{\psi_p^2(t_m)}{[\psi_{M-1}(t_m)]^4} = \gamma(p, M)\sigma_\eta^2. \tag{24}$$

This result indicates that the variance of the DGHmT coefficients depends on the coefficient index p. The mean value of the expression (24) can be now derived following the HFs orhonormality [11]:

$$\bar{\sigma}_X^2 = \frac{1}{M}\sum_{p=0}^{M-1}\sigma_X^2(p) = \frac{\sigma_\eta^2}{M^2}\sum_{m=1}^{M}\frac{1}{[\psi_{M-1}(t_m)]^2}\frac{1}{M}\sum_{p=0}^{M-1}\frac{\psi_p(t_m)\psi_p(t_m)}{[\psi_{M-1}(t_m)]^2}$$

$$= \frac{\sigma_\eta^2}{M^2}\sum_{m=1}^{M}[\psi_{M-1}(t_m)]^{-2} = \xi(M)\sigma_\eta^2. \tag{25}$$

The function $\gamma(p, M)$ for $M = 100$ is shown in Fig. 2(a) and the function $\xi(M)$ is shown in Fig. 1(b). The mean value of the function $\gamma(p, M)$ in Fig. 1(a) is 0.2753. It means that first 60 coefficients have the variance (scaled by $\gamma(p, M)$) below this mean value, while the remaining coefficients are scaled by larger values and are more sensitive to the noise. Also, the observed sparse signals are mainly concentrated on the first few DGHmT coefficients [1.8], indicating that a proper threshold can be used to distinguish between signal and noise components. Fig. 2(b) shows that the mean noise variance decreases as the number of M increases. Using these results, a polynomial fitting can be applied to approximate these functions and to define a general DGHmT-based denoising threshold.

In the case of DHmT, based on the matrix (17) orthogonality, and as the rows are normalized (being eigenvectors of matrix **T**), we conclude that the coefficient variance is

$$\bar{\sigma}_X^2(p) = \sigma_\eta^2,$$

assuming that noisy samples are available at the uniform discrete time grid in (21).

5. The Hermite transform based denoising

The presented discussion can be applied in signal denoising. The considered signal (21) is affected by a zero-mean AWGN of variance σ_η^2. Note that the noise-only DGHmT coefficient at the position p is a random variable described by the Gaussian distribution $\mathcal{N}(0, \sigma_X^2(p))$. The denoising is done using hard-thresholding

procedure [45]:

$$C_{den}(p) = \begin{cases} C(p), & |C(p)| > T(p) \\ 0, & |C(p)| \le T(p). \end{cases} \tag{26}$$

Observe that the threshold is dependent on p, due to the form of variance given by (24). Namely:

$$T(p) = l\sigma_X(p) = l\sqrt{\gamma(p, M)}\sigma_\eta, \tag{27}$$

where l is a constant ensuring that the noise-only coefficients are below the threshold level (27). For many real signals such as UWB signals or QRS complexes, the lower coefficients in the HT are the most significant ones [1,11]. The non-linear form of the threshold (27) increases the probability for the successful separation of noise-free signal and noise-only Hermite coefficients in the denoising process (Fig. 2(a)). For $l = 3$, according to the well-known 3-sigma rule, noise-only coefficients are below the threshold with probability of 99.73%. In the case of DHmT, standard threshold $T = l\sigma_\eta$ should be used.

As the presented denoising approach may serve as an alternative to the standard DFT-based denoising, the additional calculation burden is analyzed here. Based on the fast algorithms for the HT calculation [1,2], the discrete HT requires approximately $O(M\log_2^2 M)$ operations with real values, comparing with $O(M\log_2 M)$ operations with complex values in the case of DFT. The increase of the complexity by $\log_2 M$ times asymptotically is moderate even for a large M. For the threshold calculation in (27), additional $O(M)$ operations are needed.

6.1. Numerical examples and the discussion

Example 1. Consider the part of ECG signal known as QRS complex $qrs(t_m)$, sampled at the points proportional to the HP roots and sparsified according to the procedure in [1], with $M = 51$ samples. It is obtained from the MIT-BIH ECG database [43] (originally available as uniformly sampled in accordance with the sampling theorem) and corrupted with artificial zero-mean AWGN, such that SNR is 6 dB. The results for the QRS complex denoising based on DGHmT are shown in Fig. 3(a)–(d), illustrating a significant noise reduction. Parameter $l = 3$ was used in the example. Interestingly, the signal coefficient at $p = 3$, although smaller than the noisy coefficient at $p = 47$, is properly selected by the threshold (being above the threshold), due to the non-linear characteristic of the proposed threshold. Only a few signal coefficients much weaker than the noise remain under the threshold, at $p = 6$, $p = 7$ and $p = 8$. The MSE between the original noise-free and noisy signal of −28.71 dB is reduced to −35.83 dB after the denoising procedure is applied.

Now consider the shifted version of the considered noisy signal, $qrs_1(t_m) = qrs(t_m - c)$, where $c = 0.028$ s. In this case signal will not be optimally concentrated in the DGHmT domain, as illustrated in Fig. 4(a)–(d). Degradation of the denoising performance is illustrated in Fig. 4 (the MSE of the denoised signal is increased for about 2 dB). In this case, prior to the hard-thresholding procedure (26), optimally concentrated DGHmT can be found solving

$$\nu_{opt} = \min_\nu \|\mathbf{C}_\nu\|_1 = \sum_{p=0}^{M-1}\left|\frac{1}{M}\sum_{m=1}^{M}\frac{\psi_p(t_m)}{[\psi_{M-1}(t_m)]^2}s(t_m - \nu)\right|. \tag{28}$$

and shifting the analyzed signal for value $-\nu_{opt}$. Problem (28) can be solved by performing a one-dimensional search over possible values of ν. Upon finding ν_{opt}, the hard-thresholding (26) is applied on the DGHmT of signal shifted in opposite direction $-\nu_{opt}$. We calculated the concentration measure in (28) for values of ν in range [−0.04 s, 0.088 s] with step 0.004. Results are shown in Fig. 4(e). The global minimum of this function corresponds to shift value $c = 0.028$ s. DGHmT of the signal $qrs_1(t_m + \nu_{opt})$ leads to the
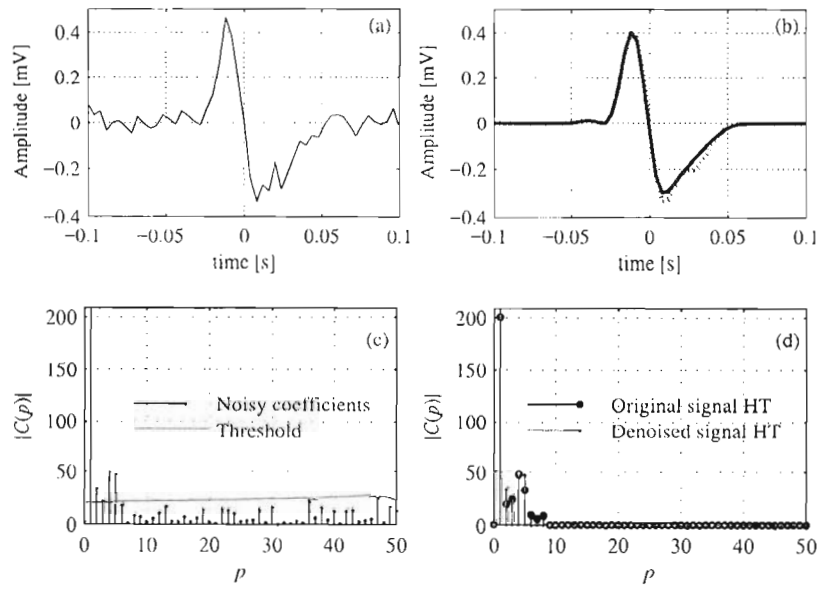
Fig. 3. Denoising a QRS complex using the hard-thresholding procedure: (a) QRS complex embedded in AWGN with SNR 6 dB, (b) Original QRS complex (solid) and denoised QRS complex (dots), (c) DGHmT of noisy QRS complex and the threshold (27) with $l = 3$, (d) DGHmT of original noise-free (circles) and denoised (dots) QRS complex.
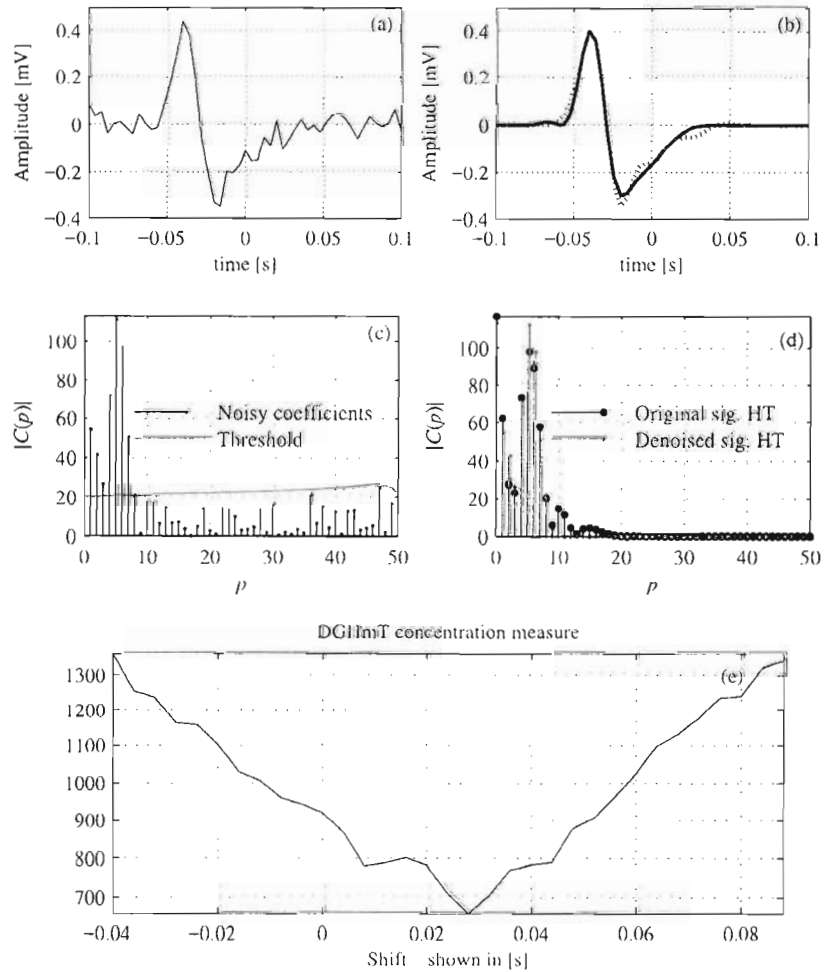

Fig. 4. Denoising a non-centered (shifted) QRS complex using the hard-thresholding procedure: (a) QRS complex embedded in AWGN with SNR – 6 dB, (b) Original QRS complex (solid) and denoised QRS complex (dots), (c) DGHmT of noisy QRS complex and the threshold (27) with $l = 3$, (d) DGHmT of original noise-free (circles) and denoised (dots) QRS complex, (e) concentration measure in (28) having a minimum at the optimal shift value 0.028 [s].
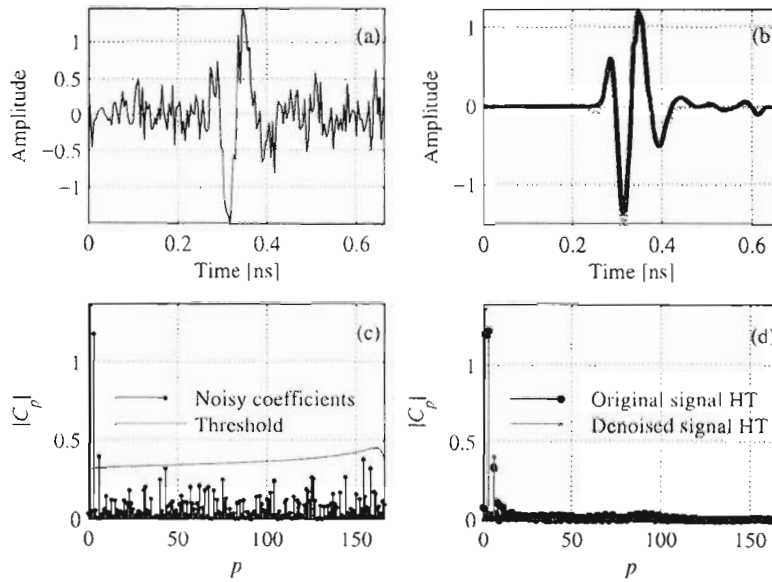
Fig. 5. Denoising a real UWB pulse using the hard-thresholding procedure based on HT: (a) UWB signal embedded in AWGN with SNR = 3 dB, (b) Original (solid) and denoised UWB signal (dots), (c) DGHmT of noisy UWB signal and the threshold (27), (d) DGHmT of original (circles) and denoised (dots) signal.
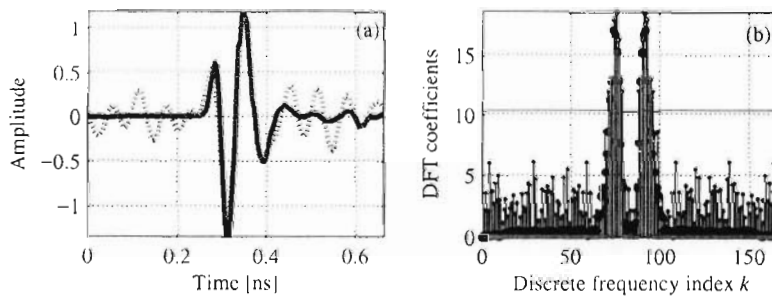

Fig. 6. Denoising a real UWB pulse using DFT-based hard-thresholding: (a) original and denoised signal (black and red, respectively), (b) DFT of noisy, denoised and original signal (blue, red and black, respectively). (For interpretation of the references to color in this figure legend, the reader is referred to the web version of this article.)

results presented in Fig. 3. Other signal examples suitable for the presented denoising procedure can be also found in [8].

Example 2. In this example, we observe a real 1.3 GHz UWB signal transmitted between two UWB antennas 1 m apart, through an indoor environment, in experiment described in [34]. First $M = 165$ samples of the signal 'ACW7FD45.dat' from the database [44] are observed. The artificial AWGN is added to this signal, such that SNR = 3 dB. The noisy UWB signal is shown in Fig. 5(a), while the corresponding DGHmT with the threshold (27) and $l = 4$ is shown in Fig. 5(c). The original signal and the denoised signal are shown in Fig. 5(b), while the corresponding HTs are shown in Fig. 5(d). It can be seen that the noise is significantly reduced. It is assumed that the noise variance σ_η^2 is known since it can be estimated as described in [45].

The non-linear threshold is able to select signal coefficients at $p = 6$ although having approximately the same value as the noise-only coefficient at $p = 154$ (that remains under the threshold). Only the smallest coefficients will remain below the threshold, but these are much weaker than the noise and do not contribute significantly to the resulting signal.

For the comparison, the signal denoising using a DFT-based hard thresholding approach is considered (with threshold $T_{DFT} = lN\sigma_\eta^2$, and the same value $l = 4$). The results are presented in Fig. 6, showing a significantly degraded denoising performance. The resulting MSE between the original (non-noisy) and denoised signal, for the case of DGHmT-based procedure is

−24.23 dB, whereas for the DFT-based procedure the achieved MSE is −16.07 dB. The MSE reduction in the first case is approximately 11.8 dB, and only 3.63 dB in the DFT case.

Example 3. Additionally, previous experiment was conducted for a range of SNR values: from −10 to 15 dB, varied with step 1. For each SNR value, the MSE between the denoised and original signal was calculated based on 500 independent realizations of artificial AWGN added to the signal. The results for the DGHmT and DFT hard threshold based denoising of the UWB signal from Example 2 are shown in Fig. 7(a). The results confirm a significant MSE improvement when using DGHmT and the proposed non-linear threshold.

Moreover, the experiment is repeated also with the Discrete wavelet transform (DWT) serving as a basis for signal denoising. We consider denoising based on Symlet 8 (sym8) and Daubechies 8 (db8) wavelets. In both cases decomposition of level 5 is considered. These particular wavelet types are chosen due to their visual similarity with the considered signal. Denoising is performed using two different threshold selection rules to the wavelet coefficients: Stein's Unbiased Risk Estimate (SURE) for db8 wavelet case, and Donoho and Johnstone's universal threshold with level-dependent estimation of the noise for sym8 wavelet [52–55]. In each case, the hard thresholding is applied. For this experiment we use MATLAB wden implementation from the Wavelet Toolbox. The threshold rescaling is done using a single estimation of level noise based on the first-level coefficients. As seen in Fig. 7(a),
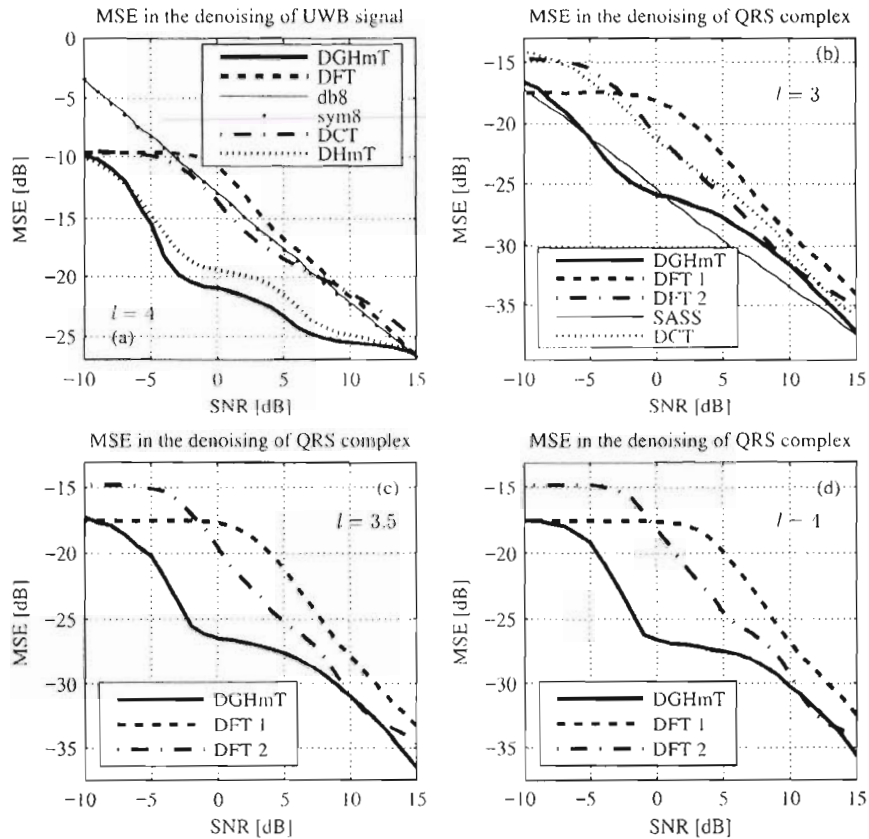
Fig. 7. The MSE between original (noise-free) and the signals denoised using various approaches, shown for various SNRs: (a) UWB signal case; (b)–(d) QRS complex denoising using various parameter *l* values.

two considered methods performed similarly. This experiment confirms that DGHmT's ability to represent signal sparsely can be crucial in the denoising, even exploited in very simple methods such as the hard-thresholding. We additionally test the performance of the Discrete cosine transform (DCT) based hard-thresholding. The threshold level is set to $T_{DCT} = l\sigma_n^2$, and the same value $l = 4$ is used as in the case of the DGHmT. The DGHmT-based method outperformed the DCT-based hard-thresholding (Fig. 7(a)).

Finally, we include the DHmT-based denoising based on hard-thresholding in our comparative analysis, with $T(p) = l\sigma_n$. The same value $l = 4$ is used as for the DGHmT. In both versions of the discrete Hermite transform, dilation (scaling) factor $\sigma = 1$ was used. As shown in Fig. 7(a), DGHmT slightly outperforms DHmT. Interestingly, visual similarity of MSE curves in accordance with the visual similarity of two sets of basis functions.

We hypothesize that the performance of DHmT can be improved by setting a proper dilation parameter (time axis scaling factor). Namely, let us denote with $\tilde{\mathbf{T}}_H(\sigma)$ the DHmT matrix, with basis functions $\tilde{\psi}_p(n, \sigma)$, $n, p = 0, ..., M - 1$. This matrix retains orthogonality [5]. The improved DHmT concentration can be obtained by solving

$$\sigma_{opt} = \min_\sigma \left\| \tilde{\mathbf{T}}_H(\sigma)\mathbf{s} \right\|_1 = \min_\sigma \sum_{p=0}^{M-1} \left| \sum_{n=0}^{M-1} s(n)\tilde{\psi}_p(n, \sigma) \right|, \qquad (29)$$

being a standard ℓ_1-norm minimization from the compressive sensing and sparse signal processing framework. Solution of (29) corresponds to the dilation parameter producing the best possible concentration of DHmT coefficients. It can be found by a direct search in the given range of possible σ values. The same procedure can be performed for DGHmT [8]. However, the fur-

ther development of this concept and a comprehensive comparative analysis of the performance in the case of these transforms with optimized parameters is outside the scope of this paper, and it is a topic of our further research. Note that in all presented experiments, for each considered SNR value, the MSE was calculated based on 500 independent realizations of the artificial AWGN added to the signal.

An experiment with a range of SNR values is also performed for the QRS complex from Example 1. Results are presented for various values of parameter l: $l = 3$ (Fig. 7(b)), $l = 3.5$ (Fig. 7(c)) and $l = 4$ (Fig. 7(d)). For a fair comparison, DFT based hard-thresholding was performed for both the original uniformly sampled signal case available in [43] (in Fig. 7(b)–(d) denoted as DFT 2) as well as for the non-uniform sampling case (in Fig. 7(b)–(d) denoted as DFT 1). In both cases, the same noise was added to signal samples. Results indicate that the DGHmT based denoising produces dominantly lower MSE values in all cases.

For $l = 3$ we compare the denoising performance with the DCT-based hard-thresholding method, where the threshold is set according to the DCT noisy coefficients variance, $T_{DCT} = l\sigma_{ij}^2$. The results shown in Fig. 7(b) indicate the lower MSE obtained using the DGHmT-based method. We also compare the results with an advanced state-of-the-art ECG denoising algorithm, Sparsity-Assisted Signal Smoothing (SASS) [46]. We use the implementation available online, with the original parameter set [47]. The results are presented in Fig. 7(b). The presented MSE curve for the SASS method is obtained in the following manner. As this algorithm is originally set to work with entire ECG signals, instead of proceeding as an input only the selected QRS complex, the original full length ECG signal from the MIT-BIH ECG database [43] (part of which is the observed QRS complex) was corrupted with AWGN with same vari-
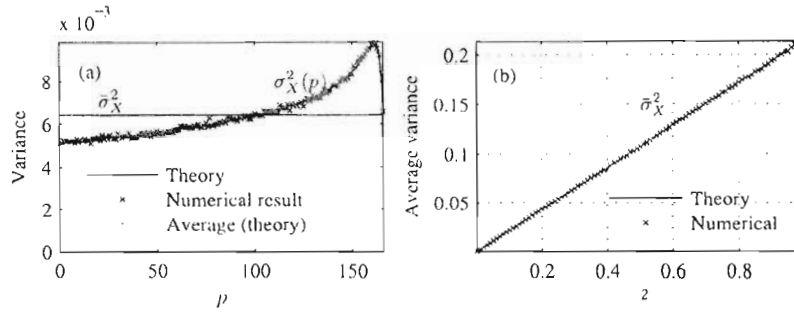
Fig. 8. HT coefficients variance for signal embedded in AWGN: (a) Variance of coefficients at position p, SNR = 5 dB, (b) Average variance in terms of the input noise variance.

ances as the QRS complex used for other methods evaluation. The denoising of this whole ECG signal was performed using SASS algorithm, with the default set of parameters. Then the QRS complex of interest was extracted from the denoised signal, and compared with the original QRS complex. As for other methods, the experiment was repeated 500 times for each SNR value, and averaged MSE is shown in Fig. 7(b). In this way, we were able to use the algorithm without any parameter changes. Results shown in Fig. 7(b) indicate that this method moderately outperforms the DGHmT-based denoising, in the SNR range from 0 dB to 10 dB. However, the cost of this improvement is a significantly higher numerical complexity of the SASS algorithm. Nevertheless, the simple hard-thresholding procedure results are comparable with the results of this advanced denoising technique (in the context of QRS complex denoising).

6.2. Statistical validation of the variance

In order to statistically confirm the derived variance (24) and its average value (25), we perform two experiments using noisy UWB signal from Example 2. In the first test, the SNR level of 5 dB is observed (the noise variance $\sigma_\eta^2 = 0.030$). The variance of DGHmT coefficients is numerically evaluated based on 10,000 independent realizations of the noise. High match with the theoretical expression (24) is achieved and shown in Fig. 8(a). The average variance (25) is also shown by dots. In the second experiment, the input noise variance σ_η^2 is varied from 10^{-6} to 1, with the step 10^{-2}, and the average variance of DGHmT coefficients is calculated. Observe that the results show high matching ratio with the variance (25), Fig 8(b).

6. Application in sparse signal reconstruction

In this Section, we present an overview of the presented theory applicability in the reconstruction of signals from a random subset of available samples (measurements, observations). To this end, observe a signal exhibiting sparsity in the DGHmT domain. Such signal can be represented with a small number K of non-zero Hermite coefficients, with positions belonging to the set $\mathbf{P} = \{p_1, p_2, \ldots, p_K\}$. It has the following form:

$$s(t_n) = \sum_{l=1}^{K} \alpha_l \psi_{p_l}(t_n). \tag{30}$$

Sparse signals can be reconstructed from a reduced set of observations [38,39,48,49]. Assume that only M_A out of M randomly positioned samples are available. The available samples have random positions denoted by

$$\hat{t}_m \in \mathbf{M}_A = \{\hat{t}_1, \hat{t}_2, \ldots, \hat{t}_{M_A}\} \subseteq \mathbf{M} = \{t_1, t_2, \ldots, t_M\}.$$

Set $\mathbf{M}$ contains the sampling points of the full-length signal, and these points correspond to the roots of the M-th order Hermite polynomial. $\mathbf{M}_A$ is the random subset of $\mathbf{M}$ containing the

sampling positions of available measurements. The common mathematical model for the compressive sensing procedure based on the randomly selected/acquired signal values involves the random measurement matrix $\boldsymbol{\Phi}$:

$$\mathbf{s}_{cs} = \boldsymbol{\Phi} \mathbf{T}_H^{-1} \mathbf{C} = \mathbf{AC}, \tag{31}$$

with $\mathbf{s}_{cs}$ denoting the vector of available samples of the analyzed signal, and $\mathbf{C} = \mathbf{T}_H \mathbf{s}$ is the DGHmT coefficients vector of signal (30) containing all samples. The matrix $\mathbf{A}$ is obtained from the inverse DGHmT matrix $\mathbf{T}_H^{-1}$, by omitting the rows corresponding to the positions of missing samples. Set of M_A linear Eq. (31) with M unknowns can be solved if the additional sparsity condition is assumed for the solution. Therefore, sparse signal reconstruction problem is formulated as

$$\min \|\mathbf{C}\|_0 \text{ subject to } \mathbf{s}_{cs} = \mathbf{AC}, \tag{32}$$

where the so called ℓ_0-norm corresponds to the number of non-zero coefficients in $\mathbf{C}$. It is known that the ℓ_0-norm cannot be used in the direct minimization and thus the problem (32) is usually reformulated using ℓ_1-norm, exploited in the application of efficient linear programming and iterative approaches. Indirectly, problem (32) can be solved by properly estimating the positions of non-zero DGHmT coefficients in the solution. If the signal support is known or appropriately estimated within a set $\hat{\mathbf{P}}$ containing $K \leq \hat{P} \leq M$ elements such that $\mathbf{P} \subseteq \hat{\mathbf{P}}$, the reconstruction is done using the pseudo-inversion [39]:

$$\mathbf{C}_K = \left(\mathbf{A}_{\hat{\mathbf{P}}}^T \mathbf{A}_{\hat{\mathbf{P}}}\right)^{-1} \mathbf{A}_{\hat{\mathbf{P}}}^T \mathbf{s}_{cs}. \tag{33}$$

often used in standard matching pursuit approaches, for example, in the OMP algorithm. The matrix $\mathbf{A}_{\hat{\mathbf{P}}}$ is the sub-matrix of matrix $\mathbf{A}$, with omitted columns corresponding to positions $p \notin \hat{\mathbf{P}}$.

If samples are omitted from the signal, it produces the same result as if these samples assume zero values [38,39,51]. Consequently, a reduced number of signal samples can be considered as a complete set of samples, where some of them are affected by an additive noise. When missing samples assume zero values, the initial discrete DGHmT of such signal is

$$C_0(p) = \sum_{i=1}^{M_A} \sum_{l=1}^{K} \frac{\alpha_l}{M} \frac{\psi_p(\hat{t}_i) \psi_{p_l}(\hat{t}_i)}{(\psi_{M-1}(\hat{t}_i))^2}, \quad p = 0, \ldots, M-1.$$

Hermite coefficients $C_0(p)$ are random variables. Two categories of these coefficients can be identified. Coefficients corresponding to signal components, that is, $p = p_l$, $l = 1, \ldots, K$ are random variables with Gaussian distribution and mean values $\alpha_l \frac{M_A}{M}$ [38,50] and variance $\sigma_s^2(p_l) : \mathcal{N}(\alpha_l \frac{M_A}{M}, \sigma_s^2(p_l))$, $l = 1, \ldots, K$. Coefficients that are not placed at positions corresponding to signal components, that is, $p \neq p_l$, are zero-mean random variables with variance [38,50,51]

$$\sigma_{cs}^2 = \frac{M_A M - M_A^2}{M^2(M-1)} \sum_{l=1}^{K} \alpha_l^2 \tag{34}$$

not depending on coefficient position as long as $p \neq p_l$ holds, that is, $\mathcal{N}(0, \sigma_{cs}^2)$.

The probability that $M - K$, $M \gg K$ independent noise alone coefficients are smaller than a value κ is

$$P_S(\kappa) = \text{erf}\left(\frac{\kappa}{\sqrt{2}\sigma_{cs}}\right)^{M-K}. \tag{35}$$

where the CDF of the Half-normal distribution being $g(\kappa, \sigma_N) = \text{erf}(\frac{\kappa}{\sqrt{2}\sigma_{cs}})$ is used. If we set this probability to a fixed value, for example $P_S(\kappa) = 0.99$, then, the threshold

$$\kappa = \sqrt{2}\sigma_{cs}\text{erf}^{-1}\left((P_S(\kappa))^{\frac{1}{M-K}}\right) \approx \sqrt{2}\sigma_{cs}\text{erf}^{-1}\left((P_S(\kappa))^{\frac{1}{M}}\right) \tag{36}$$

will, with given probability, separate noise-only coefficients from signal coefficients. If amplitudes α_l have close values, and a sufficiently large number of measurements M exists, then this threshold will help to detect positions of all coefficients corresponding to signal components, that is, $\hat{\mathbf{P}} = \arg\{|C_0(p)| > \kappa\}$. In that case, the reconstruction is simply achieved in one iteration, directly exploiting the pseudo-inversion (33).

Now assume that the available measurements are affected by a white Gaussian noise with variance σ_{η}^2. Both the external additive noise and the noise caused by missing samples are now sources of disturbances in the considered discrete Hermite domain. These disturbances are uncorrelated and Gaussian, and therefore the noise-only coefficients have the following variance

$$\sigma_T^2(p) = \sigma_{cs}^2 + \sigma_X^2(p) = \frac{M_A M - M_A^2}{M^2(M-1)}\sum_{l=1}^{K}\alpha_l^2 + \gamma(p,M)\sigma_{\eta}^2 \tag{37}$$

with constant σ_{cs}^2, whereas $\sigma_X^2(p)$ is dependent on coefficients positions. Therefore, we introduce non-linear position-dependent threshold for the detection of Hermite coefficients corresponding to signal components:

$$\kappa(p) = \sqrt{2}\sigma_T(p)\text{erf}^{-1}\left((P_S(\kappa))^{\frac{1}{M}}\right). \tag{38}$$

Threshold (38) is incorporated in the efficient reconstruction algorithm presented in [39]. If amplitudes α_l do not have close values, then the variant of CoSaMP (OMP) based reconstruction can be easily developed based on the presented theory [39]. In this algorithm, based on initial coefficient vector $\mathbf{C}_0$, the first set of component positions is estimated as

$$\hat{\mathbf{P}} = \arg\{|C_0(p)| > \kappa(p)\}. \tag{39}$$

In the next step, partial sensing matrix $\mathbf{A}_1 = \mathbf{A}_{\hat{\mathbf{P}}}$ is formed from the sensing matrix $\mathbf{A}$, using only columns with indices $\hat{\mathbf{P}}$. First components are obtained by solving the system of measurement equations, using the well-known pseudo-inversion: $\mathbf{C}_K = (\mathbf{A}_1^T\mathbf{A}_1)^{-1}\mathbf{A}_1^T\mathbf{s}_{cs}$. Subsequently, the signal $\mathbf{s}_1 = \mathbf{A}_1\mathbf{C}_K$ is calculated. In case that $\mathbf{e}$ $\mathbf{s}_1$ holds, vector $\mathbf{C}_K$ is the problem solution and algorithm terminates (single iteration variant). If this is not the case, then the estimated component is removed from $\mathbf{s}_{cs}$ and the signal $\mathbf{e} = \mathbf{s}_{cs} - \mathbf{s}_1$ is formed.

Subsequently, the procedure is repeated for signal $\mathbf{e}$, where the set $\hat{\mathbf{P}}$ is expanded with new detected positions. The process iteratively continues until the solution is found, or until a required precision ε is acquired. A reasonable choice of parameter ε is the mean variance of noisy DGHmT coefficients (25), being the new stopping criterion for the reconstruction of signals in the presence of AWGN. Detailed description and analysis of presented reconstruction concepts and algorithms (single-iteration and iterative forms) can be found in [39].

Example 4. Consider signal of the form (30), sparse in the DGHmT domain, with amplitudes $\alpha_1 = 2, \alpha_2 = -3, \alpha_3 = 2.7, \alpha_4 = 2.1, \alpha_5 = 2.1, \alpha_6 = 1.4$, and corresponding non-zero coefficients positions
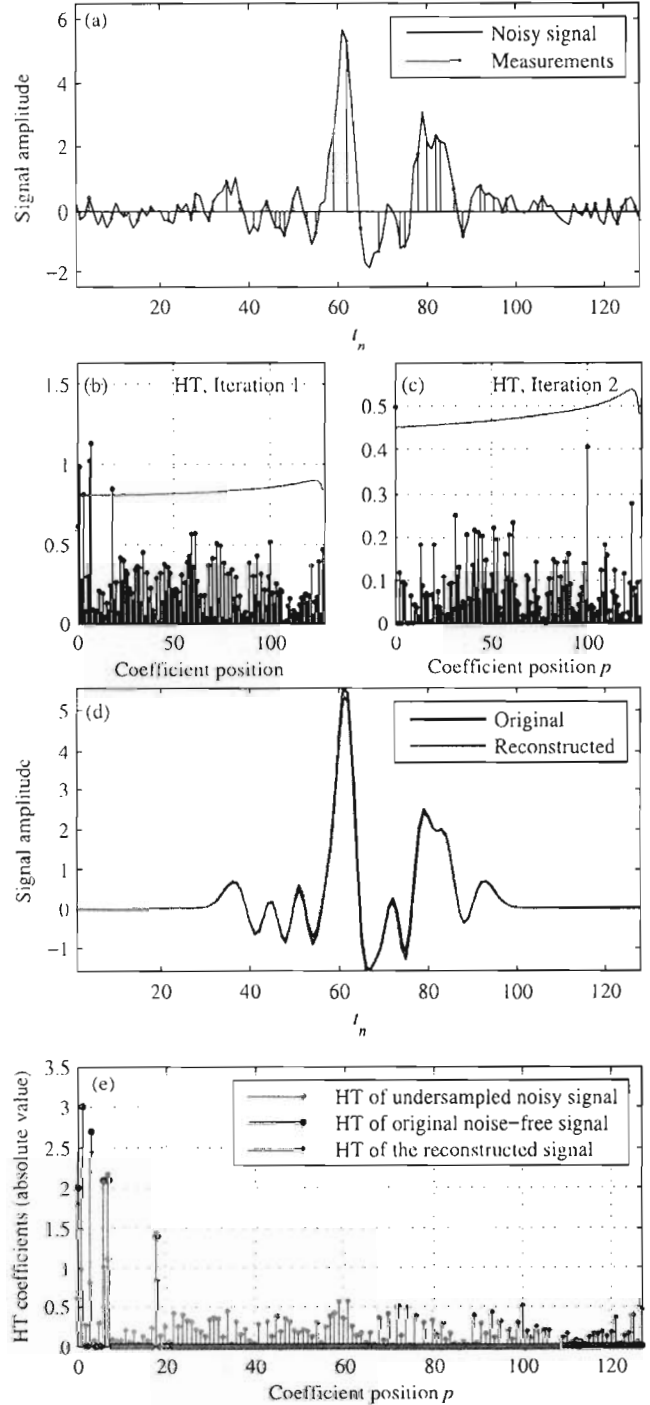

Fig. 9. Reconstruction of noisy signal sparse in the DGHmT domain with $M_A = 54$ out of $M = 128$ available samples: (a) noisy signal (black) and available measurements (red); (b) HT of available measurements (initial transform) and the first threshold (red); (c) HT calculated after removal of detected components, and the new threshold (red); (d) Original noise-free signal (blue) and the reconstructed signal (red); (e) HT of the undersampled noisy signal, original noise-free signal and the reconstructed signal. (For interpretation of the references to color in this figure legend, the reader is referred to the web version of this article.)

$p_1 = 0, p_2 = 1, p_3 = 3, p_4 = 6, p_5 = 7$, and $p_6 = 18$. It is affected by an additive white Gaussian noise; such that SNR is 7 dB. Then only $M_A = 54$ out of $M = 128$ noisy samples (42.19%) are taken at random positions. The reconstruction is performed in only two iterations of the algorithm [39] with the modified threshold (38). Results are shown in Fig. 9. The initial MSE between the original (noise-free) and noisy signal of −11.67 dB dropped for ~12 dB after the CS reconstruction. The resulting MSE between the original (noise-free) and the reconstructed signal is −23.66 dB.

7. Conclusion

The discrete Hermite transform of signals affected by zero-mean AWGN is analyzed. The particular scope was on the discrete Hermite transform calculated based on the Gauss-Hermite quadrature. The mean values and variances of corresponding noisy Hermite coefficients are derived and statistically verified. Based on the modeled noise influence, a nonlinear threshold for the separation of signal and noise-alone components in the discrete Hermite transform domain is derived. Consequently, a method for signal denoising is proposed. It is based on a hard thresholding approach. The signal denoising is tested using real UWB signal and QRS complex, showing the benefits of using the derived nonlinear threshold. Moreover, the results are easily incorporated into the sparse signal reconstruction framework.

Acknowledgment

Supplementary materials

Supplementary material associated with this article can be found, in the online version, at doi:10.1016/j.sigpro.2018.04.007.

References

[1] A. Sandryhaila, S. Saba, M. Puschel, J. Kovacevic, Efficient compression of QRS complexes using Hermite expansion, IEEE Trans. Signal Process. 60 (2) (2012) 947–955, doi:10.1109/TSP.2011.2173336.

[2] G. Leibon, D.N. Rockmore, W. Park, R. Taintor, G.S. Chirikjian, A fast Hermite transform, Theor. Comput. Sci. 409 (2) (2008) 211–228, doi:10.1016/j.tcs.2008.09.010.

[3] A. Krylov, D. Kortchagine, Fast Hermite projection method, in: Int. Conf. on Image Analysis and Recognition, Portugal, 2006, pp. 329–338.

[4] I. Orović, S. Stanković, T. Chau, C.M. Steele, E. Sejdić, Time-frequency analysis and Hermite projection method applied to swallowing accelerometry signals, EURASIP J. Adv. Signal Process. 2010 (2010) 323125 7 pages.

[5] A. Mahadevan, S. Acharya, D.B. Sheffer, D.H. Mugler, Ballistocardiogram artifact removal in EEG-fMRI signals using discrete Hermite transforms, IEEE J. Sel. Top. Signal Process. 2 (December (6)) (2008) 839–853, doi:10.1109/JSTSP.2008.2008367.

[6] D.H. Mugler, S. Clary, Yan Wu, Discrete Hermite expansion of digital signals: applications to ECG signals, in: Proceedings of 2002 IEEE 10th Digital Signal Processing Workshop, 2002 and the 2nd Signal Processing Education Workshop, 2002, pp. 262–267.

[7] X. Ning, I.W. Selesnick, ECG enhancement and QRS detection based on sparse derivatives, Biom. Sig. Proc. Control 8 (6) (2013) 713–723, doi:10.1016/j.bspc.2013.06.005.

[8] M. Brajović, I. Orović, M. Daković, S. Stanković, On the parameterization of Hermite transform with application to the compression of QRS complexes, Signal Process. 131 (February) (2017) 113–119.

[9] A.I. Rasiah, R. Togneri, Y. Attikiouzel, Modelling 1-D signals using Hermite basis functions, Vis. Image Signal Process. IEEE Proc. 144 (6) (1997) 345–354, doi:10.1049/ip-vis:19971613.

[10] S. Stanković, I. Orović, A. Krylov, The two-dimensional Hermite S-method for high resolution inverse synthetic aperture radar imaging applications, IET Signal Process. 4 (4) (2010) 352–362, doi:10.1049/iet-spr.2009.0060.

[11] M. Brajović, I. Orović, M. Daković, S. Stanković, Gradient-based signal reconstruction algorithm in the Hermite transform domain, Electron. Lett. 52 (1) (2016) 41–43, doi:10.1049/el.2015.1700.

[12] S. Stanković, I. Orović, LJ. Stanković, Compressive Sensing approach in Hermite transform domain, Math. Prob. Eng. 2015 (2015) 286590 9 pages.

[13] J.R. de Oliveira Neto, J.B. Lima, Discrete fractional Fourier transforms based on closed-form Hermite-Gaussian-like DFT eigenvectors, IEEE Trans. Signal Process. 65 (December (23)) (2017) 6171–6184, doi:10.1109/TSP.2017.2750105.

[14] C. Candan, M.A. Kutay, H.M. Ozaktas, The discrete fractional Fourier transform, IEEE Trans. Signal Process. 48 (May (5)) (2000) 1329–1337.

[15] S.C. Pei, W.L. Hsue, J.J. Ding, Discrete fractional Fourier transform based on new nearly tridiagonal commuting matrices, IEEE Trans. Signal Process. 54 (October (10)) (2006) 3815–3828.

[16] B. Santhanam, T.S. Santhanam, Discrete Gauss-Hermite functions and eigenvectors of the centered discrete fourier transform, in: 2007 IEEE International Conference on Acoustics, Speech and Signal Processing - ICASSP '07, Honolulu, HI, 2007, pp. 1385–1388.

[17] M.T. Hanna, N.P.A. Seif, W.A.E.M. Ahmed, Discrete fractional Fourier transform based on the eigenvectors of tridiagonal and nearly tridiagonal matrices, Digit. Signal Process. 18 (September (5)) (2008) 709–727.

[18] S.C. Pei, J.J. Ding, W.L. Hsue, K.W. Chang, Generalized commuting matrices and their eigenvectors for dfts, offset dfts, and other periodic operations, IEEE Trans. Signal Process. 56 (August (8)) (2008) 3891–3904.

[19] A. Serbes, L. Durak-Ata, Efficient computation of DFT commuting matrices by a closed-form infinite order approximation to the second differentiation matrix, Signal Process. 91 (3) (2011) 582–589.

[20] D.Y. Wei, Q.W. Ran, Y.M. Li, J. Ma, L.Y. Tan, Fractionalisation of an odd time odd frequency DFT matrix based on the eigenvectors of a novel nearly tridiagonal commuting matrix, IET Signal Proc. 5 (April (2)) (2011) 150–156.

[21] D. Wei, Y. Li, Novel tridiagonal commuting matrices for Types I, IV, V, VIII DCT and DST Matrices, IEEE Signal Process Lett. 21 (April (4)) (2014) 483–487.

[22] I. Bhatta, B. Santhanam, A comparative study of commuting matrix approaches for the discrete fractional fourier transform, in: 2015 IEEE Signal Processing and Signal Processing Education Workshop (SP/SPE), Salt Lake City, UT, 2015, pp. 1–6.

[23] Ç. Candan, On higher order approximations for Hermite–Gaussian Functions and discrete fractional Fourier transforms, IEEE Signal Process Lett. 14 (October (10)) (2007) 699–702.

[24] M.T. Hanna, N.P.A. Seif, W.A.E.M. Ahmed, Hermite-Gaussian-like eigenvectors of the discrete Fourier transform matrix based on the singular-value decomposition of its orthogonal projection matrices, IEEE Trans. Circuits Syst. Regul. Pap. 51 (November (11)) (2004) 2245–2254.

[25] M.T. Hanna, N.P.A. Seif, W.A.E.M. Ahmed, Hermite-Gaussian-like eigenvectors of the discrete Fourier transform matrix based on the direct utilization of the orthogonal projection matrices on its eigenspaces, IEEE Trans. Signal Processing 54 (July (7)) (2006) 2815–2819.

[26] M.T. Hanna, Direct batch evaluation of optimal orthonormal eigenvectors of the DFT Matrix, IEEE Trans. Signal Process. 56 (May (5)) (2008) 2138–2143.

[27] M.T. Hanna, Direct sequential evaluation of optimal orthonormal eigenvectors of the discrete Fourier transform matrix by constrained optimization, Digit. Signal Process. 22 (4) (2012) 681–689.

[28] A. Serbes, L. Durak-Ata, The discrete fractional Fourier transform based on the DFT matrix, Signal Process. 91 (March (3)) (2011) 571–581.

[29] S.-C. Pei, M.-H. Yeh, C.-C. Tseng, Discrete fractional Fourier transform based on orthogonal projections, IEEE Trans. Signal Process. 47 (May (5)) (1999) 1335–1348.

[30] A. Kuznetsov, Explicit Hermite-type eigenvectors of the discrete Fourier transform, SIAM J. Matrix Anal. Appl. 36 (4) (2015) 1443–1464.

[31] S.C. Pei, Y.C. Lai, Signal scaling by centered discrete dilated Hermite functions, IEEE Trans. Signal Process. 60 (January (1)) (2012) 498–503, doi:10.1109/TSP.2011.2171687.

[32] S. Clary, D.H. Mugler, Shifted Fourier matrices and their tridiagonal commutors, SIAM J. Matrix Anal. Appl. 24 (3) (2003) 809–821.

[33] M. Ghavami, L.B. Michael, R. Kohno, Ultra Wideband Signals and Systems in Communication Engineering, 2nd Ed., Wiley, 2007.

[34] R.J.M. Cramer, R.A. Scholtz, M.Z. Win, Evaluation of an Ultra-Wide Band Propagation Channel, IEEE Trans. Antennas Propag. (May) (2002), doi:10.1109/TAP.2002.1011221.

[35] S. Gezici, H. Kobayashi, H.V. Poor, A.F. Molisch, Performance evaluation of impulse radio UWB systems with pulse-based polarity randomization, IEEE Trans. Signal Process. 53 (July (7)) (2005) 2537–2549.

[36] F. Ramirez-Mireles, On the performance of ultra-wide-band signals in Gaussian noise and dense multipath, IEEE Trans. Veh. Technol. 50 (January (1)) (2001) 244–249.

[37] Y. Kopsinis, S. McLaughlin, Development of EMD-based denoising methods inspired by wavelet thresholding, IEEE Trans. Signal Process. 57 (April (4)) (2009) 1351–1362, doi:10.1109/TSP.2009.2013885.

[38] LJ. Stanković, S. Stanković, M. Amin, Missing samples analysis in signals for applications to L-estimation and compressive sensing, Signal Process. 94 (2014) 401–408.

[39] S. Stanković, I. Orović, LJ. Stanković, An Automated signal reconstruction method based on analysis of compressive sensed signals in noisy environment, Signal Process. 104 (2014) 43–50.

[40] Z. Xu, B. Huang, K. Li, On Fourier interpolation error for band-limited signals, IEEE Trans. Signal Process. 57 (6) (2009) 2412–2416, doi:10.1109/TSP.2009.2016263.

[41] A. Papoulis, Signal Analysis, McGraw-Hill, New York, 1977.

[42] JP. Berrut, A formula for the error of finite sinc-interpolation over a finite interval, Numer. Algorithms 45 (1–4) (Aug. 2007) 369–374.

[43] PhysioNet: MIT-BIH ECG compression test database, http://www.physionet.org/physiobank/database/cdb, accessed May 2017.

[44] UltRa Lab UWB data: http://ultra.usc.edu/uwb_database/tdcindoor.htm, accessed May 2017.

[45] Y. Kopsinis, S. McLaughlin, Development of EMD-based denoising methods inspired by wavelet thresholding, IEEE Trans. Signal Process. 57 (4) (2009) 1351–1362.

[46] I. Selesnick, Sparsity-assisted signal smoothing (revisited), in: 2017 IEEE International Conference on Acoustics, Speech and Signal Processing (ICASSP), New Orleans, LA, 2017, pp. 4546–4550.

[47] I.W. Selesnick, Sparsity-assisted signal smoothing (SASS) [available online], 2017. accessed January accessed January http://eeweb.poly.edu/iselesni/sass/.

[48] E. Candes, J. Romberg, T. Tao, Robust uncertainty principles: exact signal reconstruction from highly incomplete frequency information, IEEE Trans. Inf. Theory 52 (2) (2006) 489–509.

[49] E. Sejdić, A. Can, L.F. Chaparro, C.M. Steele, T. Chau, Compressive sampling of swallowing accelerometry signals using time-frequency dictionaries based on modulated discrete prolate spheroidal sequences, EURASIP J. Adv. Signal Process. 2012 (2012) 101.

[50] M. Brajović, I. Orović, M. Daković, S. Stanković, The analysis of missing samples in signals sparse in the Hermite transform domain, 23rd Telecommunications Forum TELFOR, 2015.

[51] M. Brajović, I. Orović, M. Daković, S. Stanković, Compressive sensing of sparse signals in the Hermite transform basis: analysis and algorithm for signal reconstruction, IEEE Trans. Aerosp. Electron. Syst. 54 (2) (2018) 950–967.

[52] A. Antoniadis, G. Oppenheim, Wavelets and Statistics, Lecture Notes in Statistics, 103, Springer Verlag, 1995.

[53] D.L. Donoho, Progress in Wavelet Analysis and WVD: A Ten Minute Tour, in: Y. Meyer, S. Roques (Eds.), Progress in Wavelet Analysis and Applications., Frontières Ed, 1993, pp. 109–128.

[54] D.L. Donoho, I.M. Johnstone, Ideal spatial adaptation by wavelet shrinkage, Biometrika 81 (1994) 425–455.

[55] D.L. Donoho, De-noising by soft-thresholding, IEEE Trans. Inf. Theory 42 (3) (1995) 613–627.

SIGNAL
PROCESSING

On the parameterization of Hermite transform with application to the compression of QRS complexes

CrossMark

Miloš Brajović*, Irena Orović, Miloš Daković, Srdjan Stanković

University of Montenegro/Electrical Engineering Department, 20000, Podgorica, Montenegro

ARTICLE INFO

ABSTRACT

The concentration and sparsity of signal representation in the Hermite transform (HT) basis may highly depend on a properly chosen scaling factor and discrete time shift parameter. In that sense, we propose a simple and efficient iterative procedure for automatic determination of the optimal scaling factor. The optimization criterion is based on the ℓ_1-norm acting as a measure of signal concentration in the HT domain. Instead of centering the signal at the zero time instant, we also propose to shift the center for a few points left or right, which will additionally improve the concentration. An important application of the proposed optimization approach is the compression of QRS complexes, where properly chosen scaling factor and time-shift increase the compression performance. The results are verified using synthetic and real examples and compared with the existing approach for the compression of QRS complexes.

© 2016 Elsevier B.V. All rights reserved.

1. Introduction

The Hermite transform (HT) has been studied during the last few decades, particularly as an alternative to the Fourier transform [1–16]. Although covering a wide range of possible applications due to many interesting properties, Hermite transform has been extensively used for the representation of QRS complexes, especially for their compression, as well as feature evaluation and extraction [1–9,11]. Other applications include: molecular biology [8], image processing and computed tomography [8,9,11], radar signal processing [12], physical optics [13] etc.

QRS complexes, as the most characteristic waves of ECG signals, are important for medical diagnosis and treatments. In the processing and compression of ECG signals and QRS complexes, many authors applied different kinds of wavelets and corresponding transforms [17–19]. Recently, it was shown that the Hermite transform may provide far better performance, when it is appropriately optimized [1]. Namely, the Hermite transform is found to be a suitable mathematical tool for the representation of QRS complexes due to their similarity with Hermite functions (HF). In other words, these signals can be represented using a few Hermite coefficients [1–7,10]. This property has been exploited in the development of several compression algorithms for QRS complexes [5–7], thus establishing a theoretical framework with a lack of practical applications due to the use of continuous domain

functions [1]. An algorithm that proposes the use of discrete Hermite functions is presented in [1,2]. Hence, we start from the HT based algorithm [1,2], which significantly outperforms the compression based on other transforms, such as DFT, DCT and DWT, in the applications with ECG signals. This approach uses an experimentally obtained value of the scaling factor, which "stretches" and "compresses" the QRS complex to match the orthogonal basis. Herein, we employ a concentration measure based algorithm to get optimal HF parameters [20]. It leads to better performance of approach proposed in [1,2]. The idea arises from the currently attractive area of compressive sensing and sparse signal reconstruction [14–22]. Hence, an iterative procedure for the determination of the optimal scaling factor and time-shift is proposed leading to the improved compression performance, as verified on real ECG signals database [23].

The paper is organized as follows. In Section 2, an overview of the discrete HT calculation for uniformly sampled signals is provided. The optimization of the spread factor and time-shift parameter is proposed in Section 3. Section 4 presents the numerical results, while the concluding remarks are given in Section 5.

2. The Hermite transform

2.1. Discrete Hermite transform

Hermite polynomial of the p-th order, widely known among the orthogonal polynomials, can be defined as [1–14,24]:

* Corresponding author.
E-mail address: milosb@ac.me (M. Brajović).

$$H_p(t) = (-1)^p e^{t^2} \frac{d^p(e^{-t^2})}{dt^p}. \tag{1}$$

The p-th order HF is related with p-th order Hermite polynomial as follows:

$$\psi_p(t, \sigma) = \left(\sigma 2^p p! \sqrt{\pi}\right)^{-1/2} e^{-\frac{t^2}{2\sigma^2}} H_p(t/\sigma). \tag{2}$$

where the scaling factor σ is introduced to "stretch" and "compress" HF, in order to better match the signal [1–10]. The Hermite expansion is defined as [1–14]:

$$f(t) = \sum_{p=0}^{\infty} c_p \psi_p(t, \sigma), \tag{3}$$

where c_p denotes the p-th order Hermite coefficient:

$$c_p = \int_{-\infty}^{\infty} f(t)\psi_p(t, \sigma)dt, \quad p = 0, 1, \dots, M-1. \tag{4}$$

For the numerical calculation of the integral (4) the Gauss-Hermite quadrature approximation [1–8,14]:

$$c_p = \frac{1}{M} \sum_{m=1}^{M} \frac{\psi_p(t_m, \sigma)}{\left[\psi_{M-1}(t_m, \sigma)\right]^2} f(t_m), \quad p = 0, 1, \dots, M-1, \tag{5}$$

is commonly used, where t_m denotes the zeros of the M-th order Hermite polynomial (1). As it is discussed in the literature [1,24,25], there is no closed-form expression for the roots of the Hermite polynomials. Also, some examples of the roots for the first 10 Hermite polynomials are given in [14].

In general, for the case of continuous-time signals, an infinite number of Hermite functions is needed for the representation of the signal without approximation errors in (3), [1]. In the discrete case, it is assumed that discrete HF and analyzed signals are obtained by sampling their continuous counterparts at non-equispaced sampling points associated with the roots of Hermite polynomials [1,2,4,13]. Namely, in that case any discrete signal of length M can be uniquely represented by the expansion of exactly M discrete Hermite functions in (3), meaning that the signal representation is complete [1].

The time axis scaling factor σ is used to "stretch" and "compress" HF relatively to the analyzed signal $f(t)$. As proposed in [1,2], we can alternatively fix $\sigma = 1$ and introduce an equivalent parameter λ to "stretch" and "compress" the signal $f(t)$ relatively to the HF basis.

The inverse and direct HT given by (3) and (5) can be written in matrix-vector notation. Let us introduce the HT matrix as:

$$\mathbf{W}_H = \frac{1}{M} \begin{bmatrix} \frac{\psi_0(t_1, 1)}{\psi_{M-1}^2(t_1, 1)} & \frac{\psi_0(t_2, 1)}{\psi_{M-1}^2(t_2, 1)} & \cdots & \frac{\psi_0(t_M, 1)}{\psi_{M-1}^2(t_M, 1)} \\ \frac{\psi_1(t_1, 1)}{\psi_{M-1}^2(t_1, 1)} & \frac{\psi_1(t_2, 1)}{\psi_{M-1}^2(t_2, 1)} & \cdots & \frac{\psi_1(t_M, 1)}{\psi_{M-1}^2(t_M, 1)} \\ \vdots & \vdots & \ddots & \vdots \\ \frac{\psi_{M-1}(t_1, 1)}{\psi_{M-1}^2(t_1, 1)} & \frac{\psi_{M-1}(t_2, 1)}{\psi_{M-1}^2(t_2, 1)} & \cdots & \frac{\psi_{M-1}(t_M, 1)}{\psi_{M-1}^2(t_M, 1)} \end{bmatrix}_{M \times M}. \tag{6}$$

If we introduce the vector of Hermite coefficients $\mathbf{c} = \begin{bmatrix} c_0, c_1, \dots, c_{M-1} \end{bmatrix}^T$ and vector with M signal samples $\hat{\mathbf{f}} = \begin{bmatrix} f(\lambda t_1), f(\lambda t_2), \dots, f(\lambda t_M) \end{bmatrix}^T$ at the points proportional to the roots of the M-th order Hermite polynomial: $\lambda t_1, \lambda t_2, \dots, \lambda t_M$, then according to the Gauss-Hermite quadrature formula (5) the HT can be written as:

$$\mathbf{c} = \mathbf{W}_H \hat{\mathbf{f}}. \tag{7}$$

Having in mind the expansion (3), the inverse transform matrix is:

$$\mathbf{W}_{ll}^{-1} = \begin{bmatrix} \psi_0(t_1, 1) & \psi_1(t_1, 1) & \cdots & \psi_{M-1}(t_1, 1) \\ \psi_0(t_2, 1) & \psi_1(t_2, 1) & \cdots & \psi_{M-1}(t_2, 1) \\ \vdots & \vdots & \ddots & \vdots \\ \psi_0(t_M, 1) & \psi_1(t_M, 1) & \cdots & \psi_{M-1}(t_M, 1) \end{bmatrix}.$$

Based on the previous matrix definitions, the inverse HT for the case of discrete signals reads:

$$\hat{\mathbf{f}} = \mathbf{W}_{ll}^{-1} \mathbf{c}. \tag{8}$$

2.2. Hermite transform of uniformly sampled signals

Consider a continuous-time signal $f(t)$ with compact support, such that $f(t) = 0$ for $t \notin [-T, T]$. The signal is sampled uniformly to obtain the corresponding finite duration discrete-time signal $f(n)$, of odd-length $M = 2K+1$, $n = -K, \dots, K$, with Δt being the sampling period. According to the sampling theorem, the continuous-time signal can be reconstructed and resampled at the desired points $\lambda t_1, \lambda t_2, \dots, \lambda t_M$ according to:

$$f(\lambda t_m) \approx \sum_{n=-K}^{K} f(n\Delta t) \frac{\sin(\pi(\lambda t_m - n\Delta t)/\Delta t)}{\pi(\lambda t_m - n\Delta t)/\Delta t}, \tag{9}$$

where $m = 1, \dots, M$, $n = -K, \dots, K$, or in the matrix form:

$$\hat{\mathbf{f}} \approx \mathbf{A}_\lambda \mathbf{f}, \tag{10}$$

with $\hat{\mathbf{f}}$ being the vector containing signal values sampled at the desired points $t = \lambda t_m$, corresponding to zeros of the M-th order Hermite polynomial (1) and $\mathbf{f}$ is the vector of original signal samples taken uniformly according to the sampling theorem. In the case of even-length signal $M = 2K$, the values $n = -K, \dots, K-1$ are assumed in (9).

In the expanded form, (10) can be written as:

$$\begin{bmatrix} f(\lambda t_1) \\ f(\lambda t_2) \\ \vdots \\ f(\lambda t_M) \end{bmatrix} \approx \begin{bmatrix} a_{11} & a_{12} & \cdots & a_{1M} \\ a_{21} & a_{22} & \cdots & a_{2M} \\ \vdots & \vdots & \ddots & \vdots \\ a_{M1} & a_{M2} & \cdots & a_{MM} \end{bmatrix} \begin{bmatrix} f(-K) \\ f(-K+1) \\ \vdots \\ f(K) \end{bmatrix}, \tag{11}$$

where $M = 2K+1$ and elements a_{ij} being defined as:

$$a_{ij} = \sin\left[\pi(\lambda t_i - (j-K-1)\Delta t)/\Delta t\right]/\left[\pi(\lambda t_i - (j-K-1)\Delta t)/\Delta t\right],$$

with $i, j \in \{1, 2, \dots, M\}$. As recently presented in [26], the truncation error [27] using sinc interpolation is largest for the time instants near the edges of the grid. However, in the case of compact time-support signals, the truncation error will be negligible even at the edges (e.g., -50 dB for signal given in Example 1). Furthermore, the problem of interpolation of finite signals is also discussed from the perspective of FIR filter-based sinc interpolation in [28], where it is emphasized that the truncation effects could be alleviated by multiplying the interpolation kernel $\sin(\pi(t - n\Delta t)/\Delta t)/(\pi(t - n\Delta t)/\Delta t)$ by a window function.

The uniformly sampled signal and the corresponding HT now can be related by combining (7) and (11) as:

$$\mathbf{c} = \mathbf{W}_H \hat{\mathbf{f}} \approx \mathbf{W}_{ll} \mathbf{A}_\lambda \mathbf{f}. \tag{12}$$

3. Parameter optimization

3.1. Scaling factor

In this Section, we propose to employ the concentration measure of the Hermite transform vector $\mathbf{c}$ to calculate a suitable value

of λ, which will lead to the most concentrated (or even the sparsest) signal representation. It is important to emphasize that the criterion is defined such that the classical uniform sampling of signals is assumed, without need for new sampling devices. The concentration measures, such as the ℓ_1-norm of transform coefficients, have been used in optimizations where it is crucial to concentrate a signal transform in a small number of coefficients [4,20–22]. One of the most recent applications is the compressed sensing. The ℓ_1-norm of the HT can be calculated as:

$$M = \|\mathbf{c}\|_1 = \sum_{p=0}^{M-1} |c_p|. \tag{13}$$

Thus, the optimal value of λ is obtained by solving:

$$\lambda = \arg \min_\lambda \|\mathbf{c}\|_1 = \arg \min_\lambda \|\mathbf{W}_H \mathbf{A}_\lambda \mathbf{f}\|_1. \tag{14}$$

Note that (14) is a 1D search problem over the possible range of λ values. Thus, one can perform the search over the range of possible values of λ, finding the one that minimizes the concentration measure. This range can be determined such that the roots of the Hermite polynomial are mainly placed between the existing sampling points, as discussed in [1].

The basic idea behind the proposed algorithm is to iteratively search for the optimal value λ, starting from a predefined value $\lambda^{(0)}$. In each iteration k, a small value Δ is added and subtracted from the current λ, to determine the change of concentration measure. Then, $\lambda^{(k)}$ is updated by a value which decreases the measure (13) in a steepest descent manner. Similar approach was employed to reconstruct missing samples of sparse signals [4,21]. The algorithm is given as follows:

Algorithm 1. Calculation of the optimal scaling factor λ.

Require:
- Signal vector $\mathbf{f}$ of length $M = 2K + 1$
- Step parameter μ
- Transform matrix $\mathbf{W}_H$, calculated according to (6)

1: Set $\lambda^{(0)} \leftarrow M\Delta t / \left[2\left(\sqrt{\pi(M-1)/1.7} + 1.8 \right) \right]$

2: Set $\Delta \leftarrow 2/t_M$

3: Set $\varepsilon \leftarrow 10^{-10}$
While $\Delta > \varepsilon$

4: $\mathbf{A}_\lambda^+ \leftarrow \begin{bmatrix} a_{11}^+ & a_{12}^+ & \cdots & a_{1M}^+ \\ a_{12}^+ & a_{22}^+ & \cdots & a_{2M}^+ \\ \vdots & \vdots & \ddots & \vdots \\ a_{M1}^+ & a_{M2}^+ & \cdots & a_{MM}^+ \end{bmatrix}, \mathbf{A}_\lambda^- \leftarrow \begin{bmatrix} a_{11}^- & a_{12}^- & \cdots & a_{1M}^- \\ a_{12}^- & a_{22}^- & \cdots & a_{2M}^- \\ \vdots & \vdots & \ddots & \vdots \\ a_{M1}^- & a_{M2}^- & \cdots & a_{MM}^- \end{bmatrix}$

$a_{ij}^{\mp} = \frac{\sin\left[\pi\left((i \mp \Delta)t_i - (j - K - 1)\Delta t \right)/\Delta t \right]}{\pi\left((i \mp \Delta)t_i - (j - K - 1)\Delta t\right)/\Delta t}$, $i, j \in \{1, 2, \ldots, M\}$

5: $M^+ \leftarrow \|\mathbf{c}^+\|_1 = \sum_{p=0}^{M-1} |\mathbf{W}_H \mathbf{A}_\lambda^+ \mathbf{f}|$, $M^- \leftarrow \|\mathbf{c}^-\|_1 = \sum_{p=0}^{M-1} |\mathbf{W}_H \mathbf{A}_\lambda^- \mathbf{f}|$

6: $\nabla^{(k)} \leftarrow (M^+ - M^-)/M$

7: $\lambda^{(k+1)} \leftarrow \lambda^{(k)} - \mu \nabla^{(k)}$

8: $\beta \leftarrow \text{sign}\left(\nabla^{(k)} \nabla^{(k-1)} \right)$

9: **If** $\beta < 0$ **then** $\Delta \leftarrow \Delta/2$
End while

10: **Return** $\lambda^{(k)}$

Here, $\lambda^{(0)} = M\Delta t / \left[2(\sqrt{\pi(M-1)/1.7} + 1.8) \right]$ is used as the starting point, which is the lower bound for the scaling factor defined in [15,16] in order to ensure the convergence of the algorithm. The values of μ and Δ are chosen to provide optimal results for all considered signals. A too small step μ leads to slow convergence, while on the other side μ should be as small as

possible to keep the algorithm stable (i.e., to ensure that the upper bound $\lambda < \left[\sqrt{\pi M/1.7} + 1.8 \right] / \left[2\pi W \right]$ is satisfied [15,16], with W being the frequency bandwidth). Hence, the value of μ is set up empirically as a trade-off between these two requirements.

Maximal number of iterations corresponds to the signal length (in the experiments, the convergence is obtained even for number of iterations equal to the half of the signal length). The computational complexity of the algorithm can be approximated as follows (one iteration is considered): a) to generate the argument of the sinc function in Step 4, we need $2M^2 + 2$ additions (or subtractions) and $6M^2$ multiplications with constants; b) the interpolation is done with M^2 multiplications and $M(M-1)$ additions; c) For the two HT calculations, the complexity is $2M^2$ additions and $2M^2$ multiplications; d) the concentration measure requires $2M - 2$ additions. Hence, the proposed algorithm requires $5M^2 + M$ additions and $9M^2$ multiplications in total.

Two-dimensional (2D) Hermite transform can be obtained by calculating one-dimensional Hermite transforms separately in both directions [14]. Hence, the proposed approach can be generalized in a straight-forward manner for the case of 2D signals.

3.2. Shift parameter

The basis functions can be also shifted left or right along the time axis [10]. Instead of centering the signal at the zero time instant [1,2], here we propose to shift center for a few sampling points left or right, before the calculation of the coefficients. In other words, instead of $f(n\Delta t)$, we use: $f_m(n\Delta t) = f((n \pm l)\Delta t)$ in (9), with $l = \left[-l_{\max}, l_{\max} \right]$.

For every discrete shift value l, optimal λ is calculated in order to minimize (14). The measure vector $\mathbf{L}$ is formed by using the minimal measure value (14) obtained for the optimal λ, for every considered l. Then we find the value of l corresponding to the minimum of $\mathbf{L}$, by solving:

$$l = \arg \min_l \mathbf{L} \tag{15}$$

Note that $l_{\max}$ has a small value, e.g. $l_{\max} = 3$ for the case of QRS complexes, and thus a direct search in (15) is applied. The integer shift values are used in this paper, since the fractional shifts may require an additional interpolation, which causes difficulties in the minimization of the concentration measure [10].

4. Numerical results

Example 1. Let us observe the signal of the form:

$$f(t) = -3 \sin(5\pi t) \exp\left(-\frac{(Mt)^2}{2\sigma_0^2} \right) \tag{16}$$

with $M = 61$, $\sigma_0 = 1.25$, $-1/2 < t < 1/2$, sampled with $\Delta t = 1/M$ to obtain discrete values at the uniform grid $n = -(M-1)/2, \ldots, (M-1)/2$. Original signal with uniformly sampled points and the corresponding Hermite coefficients with $\sigma = 1$ are shown on Fig. 1(a) and (b) respectively. Note that the signal is characterized by the compact time support and it has the similar shape as the Hermite basis functions. Hence, these types of signals (windowed or low-pass filtered sinusoids, QRS segments, short-duration signals such as FHDSS, or UWB signals) are amenable to the proposed approach.

The proposed iterative procedure has been applied in order to find the most concentrated HT of the resampled signal. The obtained result is $\lambda = \sigma_0 \Delta t = 1.25/M$ since we have intentionally
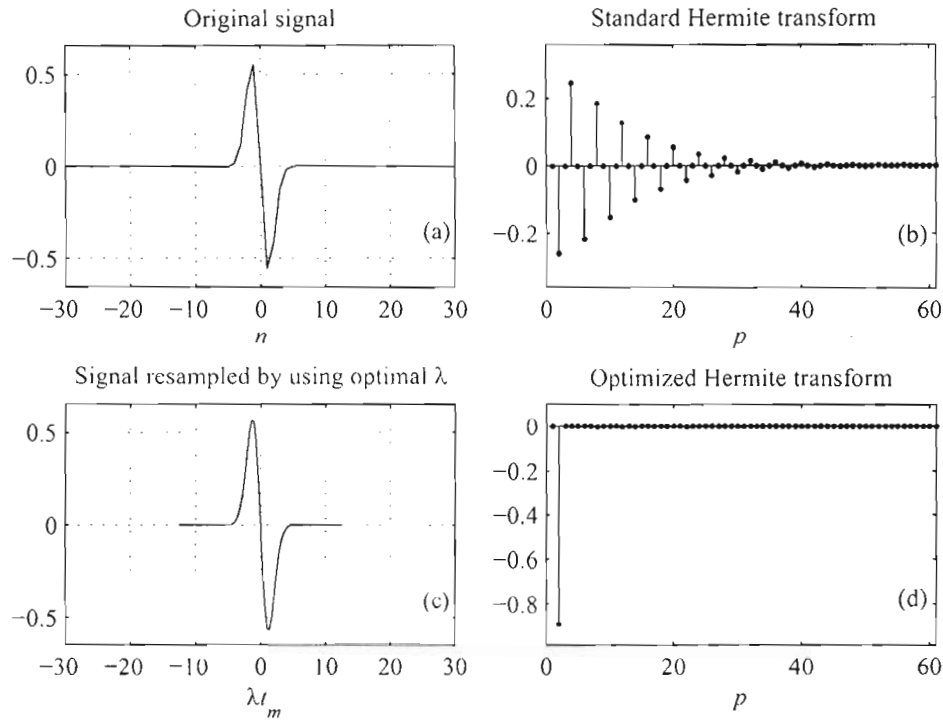
Fig. 1. Scaling factor influence on the HT: (a) original signal (16) and (b) the corresponding Hermite coefficients; (c) optimally scaled signal resampled at the roots of Hermite polynomial, and (d) Hermite coefficients of the resampled signal.

incorporated the spread factor as the parameter of the Gaussian window in (16). The resampled signal with appropriately rescaled time axis, sampled at the roots of the M-th order Hermite polynomial, and corresponding Hermite coefficients are shown on Fig. 1(c) and (d). We can observe that the optimal value of the scaling factor will assure that there is only one significant coefficient at $p=2$, while other coefficients are close or equal to zero.

In order to check whether the proposed algorithm finds the optimal value, the concentration measure is calculated for different values of scaling factor λ: $1/\Delta t \le \lambda/\Delta t \le 2/\Delta t$, varied with the step $0.01/\Delta t$. The results are plotted in Fig. 2a, where the global minimum $\lambda_{min} = 1.25/\Delta t$ is clearly visible on the curve.

Here, it is assumed that the lower and upper bounds of λ are satisfied [15,16]. Lower bound is controlled by the algorithm initialization, and suitably chosen step μ assures that the upper bound is never reached. In this interval, a global minimum is expected, corresponding to the most concentrated Hermite transform. Further, the learning curve of $\lambda/\Delta t$ with respect to iteration number is given in Fig. 2b. It can be observed that, as the algorithm reaches the minimum of the concentration measure, it stabilizes.

The influence of truncation error introduced by the finite sinc kernel is also examined calculating the MSE between the interpolated signal $f_{int}(\lambda t_m)$ (interpolation is done based on uniform

samples $f(n)$ and relation (10)) and the original (analytic) signal (16) observed at points $t = \lambda t_m$: $MSE = \frac{1}{M} \sum_{m=1}^{M} |f_{int}(\lambda t_m) - f(\lambda t_m)|^2$. Hence, the signal length M is varied from 21 to 401 samples (with step 2). The results are shown in Fig. 3 (logarithmic scale) showing that even the largest error caused by sinc interpolation is as small as -50 dB.

Example 2. In the framework of the considered compression problem, it is important to represent QRS complexes with the smallest possible number of coefficients, with a medically acceptable error. The compression algorithm proposed in [1,2] operates as follows. It is assumed that the ECG signal (i.e. QRS complex) $f(t)$ is sampled at points $\lambda t_1, \lambda t_2, ..., \lambda t_M$, to obtain the vector $\hat{\mathbf{f}}$. Then the HT coefficients $\mathbf{c}$ are calculated by (7). Further, the vector $\tilde{\mathbf{c}}$ is formed by keeping L largest coefficients in $\mathbf{c}$ and setting others to zero. The signal approximation can be obtained according to (8):

$$\tilde{\mathbf{f}} = \mathbf{W}_H^{-1}\tilde{\mathbf{c}}. \tag{17}$$

Here, we will refer to the algorithm presented in [1,2] which can be further improved, by the proposed optimization of the scaling factor and the time-shift. The continuous signal $f(t)$ was
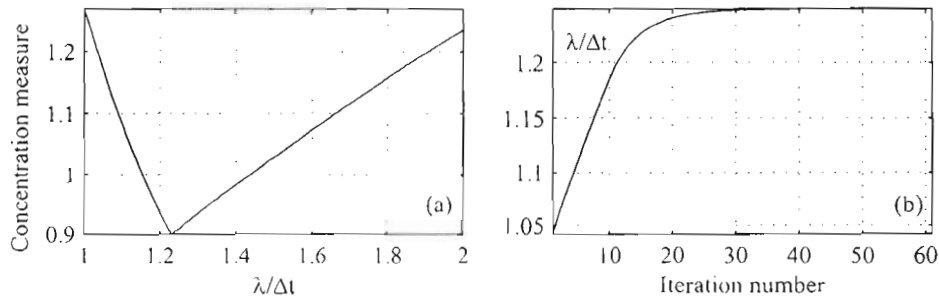

Fig. 2. a) The concentration measure in terms of $\lambda/\Delta t$, b) the learning curve of $\lambda/\Delta t$ through the iterations.
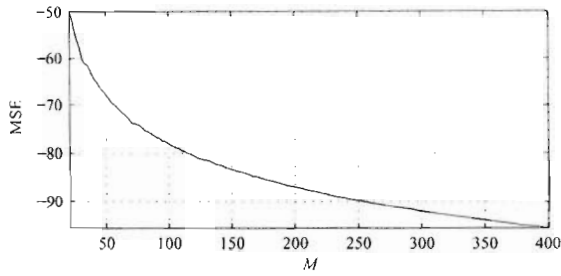
Fig. 3. MSE caused by the sinc interpolation kernel.

Table 1
Average number of coefficients and compression ratio for 10% approximation error.

Comparison criterion	Proposed HT algorithm	HT based algorithm in [1]	DFT-based	DCT-based
Average number of coefficients	5.0	5.8	8.3	7.3
Average compression ratio	6.2	5.3	3.7	4.3

sampled at the points $\lambda t_1, \lambda t_2, \ldots, \lambda t_M$, where the scaling factor λ is chosen to obtain smallest number of coefficients in $\check{c}$ under the condition that the relative reconstruction error:

$$E = \frac{\|\bar{\mathbf{f}} - \hat{\mathbf{f}}\|_2}{\|\hat{\mathbf{f}}\|_2} \tag{18}$$

is below 10%, which is medically acceptable [1,2]. However, several problems arise. To determine the optimal scaling factor λ, starting from the continuous ECG signals, sampling process needs to be repeated for every λ from a suitable range of possible values, which can be a technical problem for sampling devices. Then, the

HT is calculated for every possible λ, and (18) is used to find the optimal λ such that $E < 10\%$. The other possibility is to use a fixed value of λ. However, it can be shown that improper λ leads to the larger number of Hermite coefficients in $\check{c}$. Moreover, our experiments as well as those in [1,2] show that each QRS complex has a different optimal value of λ, which means that the sampling device has to be continuously readjusted. On the other side, when dealing with the discrete QRS complexes in [1], the signal is resampled according to (11) and search for the optimal λ is done by measuring the compression ratio, which has to be maximized under the condition that $E \leq 10\%$. However, this approach is numerically exhausting, since both direct and inverse Hermite transform need to be calculated for each observed number of the largest coefficients and for each λ.

In this paper, we propose to search for an optimal λ by minimizing the concentration measure, before the compression is done. The compression procedure is done as in [1], while the improvement is provided using the scaling factor optimization and the time-shift optimization based on concentration measure (14).

We have extracted $Q = 1486$ QRS complexes, from the first 10 s (first lead) of 168 ECG signals obtained from the MIT-BIH Compression Test Database [23]. The signals are uniformly sampled with $\Delta t = 1/250$. Three different signal lengths are used [1]: $2K + 1 \in \{27, 29, 31\}$. The compression results are shown in Table 1 in terms of the average number of coefficients (producing $E \leq 10\%$) and the average compression ratio: $ACR = \sum_{i=0}^{Q} (2K_i + 1) / \sum_{i=0}^{Q} L_i$. (where L_i is the number of nonzero HT coefficients in the i-th complex producing $E \leq 10\%$, while $2K_i + 1$ is the length of the i-th QRS complex). The second column (as well as the third and the fourth) shows the result published in [1].

In the original approach [1] that uses a demanding search over all possible λ, average number of 5.8 coefficients is needed for the proper reconstruction with $E \leq 10\%$. The proposed method (first column of Table 1) shows further improvement, if the set of
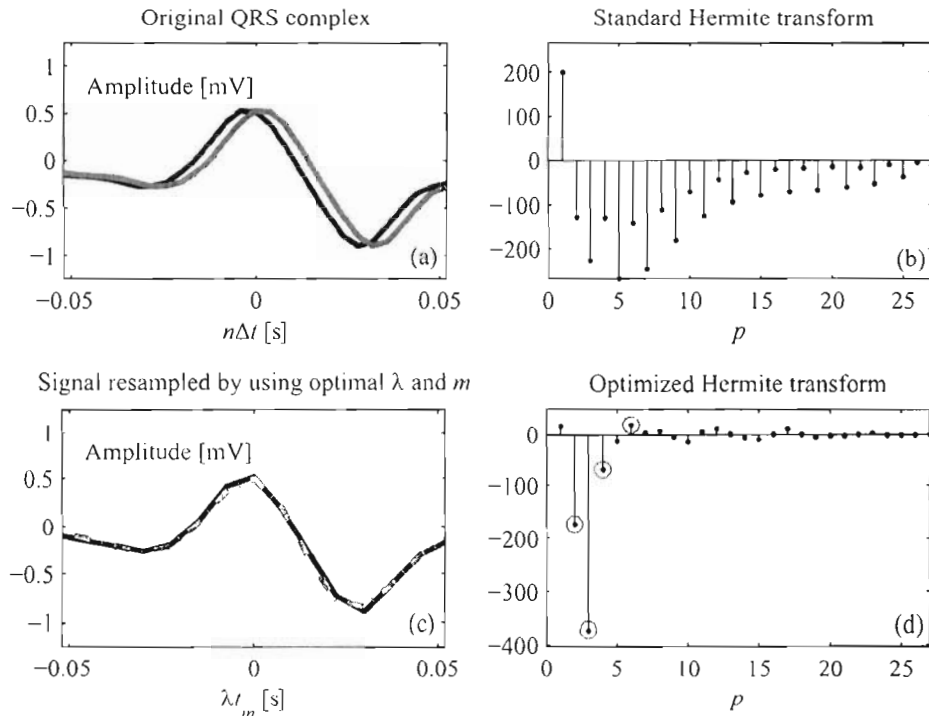

Fig. 4. Optimal scaling, shifting and resampling of QRS complex: (a) original signal (blue) and its shifted version (red); (b) Hermite coefficients of the original signal (standard Hermite transform); (c) shifted resampled signal with the optimal scaling factor (solid line) and reconstructed signal using the largest 4 Hermite coefficients (relative error < 10%); (d) Optimized Hermite transform of rescaled and resampled signal (circles denote the largest 4 coefficients). (For interpretation of the references to color in this figure legend, the reader is referred to the web version of this article.)
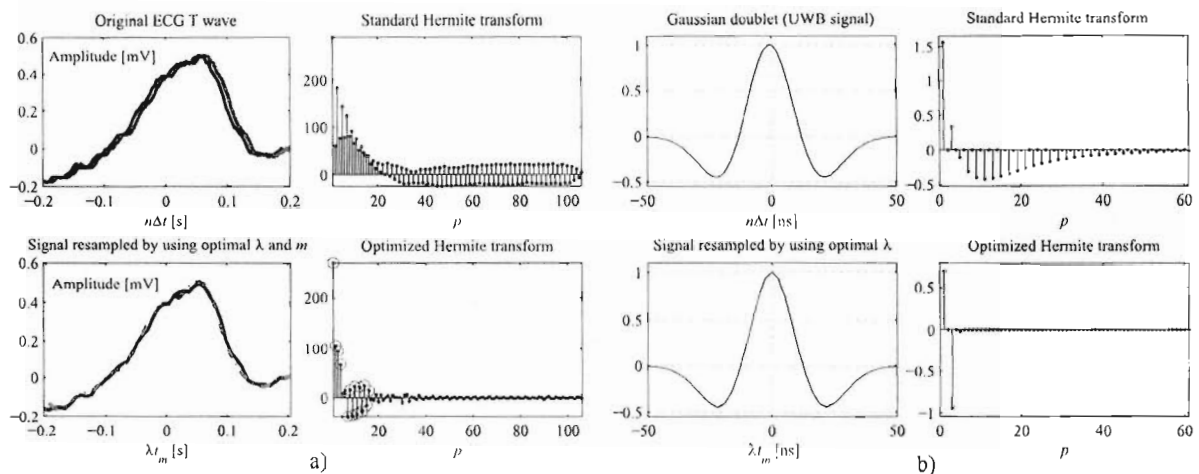
Fig. 5. a) Application to the ECG T waves, b) application to the UWB signals.

considered time-shifts is extended with $l_{max} = 3$, $l \in \{-3, -2, -1, 0, 1, 2, 3\}$. Namely, when both the time-shift and scaling factor are optimized as proposed, the same error level is achieved even if only 5 coefficients are used, which means that the improvement over the original algorithm is about 13.8%. The average value of the scaling factor over all $Q = 1486$ QRS complexes is $\lambda/\Delta t = 4.2495$ (in seconds $\lambda = 4.2495/250 = 0.017$, which is the value experimentally obtained in [2], thus confirming the accuracy of the proposed approach). The step $\mu = 0.05$ is used in the experiment.

Let us consider the estimate of the average number of bits per sample: a) for the time domain we need 9 bps, b) in the case of optimized HT, there are 5 most important real-valued coefficients out of 31 within QRS complex (one zero value may appear between 5 nonzero coefficients, and thus approximately 6 coefficients are encoded), which results in the rate 2 bps; c) in the case of DFT, there are approximately 8 most important coefficients (with real and imaginary parts) to be encoded out of 31, which is approximately 7 bps in average.

An example of the analyzed QRS complexes from the database [23] is shown in Fig. 4. Original signal is shown on Fig. 4. (a), with the Hermite coefficients in Fig. 4(b). The concentration measure is lowest for the time-shift $l = 1$, with the corresponding optimal scaling factor $\lambda/\Delta t = 0.4352$ (in seconds $\lambda = 0.0176$). The optimally shifted signal, resampled at the roots of Hermite polynomial (with $M = 27$ and $\lambda/\Delta t = 0.4352$), is shown in Fig. 4(c), with the Hermite coefficients given in Fig. 4(d). The reconstructed signal is given by dash-dotted line in Fig. 4(c).

Example 3. It is interesting to emphasize that the same approach can be applied to other types of signals such as the T waves of ECG signals, but also to the commonly present UWB signals (known as Gaussian doublets). Transmitting common Gaussian pulses directly to the antennas results in filtered pulses modeled as a derivative operation producing [29–31]: $s(t) = \left[1 - 4\pi (t/\tau_m)^2\right] e^{-2\pi (t/\tau_m)^2}$. A discrete version of this signal is considered, sampled at 2 GHz, of length 100 ns and with $\tau_m = 22.2$ ns. The results of applying the proposed method on the ECG T waves are shown in Fig. 5a. After applying the proposed algorithm, the observed part of ECG signal can be represented with only 14 coefficients out of 106 (13%), assuring the relative error (18) smaller than 10%. The average number of coefficients for the entire MIT-BIH Compression Test Database (first lead, first 10 s of 168 ECG signals) [23] is approximately 23% of the total length. In the case of UWB signals, the algorithm shows a high level of efficiency, providing a compact support with only 2 significant coefficients (Fig. 5b). Hence, in the context of UWB signals, the proposed approach has a potential

in design of UWB receivers, allowing the signals to be easily detected at the receiver.

5. Conclusion

An optimization approach for the Hermite transform scaling factor and time-shift is presented. Concentration measure of the transform is employed as the optimization criterion. An iterative search algorithm for the scaling factor optimization is presented. The results are confirmed on both synthetic signal and real ECG signals. The presented theory is applied in the compression of QRS complexes, reducing the average number of coefficients that need to be stored. Finally, it has been shown that the same concept can be also applied to other segments of ECG signal (such as T waves), but also to the UWB signals in communications.

References

[1] A. Sandryhaila, S. Saba, M. Puschel, J. Kovacevic, Efficient compression of QRS complexes using Hermite expansion, IEEE Trans. Signal Process. 60 (2) (2012) 947–955, http://dx.doi.org/10.1109/TSP.2011.2173336.

[2] A. Sandryhaila, J. Kovacevic, M. Püschel, Compression of QRS complexes using Hermite expansion, in: International Conference on Acoustics, Speech and Signal Process. (ICASSP), IEEE, Prague, 2011, pp. 581–584, http://dx.doi.org/10.1109/ICASSP.2011.5946470.

[3] L.R.L. Conte, R. Merletti, G.V. Sandri, Hermite expansion of compact support waveforms: applications to myoelectric signals, IEEE Trans. Biomed. Eng. 41 (12) (1994) 1147–1159, http://dx.doi.org/10.1109/10.335863.

[4] M. Brajović, I. Orović, M. Daković, S. Stanković, Gradient-based signal reconstruction algorithm in the Hermite transform domain, Electron. Lett. 52 (1) (2016) 41–43, http://dx.doi.org/10.1049/el.2015.1700.

[5] P. Laguna, R. Jané, S. Olmos, N.V. Thakor, H. Rix, P. Caminal, Adaptive estimation of QRS complex wave features of ECG signal by the Hermite model, Med. Biol. Eng. Comput. 34 (1) (1996) 58–68, http://dx.doi.org/10.1007/BF02637023.

[6] P. Sörnmo, P.O. Börjesson, P. Nygards, O. Pahlm, A method for evaluation of QRS shape features using a mathematical model for the ECG, IEEE Trans. Biomed. Eng. 28 (10) (1981) 713–717, http://dx.doi.org/10.1109/TBME.1981.324666.

[7] M. Lagerholm, C. Peterson, G. Braccini, L. Edenbrandt, L. Sörnmo, Clustering ECG complexes using Hermite functions and self-organizing maps, IEEE Trans. Biomed. Eng. 47 (7) (2000) 838–848, http://dx.doi.org/10.1109/10.846677.

[8] G. Leibon, D.N. Rockmore, W. Park, R. Taintor, G.S. Chirikjian, A fast Hermite transform, Theor. Comput. Sci. 409 (2) (2008) 211–228, http://dx.doi.org/10.1016/j.tcs.2008.09.010.

[9] J.-B. Martens, The Hermite transform—theory, IEEE Trans. Acoust., Speech, Signal Process 38 (9) (1990) 1595–1605, http://dx.doi.org/10.1109/29.60086.

[10] A.I. Rasiah, R. Togneri, Y. Attikiouzel, Modelling 1-D signals using Hermite basis functions, IEE Proc. Vis., Image Signal Process 144 (6) (1997) 345–354, http://dx.doi.org/10.1049/ip-vis:19971613.

[11] E. Moya-Albora, B. Escalante-Ramíreza, E. Vallejob, Optical flow estimation in cardiac CT images using the steered Hermite transform, Signal Process.: Image Commun. 28 (3) (2013) 267–291, http://dx.doi.org/10.1016/j.image.2012.11.005.

[12] S. Stanković, I. Orović, A. Krylov, The two-dimensional Hermite S-method for high resolution inverse synthetic aperture radar imaging applications, IET Signal Process 4 (4) (2010) 352–362, http://dx.doi.org/10.1049/iet-spr.2009.0060.

[13] P. Lazaridis, G. Debarge, P. Gallion, Discrete orthogonal Gauss–Hermite transform for optical pulse propagation analysis, J. Opt. Soc. Am. B 20 (7) (2003) 1508–1513, http://dx.doi.org/10.1364/JOSAB.20.001508.

[14] S. Stanković, I. Orović, E. Sejdić, Multimedia Signals and Systems, Springer, Verlag, New York 2012 http://dx.doi.org/10.1007/978-1-4614-4208-0.

[15] R. Ma, L. Shi, Z. Huang, Y. Zhou, EMP signal reconstruction using associated-hermite orthogonal functions, IEEE Trans. Electromagn. Compat. 56 (5) (2014) 1242–1245, http://dx.doi.org/10.1109/TEMC.2014.2312003.

[16] Mengtao Yuan, A. De, T.K. Sarkar, Jinhwan Koh, Baek Ho Jung, Conditions for generation of stable and accurate hybrid TD-FD MoM solutions, IEEE Trans. Microw. Theory Tech. 54 (6) (2006) 2552–2563, http://dx.doi.org/10.1109/TMTT.2006.875823.

[17] B.A. Rajoub, An efficient coding algorithm for the compression of ECG signals using the wavelet transform, IEEE Trans. Biomed. Eng. 49 (4) (2002) 355–362, http://dx.doi.org/10.1109/10.991163.

[18] N. Boukhennoufa, K. Benmahammed, M.A. Abdi, F. Djeffal, Wavelet-based ECG signals compression using SPIHT technique and VKTP coder, in: 3rd Int. Conf. on Signals, (Circuits and Systems (SCS), Medenine), 2009, pp. 1–5, http://dx.doi.org/10.1109/ICSCS.2009.5412584.

[19] S. Olmosa, J. Garcíaa, R. Janéb, P. Lagunaa, ECG signal compression plus noise filtering with truncated orthogonal expansions, Signal Process 79 (1) (1999) 97–115, http://dx.doi.org/10.1016/S0165-1684(99)00083-3.

[20] LJ. Stanković, A measure of some time-frequency distributions concentration, Signal Process 81 (3) (2001) 621–631, http://dx.doi.org/10.1016/S0165-1684(00)00236-X.

[21] LJ. Stanković, M. Daković, S. Vujović, Adaptive variable step algorithm for missing samples recovery in sparse signals, IET Signal Process 8 (3) (2014) 246–256, http://dx.doi.org/10.1049/iet-spr.2013.0385.

[22] M. Elad, Sparse and Redundant Representations: From Theory to Applications in Signal and Image Processing, Springer, New York, 2010.

[23] MIT-BIH ECG Compression Test Database [Online]. ⟨http://www.physionet.org/physiobank/database/cdb⟩.

[24] Handbook of mathematical functions, in: M. Abramowitz, I.A. Stegun (Eds.), Dover Publ, New York, 1992.

[25] W. Gautschi, Orthogonal Polynomials: Computation and Approximation, Oxford Univ. Press, Oxford, U.K, 2004.

[26] Z. Xu, B. Huang, K. Li, On Fourier interpolation error for band-limited signals, IEEE Trans. Signal Process 57 (6) (2009) 2412–2416, http://dx.doi.org/10.1109/TSP.2009.2016263.

[27] A. Papoulis, Signal Analysis, McGraw-Hill, New York, 1977.

[28] T.I. Laakso, V. Valimaki, M. Karjalainen, U.K. Laine, Splitting the unit delay [FIR/all pass filters design], IEEE Signal Process. Mag. 13 (1) (1996) 30–60, http://dx.doi.org/10.1109/79.482137.

[29] M.Z. Win, R.A. Scholtz, Ultra-wide bandwidth time-hopping spread spectrum impulse radio for wireless multiple-access communication, IEEE Trans. Commun. 48 (4) (2000) 679–691, http://dx.doi.org/10.1109/26.843135.

[30] F. Ramirez-Mireles, On the performance of ultra-wide-band signals in Gaussian noise and dense multipath, IEEE Trans. Veh. Technol. 50 (1) (2001) 244–249, http://dx.doi.org/10.1109/25.917932.

[31] M. Ghavami, L.B. Michael, R. Kohno, Ultra Wideband Signals and Systems in Communication Engineering, 2nd ed., Wiley, Chichester, UK, 2007.

Post-processing of time-frequency representations in instantaneous frequency estimation based on ant colony optimization

CrossMark

Miloš Brajović, Vesna Popović-Bugarin*, Igor Djurović, Slobodan Djukanović

University of Montenegro, Faculty of Electrical Engineering, 20 000, Podgorica, Montenegro

ARTICLE INFO

ABSTRACT

Instantaneous frequency (IF) estimation of non-stationary signals embedded in high noise is addressed. When present, high noise represents a dominant error source in the IF estimation. Additive Gaussian noise with variance proportional to the signal power is assumed. An estimation approach based on the ant colony optimization (ACO) and time-frequency (TF) analysis is proposed. The ACO algorithm is adapted for the IF estimation starting from the Wigner distribution (WD) of the considered signal. The proposed technique is also applicable to numerous other representations, without any change in the parameter setup. This method surpasses the influence of high noise in the IF estimation; for that purpose, we have designed a pheromone deposition gradient and a mechanism for the variation of the agents' population size. The introduced approach improves the fast-varying IF estimation accuracy, overcoming known issues in the state-of-the-art algorithms dealing with high noise. The basic principles of the proposed method are illustrated and performance validated through numerical examples.

© 2017 Elsevier B.V. All rights reserved.

1. Introduction

Time-frequency (TF) signal analysis has drawn a significant attention during the last few decades [1–43]. Various TF representations enable efficient analysis and extraction of information contained within time variations of the signal's spectral content [4,6]. One of the key topics in this area is the instantaneous frequency (IF) estimation of a signal [4–10]. Numerous TF representations and algorithms have been proposed in order to facilitate the IF estimation, but no TF representation exists, nor the estimation algorithm, that resolves this problem for all classes of signals and under all circumstances [4,5]. These facts make the IF estimation problem still scientifically attractive [6].

The IF estimation arises in numerous application fields including communications based on frequency modulation (FM), radar and sonar systems, speech analysis and recognition, analysis of video signals, seismology, biology, bio-medicine [6,16,25].

Many TF representations have the property of concentrating the signal energy at and around the IF [15,29–31]. This is the reason why the IF estimation formulation, in classical estimation approaches, reduces to determination of the TF representation maxima [4,5,6]. The Wigner distribution (WD) has been widely used as an IF estimator of FM signals, since the signal representation

in the TF plane is highly concentrated [8,26,27]. However, due to higher-order signal phase derivatives, the WD contains inner interferences. Moreover, when multicomponent signals are considered, the undesired cross-terms appear in addition to signal components referred to as the auto-terms. The cross-terms can mask the auto-terms in the TF plane [3,25]. Besides the principles presented in [4] and [6], a comprehensive analysis of the WD as an IF estimator is given in [7] and [8], where the estimation error sources were classified into four categories: bias, errors due to variations within the signal's auto-terms, errors due to frequency discretization and errors due to high noise. Techniques that deal with the first three error sources are presented in [4,9,27,28]. The influence of high noise has attracted a significant attention, since it represents a dominant error source when it occurs [7–9]. Errors due to high noise appear since the high noise induces false maxima (maxima outside of the auto-terms) in the TF plane. Under the term "high noise" we assume additive Gaussian noise of the constant variance proportional to the power of the contaminated signal, as considered in [6–9,14].

An instance of the Viterbi algorithm (VA), originally introduced in [8], has been applied in the IF estimation in order to overcome the negative high noise impact. The performance of the VA-based approach in various estimation problems involving high noise has been confirmed during the recent years [6,9–13]. Another IF estimation approach based on a high-dimensional search of the IF curves in the TF plane has been proposed in [30], for the case

---

of wavelets. The search of curves is based on a stochastic re-laxation procedure. This approach has certain robustness to high noise. The generalization of this approach towards the TF representations with an introduction of a new stochastic search procedure has been presented in [31].

Artificial ant colonies (AACs), a biologically inspired paradigm, represent multi-agent tools for problem solving without a centralized control [44–59]. The whole set of optimization techniques based on the AAC concept, widely known as the ant colony optimization (ACO), has been developed and applied in different scientific areas, especially where the hard-solving local optimization problems arise [46–56]. The AACs are one of many concepts in the so-called swarm intelligence, where a population of artificial agents forms a collective intelligence over a specific environment [44]. Important application fields in digital image processing include edge detection, pattern recognition and feature extraction [48–56]. For the problem considered in this paper, an especially interesting ACO application is in edge detection in digital images [49,54,56]. By taking into account that edges represent image segments with high contrast and/or color variations, the median difference in agents' neighboring points has been used as the main criterion for edge detection [50,54,56].

In this paper, the ACO algorithms proposed in [49] and [50] are adapted for the TF-based IF estimation. A new gradient which takes into account the IF properties is introduced in order to achieve a robust estimation in high noise: the IF should pass through as many as possible points of the TFR with highest magnitudes, while the IF variation between two consecutive points should not be too fast [8].

The estimation is performed based on a generated pheromone map, representing a new TF representation with significantly reduced disturbances. The initial version of the algorithm is proposed in [59]. In this paper, we improve the performance of the algorithm [59] by introducing variable population size [49,50]. In addition, we evaluate the performance of the proposed method versus signal-to-noise ratio (SNR), provide comparison with the state-of-the-art VA-based algorithm and illustration of cross-terms suppression in the case of multicomponent signals, as well as the IF estimation illustration for real-life signals. The concept of variable population size provides an additional control mechanism for the mass behavior of an AAC. The basic idea is to retain the agents moving across the TF points corresponding to the auto-terms, while tending to eliminate as many those not corresponding to the auto-terms as possible. The agent's ability to survive during the iterations is measured by its energy, which is related to the proposed gradient. In this way, the influence of the gradient on the mass behavior of agents is emphasized. The distributed nature of the proposed algorithm and carefully designed gradient make the estimation more robust to fast IF variations. In this way, it overcomes, at a certain level, the sensitivity of the VA to fast IF variations, which is confirmed for signals with fast IF variations. Additionally, the proposed approach suppresses inner interferences, as well as cross-terms in multi-component signals.

Basic theory concerning the IF estimation problem is given in Section 2. The ACO algorithm within the framework of the TF-based IF estimation is presented in Section 3. Section 3 also introduces the pheromone deposition gradient and the variable population concept, both adapted for the IF estimation, the estimation algorithm and a discussion on the algorithm parameters. Section 4 presents numerical examples with the estimation results and a statistical verification of the proposed method by a comparison with the WD maxima and the VA estimators. Section 5 concludes the paper.

2. Background theory

Consider a complex amplitude and frequency modulated signal [6–9]:

$$s(t) = A(t)e^{j\phi(t)}, \qquad (1)$$

where $A(t)$ is a slowly varying amplitude with respect to phase variations, i.e. $|dA(t)/dt| \ll |d\phi(t)/dt|$ and $\phi(t)$ is the signal instantaneous phase. Note that for real-valued signals positive frequencies are taken into account or the corresponding Hilbert transform of the signal is calculated. Some alternative signal models are also discussed in the literature [17–22]. The IF of $s(t)$ is defined as the first derivative of its phase, i.e.

$$\Omega(t) = d\phi(t)/dt. \qquad (2)$$

The signal of interest is embedded in complex additive white Gaussian noise (AWGN) $\varepsilon(t)$ with zero-mean and variance σ^2, with independent and identically distributed (i.i.d.) real and imaginary parts, that is

$$x(t) = s(t) + \varepsilon(t). \qquad (3)$$

The signal is sampled with the sampling interval Δt to obtain $x(n) = x(n\Delta t)$, where n represents discrete time variable. In the case when $s(t)$ contains multiple components, i.e. when $x(t)$ can be written as

$$x(t) = \sum_{l=1}^{S} s_l(t) + \varepsilon(t), \qquad (4)$$

where S represents the number of components $s_l(t)$ defined by (1), the IF of each component can be calculated as the first derivative of the corresponding phase component. This concept has not full theoretical foundation, but it has clear justification when components are well-separated in the TF plane.

Further, we observe the WD of the signal $x(n)$, well known for its advantageous properties in the IF estimation of noisy signals. The IF approach that we present may be applied on other TF representations as well.

The WD of $x(n)$ [8] is defined as

$$WD(n, k) = \sum_{m=-K/2}^{K/2-1} w(m)x(n+m)x^*(n-m)e^{-j4\pi mk/K}, \qquad (5)$$

where $-K/2 \leq k \leq K/2-1$ represents discrete frequency index, K denotes the length of a real-valued symmetric window $w(n)$, whereas * denotes complex conjugation. Without loss of generality even K is assumed. It is also assumed that the discrete signal length is N_s. For a given instant n, the IF ($\omega(n)$ or $\Omega(n\Delta t) = \omega(n)/\Delta t$) is estimated as the WD maximum position [6,8,25]:

$$\hat{k} = \arg\max_k WD(n, k). \qquad (6)$$

This simple IF estimator is a common tool in practice. However, a high noise causes the WD maxima to be located away from the IF points, thus resulting in erroneous IF estimation [7,8].

The state-of-the-art approach overcoming the IF estimation problem in high noise is an instance of VA, originally introduced in [8], whose performance is reviewed in [6]. This algorithm combines a non-parametric method based on the WD maxima with the minimization of IF variations between consecutive points. As the VA incorporates a criterion that assumes slow IF variations between consecutive points, it is sensitive to fast IF variations.

3. IF estimation by using ant colony optimization algorithm

3.1. The review of basic ACO concepts, notation and terminology

Basic ACO algorithm is explained in [46], while details on ACO applications in edge detection and feature extraction can be found

in [49–53]. The discrete WD, i.e. a matrix of size $N \times K$, where $N = N_s - K$ can be observed as a rectangular grid in which artificial ants move across adjacent cells. In other words, we observe the domain consisted of TF points $(n, k) \in [0, N) \times [-K/2, K/2)$. Ants are initially placed at random grid positions, with random orientations.

Transition of an ant from cell $(n', k') \in [0, N) \times [-K/2, K/2)$ to a new cell (n, k) occurs in each iteration l. An iteration is finished when each ant from the colony moves from a previous position (n', k') to allowed neighboring position (n, k). In every cell visited by an ant a certain pheromone level is added. Pheromone level deposited at the position (n, k) is denoted by $\Phi(n, k)$. A matrix known as the pheromone map Φ is used to store the pheromone level for every cell (position) in the observed grid. In this paper, the pheromone map represents a new TF representation, which is used for the IF estimation. When a predefined number of iterations is reached, or another stopping criterion is met, the algorithm terminates.

The general ant transition rule from the current cell (n', k') to the new cell (n, k) in iteration l, is defined by probability $P^{(l)}_{(n', k')}(n, k)$, which depends on the pheromone level $\Phi(n, k)$, and a heuristic function $d_{(n', k')}(n, k)$, [46,50–53]. Herein, we use the adaptation of the basic ACO algorithm [46] for the case of digital images, presented in [50], where this probability is defined as:

$$P^{(l)}_{(n', k')}(n, k) = \begin{cases} \dfrac{(\Phi^{(l)}(n, k))^{\beta} d_{(n', k')}(n, k)^{\zeta}}{\sum_{(n, k) \in \mathbf{Q}(n', k')} (\Phi^{(l)}(n, k))^{\beta} d_{(n', k')}(n, k)^{\zeta}}, & (n, k) \in \mathbf{Q}(n', k') \\ 0, & \text{otherwise}. \end{cases} \quad (7)$$

where $\mathbf{Q}(n', k')$ is the set representing the permissible ant's movement range, i.e. the local neighborhood of the current ant's position (n', k'); parameters β and ζ control the influence of pheromone and heuristic information, respectively [46,50,52]. As it is emphasized in [45], instead of $(\Phi^{(l)}(n, k))^{\beta}$ and $d_{(n', k')}(n, k)^{\zeta}$ other monotonic non-decreasing functions $g(\Phi(n, k))$ of the pheromone level can be used, and several of them are proposed in the literature, depending on applications [45–55]. In this paper, we fix $\zeta = 1$ and adapt the original ACO algorithm via a pheromone update rule. In the end of each iteration, the pheromone decreases globally in the whole pheromone map, thus allowing the control of the pheromone map content by a suitably defined pheromone update rule.

3.2. Ant colony optimization

3.2.1. Initialization

At the beginning of the optimization algorithm, γ percents of the TF representation points are randomly covered with intelligent agents (ants). The initial ant positions $(n_0, k_0) \in [0, N) \times [-K/2, K/2)$ are obtained by a random number generator with uniform distribution. The initial ant orientations are defined by values $P(n, k)$ stored in an auxiliary matrix $\mathbf{P}$ with elements:

$$P(n, k) = \begin{cases} r, & (n, k) = (n_0, k_0) \\ 0, & (n, k) \neq (n_0, k_0) \end{cases} \quad (8)$$

where r is a random integer with uniform distribution in the range $\{1, 2, ..., 8\}$. Each r value corresponds to one of eight possible orientations (1 denotes the upwards orientation, 2 left upwards, 3 left etc.). In all subsequent iterations, the ant orientation for the new cell (n, k) is determined by its movement from the old cell (n', k'). For example, if an ant moves from $(n', k') = (n + 1, k)$ to (n, k), then it is upwards oriented, i.e. $P(n, k)$ equals 1. When ant leaves (n', k'), the corresponding value in the matrix $\mathbf{P}$ is set to zero.

Ants communicate with each other via a crucial concept of pheromone deposition and evaporation. Initially, the elements of
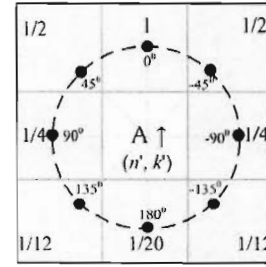

Fig. 1. Agent oriented upwards with $P(n', k') = 1$ and corresponding values of $d(\Theta_{(n', k')}(n, k))$ for possible discrete directions – angles (dots). The permissible ant's movement range $\mathbf{Q}(n', k')$ is shaded.

the pheromone map at the positions occupied by ants are set to a small positive constant $\Phi_0 < 1$:

$$\Phi^{(0)}(n, k) = \begin{cases} \Phi_0, & (n, k) = (n_0, k_0) \\ 0, & (n, k) \neq (n_0, k_0). \end{cases} \quad (9)$$

The ant movement and pheromone deposition mechanisms are crucial for the control of mass behavior of artificial ants [45–56].

3.2.2. Ant transition rule

After the initialization, in each algorithm iteration ants move according to certain rules. Let us observe one ant's transition from cell (n', k') to a neighboring cell $(n, k) \in \mathbf{Q}(n', k')$. Every agent can move only to adjacent cells (positions), depositing a certain level of pheromone on that cell. One cell can be occupied by only one ant, and ants do not move if they are completely surrounded by other ants. An iteration ends when all the ants move to adjacent cells (except the totally surrounded ones).

An ant chooses a cell to move to based on two criteria: the pheromone level in adjacent cells [46,50] and its current orientation [53–55]. Since a discrete rectangular grid is considered, an ant located at the position (n', k') in the l-th iteration can move to one of eight adjacent cells (n, k) belonging to the set $\mathbf{Q}(n', k')$. An ant at the position (n', k') is shown in Fig. 1, where the corresponding neighboring cells $(n, k) \in \mathbf{Q}(n', k')$ are shaded.

An ant at the original position (n', k') has a certain orientation $P(n', k')$ according to (8), that is, the orientation of the point (n', k') towards the adjacent cells $(n, k) \in \mathbf{Q}(n', k')$ as depicted in Fig. 1. Values of $P(n', k')$ are fixed, $P(n', k') \in \{1, 2, ..., 8\}$, where $P(n', k') = 1$ denotes an upward oriented ant, while other numbers correspond to the orientations towards the remaining 7 cells in counterclockwise direction. The orientation has an important role in the choice of the targeting cell $(n, k) \in \mathbf{Q}(n', k')$. The angles between an upwards oriented ant at (n', k') and the adjacent cells positions are illustrated in Fig. 1. As in [54], a discrete variable $\Theta_1(n, k) \in \{0°, \pm45°, \pm90°, \pm135°, 180°\}$ is introduced, depending only on the position of the cell $(n, k) \in \mathbf{Q}(n', k')$ relative to the cell (n', k') corresponding to the ant's orientation shown in Fig. 1. The corresponding angles $\Theta_{(n', k')}(n, k)$ for other possible ant's orientations can be calculated as:

$$\Theta_{(n', k')}(n, k) = \Theta_1(n, k) - [P(n', k') - 1] \cdot 45 \quad (10)$$

where $\Theta_{(n', k')}(n, k)$ represents the angle between the current ant's orientation and the adjacent cell.

Depending on the application, different heuristic functions $d_{(n', k')}(n, k)$ used for defining the probability (7) have been proposed [45–59]. In this paper, we use the heuristic function $d(\Theta_{(n', k')}(n, k))$ as defined in [49,53–55], i.e. the function of angles

$\Theta_{(n',k')}(n,k)$ calculated as:

$$d\left(\Theta_{(n',k')}(n,k)\right) = \begin{cases} 1, & \Theta_{(n',k')}(n,k) = 0 \\ 1/2, & \Theta_{(n',k')}(n,k) = \pm 45^\circ \\ 1/4, & \Theta_{(n',k')}(n,k) = \pm 90^\circ \\ 1/12, & \Theta_{(n',k')}(n,k) = \pm 135^\circ \\ 1/20, & \Theta_{(n',k')}(n,k) = 180^\circ, \end{cases} \quad (11)$$

for $(n,k) \in \mathbf{Q}(n',k')$.

Heuristic function $d(\Theta_{(n',k')}(n,k))$ in (11) is defined so that agents most likely preserve the orientation from the previous iteration, thus $d(\Theta_{(n',k')}(n,k))$ has the largest value for angle $\Theta(n,k) = 0^\circ$. With the increase of the angle, the value of $d(\Theta_{(n',k')}(n,k))$ gradually decreases, also decreasing the probability that ant moves to these directions, as it can be seen in (7). In this way, very sharp turns are much less likely than turns through smaller angles [53–55], which is also in accordance with the IF estimation problem [6–9,25].

The second parameter that influences the movement of an ant, and which can be used for the ant colony behavior control, is dependence on the pheromone level $\Phi(n,k)$, given by a function defined as [46–54]:

$$g(\Phi(n,k)) = \left(1 + \frac{\Phi(n,k)}{1 + \delta \Phi(n,k)}\right)^\beta. \quad (12)$$

A large value of β results in ants heavily attracted by the pheromone level and vice versa. The parameter δ controls the ant's sensitivity to the pheromone concentration [53–56]. With the introduced function $g(\Phi(n,k))$, the probability (7) is now given by [46–49]:

$$P^{(l)}_{(n',k')}(n,k)$$
$$= \begin{cases} \frac{g(\Phi^{(l)}(n,k))d(\Theta_{(n',k')}(n,k))}{\sum_{(n,k) \in \mathbf{Q}(n',k')} g(\Phi^{(l)}(n,k))d(\Theta_{(n',k')}(n,k))}, & (n,k) \in \mathbf{Q}(n',k') \\ 0, & \text{otherwise}. \end{cases} \quad (13)$$

3.2.3. Pheromone update

When an ant moves to a neighboring cell $(n,k) \in \mathbf{Q}(n',k')$, the pheromone level is updated according to [46–49]:

$$\Phi^{(l+1)}(n,k) = \Phi^{(l)}(n,k) + \mu \nabla(n,k) + \xi. \quad (14)$$

with ξ being a small constant level of pheromone, $\nabla(n,k)$ is the gradient, i.e. a dynamic pheromone value which is added to new position (n,k) visited by the agent and μ is a positive step that controls the pheromone amount added by $\nabla(n,k)$. The fixed pheromone amount ξ is added in order to ensure that, after the pheromone evaporation at the end of the current iteration l by value ξ, all visited positions have the pheromone level at least equal to the gradient $\nabla(n,k)$ value [53–55]. For the IF estimation, the gradient $\nabla(n,k)$ is defined taking into account the specific nature of the considered problem. It is analyzed in the following subsection.

At the end of each iteration a constant pheromone amount ξ evaporates from all cells, as it is discussed in detail in [45–56], i.e. for each (n,k) the pheromone map is updated according to

$$\Phi^{(l+1)}(n,k) = \begin{cases} \Phi^{(l)}(n,k) - \xi, & \Phi^{(l)}(n,k) \geq \xi \\ 0. & \Phi^{(l)}(n,k) < \xi. \end{cases} \quad (15)$$

If the new pheromone level is negative, then it is set to zero.

The previously described algorithm is summarized in Appendix A.

3.3. Pheromone deposition gradient in the IF estimation

For the definition of gradient, the nature of the considered problem, i.e., the IF estimation, has to be taken into account. The IF
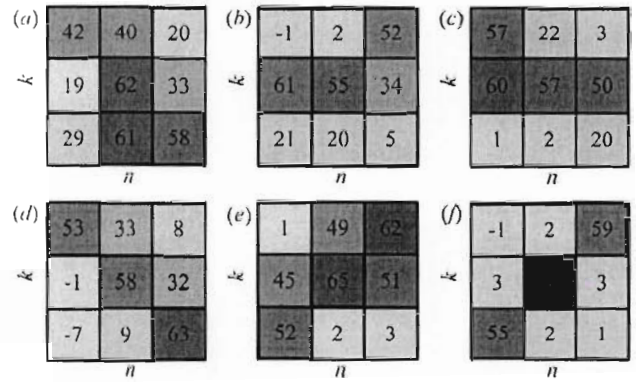

Fig. 2. Illustration of the 3 × 3 neighborhoods of (n,k), which correspond to auto-term positions. The WD values have been rounded to the nearest integer for illustration clarity.

Table 1
Values of functions (17), (17) and (18) for 3 × 3 matrices shown in Fig. 2.

	(a)	(b)	(c)	(d)	(e)	(f)
$\Psi(n,k)$	60.310	21.021	25.842	17.167	48.840	8911
$\Xi(n,k)$	40.44	27.67	30.22	27.56	36.67	20.78
$\Lambda(n,k)$	151.032	114.070	171.000	193.662	209.560	204.435

Table 2
Values of functions (17), (17) and (18) for 3 × 3 matrices shown in Fig. 3.

	(a)	(b)	(c)	(d)	(e)	(f)
$\Psi(n,k)$	4344.9	−29.63	−10,920	0	63.33	3422.2
$\Xi(n,k)$	7.11	−0.78	5	13.44	−11.33	23
$\Lambda(n,k)$	10,488	660	29,140	2440	17,496	12,400

estimate should be extracted from the pheromone map, obtained after the algorithm has finished. To this aim, we use the fact that although the WD maxima in a high noise environment are likely to be dislocated from the true IF of the signal [7], at each time instant n one of the largest WD values will still be positioned at the IF [7,9,25]. Dislocation is a consequence of high-level noise peaks which surpass the WD values inside the auto-terms. On the other side, it is known that IF variation between two consecutive time instants should not be large, which is the most common case in real applications [8]. Taking into account these two facts, we introduce a new gradient $\nabla(n,k)$ form, which defines the pheromone gradient in (14)

$$\nabla(n,k) = \Psi(n,k)\Xi(n,k)\Lambda(n,k). \quad (16)$$

We define the function $\Psi(n,k)$ as

$$\Psi(n,k) = \frac{1}{27} \prod_{i=-1}^{1} \sum_{j=-1}^{1} WD(n+j,k+i), \quad (17)$$

i.e. as the product of the mean values of columns of the 3 × 3 adjacency in the WD matrix, centered at point (n,k). Namely, if an auto-term appears within the observed 3 × 3 adjacency of the point (n,k) then a large value of $\Psi(n,k)$ is expected. It is expected that an auto-term appears in all three columns of the 3 × 3 adjacency, as shown in Fig. 2(a)–(f). On the other side, if a 3 × 3 adjacency contains only noise, then $\Psi(n,k)$ has a small value, since high-level noisy WD points are usually isolated in the TF plane. Hence, it is expected that only few high-level noisy points exist in the local neighborhood of (n,k), whereas other points are of lower level (Fig. 3(a)–(f)). The function $\Psi(n,k)$, whose values are presented in Tables 1 and 2, has high values for the matrices from Fig. 2, containing the WD auto-terms, and lower values for the matrices in Fig. 3, which represents 3 × 3 neighborhoods of point
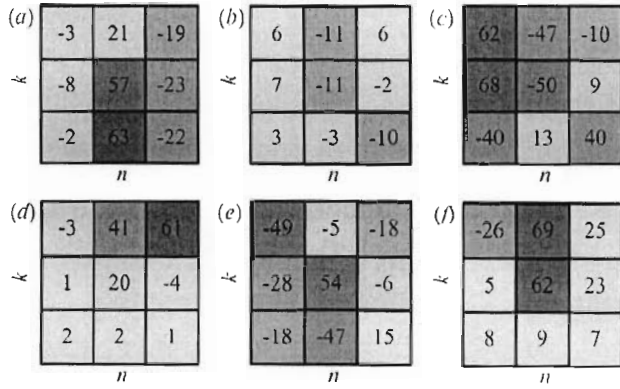
Fig. 3. Illustration of the 3×3 neighborhoods of (n, k), which correspond to non-IF positions (noise). The WD values have been rounded to the nearest integer for illustration clarity.

Table 3
Gradient values (16) calculated for matrices shown in Fig. 2 (second row) and Fig. 3 (third row). Values are scaled by 10^{10} for better presentation.

	(a)	(b)	(c)	(d)	(e)	(f)
$\nabla_1(n, k)/10^{10}$	36.84	6.63	13.36	9.16	37.53	3.78
$\nabla_2(n, k)/10^{10}$	0.0324	0	−0.1591	0	−0.0013	0.0976

(n, k) placed outside the auto-terms, containing noise only. In this way, $\Psi(n, k)$ emphasizes the auto-terms presence in the gradient calculation (16).

We define $\Xi(n, k)$ as the mean value of the observed 3×3 adjacency, i.e.

$$\Xi(n, k) = \frac{1}{9} \sum_{i=-1}^{1} \sum_{j=-1}^{1} WD(n + j, k + i). \tag{18}$$

It is expected that $\Xi(n, k)$ has small values for noisy WD points (outside of the auto-terms), since high-level noise peaks are usually isolated [6–9]. On the other hand, due to the windowing effects in the WD calculation and the fact that only linear FM (LFM) signals are ideally concentrated in the WD, it is expected that if the local 3×3 adjacency centered at point (n, k) contains an auto-term, it will occupy three or more points in the neighborhood. If the signal is not ideally concentrated, even the whole observed 3×3 WD sub-matrix may be occupied by an auto-term, thus producing a large $\Xi(n, k)$ value. Therefore, the largest values of $\Xi(n, k)$ are expected to occur for auto-terms. Note that the WD values are Gaussian in nature, with non-zero mean within the auto-terms and zero mean outside the auto-terms [7].

Now consider again the matrices shown in Figs. 2 and 3. The corresponding values of $\Xi(n, k)$ are shown in Tables 1 and 2 (second rows). This function mainly produces higher values for the matrices from Fig. 2 than those from Fig. 3. The exception is the matrix shown in Fig. 3(f), whose $\Xi(n, k)$ value exceeds that of the matrix shown in Fig. 2(f). This problem is solved by incorporating the function $\Lambda(n, k)$ in (16), which is shown to output significantly higher values for the matrix in Fig. 2(f) than for that in Fig. 3(f). The function $\Lambda(n, k)$ takes into account the fact that the IF has small variations at consecutive time instants n, also in the 3×3 neighborhood of the point $WD(n, k)$:

$$\Lambda(n, k) = \max\left(\left[\prod_{i=-1}^{1} WD(n + i, k + i) \quad \prod_{i=-1}^{1} WD(n + i, k - i)\right.\right.$$
$$\prod_{i=-1}^{1} WD(n + i, k - 1) \quad \prod_{i=-1}^{1} WD(n + i, k)$$
$$\left.\left.\prod_{i=-1}^{1} WD(n + i, k + 1)\right]\right). \tag{19}$$

The first term is the product of the elements on the main diagonal of a 3×3 neighborhood of the point $WD(n, k)$, whereas the second term is the element product on the secondary diagonal

of this neighborhood; third, fourth and fifth elements are element products in the first, second and third rows of the neighborhood, respectively. The heuristic function (19) takes the maximal value of the vector consisted of these products.

If the WD values corresponding to the IF are within the observed 3×3 neighborhood of the point $WD(n, k)$, at least one of the products in (19) is expected to have a large value. On the other side, one or two isolated WD points with a large value corresponding to the noise will probably produce smaller $\Lambda(n, k)$ values.

The values of $\Lambda(n, k)$, calculated for 3×3 neighborhoods of the point (n, k) given in Fig. 2 and Fig. 3, are shown in Tables 1 and 2 (third rows). Clearly, this function gives preferences to matrices with large values distributed along rows or diagonals of the matrix. These shapes most likely correspond to the IF points (auto-terms).

Finally, the heuristic functions product in (16) results in a large value for the neighborhood of auto-terms. Table 3 summarizes the gradient values for the matrices in Fig. 2, denoted as $\nabla_1(n, k)$, and the matrices in Fig. 3, denoted as $\nabla_2(n, k)$. As expected, $\nabla_1(n, k)$ exceeds $\nabla_2(n, k)$ to a great extent in all considered cases.

The summary of the proposed algorithm for the pheromone map generation is given in Appendix B.

3.4. Population size variation

In the literature, methods for the variation of agents population based on both aging/dying and reproduction process, i.e. positive and negative feedback are presented [49,53–55]. Our adaptation consists of the elimination of the agents which move through undesirable positions, i.e. points where the pheromone level is sufficiently low during a certain number of iterations. In this way, ants which are too far from the TF points corresponding to the auto-terms are eliminated.

The IF estimation is performed using the pheromone map Φ. Since the pheromone deposition control is established through the gradient (16) in (14) for each ant independently and locally, our aim is to find a method for additional control of the ants number, based on the pheromone amount which they have left during the previous iterations. In the considered framework, it is important to eliminate as many undesirable agents as possible, since their pheromone trace usually causes large estimation errors. Namely, the idea is to give an advantage to ants that often move to cells corresponding to the auto-terms, depositing more pheromone in these cells. This can be measured with the gradient $\nabla(n, k)$. The population reduction concepts are implemented as presented below.

At the beginning of the algorithm described in Appendix A, in Step 0, a fixed level of energy $1 + \alpha$ is assigned to every ant, stored in auxiliary matrix **E**:

$$E^{(0)}(n, k) = \begin{cases} 1 + \alpha, & (n, k) = (n_0, k_0) \\ 0, & (n, k) \neq (n_0, k_0). \end{cases} \tag{20}$$

The parameter $\alpha < 1$ is a small positive constant. The initial α value gives agents a chance to survive during at least two following iterations [49,53–55].

Let us observe again one ant's transition from cell (n', k') to a neighboring cell $(n, k) \in Q(n', k')$. In Appendix A, Step 2, the energy corresponding to new position determined by the probability

Table 4
Parameter values used in the proposed approach. The Range row represents the ranges of tested values of some parameters that produced satisfactory results in numerical examples.

Parameter	μ	γ	ξ	α	Φ_0	β	δ
Value	$2/L^4$	70%	0.07	0.7	0.2	3.5	0.2
Range	$\mu \geq 1/L^4$	$50\% \leq \gamma \leq 90\%$	$0 < \xi < 0.1$	$0 < \alpha < 1$	$0.1 \leq \Phi_0 \leq 0.2$		

$\cdots$ is updated according to [49–54]:

$$E^{(l+1)}(n, k) = E^{(l)}(n', k') + \alpha \mu \nabla(n, k).\tag{21}$$

where the gradient $\nabla(n, k)$ calculated in (16) is used. Then, the energy matrix $\mathbf{E}$ is updated by setting the element corresponding to the previous ant position (n', k') to zero, i.e.:

$$E^{(l+1)}(n', k') = 0.\tag{22}$$

In Step 3, the energy level of all ants kept in the matrix $\mathbf{E}$ is decreased by α, for every

$(n, k) \in [0, N) \times [-K/2, K/2)$

$$E^{(l+1)}(n, k) = E^{(l)}(n, k) - \alpha.\tag{23}$$

In this step, all ants at positions with energy $E(n, k) \leq 0$ are eliminated by removing the corresponding elements of the matrix $\mathbf{P}$, for each $(n, k) \in [0, N) \times [-K/2, K/2)$:

$$P^{(l+1)}(n, k) = 0 \text{ if } E^{(l+1)}(n, k) < 0.\tag{24}$$

Since the population of agents is decreased during the iterations when the IF is detectable, the stopping criterion of the algorithm can be the minimal permitted number of agents, obtained from the matrix $\mathbf{P}$ as the number of non-zero elements. In the case of ideally concentrated TF representation of a non-noisy monocomponent signal, the IF will have exactly N non-zero values, i.e. one value for each time instant n, if it is defined for every N. However, if we take into account that in a high noise environment the algorithm can remove a certain number of auto-term points, as well as the fact that, in general, signals are not ideally concentrated, the algorithm can be stopped when the number of agents falls below 80–100% of N.

3.5. Parameter discussion

Determination of the optimal ACO algorithm setup is a complex task [44–59], especially in applications such as image processing, due to a large number of parameters [49–56]. The same holds for the application of ACO in the IF estimation problem. It is also important to emphasize that the parameter setting of ACO could not be mathematically derived [50]. Hence, in this paper, as it is usual in ACO applications [44–59], a part of suitable parameters is determined empirically, whereas the certain number of them is set based on detailed analysis and numerical results in the literature [49–56], as it is presented in the sequel. In Table 4, the set of parameters used to obtain numerical results in the paper is given. In Section 4.4 some numerical results regarding the parameter selection are presented.

1. Step μ represents one of the most important parameters in the pheromone update (14) and energy update (21). In the proposed algorithm, the μ value is heuristically determined. It is in fact a normalization factor for the proposed gradient (16), and thus it has to be set in accordance with the gradient structure. If the step is too small, the influence of $\nabla(n, k)$ is not strong enough to dictate the pheromone deposition on the auto-term points.
   Let us denote with c the maximal value of WD(n, k) 3×3 neighborhood, when it belongs to an auto-term. If we analyze the functions (17), (18) and (19), it follows that $\Psi(n, k) \sim c^3$,

$\Xi(n, k) \sim c$ and $\Lambda(n, k) \sim c^3$. Therefore, when the gradient "detects" an auto-term, it is proportional to c^7. Generally, c is not constant due to amplitude variations and noise influence. In addition, it is generally smaller than the global TF maximum

$$L = \max_{(n,k)} \{WD(n, k)\}, \quad (n, k) \in [0, N) \times [-K/2, K/2).\tag{25}$$

Hence, we propose to choose the step μ in (14) and (21), used for scaling the gradient $\nabla(n, k)$, as follows

$$\mu \geq \frac{1}{L^4}.\tag{26}$$

Note that although the same fixed value of the step $\mu = 2/L^4$ is used for all presented numerical results, a more suitable choice of this parameter may lead to better estimation results of the proposed approach. The condition (26) is experimentally evaluated as shown in Section 4.4.

2. The next important parameter is the initial population size, defined as the percentage γ of the product $N \times K$, where N and K are the TF grid dimensions. If the initial population is set too small, there is a risk that agents will be eliminated from the TF plane before they even approach the auto-terms. Moreover, there is a risk that, due to the auto-terms corruption in a high noise environment, only a small number of ants will reach the auto-terms, deposit pheromone according to (14) and consequently attract other ants. In addition, the population control using (21) would not be efficient. In this case, it is reasonable to choose a population size which is not too low. We have analyzed the performance of the proposed method with various values of γ and it has been shown (Section 4.4) that $0.5 \leq \gamma \leq 0.9$ cannot endanger the algorithm output. Thus, in this paper $\gamma = 0.7$ is used for all presented results.

3. The constant ξ is known as the pheromone evaporation rate, which is used to avoid limitless deposition of the pheromone trails and restrain the ants from choosing the same cells [50]. It is also the part of the pheromone update rule (14), ensuring that all positions visited by ants have the pheromone level at least proportional to the normalized gradient after the evaporation. Our numerical results indicate that $\xi < 0.1$ should be used.
   The pheromone constant Φ_0 used for the initialization of the pheromone matrix in (9) can be set such that $\Phi_0 \leq 0.2$. In this way, during the first few iterations pheromone level still remains positive in these cells after the evaporation. We have tested many proposed values of this parameter [49–54] with different signals and different SNRs, and our experimental results have shown that in the range of values presented in the literature $0.1 \leq \Phi_0 \leq 2$ algorithm is quite robust to the selection of this parameter at lower SNRs, whereas it should have smaller values $\Phi_0 \leq 0.2$ at higher SNR values.
   We have found suitable to use values $\xi = 0.07$ and $\Phi_0 = 0.2$ obtained empirically and confirmed numerically as presented in the literature [49,53,54].

4. Parameter α is used for the energy update (21) and for the energy decrease in (23), similarly as the parameter ξ is used in the pheromone update process. Parameter α is originally introduced in [49,53,54]. However, unlike the pheromone that is related to a position in the pheromone map, the energy is associated with the observed ant. According to (21), when an ant moves, the energy matrix is updated in a way that the energy

in new agent's position (n, k) is calculated based on the energy in previous agent's position (n', k'). This fact explains the need for new parameter, different from ξ. This parameter dictates the rate of energy decrease, and the dynamics of ant dying process. A too large value leads to the elimination of all agents. However, note that in order to prevent this, we have proposed that the algorithm terminates not only when the maximal allowed number of iterations I_{max} is reached, but also when the number of agents falls below 100% of N, to ensure that a reasonable number of agents remain to perform the estimation. Since the gradient normalized with the parameter μ is used in (21), we experimentally determined value of the parameter as $\alpha = 0.7$. This value is used in all presented numerical results, and it has shown a robustness to IF form, SNR level or TF plane dimensions N and K, as it is shown in Section 4.4.

5. The last parameters are the design parameters β and δ. The parameter β is well discussed in wide ACO literature [45–59]. It controls the influence of the pheromone on the transition of ants in (13), whereas δ controls the ant's sensitivity to the pheromone concentration [53–56]. We use the values of these parameters $\beta = 3.5$, $\delta = 0.2$ as proposed in [53–56].

3.6. The IF estimation from the pheromone map

The pheromone map Φ can be understood as a new TF representation robust to high noise influence. Thus, the IF estimation problem can be formulated as:

$$\hat{k} = \arg\max_k \Phi(n, k). \tag{27}$$

Median filter could be applied on the IF estimation to connect discontinuities (due to dying of agents) in the IF estimation provided by the pheromone map [14]. Since the variable population approach is used to remove as many TF outliers as possible, the IF estimation is conducted based on the kept points. In a high noise environment, several percents of the TF points corresponding to the auto-terms is expected to be removed due to high noise corruption, and thus, interpolation techniques such as cubic interpolation [60] could also be used for the proper IF estimation in regions with missing auto-term values. Instants with eliminated points are easy to detect, since the estimation (27) is equal to zero at these instants. When the ending points are missing, their values should be set to the nearest non-zero values, or extrapolation can be used.

4. Numerical study and examples

The presented theoretical concepts and the proposed estimation procedure's performance are verified through a set of numerical examples. The WD is calculated using the Hanning window.

We set $I_{max} = 100$ and all parameters as in Table 4. Median filter with length 3 is applied in the IF estimation (27) in all examples.

Note also that the true IF is obtained from the corresponding non-noisy WD, or other considered TFR. In this way, other error sources, primarily the estimation bias due to IF nonlinearity, are not taken into account. Since our aim is to improve the estimation robustness in high noise, and not to deal with high-accuracy IF estimation, the true IF is adopted in this manner [6–8]. The considered synthetic signals have a unity amplitude. Slow variations of the amplitude do not affect the algorithm's accuracy, i.e., these variations affect the accuracy as the overall SNR affects the accuracy of all algorithms analyzed in this section. The considered real signal has a time-varying amplitude.

4.1. Monocomponent signals

The influence of complex zero-mean AWGN $\varepsilon(n)$ with variance σ^2 and with i.i.d. real and imaginary parts is analyzed in all exam-
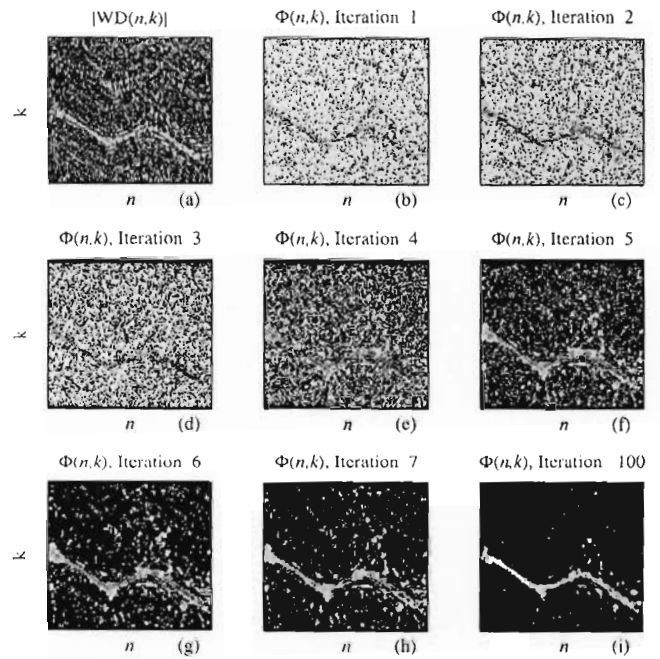

Fig. 4. (a) WD of an FM signal from Example 1; (b)–(i) pheromone map at the end of iterations 1–7 and 100 (last iteration).

ples. The SNR of the mono-component FM signal (1) is defined as:

$$SNR[dB] = 10\log_{10}\left(\frac{A^2}{\sigma^2}\right). \tag{28}$$

Example 1. Consider an FM signal

$$x(n) = \exp\left(j\pi \sin\left(\frac{3.5\pi(n+64)}{128}\right) - j35\left(\frac{n+64}{128}\right)^2\right) + \varepsilon(n) \tag{29}$$

of length $N_s = 256$. The WD is calculated for the middle $N = 128$ points, the signal values are defined at instants $n \in [-N/2, 3N/2)$, and the window length is $K = 128$. The signal is corrupted with noise with SNR $= -2$ dB The WD of the signal, as the starting point of the proposed algorithm, is shown in Fig. 4(a). The pheromone maps observed after first 7 iterations, and after the 100-th iteration, are shown in Fig. 4(b)–(i). It can be observed that after the first iteration a large number of ants have deposited the pheromone at many TF points. However, due to the gradient influence in (14), the pheromone has already started to concentrate at the auto-terms, as can be seen from Fig. 4(b).

At the end of iteration 3 (Fig. 4(d)), the number of ants is reduced at points outside the auto-term, due to the energy update mechanism (21)–(24), and small gradient (16) values, used in (21).

Fig. 5 presents the true IF (circles), the IF estimation obtained using the proposed approach (red solid line), the WD-maxima based estimator (dotted line) and the VA-based estimator (blue solid line) [8].

Example 2. Here, we consider again a noisy FM signal with polyharmonic frequency modulation

$$x(n) = \exp\left(j2\sin\left(\frac{13\pi(n+32)}{256}\right) + j3\sin\left(\frac{5\pi(n+32)}{256}\right)\right) + \varepsilon(n) \tag{30}$$
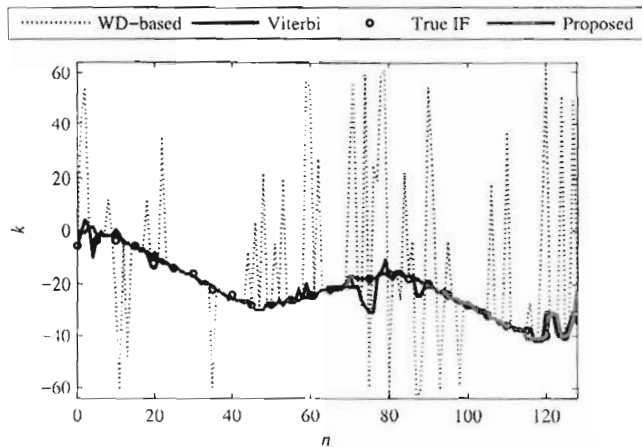
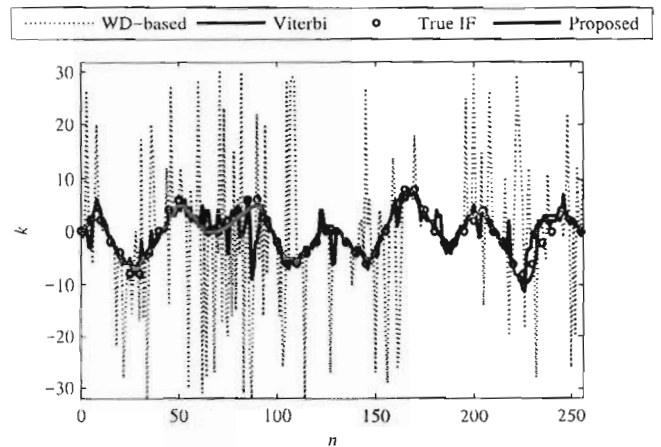Fig. 5. IF estimation for the signal from Example 1.

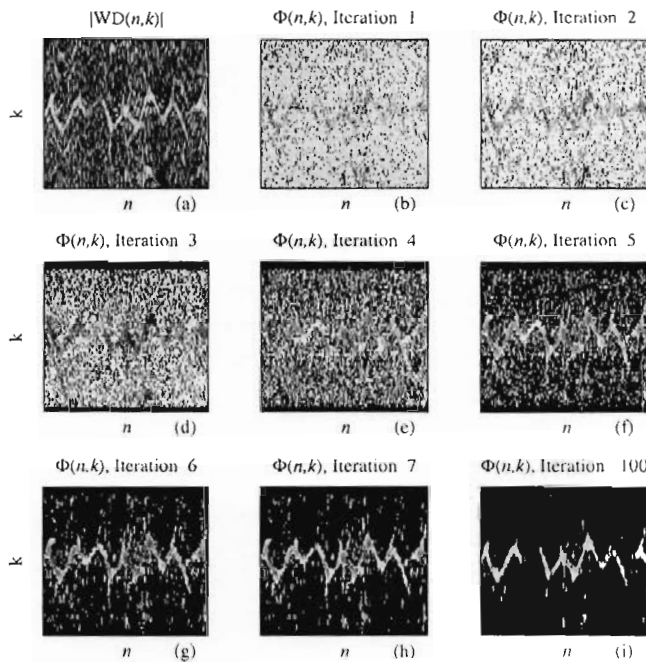Fig. 7. IF estimation for the signal from Example 2.

Fig. 6. (a) WD of a FM signal with poly-harmonic modulation from Example 2; (b)-(i) pheromone map at the end of iterations 1-7 and 100 (last iteration).

of length $N_s = 320$, defined at time instants $n \in [-N/2, 3N/2)$, where the WD is calculated for the middle $N = 256$ points. The WD window length is $K = 64$ and SNR = −2 dB

The pheromone map changes over iterations are shown in Fig. 6(b)–(i). Fig. 7 depicts the true IF, as well as the IF estimations obtained using the proposed method, the WD-maxima approach and VA-based estimator. The proposed approach significantly outperforms the other methods.

Observe the pheromone map (TF representation) after the last iteration (Fig. 6(i)). It can be noticed that some points corresponding to the IF are missing. However, they are easily detectable and, after the cubic interpolation [60], the IF is reconstructed based on the existing neighboring values.

4.2. Multicomponent signals

The carried out numerical experiments show that the proposed method significantly suppresses WD inner interferences. In order

to further illustrate this property, as well as the property of the proposed method to suppress cross-terms, consider a multicomponent signal comprised of two sinusoidally FM signals:

$$x(n) = \exp\left(-j2\pi \sin\left(\frac{-3\pi n}{128}\right) + j\frac{100n}{128}\right)$$
$$+ \exp\left(j2\pi \cos\left(\frac{2\pi n}{128}\right) + j\frac{30\pi n}{128}\right) + \varepsilon(n). \tag{31}$$

In the non-noisy signal case, the cross terms as well as inner interferences are suppressed by the proposed algorithm (Fig. 8, first two plots). It can be explained by the similarity of these disturbances with noisy TF regions, which are detected and suppressed by the proposed pheromone deposition gradient. When the signal is corrupted with noise, the algorithm performs similarly to the non-noisy case. The second two plots in Fig. 8 show the WD and pheromone map of a noisy signal with SNR = −1 dB

The IF estimation of multicomponent signals can be performed using the obtained pheromone map and classical estimation approaches [5,8,25]. The approach based on the elimination of the strongest components cannot be successfully applied here, since the pheromone level is not dependent on components amplitudes, and this information is lost in the pheromone map. Hence, the estimation can be performed by identifying the regions of components and estimating IF of each region separately [25].

4.3. Statistical analysis

For all following experiments, we have calculated the MSE versus variable SNR (from −10 to 5 dB in Experiment 1 below, and from −10 to 13 dB for Experiments 2 and 3 below, with an 1 dB step). The MSE is defined as

$$MSE = E[|\hat{k}(n) - k_T(n)|^2]. \tag{32}$$

where $\hat{k}(n)$ represents the estimated IF and $k_T(n)$ the true IF frequency index, i.e. position of the WD frequency bin closest to the true frequency for a given n. The MSE is calculated over 100 iterations. We consider the IF estimation using the WD-maxima based approach, the proposed ACO-based algorithm and the VA-based estimator [8]. The IF variations are measured using the instantaneous chirp rate, that is, the second derivative of the signal (1):

$$\mathcal{M}(t) = \phi''(t). \tag{33}$$

For all considered signals, we calculate (33) for their continuous-time form, and then take the maximal absolute value of the discretized instantaneous chirp rate in the considered interval of discrete-time index n for which the WD was calculated.
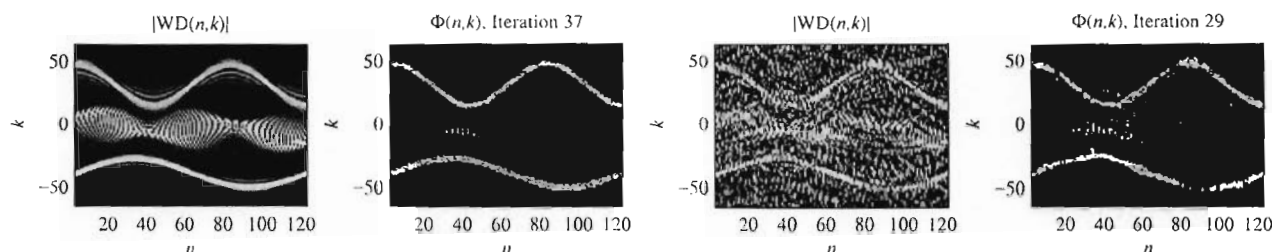
Fig. 8. Suppression of inner interferences and cross-terms reduction in multi-component signals. Noise-free multicomponent signal (first two subplots); Noisy multicomponent signal (second two subplots).
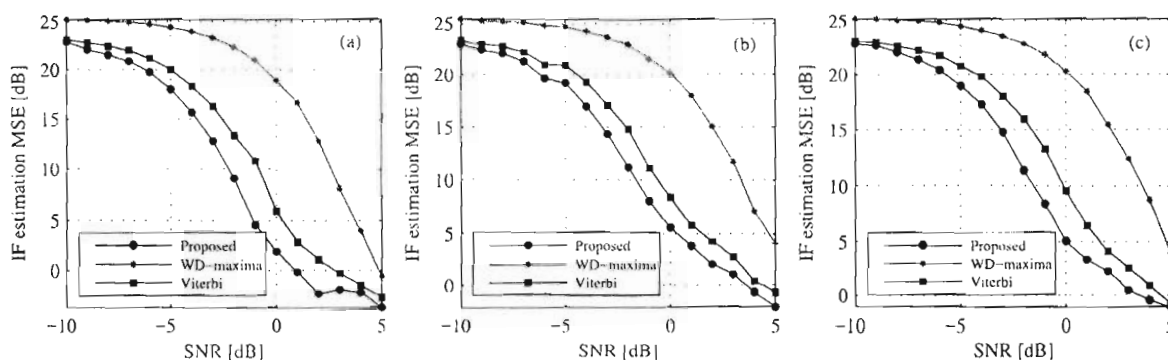

Fig. 9. IF estimation MSE for signals (34) in Experiment 1, using: WD-maxima based estimation (red stars), proposed approach (blue circles) and VA-based approach (black squares). For interpretation of the references to colour in this figure legend, the reader is referred to the web version of this article.

Table 5
Parameter values used in (34) to define three signals from Experiment 1.

	a	b	c	d	Measure of IF variations based on (33)
Signal 1	1	15	2	5	20.6981
Signal 2	2	13	3	5	31.7746
Signal 3	1	20	1	6	33.5403

Table 6
Parameter values used in (35) to define four signals from Experiment 2.

	a	b	c	d	e	f	Measure of IF variations based on (33)
Signal 1	4	27	3	11	10	9	71.5671
Signal 2	3	35	5	10	5	10	90.1180
Signal 3	5	32	10	3	10	3	102.0618
Signal 4	4	41	3	10	5	10	143.2051

Experiment 1. Let us consider three signals of the form

$$x(n) = \exp\left(ja\sin\left(\frac{b\pi(n+32)}{256} \right) + jc\sin\left(\frac{d\pi(n+32)}{256} \right) \right) + \varepsilon(n).$$ (34)

The signals are of length $N_s = 320$, defined at $n \in [-N/2, 3N/2)$, where the WD is calculated for middle $N = 256$ points. The WD window length is $K = 64$. Parameters defining the three considered signals are given in Table 5.

We consider the IF estimation using the WD-maxima based approach, the proposed ACO-based algorithm and the VA-based estimator [8]. The obtained MSEs are shown in Fig. 9 (left, middle, right) for signals 1–3 defined as (34) with parameters given in Table 5, respectively. Signals with fast IF variations have been selected in order to confirm good performance of the proposed approach in such scenarios.

Due to the distributed nature of the optimization, the proposed approach is robust to the IF's shape, i.e. to the IF's non-linearity. Observing the results in Fig. 9, we conclude that by slightly increasing the IF variations, similar improvement level of the proposed method over VA-based and the standard WD-based estimator is obtained.

Experiment 2. Let us now consider four signals of the general form

$$s(n) = \exp\left(ja\sin\left(\frac{b\pi(n+32)}{2M} \right) + jc\cos\left(\frac{d\pi(n+32)}{2M} \right) \right.$$
$$\left. + jc\cos\left(\frac{f\pi(n+32)}{2M} \right) \right) + \varepsilon(n),$$ (35)

of length $N_s = 320$, defined at time instants $n \in [-N/2, 3N/2)$, where the WD is calculated for the middle $N = 256$ points. The WD window length is $K = 64$. This type of signal was used in [35] to evaluate the level of IF variations. The parameter values in (35) defining considered signals along with the IF variations measure values are given in Table 6.

The considered signals have different IF shapes, as well as different levels of IF variations. The estimation results are shown in Fig. 10(a)–(d), for signals 1–4 respectively. The proposed approach outperforms both the WD-maxima based and the VA estimator. It can be observed also that, in general, as the level of IF variations increases, the relative improvement of the proposed method compared with the VA estimator also becomes higher.

Experiment 3. With the aim to analyze the influence of the level of IF variations, we consider the signal of the form

$$x(n) = \exp\left(\frac{j30}{a}\sin\left(\frac{a\pi(n+16)}{M} \right) \right) + \varepsilon(n)$$ (36)
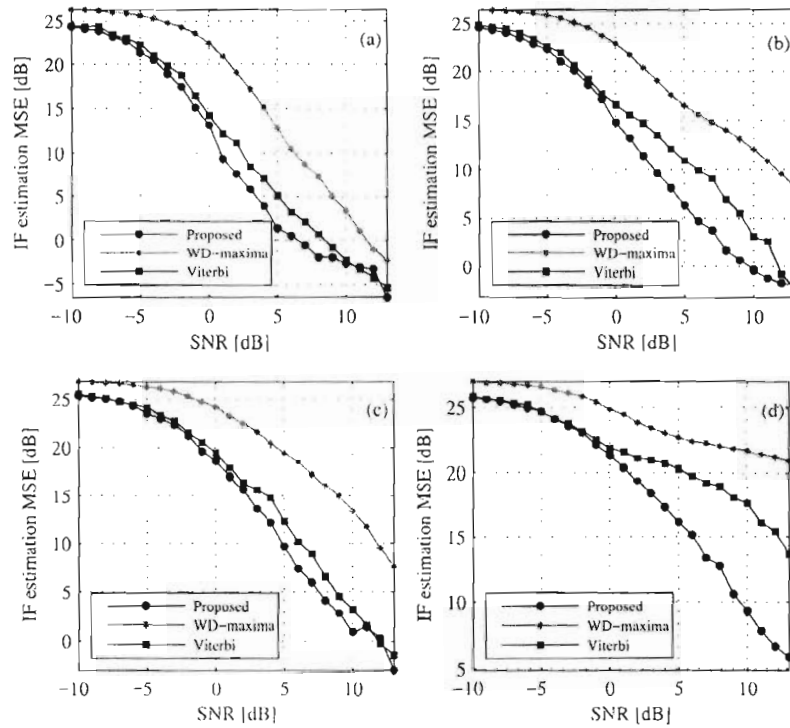
Fig. 10. IF estimation MSE for signals (35) from Experiment 2 using: WD-maxima based estimation (red stars), proposed approach (blue circles) and VA-based approach (black squares). For interpretation of the references to colour in this figure legend, the reader is referred to the web version of this article.

with length $N_s = 160$, defined at time instants $n \in [\ -N/2, 3N/2)$, where the WD is calculated for the middle $N = 128$ points. The WD window length is $K = 32$. It can be easily seen that the second derivative of the signal (36) is directly proportional to the constant a. Hence, by increasing a, the introduced measure of IF variations linearly increases. The parameter a is varied in range [13,21] with step 1. Observing the results in Fig. 11, we conclude that by increasing the IF variations, better performance of the proposed method over the VA-based and the standard WD-based estimator is obtained. Note that the WD-based IF estimation can be affected by fast IF variations even in noiseless case, which in turn can compromise our "True IF" estimation. However, we have kept the value of a within the range that ensures a meaningful "True IF" estimation. In this paper, the estimation bias due to IF nonlinearity is not taken into account since our aim is to improve the estimation robustness in high noise, and not to deal with bias removal in the WD-based IF estimation [6–8].

4.4. Numerical study of parameters

The parameter setup has been determined based on a large number of statistical tests as well as on the results presented in the literature [49–56]. Some statistical results for parameter selection are presented next.

In our numerical analysis we have observed four noisy signals of the form

$$x(n) = \exp\left(j\frac{40}{a} \sin\left(\frac{a\pi (n + 16)}{256} \right) \right) + \varepsilon(n) \qquad (37)$$

with $a \in \{12, 15, 18, 21\}$, having a different level of IF variations, as discussed in Section 4.3. The signal length is $N_s = 160$, defined at time instants $n \in [-N/2 - K/2, N/2 + K/2)$, where the WD is calculated for middle $N = 128$ points. The WD window length is $K = 32$. Three different SNR values are considered: 50 dB, 3 dB, and 0 dB In every experiment, for each observed signal, each SNR level and

each parameter value, MSE (32) was calculated based on 100 independent realizations of noisy signals. The last set of parameters was tested on a signal with $a = 15$.

During the variations of each considered parameter, all remaining parameters were fixed to their values presented in Table 4 (first row).

The step μ was varied in a wide range, from 10^{-10} to 10^2, with each value 10 times higher than the previous. The results are shown in Fig. 12 (first row). The vertical line shows the value $\mu = 1/L^4$ used for each considered signal, with L defined in (25), indicating that the maximal WD value can be used to define the lower bound for the step. It can be observed that for each SNR value and each considered signal, the step satisfying (26) produces approximately the same MSE value. It can be also concluded that the estimation breakdown occurs only when a too small step is used.

The initial population size, defined as the percentage γ of the product $N \times K$, was varied from 10 to 100%. The results shown in Fig. 12 (second row) indicate that γ values greater than 50% and smaller than 90% guarantee the lowest MSE. The vertical line indicates the value of 70% used for the results presented in this paper.

The pheromone evaporation rate ξ was varied in a wide range, from 10^{-2} to 1 with the step 0.02 and from 1.5 to 5 with step 0.5. According to the obtained results shown in Fig. 12 (third row) best estimation results are obtained for $\xi < 0.1$. This is in accordance with the results presented in the literature [49,53,54], where the value ξ - 0.07 is suggested, which is also used in our numerical results (vertical line).

The energy update constant α was studied together with the stopping criterion of the algorithm, as these two parameters are closely related. Namely, we propose to stop the algorithm when the number of agents falls below 100% of N. Parameter α was varied from 0.1 to 2, whereas the stopping criterion was varied from 40% of N to 400% of N. From Fig. 12 (fourth row) we can observe that the algorithm is quite insensitive to the values of α in the
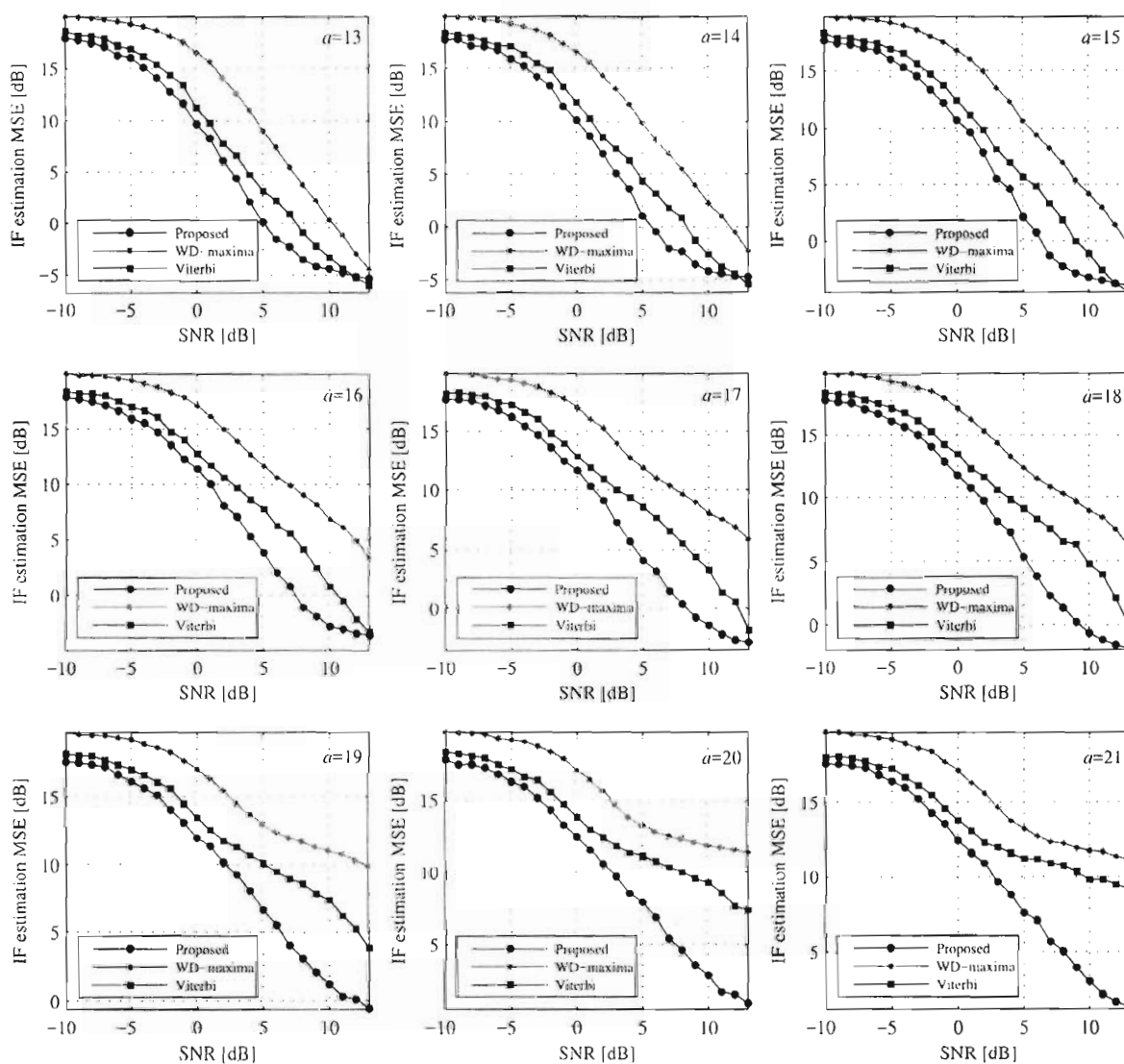
Fig. 11. IF estimation MSE for signal [36] with various a values using: WD-maxima based estimation (red stars), proposed ACO-based approach (blue circles) and VA-based approach (black squares). For interpretation of the references to colour in this figure legend, the reader is referred to the web version of this article.

considered range (except for small MSE increase for values larger than 0.5 at high SNR (please have in mind that MSE is not shown in dB)), as the gradient used for the energy update (21) is already scaled with step μ. In this paper, we use $\alpha = 0.7$.

4.5. Real signal

We consider a real-life signal to additionally verify the proposed method. A mono-component bat (*Myotis Daubentoni*) echolocation sonar signal $s(n)$ is observed. It was recorded with a sampling frequency of 230.4 kHz and an effective bandwidth of [8 kHz, 80 kHz] as described in [42]. Estimation of parameters of these signals, especially IF, is a well-known problem in TF signal analysis [41–43]. We added artificial additive Gaussian noise with SNR=−3 dB Since the observed signal is real-valued, the corresponding Hilbert transform is calculated prior to WD calculation, to avoid the appearance of the component at negative frequencies and cross-terms [6,9,28]. The WD of the original signal $s(t)$ and the corresponding noisy version, calculated with the Hanning window of length $K = 128$ are shown in Fig. 13(a) and (b) respectively. The estimation results are shown in Fig. 13(c). It can be observed that the WD-maxima

based estimator does not provide accurate results except in short ranges where the auto-term is very strong. The VA-based estimator provides accurate estimation results, with the exception of certain number of errors in the first half of the considered time interval where the signal strength is low. As it can be observed in Fig. 13(c), the IF estimate obtained by the proposed approach matches the true IF.

4.6. Applicability to other time-frequency representations

The presented algorithm can be applied to other TFRs having the property to concentrate the signal energy at or around the IF. The approach has been successfully applied to STFT, S-method [29], reassigned spectrogram [36,37], and wavelet transform [30,32,39]. TFRs are shown for clean and noisy signals, as well as the pheromone maps obtained in the noisy signal cases. Estimation results are shown for TFR maxima approach (in case of complex TFRs absolute value is exploited) and for the proposed technique and the VA applied on noisy TFRs.
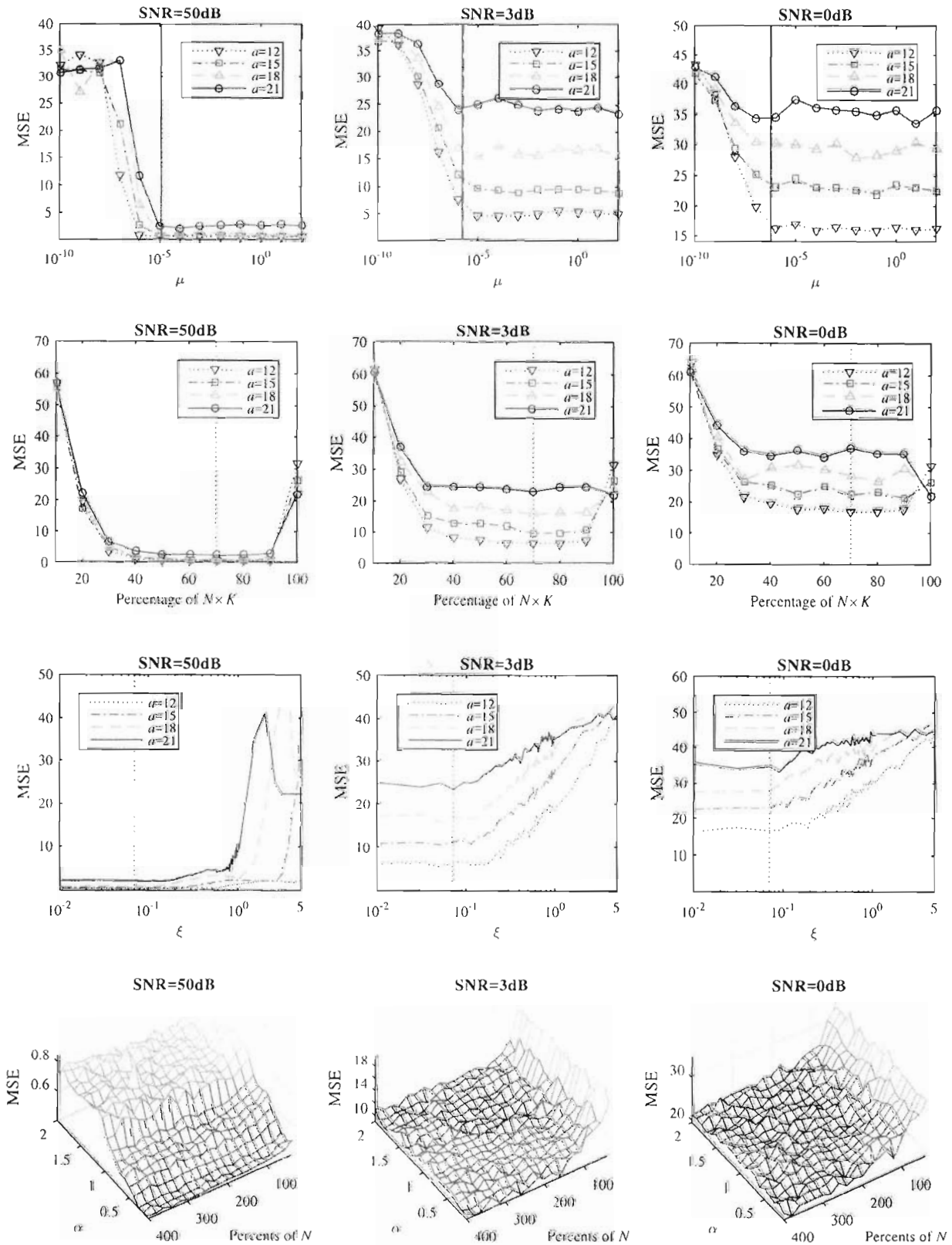
Fig. 12. MSE versus: step μ (first row), initial population size constant γ (second row), pheromone evaporation constant ξ (third row), energy update parameter α and the percent of N used as the stopping criterion (fourth row), shown for three considered SNR levels.
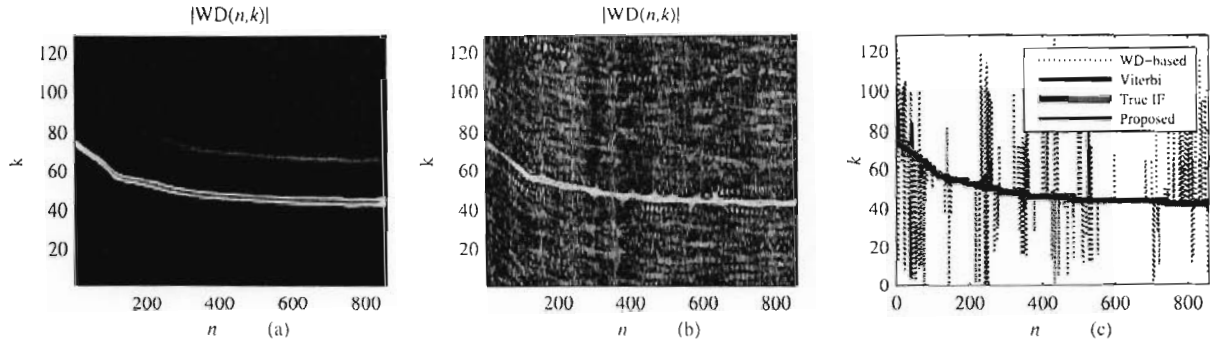
Fig. 13. IF estimation of a bat echolocation sonar signal: (a) WD of the original signal, (b) WD of the signal embedded in high noise and (c) IF estimation results.
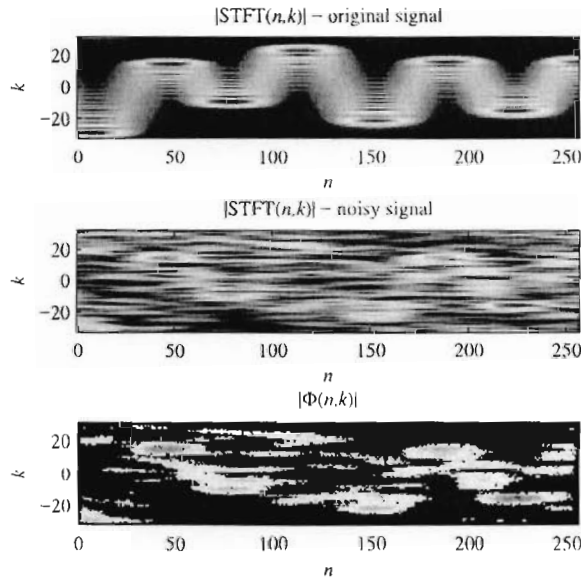

Fig. 14. STFT of a non-noisy sinusoidally modulated signal (first row) and the noisy signal (second row); the obtained pheromone map (third row).

The noisy signal of the form

$$x(n) = \exp\left(j22\sin\left(\frac{14\pi(n+32)}{2M}\right) + j16\cos\left(\frac{7\pi(n+32)}{2M}\right) + j16\cos\left(\frac{5\pi(n+32)}{2M}\right)\right) + \varepsilon(n) \quad (38)$$

is considered for the case of STFT (SNR level of -1 dB), whereas the signal

$$x(n) = \exp\left(j8\sin\left(\frac{36\pi(n+32)}{2M}\right) + j6\cos\left(\frac{9\pi(n+32)}{2M}\right) + j10\cos\left(\frac{8\pi(n+32)}{2M}\right)\right) + \varepsilon(n) \quad (39)$$

is considered in the case S-method (SNR level 4 dB). As the STFT is complex valued, its absolute value is used as the ACO algorithm input. Both signals have length $N_s = 320$, and they are defined at time instants $n \in [-N/2, 3N/2)$, where the TFR is calculated for the middle $N = 256$ points, with window length $K = 64$.

The STFT of the non-noisy and noisy signal as well as the obtained pheromone map are shown in Fig. 14. The estimation results are given in Fig. 15 for the proposed method, STFT absolute value maxima and the corresponding VA estimator. For the case of the S-method, the results are shown in Figs. 16 and 17.
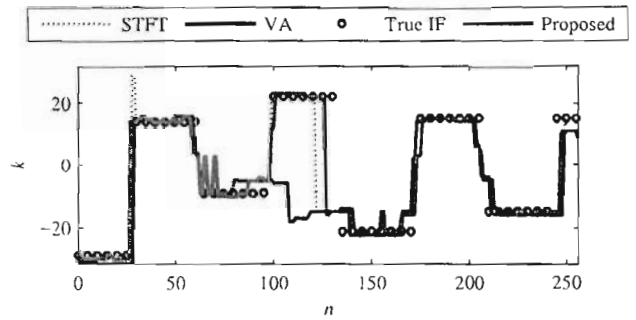

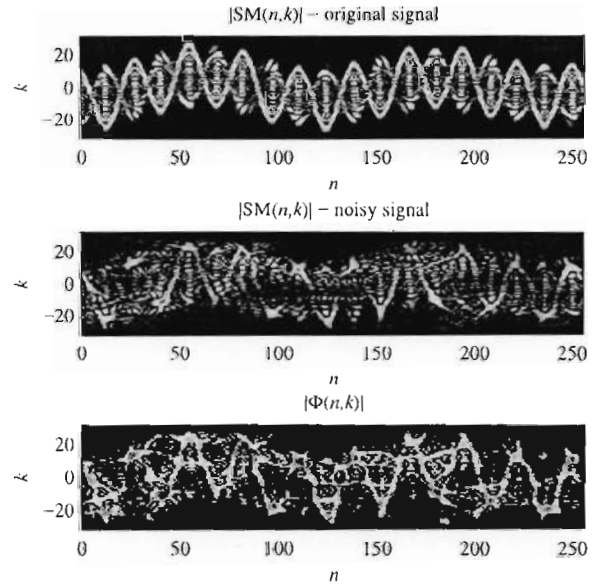Fig. 15. IF estimation results for the signal (38) based on STFT.

Fig. 16. S-method of a non-noisy sinusoidally modulated signal (first row and the noisy signal (second row); the obtained pheromone map (third row).

For the case of reassigned spectrogram, we consider the signal

$$x(n) = \exp\left(j2\sin\left(\frac{15\pi(n+32)}{2M}\right) + j22\cos\left(\frac{6\pi(n+32)}{2M}\right) + j20\cos\left(\frac{5\pi(n+32)}{2M}\right)\right) + \varepsilon(n). \quad (40)$$

The signal length is $N_s = 320$. The reassigned spectrogram and the obtained pheromone map are shown in Fig. 18, where the SNR of 1 dB is considered in the noisy signal. From Fig. 19 we can ob-
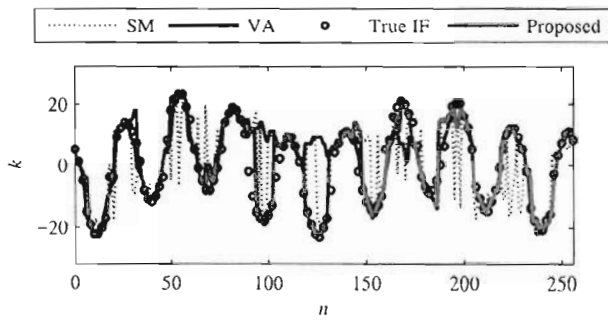
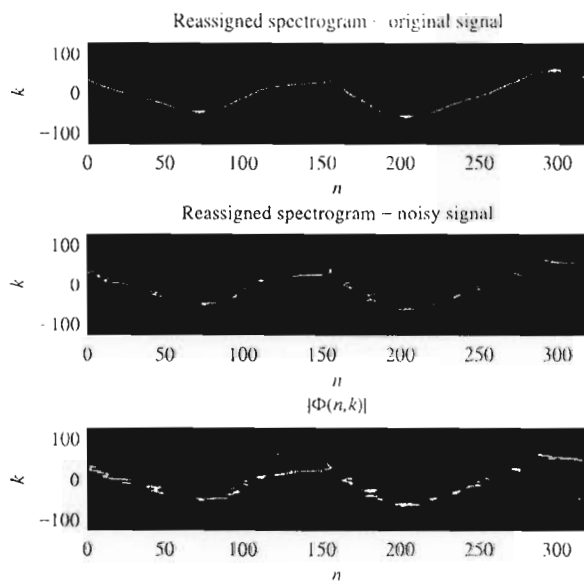Fig. 17. IF estimation results for the signal (39) based on S-method.

Fig. 18. Reassigned spectrogram of a non-noisy sinusoidally modulated signal (first row) and the noisy signal (second row); the obtained pheromone map (third row).
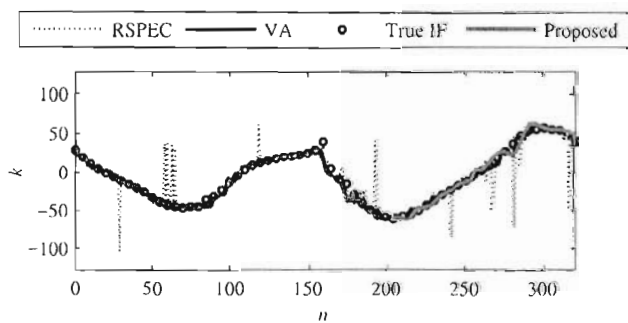

Fig. 19. IF estimation results for the signal (40) based on the reassigned spectrogram.

serve that the reassigned spectrogram maxima based estimator has outliers that both ACO and VA estimators can correct.

In the case of wavelet transform (Morlet wavelet) the PPS signal

$$x(n) = \exp\left(j5\pi\left(\frac{n+32}{2M}\right)^7 - j50\left(\frac{n+32}{2M}\right)\right) + \varepsilon(n). \qquad (41)$$

is considered. The signal length is Ns =320. The scalogram is shown with discrete frequency indices k in Fig. 20, whereas the estimation results for wavelet transform is shown in Fig. 21 for the SNR level of −4 dB. We may observe that the proposed approach
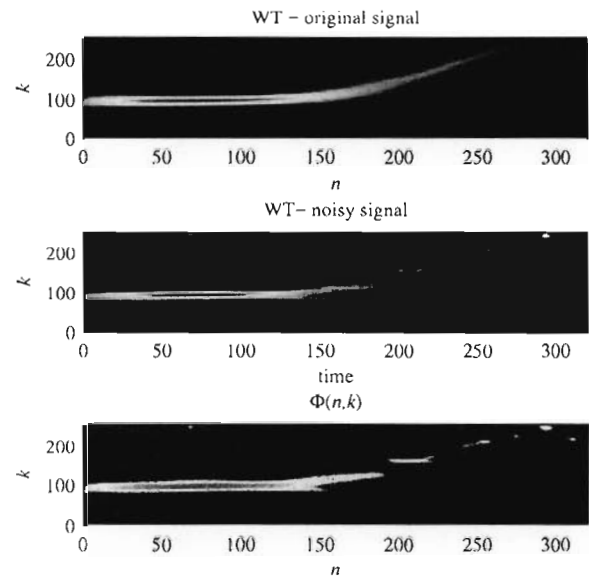

Fig. 20. Scalogram of a non-noisy sinusoidally modulated signal (first row) and the noisy signal (second row); the obtained pheromone map (third row).
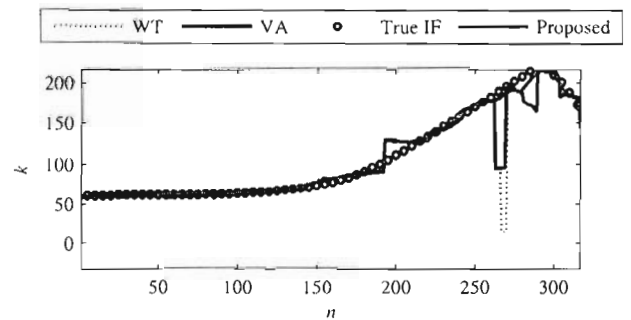

Fig. 21. IF estimation results for the signal (41) based on the wavelet transform.

shows better results at higher frequencies where the signal energy concentration is low.

4.7. Time-frequency plane splitting on non-overlapped subintervals

The PPS signal

$$x(n) = \exp\left(-j1200\pi\left(\frac{n-96}{512}\right)^3 + j100\left(\frac{n+32}{512}\right)\right) + \varepsilon(n) \qquad (42)$$

of length N_s =320, defined at time instants $n \in [-N/2, 3N/2)$ is considered, where the WD is calculated for the middle $N = 256$ points. The WD window length is $K = 64$. The WD TFR plane is divided into non-overlapped strips of width 8, 16, 32, and 64. The proposed algorithm is applied on each strip (subinterval of the time axis) separately and the MSE in the IF estimation was calculated, for various SNR levels based on 100 signal realizations for each SNR level. The results are provided in Table 7. For comparison, the MSE results obtained when the algorithm is applied on the entire TF plane are also presented in the table. We can conclude that good results are obtained even for subintervals of length 16 and 32, whereas in the case when the TFR plane is divided in strips of width 64 results are very close to those obtained when the algorithm is applied on the entire TF plane.

Table 7
MSE of the IF estimation based on WD and the proposed algorithm shown for different subinterval lengths.

SNR [dB]	MSE [dB] subinterval size: 8	MSE [dB] subinterval size: 16	MSE [dB] subinterval size: 32	MSE [dB] subinterval size: 64	MSE [dB] Entire TF plane
3	12.09	−2.29	−4.79	−4.95	−5.07
2	12.22	−2.54	−4.06	−4.81	−5.06
1	12.71	1.31	−1.53	−3.10	−3.54
0	12.03	5.41	−0.08	−0.12	−1.06
−1	14.68	8.88	7.99	4.06	3.64
−2	16.55	13.44	9.99	10.53	10.52
−3	17.98	16.48	15.06	14.70	13.64

5. Conclusion

The modified ACO-based algorithm is proposed for the IF estimation in high Gaussian noise environments. The algorithm is adapted to the IF estimation from the WD of the considered signal. The pheromone deposition gradient is developed based on the two important IF properties: IF should pass through as many as possible points of the WD with highest magnitudes, whereas the IF variations between two consecutive points should not be too fast. The varying population concept has been introduced to improve the IF estimation. The estimation performance of the proposed algorithm is illustrated with numerical experiments including a real-life signal, which clearly confirm that it outperforms the WD-maxima based estimator in high noise environments. Moreover, it outperforms the state-of-the-art VA-based estimator when IF fast variations are involved. The presented approach is applicable to other time-frequency representations as well. Algorithm parameters were studied in extensive statistical test, showing the robustness of the approach to parameter selection in wide ranges. The algorithm was compared with the VA and the WD-maxima estimators in statistical tests with various signals with different levels of IF variations, measured using the maximal instantaneous chirp rate of the considered signals. The presented algorithm can be applied in post-processing of WD, reducing inner interferences and cross-components in multi-component signals. The applications in post-processing of multi-component signals with close components as well as in real practical scenarios are the part of our further research.

Acknowledgment

Appendix A

Summarization of the basic ACO algorithm is given as follows.

> **Step 0**: Place the agents at random positions and with random orientations over the discrete grid, by forming the matrix **P** according to (8). Initialize the pheromone matrix Φ according to (9).
> Repeat steps 1–3 I_{max} times:
> > **Step 1**: For every agent compute the probability (13), and move the agent to an adjacent cell which
> > > •is characterized by the highest probability and
> > > •is not occupied by other ants.
> > Update the corresponding elements of the matrix **P**.
> > **Step 2**: For each grid point (n, k) visited by an agent in Step 1 update the matrix Φ using (14).
> > **Step 3**: Update the pheromone matrix Φ according to (15).

Appendix B

The proposed algorithm for the pheromone map generation can be summarized as follows.

> *Input*: *time-frequency matrix* of size $N \times K$
> *Initialization*:
> Place ants at initial random positions (n_0, k_0), by forming the auxiliary matrix **P** according to (8) and initialize the pheromone matrix Φ and the energy matrix **E** according to (9) and (20), respectively. Form the auxiliary orientation matrix **d** according to (11).
> *Calculations*:
> > While the number of iterations is less than I_{max} and the number of non-zero elements in **P** is larger than 80–100% of N repeat:
> > **Step 1**: For every non-zero element in **P** compute probabilities (13), based on (11) and (12), and move the agent to an adjacent cell which is characterized by the highest probability and which is not occupied by other ants.
> > Update the corresponding elements of position matrix **P**.
> > **Step 2**: For every grid point visited by the agent in Step 1, calculate the gradient $\nabla(n, k)$ according to (16). Update the pheromone matrix Φ using (14) and the energy matrix **E** using (21) and (22).
> > **Step 3**: Update the pheromone matrix Φ according to (15). Update the energy matrix **E** according to (23). Update the matrix **P** according to (24).
> *Output*: *pheromone matrix* Φ

References

[1] B. Boashash (Ed.), Time-Frequency Signal Analysis and Processing, a Comprehensive Reference, Elsevier, The Boulevard, Langford Lane, Kidlington, Oxford, UK, 2003.

[2] B. Boashash, P. O' Shea, Use of the cross Wigner–Ville distribution for estimation of instantaneous frequency, IEEE Trans. Signal Process. 41 (3) (1993) 1439–1445.

[3] L. Cohen, Time–Frequency Analysis, Prentice-Hall, New York, 1995.

[4] B. Boashash, Estimating and interpreting the instantaneous frequency of a signal –Part 1: Fundamentals, Proceedings of the IEEE 80 (4) (1992) 519–538.

[5] B. Boashash, Estimating and interpreting the instantaneous frequency of a signal: a tutorial review-Part 2: algorithms and applications, Proc. IEEE 80 (4) (April 1992) 540–568.

[6] Lj. Stanković, I. Djurović, S. Stanković, M. Simeunović, S. Djukanović, M. Daković, Instantaneous frequency in time–frequency analysis: enhanced concepts and performance of estimation algorithms, Digital Signal Process. 35 (2014) 1–13.

[7] I. Djurović, Lj. Stanković, Influence of high noise on the instantaneous frequency estimation using time-frequency distributions, IEEE Signal Process. Lett. 7 (11) (2000) 317–319.

[8] I. Djurović, Lj. Stanković, An algorithm for the Wigner distribution based instantaneous frequency estimation in a high noise environment, Signal Process. 84 (3) (2004) 631–643.

[9] I. Djurović, Viterbi algorithm for chirp-rate and instantaneous frequency estimation, Signal Process. 91 (5) (2011) 1308–1314.

[10] Z. Xiaoping, Z. Xiuli, Z. Yuhui, X. Shengdong, A robust instantaneous frequency estimation of rotating machinery, in: International Conference on Mechatronic Science, Electric Engineering and Computer (MEC), 2011, 2011, pp. 1922–1925.

[11] P. Li, D. Wang, L. Wang. Separation of micro-Doppler signals based on time frequency filter and Viterbi algorithm, Signal, Image Video Process. 7 (3) (2013) 593–605.

[12] C. Wang, F. Kong, Q. He, F. Hu, F. Liu, Doppler effect removal based on instantaneous frequency estimation and time domain re-sampling for wayside acoustic defective bearing detector system, Measurement 50 (April 2014) 346–355.

[13] C. Ioana, J. Mars, A. Serbanescu, S. Stanković, Time-frequency-phase tracking approach: application to underwater signals in a passive context, in: IEEE International Conference on Acoustics, Speech, and Signal Processing (ICASSP 2010), 2010, pp. 5634–5637.

[14] I. Djurović, Lj. Stanković, Modification of the ICI rule based IF estimator for high noise environments, IEEE Trans. Signal Process. 52 (9) (2004) 2655–2661.

[15] J. Lerga, V. Sucic, Nonlinear IF estimation based on the pseudo WVD adapted using the improved sliding pairwise ICI rule, IEEE Signal Process. Lett. 16 (11) (2009) 953–956.

[16] V.C. Chen, H. Ling, Time-Frequency Transforms for Radar Imaging and Signal Analysis, Artech House, Boston, 2002.

[17] S. Marchand, The simplest analysis method for non-stationary sinusoidal modeling, in: Proceedings of the Digital Audio Effects (DAFx'12) Conference, York, United Kingdom, 2012, pp. 23–26.

[18] F. Auger, P. Flandrin, Y-T. Lin, S. McLaughlin, S. Meignen, T. Oberlin, H-T. Wu, Time-frequency reassignment and synchrosqueezing : an overview, IEEE Signal Process. Mag. 30 (6) (2013) 32–41.

[19] T. Oberlin, S. Meignen, S. McLaughlin, A novel Time-Frequency technique for multicomponent signal denoising, European Signal Processing Conference (EUSIPCO), 2013.

[20] D. Iatsenko, P.V.E. McClintock, A. Stefanovska, Extraction of instantaneous frequencies from ridges in time–frequency representations of signals, Signal Process. 126 (2016) 290–303.

[21] M. Jabloun, N. Martin, F. Leonard, M. Vieira, Estimation of the instantaneous amplitude and frequency of non-stationary short-time signals, Signal Process. 88 (7) (2008) 1636–1655.

[22] M. Jabloun, F. Leonard, M. Vieira, N. Martin, A new flexible approach to estimate the IA and IF of nonstationary signals of long-time duration, IEEE Trans. Signal Process. 55 (7) (2007) 3633–3644.

[23] M. Aoi, K. Lepage, Y. Lim, U.T. Eden, T.J. Gardner, An approach to time-frequency analysis with ridges of the continuous chirplet transform, IEEE Trans. Signal Process. 63 (3) (2015) 699–710.

[24] C. Wang, M. Amin, Performance analysis of instantaneous frequency-based interference excision techniques in spread spectrum communications, IEEE Trans. Signal Process. 46 (1) (1998) 70–82.

[25] Lj. Stanković, M. Daković, T. Thayaparan, Time-Frequency Signal Analysis with Applications, Artech house, 2013.

[26] P. Rao, F.J. Taylor, Estimation of instantaneous frequency using the discrete Wigner distribution, Electron. Lett. 26 (4) (1990) 246–248.

[27] V. Katkovnik, Lj. Stanković, Instantaneous frequency estimation using the Wigner distribution with varying and data-driven window length, IEEE Trans. Signal Process. 46 (9) (1998) 2315–2326.

[28] V.N. Ivanović, M. Daković, Lj. Stanković, Performance of Quadratic Time-Frequency Distributions as Instantaneous Frequency Estimators, IEEE Transactions on Signal Processing 51 (1) (2003) 77–89.

[29] Lj. Stanković, A method for time-frequency signal analysis, IEEE Trans. Signal Process. 42 (1) (1994) 225–229.

[30] R.A. Carmona, W.L. Hwang, B. Torresani, Characterization of signals by the ridges of their wavelet transforms, IEEE Trans. Signal Process. 45 (10) (1997) 2586–2590.

[31] R.A. Carmona, W.L. Hwang, B. Torresani, Multiridge detection and time-frequency reconstruction, IEEE Transactions on Signal Processing 47 (2) (1999) 480–492.

[32] A. Grossmann, J. Morlet, Decomposition of Hardy functions into square integrable wavelets of constant shape, Soc. Int. Am. Math. (SIAM), J. Math. Anal. 15 (4) (1984) 723–736.

[33] I. Djurović, C. Ioana, T. Thayaparan, Lj. Stanković, P. Wang, V. Popović-Bugarin, M. Simeunović, Cubic-phase function evaluation for multicomponent signals with application to SAR imaging, IET Signal Process. 4 (4) (2010) 371–381.

[34] J. Lerga, V. Sucic, B. Boashash, An efficient algorithm for instantaneous frequency estimation of nonstationary multicomponent signals in low SNR, EURASIP J. Adv. Signal Process. (2011), doi:10.1155/2011/725189.

[35] A. Omidvarnia, G. Azemi, J.M. O'Toole, B. Boashash, Robust estimation of highly-varying nonlinear instantaneous frequency of monocomponent signals using a lower-order complex-time distribution, Signal Process. (93) (2013) 3251–3260.

[36] F. Auger, P. Flandrin, Improving the readability of time-frequency and time-scale representations by the reassignment method, IEEE Trans. Signal Process. 43 (5) (1995) 1068–1089.

[37] K. Kodera, R. Gendrin, C. de Villedary, Analysis of time-varying signals with small BT values, IEEE Trans. Acoustics, Speech Signal Process. 26 (1) (1978) 64–76.

[38] K. Czarnecki, The instantaneous frequency rate spectrogram, Mech. Syst. Signal Process. 66 (2016) 361–373 No. 67.

[39] J.P. de León, J.R. Beltrán, F. Beltrán, Instantaneous frequency estimation and representation of the audio signal through Complex Wavelet Additive Synthesis, Int. J. Wavelets, Multiresolution Inf. Process. 12 (3) (2014).

[40] V. Katkovnik, I. Djurović, Lj. Stanković, Robust Time-Frequency Distributions, in: B. Boashash (Ed.), Time-Frequency Signal Analysis and Processing, Academic Press, 2015.

[41] Y. Kopsinis, E. Aboutanios, D.A. Waters, S. McLaughlin, Investigation of bat echolocation calls using high resolution spectrogram and instantaneous frequency based analysis, in: 2009 IEEE/SP 15th Workshop on Statistical Signal Processing, Cardiff, 2009, pp. 557–560.

[42] P. Flandrin, On detection-estimation procedures in the time-frequency plane, in: IEEE International Conference on Acoustics, Speech, and Signal Processing (ICASSP '86), 1986, pp. 2331–2334.

[43] Y. Yang, W. Zhang, Z. Peng, G. Meng, Multicomponent Signal Analysis Based on Polynomial Chirplet Transform, IEEE Trans. Indus. Electron. 60 (9) (2013) 3948–3956.

[44] E. Bonabeau, M. Dorigo, G. Theraulaz, Swarm Intelligence: from Natural to Artificial Systems, Oxford University Press, 1999.

[45] M. Dorigo, T. Stützl, Ant Colony Optimization, Bradford Co. Scituate, MA, USA, 2004.

[46] M. Dorigo, M. Birattari, T. Stutzle, Ant colony optimization, IEEE Comput. Intell. Mag. 1 (4) (2006) 28–39.

[47] M. Dorigo, L.M. Gambardella, Ant colony system: a cooperative learning approach to the traveling salesman problem, IEEE Trans. Evol. Comput. 1 (1) (1997) 53–66.

[48] M. Dorigo, V. Maniezzo, A. Colorni, Ant system: optimization by a colony of cooperating agents, IEEE Trans. Syst. Man. Cybern. Part B 26 (1) (1996) 29–41.

[49] C. Fernandes, V. Ramos, A.C. Rosa, Self-regulated artificial ant colonies on digital image habitats, Int. J. Lateral Comput. 2 (1) (2005).

[50] X. Liu, S. Fang, A convenient and robust edge detection method based on ant colony optimization, Optics Commun. 353 (2015) 147–157.

[51] H. Nezamabadi-pour, S. Saryazdi, E. Rashedi, Edge detection using ant algorithms, Soft Comput. 10 (7) (2005) 623–628.

[52] B. Chen, L. Chen, Y. Chen, Efficient ant colony optimization for image feature selection, Signal Process. 93 (6) (2013) 1566–1576.

[53] C. Fernandes, V. Ramos, A.C. Rosa, Varying the population size of artificial foraging swarms on time varying landscapes, Proc. Artif. Neural Netw. 3696 (2005) 311–316.

[54] V. Ramos, F. Almeida, Artificial ant colonies in digital image habitats – a mass behaviour effect study on pattern recognition, in: Proc. ANTS'2000, 2000, pp. 113–116.

[55] A. Mora, C.M. Fernandes, J.J. Merelo, V. Ramos, J.L.J. Laredo, A.C. Rosa, et al., KohonAnts: a self-organizing ant algorithm for clustering and pattern classification, in: S. Bullock, et al. (Eds.), Proceedings of the 11th International Conference on Artificial Life, Cambridge, MA, MIT Press, 2008, pp. 428–435.

[56] A. Jevtić, D. Andina, Adaptive artificial ant colonies for edge detection in digital images, in: IECON 2010 - 36th Annual Conference on IEEE Industrial Electronics Society, 2010, pp. 2813–2816.

[57] S. Le Hegarat-Mascle, A. Kallel, X. Descombes, Ant colony optimization for image regularization based on a nonstationary Markov modeling, IEEE Trans. Image Process. 16 (3) (2007) 865–878.

[58] G.K. Apostolidis, Lj. Hadjileontiadis, Swarm decomposition: a novel signal analysis using swarm intelligence, Signal Process. 132 (2017).

[59] M. Brajović, V. Popović-Bugarin, Instantaneous frequency estimation using ant colony optimization and Wigner distribution, in: 4th Mediterranean Conference on Embedded Computing - MECO 2015, 2015, pp. 349–352.

[60] F.N. Fritsch, R.E. Carlson, Monotone piecewise cubic interpolation, SIAM J. Numer. Anal. (SIAM) 17 (2) (1980) 238–246.
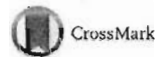
Time-frequency decomposition of multivariate multicomponent signals

Ljubiša Stanković[a,*], Danilo Mandić[b], Miloš Daković[a], Miloš Brajović[a]

[a] Electrical Engineering Department, University of Montenegro, Montenegro
[b] Imperial College London, United Kingdom

ABSTRACT

A solution of the notoriously difficult problem of characterization and decomposition of multicomponent multivariate signals which partially overlap in the joint time-frequency domain is presented. This is achieved based on the eigenvectors of the signal autocorrelation matrix. The analysis shows that the multivariate signal components can be obtained as linear combinations of the eigenvectors that minimize the concentration measure in the time-frequency domain. A gradient-based iterative algorithm is used in the minimization process and for rigor, a particular emphasis is given to dealing with local minima associated with the gradient descent approach. Simulation results over illustrative case studies validate the proposed algorithm in the decomposition of multicomponent multivariate signals which overlap in the time-frequency domain.

Crown Copyright © 2017 Published by Elsevier B.V. All rights reserved.

1. Introduction

Signals with time-varying spectral content are not readily characterized by the conventional Fourier analysis, and are commonly studied within the time-frequency (TF) analysis [1–8]. Research in this field has resulted in numerous representations and algorithms which have been almost invariably introduced for the processing of univariate signals, with most frequent characterization through amplitude and frequency-modulated oscillations [6,9].

Recently, the progress in sensing technology for multidimensional signals has been followed by a growing interest in time-frequency analysis of such multichannel (multivariate and/or multidimensional) data. Namely, developments in sensor technology have made accessible multivariate data. Indeed, the newly introduced concept of modulated bivariate and trivariate data oscillations (3D inertial body sensor, 3D anemometers [9]) and the generalization of this concept to an arbitrary number of channels have opened the way to exploit multichannel signal interdependence in the joint time-frequency analysis [10–12].

The concept of multivariate modulated oscillations has been proposed in [10], under the restricting assumption that one common oscillation fits best all individual channel oscillations. In other words, a joint instantaneous frequency (IF) aims to characterize multichannel data by capturing the combined frequency of all individual channels. It is defined as a weighted average of the IFs in all individual channels. The deviation of multivariate oscillations in each channel from the joint IF is characterized by the joint instantaneous bandwidth. With the aim to estimate the joint IF of multichannel signals, the synchrosqueezed transform, a highly concentrated time-frequency representation (TFR) belonging to the class of reassigned TF techniques, has been recently extended to the multivariate model [9]. Following the same aim of extracting the local oscillatory dynamics of a multivariate signal, the wavelet ridge algorithm has also been introduced within the multivariate framework [10]. Another very popular concept, empirical mode decomposition (EMD), has been studied for multivariate data, [18–22]. However, successful EMD-based multicomponent signal decomposition is possible only for signals which exhibit nonoverlapping components in the TF plane.

By virtue of high concentration and many other desirable properties, the Wigner distribution is commonly exploited in numerous IF estimators developed within the TF signal analysis [6–8]. However, in the case of multicomponent signals, undesirable oscillatory interferences known as cross-terms appear, sometimes masking the presence of desirable auto-terms. To this end, other representations have been developed, commonly aiming to preserve Wigner distribution concentration, while suppressing the cross-terms. One such algorithm is the S-method [6] which was also used as a basis for the multi-component signal decomposition algorithm, proposed in [1]. This particular type of decomposition makes it possible to analyze and characterize signal components independently, allowing the IF estimation for each separate component [1–4].

* Corresponding author.
E-mail addresses: l.stankovic@ieee.org, ljubisa@ac.me (L. Stanković).

In this paper, multivariate Wigner distribution is studied as the basis of multicomponent multichannel signal decomposition. Namely, the strong interdependence of modulations of individual components within all the available data channels is exploited in the joint TF analysis, leading to a reduction of undesirable oscillations present in cross-terms. The inverse multivariate Wigner distribution matrix is decomposed into eigenvectors which contain signal components in the form of their linear combination. Further, a steepest-descent algorithm that enables a fast search for a linear combination of eigenvectors that produces the best possible components concentration is applied. Using the advantages of multichannel interdependence, the proposed TF-based decomposition is shown to be successful in the case of multivariate signals which overlap in the TF plane, while preserving the integrity of each extracted signal component.

Notice that the conventional time-frequency decomposition techniques cannot separate crossing components of arbitrary forms, which may appear in various signal processing applications. One such scenario is in radar signal processing, where reflecting points may assume the same velocity along the line-of-sight. These components will cross in the time-frequency (time-Doppler) representation. The same effect appears when the target signature crosses with the clutter or stationary body reflecting component in the time-frequency representation of radar signal return. The proposed method assumes that multiple phase independent received signals are available. They can be obtained using polarization or multiple antenna systems [23]. Signals with low frequency variations, when the amplitude changes are of the same order as the phase changes, can also be treated as signals with crossing components. Such are the ECG signals, for example. Multivariate forms of these signals are obtained using multiple sensors at different locations. The presented approach can be applied to the decomposition of this class of signals as well.

The paper is organized as follows. Basic theory regarding multivariate TF signal analysis is presented in Section 2. In Section 3, the Wigner distribution of multivariate multicomponent signals is analyzed. In Section 4, we present the basic theory leading to the decomposition of multivariate multi-component signals, whereas the decomposition algorithm is presented in Section 5. The theory is verified through several numerical examples in Section 6.

2. Multivariate time-frequency analysis

Consider a multivariate signal

$$
\mathbf{x}(t) = \begin{bmatrix} a_1(t)e^{j\phi_1(t)} \\ a_2(t)e^{j\phi_2(t)} \\ \vdots \\ a_N(t)e^{j\phi_N(t)} \end{bmatrix}
\tag{1}
$$

obtained by measuring a complex-valued signal $x(t)$ with N sensors, where by each sensor the amplitude and phase of the original signal are modified to give $a_i(t)\exp(j\phi_i(t)) = \alpha_i x(t)\exp(j\varphi_i)$. If the measured signal is real-valued, its analytic extension

$$
x(t) = x_R(t) + jH\{x_R(t)\}
$$

is commonly used, with $x_R(t)$ being real-valued measured signal and $H\{x_R(t)\}$ its Hilbert transform. Analytic signal contains only nonnegative frequencies and the real-valued counterpart can be reconstructed. This form of signal is especially important in the instantaneous frequency interpretation within the time-frequency moments framework.

Since all time-frequency representations may be considered as smoothed versions of the Wigner distribution, this distribution will be the starting point for a review of time-frequency based multivariate signal analysis. The Wigner distribution of a multivariate

signal $\mathbf{x}(t)$ is defined as

$$
WD(\omega, t) = \int_{-\infty}^{\infty} \mathbf{x}^{H}(t - \frac{\tau}{2})\mathbf{x}(t + \frac{\tau}{2})e^{-j\omega\tau}d\tau,
\tag{2}
$$

where $\mathbf{x}^{H}(t)$ is a Hermitian transpose of the vector $\mathbf{x}(t)$.

The inverse Wigner distribution is then given by

$$
\mathbf{x}^{H}(t - \frac{\tau}{2})\mathbf{x}(t + \frac{\tau}{2}) = \frac{1}{2\pi}\int_{-\infty}^{\infty} WD(\omega, t)e^{j\omega\tau}d\omega.
\tag{3}
$$

The center of mass in the frequency axis of the Wigner distribution of a multivariate signal $\mathbf{x}(t)$, defined by (1), is given by

$$
\langle \omega(t) \rangle = \frac{\int_{-\infty}^{\infty} \omega WD(\omega, t)d\omega}{\int_{-\infty}^{\infty} WD(\omega, t)d\omega}
$$

or, more explicitly

$$
\langle \omega(t) \rangle = \frac{\frac{d}{jd\tau}\left[\mathbf{x}^{H}(t - \frac{\tau}{2})\mathbf{x}(t + \frac{\tau}{2})\right]_{|\tau=0}}{\mathbf{x}^{H}(t - \frac{\tau}{2})\mathbf{x}(t + \frac{\tau}{2})_{|\tau=0}}
$$

$$
= \frac{1}{2j}\frac{\left[\mathbf{x}^{H}(t)\mathbf{x}'(t) - \mathbf{x}'^{H}(t)\mathbf{x}(t)\right]}{\mathbf{x}^{H}(t)\mathbf{x}(t)},
$$

where $\mathbf{x}'(t) = d\mathbf{x}(t)/dt$ denotes derivative in time.

The expression for instantaneous frequency of a multivariate signal follows straightforwardly from the previous relation in the form:

$$
\langle \omega(t) \rangle = \frac{\sum_{n=1}^{N} \phi'_n(t)a_n^2(t)}{\sum_{n=1}^{N} a_n^2(t)}.
\tag{4}
$$

If a multivariate signal is obtained by sensing a monocomponent signal $x(t)$ as $a_i(t)\exp(j\phi_i(t)) = \alpha_i x(t)\exp(j\varphi_i)$ with $x(t) = A(t)\exp(j\psi(t))$ and $|dA(t)/dt| \ll |d\psi(t)/dt|$, then $\langle \omega(t) \rangle = d\psi(t)/dt$, since $d\phi_i(t)/dt = d\psi(t)/dt$. The condition for amplitude and phase variations of real-valued monocomponent signals $a_i(t)\cos(\phi_i(t))$ can be defined by Bedrosian's product theorem [13]. It states that the complex analytic signal $a_i(t)\exp(j\phi_i(t)) = a_i(t)\cos(\phi_i(t)) + jH\{a_i(t)\cos(\phi_i(t))\}$ is a valid representation of the real amplitude-phase signal $a_i(t)\cos(\phi_i(t))$ if the spectrum of $a_i(t)$ is nonzero only within the frequency range $|\omega| < B$ and the spectrum of $\cos(\phi_i(t))$ occupies nonoverlapping higher frequency range. A signal is monocomponent if the spectrum of $a_i(t)$ is of lowpass type.

This analysis can be generalized to other time-frequency and time-scale signal representations.

A deviation of the signal spectral content from the instantaneous frequency is described by the local second order moments (instantaneous bandwidths). The expression for the instantaneous bandwidth is obtained from

$$
\sigma_{\omega}^2(t) = \frac{1}{2\pi \mathbf{x}^{H}(t)\mathbf{x}(t)}\int_{-\infty}^{\infty} \omega^2 WD(t, \omega)d\omega - \langle \omega(t) \rangle^2
$$

$$
= \frac{-\frac{d^2}{d\tau^2}\left[\mathbf{x}^{H}(t - \frac{\tau}{2})\mathbf{x}(t + \frac{\tau}{2})\right]\Big|_{\tau=0}}{\mathbf{x}^{H}(t)\mathbf{x}(t)} - \langle \omega(t) \rangle^2.
$$

For the signal in (1) it has the following form:

$$
\sigma_{\omega}^2(t) = \frac{\sum_{n=1}^{N} (a'_n(t))^2 - \sum_{n=1}^{N} a_n(t)a''_n(t)}{2\sum_{n=1}^{N} a_n^2(t)}.
$$

In general, for the case of multicomponent signals, the components are localized over more than one instantaneous frequency.

3. Multicomponent signals

Consider a multicomponent signal

$$
x(t) = \sum_{p=1}^{P} x_p(t)
$$

the components of which are of the form

$$x_p(t) = A_p(t)e^{j\psi_p(t)}$$

with the component amplitudes $A_p(t)$ having a slow-varying dynamics as compared to the variations of the phases $\psi_p(t)$, i.e., $|dA_p(t)/dt| \ll |d\psi_p(t)/dt|$. The corresponding multivariate signal is then given by

$$\mathbf{x}(t) = \sum_{p=1}^{P} \begin{bmatrix} \alpha_{p1}x_p(t)e^{j\varphi_{p1}} \\ \alpha_{p2}x_p(t)e^{j\varphi_{p2}} \\ \vdots \\ \alpha_{pN}x_p(t)e^{j\varphi_{pN}} \end{bmatrix}. \tag{5}$$

The individual components $x_1(t), \ldots, x_P(t)$, measured at different sensors, differ in their amplitudes and phases but share the instantaneous frequency $\omega_p(t) = d\psi_p(t)/dt$ corresponding to $\langle \omega_p(t) \rangle$ in (4), with p being the component index.

The Wigner distribution of this multivariate multicomponent signal is

$$WD(\omega, t) = \sum_{p=1}^{P}\sum_{q=1}^{P}\sum_{i=1}^{N}\int_{-\infty}^{\infty} \alpha_{pi}\alpha_{qi}x_p(t+\tfrac{\tau}{2})x_q^*(t-\tfrac{\tau}{2})e^{j(\varphi_{pi}-\varphi_{qi})}e^{-j\omega\tau}\,d\tau.$$

with i being the sensor index. It may be written as a sum of auto-terms and cross-terms

$$WD(\omega, t) = \sum_{p=1}^{P}\sum_{i=1}^{N}\alpha_{pi}^2\int_{-\infty}^{\infty} x_p(t+\tfrac{\tau}{2})x_p^*(t-\tfrac{\tau}{2})e^{-j\omega\tau}\,d\tau$$
$$+ \sum_{p=1}^{P}\sum_{\substack{q=1\\q\neq p}}^{P}\sum_{i=1}^{N}\alpha_{pi}\alpha_{qi}\int_{-\infty}^{\infty} x_p(t+\tfrac{\tau}{2})x_q^*(t-\tfrac{\tau}{2})e^{j(\varphi_{pi}-\varphi_{qi})}e^{-j\omega\tau}\,d\tau.$$
$$= WD_a(\omega, t) + WD_c(\omega, t) \tag{6}$$

The phase shifts of the components of the multivariate signal in (6) cancel out in the auto-terms $WD_a(\omega, t)$. This important property implies that the auto-terms, obtained from each variate of a multivariate signal, are summed in-phase, independently from the (different) initial phases in the individual signal components. In the cross-terms, the phase shifts do not cancel-out in the resulting $WD_c(\omega, t)$, leading to an out-of-phase summation. The cross-terms in the multivariate case are a sum of N signals with arbitrary (random) phases. They are consequently reduced with respect to the Wigner distribution of an univariate signal. Therefore, for a large N we would expect the auto-terms only, while the cross-terms will tend to a small value with respect to the auto-terms. It is expected that the cross-terms, for a large number of sensors N, behave as a time-frequency dependent zero-mean Gaussian random variable, the variance of which depends on the cross-terms value, $\mathrm{var}\{WD(\omega,t)\} = \sigma^2(WD_c(\omega,t))$. The auto-terms are deterministic for a given signal, since they do not depend on random phases, as seen in the corresponding Wigner distribution term $WD_a(\omega, t)$. This means that for a large N

$$WD(\omega, t) \sim \mathcal{N}(WD_a(\omega, t), \sigma^2(WD_c(\omega, t))).$$

4. Inversion and signal decomposition

The inversion of a Wigner distribution of a multivariate signal in the analog domain is given by

$$\mathbf{x}^H(t_2)\mathbf{x}(t_1) = \frac{1}{2\pi}\int_{-\infty}^{\infty} WD\left(\frac{t_1+t_2}{2}, \omega\right)e^{j\omega(t_1-t_2)}\,d\omega.$$

By the discretization of angular frequency, $\omega - k\Delta\omega$, and the time, $t_1 = n_1\Delta t$, $t_2 = n_2\Delta t$, with an appropriate definition of discrete values, we easily obtain

$$\mathbf{x}^H(n_2)\mathbf{x}(n_1) = \frac{1}{K+1}\sum_{k=-K/2}^{K/2} WD\left(\frac{n_1+n_2}{2}, k\right)e^{j\frac{\pi}{K+1}k(n_1-n_2)}. \tag{7}$$

Upon introducing the notation

$$R(n_1, n_2) = \frac{1}{K+1}\sum_{k=-K/2}^{K/2} WD\left(\frac{n_1+n_2}{2}, k\right)e^{j\frac{\pi}{K+1}k(n_1-n_2)}. \tag{8}$$

we obtain

$$R(n_1, n_2) = \mathbf{x}^H(n_2)\mathbf{x}(n_1). \tag{9}$$

Therefore, for multicomponent multivariate signals, the inversion produces a matrix with the elements of the form

$$R(n_1, n_2) = \sum_{i=1}^{N}\sum_{p=1}^{P}\sum_{q=1}^{P}\alpha_{pi}\alpha_{qi}x_p(n_1)x_q^*(n_2)e^{j(\varphi_{pi}-\varphi_{qi})}. \tag{10}$$

If we now use the assumption that the cross-terms in the Wigner distribution of multivariate signals can be neglected with respect to the auto-terms summed in phase, this yields

$$R(n_1, n_2) = \sum_{i=1}^{N}\sum_{p=1}^{P}\alpha_{pi}^2 x_p(n_1)x_p^*(n_2) = \sum_{p=1}^{P}B_p x_p(n_1)x_p^*(n_2) \tag{11}$$

where $B_p = \sum_{i=1}^{N}\alpha_{pi}^2$.

As for any square matrix, the eigenvalue decomposition of a $K \times K$ dimensional matrix $\mathbf{R}$ gives

$$\mathbf{R} = \mathbf{Q}\boldsymbol{\Lambda}\mathbf{Q}^T = \sum_{p=1}^{K}\lambda_p\mathbf{q}_p(n)\mathbf{q}_p^*(n). \tag{12}$$

where λ_p are the eigenvalues and $\mathbf{q}_p(n)$ are the corresponding eigenvectors of $\mathbf{R}$. Note that the eigenvectors $\mathbf{q}_p(n)$ are orthonormal.

For a P-component signal, in a noiseless case, the elements of this matrix are

$$R(n_1, n_2) = \sum_{p=1}^{P}\lambda_p q_p(n_1)q_p^*(n_2). \tag{13}$$

Let us consider several special cases:

1) For a univariate signal and the Wigner distribution, the signal itself is equal to the eigenvector $\mathbf{q}_1(n)$, up to a scaling by a complex-valued constant [1], with the corresponding eigenvalues $\lambda_1 = E_x$, $\lambda_2 = 0, \ldots, \lambda_K = 0$. The fact that the Wigner distribution based inversion produces only one nonzero eigenvalue is also used to check if a given two-dimensional function is a valid Wigner distribution.

2) If the components of a multicomponent univariate signal do not overlap in the time-frequency plane, then it is possible to calculate the distribution which will be equal to a sum of the Wigner distributions of the individual signal components. This calculation is performed using the S-method and the property [1]:

$$SM(n, k) = \sum_{p=1}^{P} WD_p(n, k). \tag{14}$$

Since the non-overlapping components are orthogonal, the eigenvalue decomposition will produce

$$B_p\mathbf{x}_p(n) = \lambda_p\mathbf{q}_p(n), \qquad p = 1, 2, \ldots, P.$$

where B_p is a constant. Note that, by definition, the energy of the corresponding eigenvector is equal to 1,

$$\|\mathbf{q}_p(n)\|^2 = 1. \tag{15}$$

We can conclude that

$$B_p\mathbf{x}_p(n)\mathbf{x}_p^*(n) = \left(\sqrt{\lambda_p}\mathbf{q}_p(n)\right)\left(\sqrt{\lambda_p}\mathbf{q}_p(n)\right)^*$$

and

$$\lambda_p = \left\| \sqrt{\lambda_p} \mathbf{q}_p(n) \right\|^2 = \| B_p \mathbf{x}_p(n) \|^2 = \sum_{n=-K/2}^{K/2} B_p x_p^2(n) = B_p E_{x_p}.$$

where E_{xp} is the energy of the signal pth component. The eigenvector $\mathbf{q}_p(n)$ is equal to the signal vector $\mathbf{x}_p(n)$, up to the constant amplitude and phase ambiguity.

3) If the signal components $\mathbf{x}_p(n)$ overlap in the frequency plane, then the decomposition on the individual components is not possible using the state-of-art methods, except in cases of quite specific signal forms (such as linear frequency modulated signals, using chirplet transform, Radon transform or similar techniques [14,], or for sinusoidally modulated signals using inverse Radon transform, [16,17]). In general, these kinds of signals cannot be separated into individual components in the univariate case. However, the multivariate form of signals reduces (changes) the cross-terms in the Wigner distribution, thus offering a possibility to decompose the components which overlap in the time-frequency plane.

5. Decomposition algorithm

Consider a multicomponent signal of the form (5), with signal components $\mathbf{x}_p$, $p = 1, 2, \ldots, P$ whose supports $\mathbb{D}_p$ may partially overlap in the time-frequency domain. We also make a realistic assumption that there is no signal component whose time-frequency support completely overlaps with other component, and $D_1 \le D_2 \le \cdots \le D_P$, where D_p is the area of the support $\mathbb{D}_p$.

The first signal component can be expressed as linear combination of vectors $\mathbf{q}_p$ with coefficients η_{1p} to give

$$\mathbf{x}_1 = \eta_{11} \mathbf{q}_1 + \eta_{21} \mathbf{q}_2 + \cdots + \eta_{P1} \mathbf{q}_P. \tag{16}$$

Since we have assumed that the signal components are well concentrated in the time-frequency domain, we can use a concentration measure in order to find the coefficients η_{p1}. To this end, we form a linear combination of the basis vectors $\mathbf{q}_p$, with weighting coefficients β_p, $p = 1, 2, \ldots, P$, to arrive at

$$\mathbf{y} = \beta_1 \mathbf{q}_1 + \beta_2 \mathbf{q}_2 + \cdots + \beta_P \mathbf{q}_P. \tag{17}$$

and calculate the concentration measure $\mathcal{M}\{TFR(n, k)\}$ of the time-frequency representation $TFR(n, k)$ of the normalized signal $\mathbf{y}/\|\mathbf{y}\|_2$. The choice of the TFR is not crucial here. We can use the spectrogram as the simplest TFR. By solving the concentration measure minimization problem we then obtain the global minimum corresponding to the best concentrated signal component.

The most straightforward way to solve this problem would be to use the zero-norm as the concentration measure of $TFR(n, k)$ and perform a direct search over the coefficients β_p, $p = 1, 2, \ldots, P$. Then, the coefficients η_{p1} are the solution of the minimization problem

$$[\eta_{11}, \eta_{21}, \ldots, \eta_{P1}] = \arg \min_{\beta_1, \ldots, \beta_P} \| TFR(n, k) \|_0.$$

For these values of coefficients $\| TFR(n, k) \|_0$ is equal to the area of the best concentrated component support D_1. If any two the smallest areas are equal we still find one of them.

Note that this minimisation problem has several local minima as the coefficients β_p in $\mathbf{y} = \beta_1 \mathbf{q}_1 + \beta_2 \mathbf{q}_2 + \cdots + \beta_P \mathbf{q}_P$ which correspond to any signal component $\mathbf{x}_p$ will also produce a local minimum of the concentration measure, equal to the area of corresponding component support. In addition, any linear combination of $K < P$ signal components $\mathbf{x}_p$ will also produce a local minimum equal to the area of the union of the supports of included signal components.

After the best concentrated component is detected, the corresponding vector $\mathbf{q}_1$ is replaced with the extracted signal component. The extracted component is then removed from the remaining vectors $\mathbf{q}_k$ by subtracting the projection of the extracted component to the vectors $\mathbf{q}_p$, $p = 2, 3, \ldots, P$ (signal deflation procedure [31]). The procedure is repeated with the new set of vectors $\mathbf{q}_p$ by forming the signal $\mathbf{y} = \beta_2 \mathbf{q}_2 + \cdots + \beta_P \mathbf{q}_P$, and then by varying the coefficients β_p a new global minimum of the concentration is found, which corresponds to the second signal component. The procedure is iterated P times.

However, since in practical applications neither the direct search nor the norm-zero concentration can be used, several methods have been developed in literature based on the optimization of problems with several local minima. In general, all these methods can be divided into three large classes: deterministic [27], stochastic [25,26], and heuristic (ant colony optimization [28], genetic algorithm, hill climbing [30], simulated annealing [29], particle swarm optimization...). In this paper we will adapt a gradient-based approach to solve the minimization problem. The zero-norm is replaced by its closest convex counterpart, the one-norm. The proposed algorithm is presented next.

- In the first step, we calculate the matrix $\mathbf{R}$ of the multivariate signal $\mathbf{x}(n)$ according to (8) or (9). The number of signal components P is equal to the number of non-zero eigenvalues of matrix $\mathbf{R}$. In the noisy signal cases two approaches for determining the number of components can be utilized: (a) The number of components is assumed. As long as it is larger than or equal to the true number of components P, the algorithm works properly, producing noise only as the extra components. (b) A threshold is set to separate eigenvalues corresponding to signal components from those corresponding to the noise. This threshold determines the number of components in the decomposition.

- For the time-frequency representation of the signal we can use the spectrogram, the S-method with narrow frequency window (for example $L_s = 1$), or any other appropriate representation. Since these time-frequency representations are quadratic, a concentration measure equivalent to the one-norm should be defined as [24]

$$\mathcal{M}\{TFR(n, k)\} = \sum_n \sum_k | TFR(n, k)|^{1/2} \tag{18}$$

where the summation is performed over all available time and frequency indices n and k.

The decomposition procedure is outlined in Algorithm 1.

- The measure minimization is implemented by using a steepest descent approach presented in Algorithm 2. Here, we fix the coefficient $\beta_p = 1$ and vary the real and imaginary parts of the remaining coefficients by $+\Delta$. The gradient of the normalized measure, γ_p, is then calculated and is used for coefficient update. The initial value of the parameter Δ is 0.1 and it is reduced whenever a further coefficients update does not yield a smaller measure.

- When the pth component is extracted, the corresponding vector $\mathbf{q}_p$ is replaced with the extracted signal component. The extracted component is then removed from the remaining vectors $\mathbf{q}_k$ by subtracting the projection of the extracted component to vectors $\mathbf{q}_k$, $k = p + 1, p + 2, \ldots, P$. In this manner, we ensure that the pth signal component will not be detected again.

- This procedure is repeated until there is no more updates of vectors $\mathbf{q}_k$.

For a two-component signal, the considered minimization problem is now convex, with a single, global, minimum. For a three-component signal, the local minima exists for signals obtained as a sum of any two components. This is the reason why the decomposition procedure is repeated after minimum of the concentration measure is found. In the next iteration, the pair of components corresponding to the local minimum are separated as in the

Algorithm 1 Multivariate signal decomposition.

Input:

- Multivariate signal $\mathbf{x}(n)$

1: Calculate S-Method $SM(n, k)$ of the multivariate signal $\mathbf{x}(n)$ and matrix $\mathbf{R}$ with elements

$$R(n_1, n_2) = \frac{1}{K+1} \sum_{k=-K/2}^{K/2} SM\left(\frac{n_1 + n_2}{2}, k\right) e^{j \frac{2\pi}{\kappa} k(n_1 - n_2)}.$$

as in [1]. If the Wigner distribution is used then the $SM(n, k)$ should be replaced with $WD(n, k)$, or we can calculate elements of matrix $\mathbf{R}$ as $R(n_1, n_2) = \mathbf{x}^H(n_2)\mathbf{x}(n_1)$.

2: Find eigenvectors $\mathbf{q}_i$ and eigenvalues λ_i of matrix $\mathbf{R}$.

3: $P \leftarrow$ number of non-zero eigenvalues

4: **repeat**

5: $\quad N_{updates} \leftarrow 0$

6: $\quad$ **for** $i = 1, 2, \ldots, P$ **do**

7: $\quad\quad$ Solve minimization problem

$$\min_{\beta_1, \ldots, \beta_P} \mathcal{M}\left\{ \text{TFR}\left\{ \frac{1}{C} \sum_{p=1}^{P} \beta_p \mathbf{q}_p \right\} \right\} \quad \text{subject to } \beta_i = 1$$

where $\mathcal{M}\{\cdot\}$ is concentration measure, $\text{TFR}\{\cdot\}$ is time-frequency representation of a provided signal, and

$$C = \sqrt{\left\| \sum_{p=1}^{P} \beta_p \mathbf{q}_p \right\|_2}$$

is used to normalize energy of the combined signal to 1. Coefficients $\beta_1, \beta_2, \ldots, \beta_P$ are obtained as a result of the minimization.

8: $\quad\quad$ **if** any $\beta_p \neq 0$, $p \neq i$ **then**

9: $\quad\quad\quad \mathbf{q}_i \leftarrow \frac{1}{C} \sum_{p=1}^{P} \beta_p \mathbf{q}_p$

10: $\quad\quad\quad$ **for** $k = i+1, i+2, \ldots, P$ **do**

11: $\quad\quad\quad\quad s \leftarrow \mathbf{q}_i^H \mathbf{q}_k$

12: $\quad\quad\quad\quad \mathbf{q}_k \leftarrow \frac{1}{\sqrt{1-|s|^2}} (\mathbf{q}_k - s\mathbf{q}_i)$

13: $\quad\quad\quad$ **end for**

14: $\quad\quad\quad N_{updates} \leftarrow N_{updates} + 1$

15: $\quad\quad$ **end if**

16: $\quad$ **end for**

17: **until** $N_{updates} = 0$

Output:

- Number of signal components P
- Reconstructed signal components $\mathbf{q}_1, \mathbf{q}_2, \ldots, \mathbf{q}_P$

Algorithm 2 Minimization procedure.

Input:

- Vectors $\mathbf{q}_1, \mathbf{q}_2, \ldots, \mathbf{q}_P$
- Index i where corresponding vector $\mathbf{q}_i$ should be kept with unity coefficient $\beta_i = 1$
- Required precision ε

1: $\beta_p = \begin{cases} 1 & \text{for } p = i \\ 0 & \text{for } p \neq i \end{cases}$ for $p = 1, 2, \ldots, P$

2: $M_{old} \leftarrow \infty$

3: $\Delta = 0.1$

4: **repeat**

5: $\quad \mathbf{y} \leftarrow \sum_{p=1}^{P} \beta_p \mathbf{q}_p$

6: $\quad M_{new} \leftarrow \mathcal{M}\left\{ \text{TFR}\left\{ \frac{\mathbf{y}}{\|\mathbf{y}\|_2} \right\} \right\}$

7: $\quad$ **if** $M_{new} > M_{old}$ **then**

8: $\quad\quad \Delta \leftarrow \Delta/2$

9: $\quad\quad \beta_p \leftarrow \beta_p + \gamma_p$, for $p = 1, 2, \ldots, P$ ▷ Cancel the last coefficients update

10: $\quad\quad \mathbf{y} \leftarrow \sum_{p=1}^{P} \beta_p \mathbf{q}_p$

11: $\quad$ **else**

12: $\quad\quad M_{old} \leftarrow M_{new}$

13: $\quad$ **end if**

14: $\quad$ **for** $p = 1, 2, \ldots, P$ **do**

15: $\quad\quad$ **if** $p \neq i$ **then**

16: $\quad\quad\quad M_r^+ \leftarrow \mathcal{M}\left\{ \text{TFR}\left\{ \frac{\mathbf{y} + \Delta \mathbf{q}_p}{\|\mathbf{y} + \Delta \mathbf{q}_p\|_2} \right\} \right\}$

17: $\quad\quad\quad M_r^- \leftarrow \mathcal{M}\left\{ \text{TFR}\left\{ \frac{\mathbf{y} - \Delta \mathbf{q}_p}{\|\mathbf{y} - \Delta \mathbf{q}_p\|_2} \right\} \right\}$

18: $\quad\quad\quad M_i^+ \leftarrow \mathcal{M}\left\{ \text{TFR}\left\{ \frac{\mathbf{y} + j\Delta \mathbf{q}_p}{\|\mathbf{y} + j\Delta \mathbf{q}_p\|_2} \right\} \right\}$

19: $\quad\quad\quad M_i^- \leftarrow \mathcal{M}\left\{ \text{TFR}\left\{ \frac{\mathbf{y} - j\Delta \mathbf{q}_p}{\|\mathbf{y} - j\Delta \mathbf{q}_p\|_2} \right\} \right\}$

20: $\quad\quad\quad \gamma_p \leftarrow 8\Delta \frac{M_r^+ - M_r^-}{M_{new}} + j8\Delta \frac{M_i^+ - M_i^-}{M_{new}}$

21: $\quad\quad$ **else**

22: $\quad\quad\quad \gamma_p \leftarrow 0$

23: $\quad\quad$ **end if**

24: $\quad$ **end for**

25: $\quad \beta_p \leftarrow \beta_p - \gamma_p$, for $p = 1, 2, \ldots, P$ ▷ Coefficients update

26: **until** $\sum_{p=1}^{P} |\gamma_p|^2$ is below required precision ε

Output:

- Coefficients $\beta_1, \beta_2, \ldots, \beta_P$

---

two-component signal case. For a higher number of signal components, the number of local minima increases. Then several repetitions of the procedure are needed in order to separate the components in an iterative way. Recall that a gradient-based algorithm can find any local minimum, each corresponding to a combinations of $K < P$ signal components. This means that each local minimum reduces the complexity of decomposition vectors $\mathbf{q}_p$, leading to the full signal decomposition in an iterative way. For more details, see Algorithm 2.

6. Numerical examples

Example 1. Consider a real bivariate signal $\mathbf{x}(t) = [x_1(t), x_2(t)]^T$, where the signal from channel i has the form

$$x_i(t) = e^{-(t/128)^2} \cos\left((t/16)^4/128 - 8\pi (t/16)^2/64 + \varphi_i\right)$$
$$= 0.5e^{-(t/128)^2} \left[e^{j((t/16)^4/128 - 8\pi (t/16)^2/64 + \varphi_i)} \right.$$
$$\left. + e^{-j((t/16)^4/128 - 8\pi (t/16)^2/64 + \varphi_i)} \right]$$
$$= x_{1i}(t) + x_{2i}(t), \quad i = 1, 2, \tag{19}$$

for $-128 \leq t \leq 128$, as shown in Fig. 1 (a) (for the first channel). The phases $\varphi_1 \neq \varphi_2$ are random numbers with a uniform distribution drawn from the interval $[0, 2\pi]$. As this signal is real-valued, two symmetric components $x_{1i}(t)$ and $x_{2i}(t)$ exist in the Fourier transform and the time-frequency domains. However, these

(a)

Exact and estimated instantaneous frequency

(b)

time–frequency of analytic signal

(c)

time–frequency of signal

(d)

time–frequency of eigenvector one

(e)

time–frequency of eigenvector two

(f)

time–frequency of component one
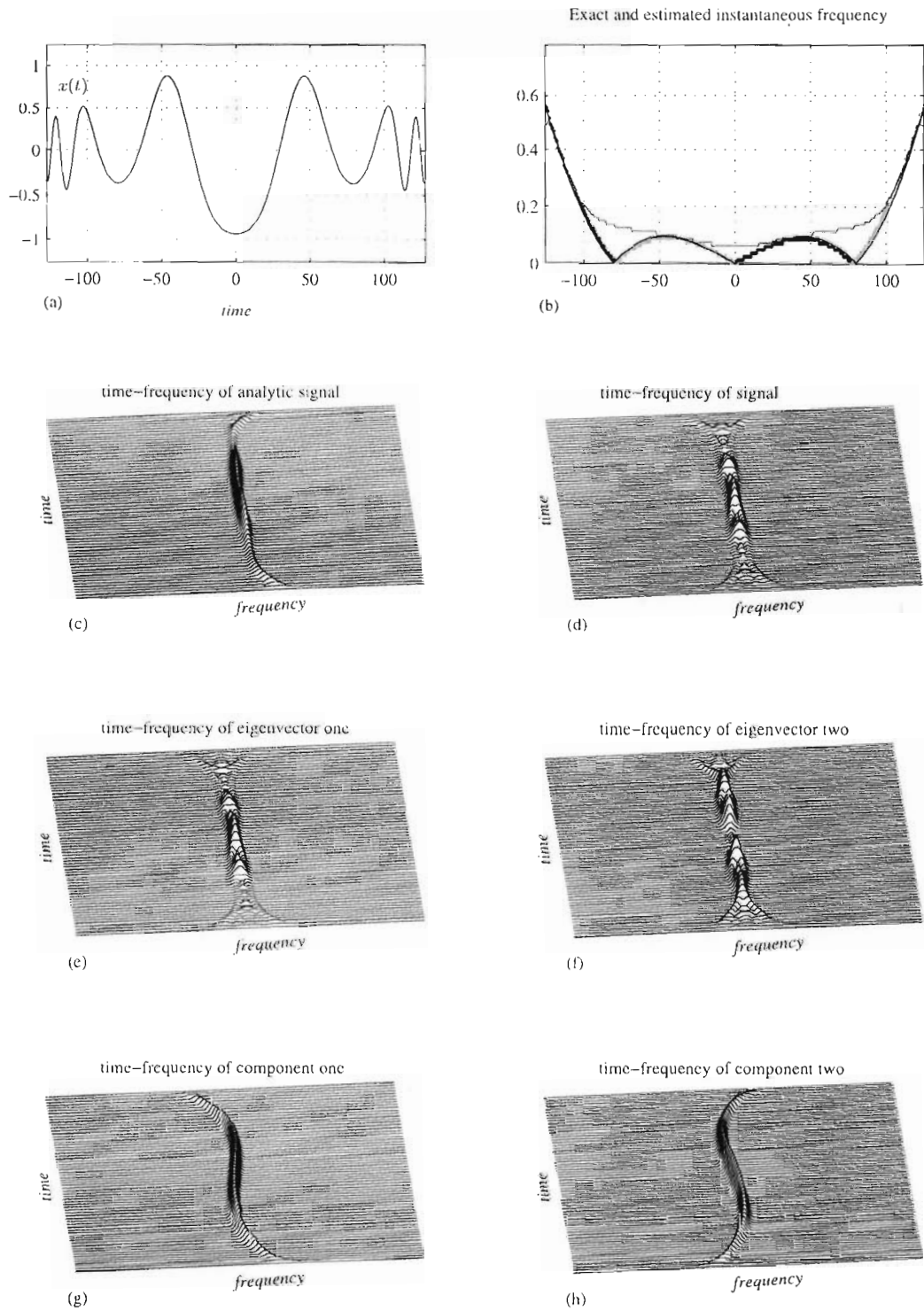

(g)

time–frequency of component two

(h)

Fig. 1. Bivariate real signal analyzed in Example 1. (a) signal shown in time domain. (b) estimation of the IF: black - true IF, red - IF estimation using the analytic signal, green and blue - IF estimation based on components extracted using the proposed approach. (c) PWD of the analytic signal. (d) PWD of the original signal. (e) and (f) PWD of the eigenvectors. (g) and (h) PWD of components extracted using the proposed approach. (For interpretation of the references to colour in this figure legend, the reader is referred to the web version of this article.)

components partially overlap, and thus they are inseparable using these representations.

A common problem is to estimate the instantaneous frequency (IF) of the signal. To this end, for real signals it is usual to calculate its analytic form based on the Hilbert transform. The true IF is shown in Fig. 1 (b), black line. The time-frequency representation (TFR) of this analytic signal is shown in Fig. 1 (c). However, the IF estimate based on the analytic signal, shown in Fig. 1 (b), red line, obviously significantly differs from the true IF. Namely, the IF estimation based on the standard TFR maxima approach does not appropriately track the IF variations, as they are lost in the
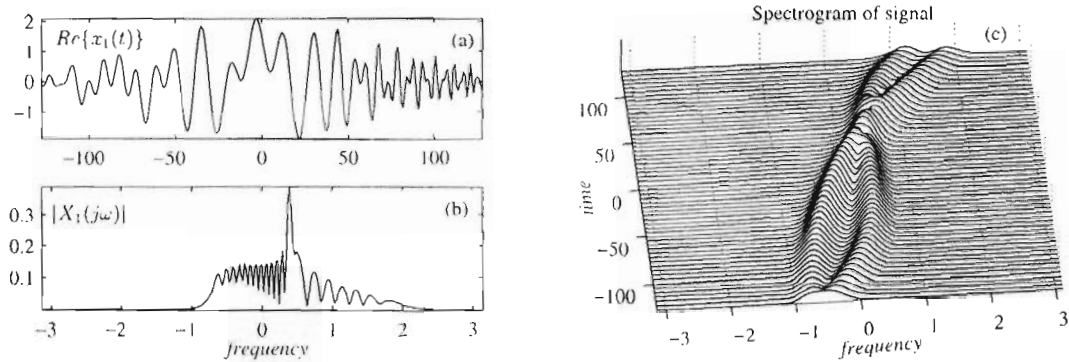
Fig. 2. Bivariate two-component signal shown in: (a) time domain, (b) frequency domain, (c) time-frequency domain (spectrogram).

corresponding TFR due to significant overlapping of the components and the fact that amplitude and phase variations are of the same order. Notice that Bedrosian's product theorem condition for amplitude and phase is not satisfied in this case.

On the other hand, if one calculates the TFR of the original signal (19), the two components $x_{1i}(t)$ and $x_{2i}(t)$ overlap in the TF plane, as shown in Fig. 1 (d). These components are also nonlinear and thus, none of the known techniques can be applied for their separation in order to estimate the IF of such overlapping highly nonlinear components. As these components highly overlap, they are not orthogonal, and consequently the S-method based decomposition [1] cannot be applied in a straightforward manner.

However, it is crucial to note that the cross-terms in Wigner distribution (WD) are changed and two eigenvalues different from zero do appear. Therefore, the two corresponding eigenvectors, whose pseudo Wigner distributions (PWD) are shown in Fig. 1 (e) and (f), contain both components, appearing as a linear combination. Using the proposed multi-component decomposition algorithm, we were able to calculate the coefficients β_1 and β_2, forming the linear combination (17) of eigenvectors. The minimum concentration (sparsity) measure of this linear combination corresponds to two separate signal components, as shown in Fig. 1 (g) and (h). It can be observed that the IF estimation based on these two TFRs maxima (using positive IF parts), shown in Fig. 1 (b), green and blue dots, is accurate up to the theoretically expected bias caused by the IF non-linearity, which can be further reduced using some well-known IF estimation techniques [6].

Example 2. In this example we consider a bivariate two-component signal $\mathbf{x}(t)$ assuming that each sensor measures

$$x_i(t) = x_{1i}(t) + x_{2i}(t), \quad i = 1, 2 \tag{20}$$

whose components are given by

$$x_{1i}(t) = 1.2e^{-(t/96)^2}e^{-j12\pi(t/16)^2/25 - jt^3/256^2 \cdot \varphi_{1i}} \tag{21}$$

$$x_{2i} = 0.9e^{-(t/128)^2}e^{-j\pi t/8 + jt/16)^5/100 + \varphi_{2i}} \tag{22}$$

with phases φ_{1i}, φ_{2i}, $i = 1, 2$ simulated as random numbers with a uniform distribution drawn from the interval $[0, 2\pi]$. The real part of the signal from the first channel, and the corresponding Fourier transform are shown in Fig. 2 (a) and (b), whereas the multivariate spectrogram is shown in Fig. 2 (c). It can be observed that the signal components cannot be separated using the spectrogram, without significant auto-term degradation. Note that the two signal components have non-linear frequency modulation, and are thus inseparable using common component decomposition algorithms.

When the proposed algorithm for decomposition of multicomponent signals is applied, aiming to extract each component of the

analyzed signal, then in accordance with the presented theory, the Wigner distribution is used as the initial time-frequency representation for the eigenvalue decomposition. The Wigner distribution of the analyzed signal is shown in Fig. 3 (a) whereas the eigenvalues of autocorrelation matrix $\mathbf{R}$ are shown in Fig. 3 (b). It can be seen that there are two non-zero eigenvalues containing linear combinations of the signal component. Further steps of the proposed decomposition method assume that a TFR is calculated and the proposed minimization procedure is applied in order to find the coefficients producing the eigenvectors combination (17), leading to the best component concentration. Our numerical experiments have shown that a similar performance of the minimization using Algorithm 2 is obtained when the Wigner distribution, the spectrogram and the S-method are applied as underlying TFRs on the observed eigenvectors. In Fig. 3, we present the results obtained in the case of the Wigner distribution. For visual clarity, pseudo Wigner distribution with Hanning window of length 256 is shown for each eigenvector in Fig. 3 (c) and (e), although the Wigner distribution was used in the minimization procedure. Similar results would be obtained for any other TFR in the minimization step. The pseudo Wigner distribution for each separated signal component is shown in Fig. 3 (d) and (f), for signals $x_{1i}(t)$ and $x_{2i}(t)$, respectively.

Example 3. Consider a multivariate three-component signal $\mathbf{x}(t)$ for $N = 4$, for which the ith channel signal is defined as

$$x_i(t) = x_{1i}(t) + x_{2i}(t) + x_{3i}(t), \quad i = 1, \ldots, 4, \tag{23}$$

the components $x_{1i}(t)$ and $x_{2i}(t)$ are given by (21) and (22), for $i = 1, \ldots, 4$ whereas the third component has the following form

$$x_{3i} = 0.9e^{-(t/128)^2}e^{-j\pi t/8 - j(t/16)^4/100 + \varphi_{3i}}, \tag{24}$$

also having the phase φ_{3i}, $i = 1, \ldots, 4$ simulated as a random number with a uniform distribution drawn from the interval $[0, 2\pi]$. The signal from the first channel, its Fourier transform and the multivariate spectrogram are shown in Fig. 4 (a)–(c) respectively.

The Wigner distribution of the analyzed signal is shown in Fig. 5 (a), whose inverse matrix $\mathbf{R}$ is the subject of eigenvalue decomposition. The obtained eigenvalues are shown in Fig. 5 (b) while Fig. 5 (c), (e) and (g) show the pseudo Wigner distributions of the eigenvectors with largest eigenvalues in subplot (b), and illustrate that the components are not separated. Namely, as in the previous example, the intersected components are not orthogonal and consequently, each considered eigenvector contains a linear combination of signal components. For the obtained eigenvectors, we apply the proposed minimization procedure, in order to find the coefficients that combine these eigenvectors to produce the best concentration, corresponding to the signal components. All three signal components were successfully extracted, as shown in Fig. 5 (d), (f) and (h).
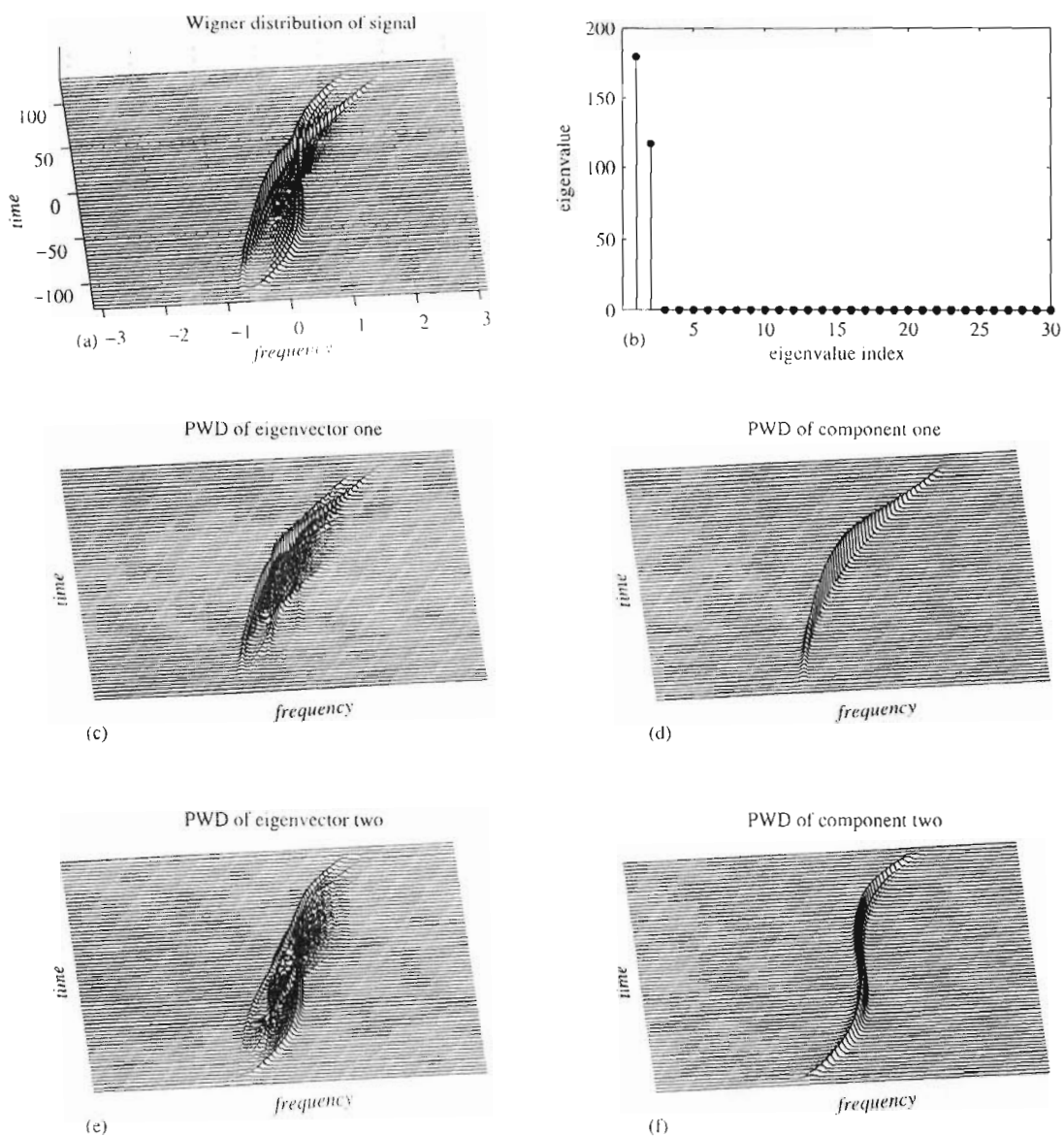
Fig. 3. Decomposition of the bivariate two-component signal from Example 2. (a) WD of the analyzed signal. (b) Eigenvalues of the autocorrelation matrix **R**. (c) and (e): PWD of the first and second eigenvector. (d) and (f) PWDs of extracted signal components.
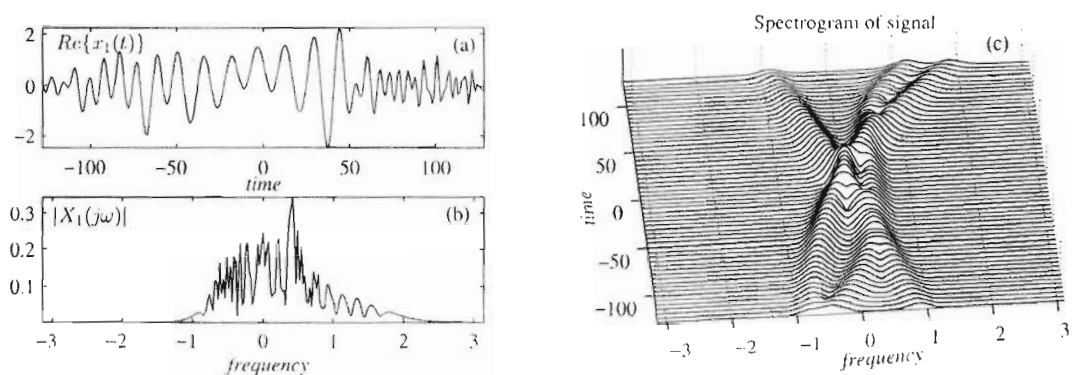

Fig. 4. Multi-variate signal having 3 components, with $N = 4$ shown in: (a) time domain. (b) frequency domain. (c) time-frequency domain (spectrogram).
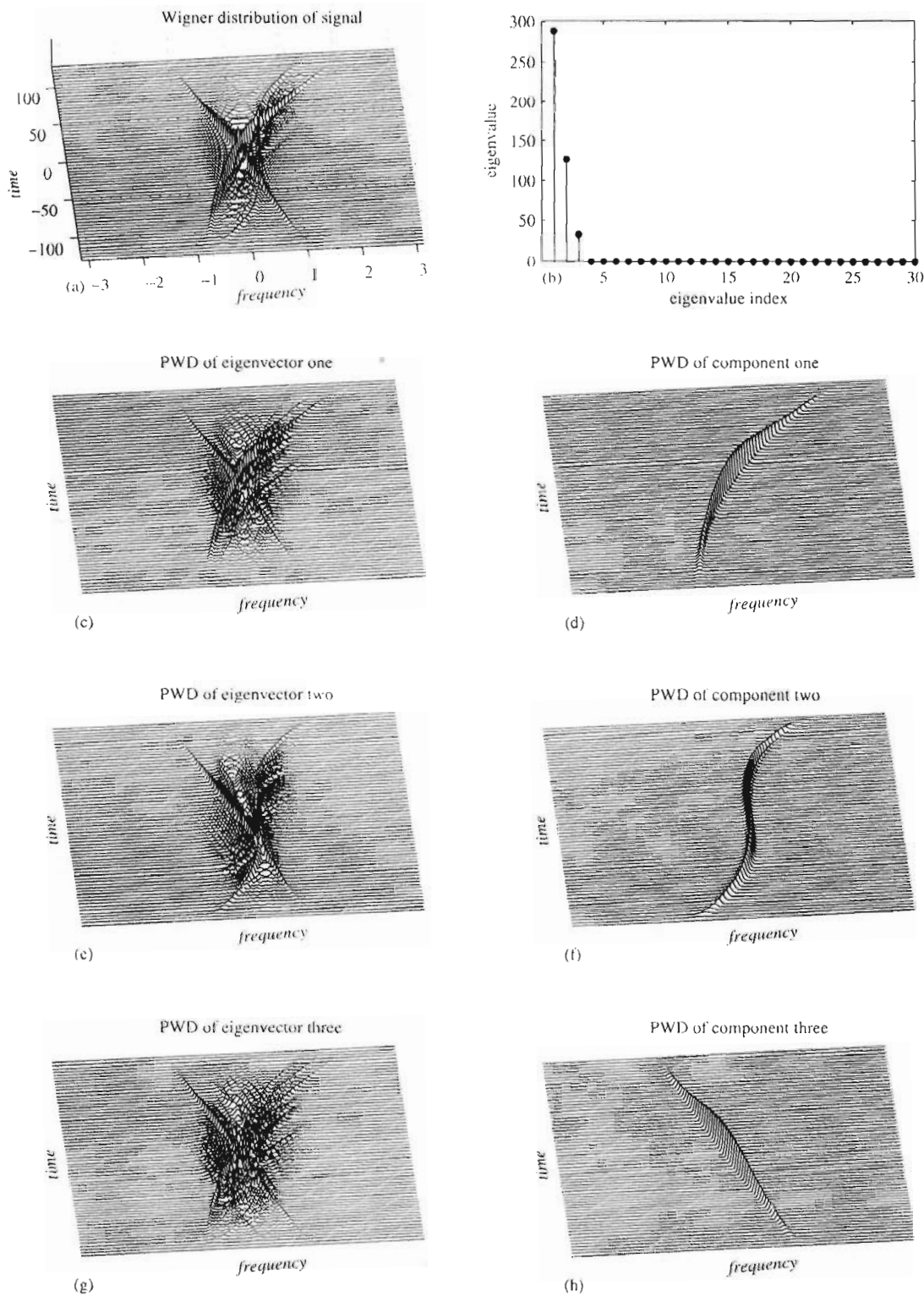
Wigner distribution of signal

(a)

(b)

PWD of eigenvector one

(c)

PWD of component one

(d)

PWD of eigenvector two

(e)

PWD of component two

(f)

PWD of eigenvector three

(g)

PWD of component three

(h)

Fig. 5. Decomposition of a multivariate signal from Example 3 with $N = 4$, having three components (auto-terms). (a) Wigner distribution of the signal. (b) Eigenvalues of the autocorrelation matrix **R**. (c), (e) and (g): PWD of the first, second and third eigenvector; (d), (f) and (h) PWDs of extracted signal components.

Example 4. A multivariate signal $\mathbf{x}(t)$ consisted of three intersected components and two non-overlapping components in the TF plane, given by

$$x_i(t) = x_{1i}(t) + x_{2i}(t) + x_{3i}(t) + x_{4i}(t) + x_{5i}(t). \tag{25}$$

The signals from each of $N = 3$ channels are defined as follows

$$x_{1i}(t) = e^{-(t/96)^2} e^{j(-\pi(t/16)^2/5 \cdot \varphi_i)} \tag{26}$$

$$x_{2i}(t) = 1.2 e^{-(t/96)^2} e^{j(\pi(t/16)^3/32 \cdot 3\pi(t/16)^2/10 \cdot \varphi_{2i})} \tag{27}$$
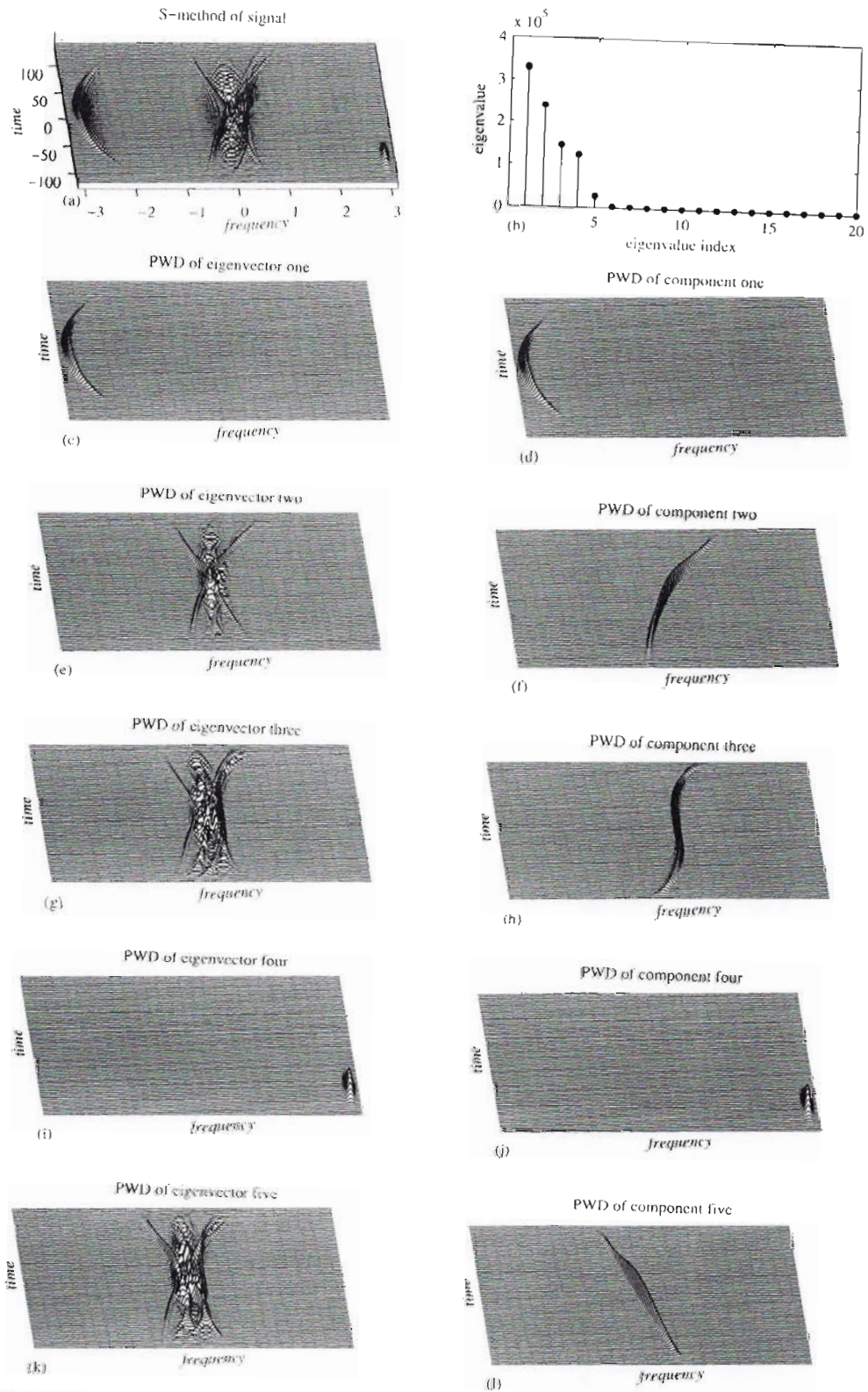
Fig. 6. Decomposition of multivariate five-component signal from Example 4 with $N = 3$, based on S-method as underlying TFR. (a) S-method of the analyzed signal. (b) eigenvalues of the autocorrelation matrix **R**. (c), (e), (g), (i), (k) PWDs of eigenvectors corresponding to the largest five eigenvalues. (d), (f), (h), (j) and (l) PWDs of extracted signal components.
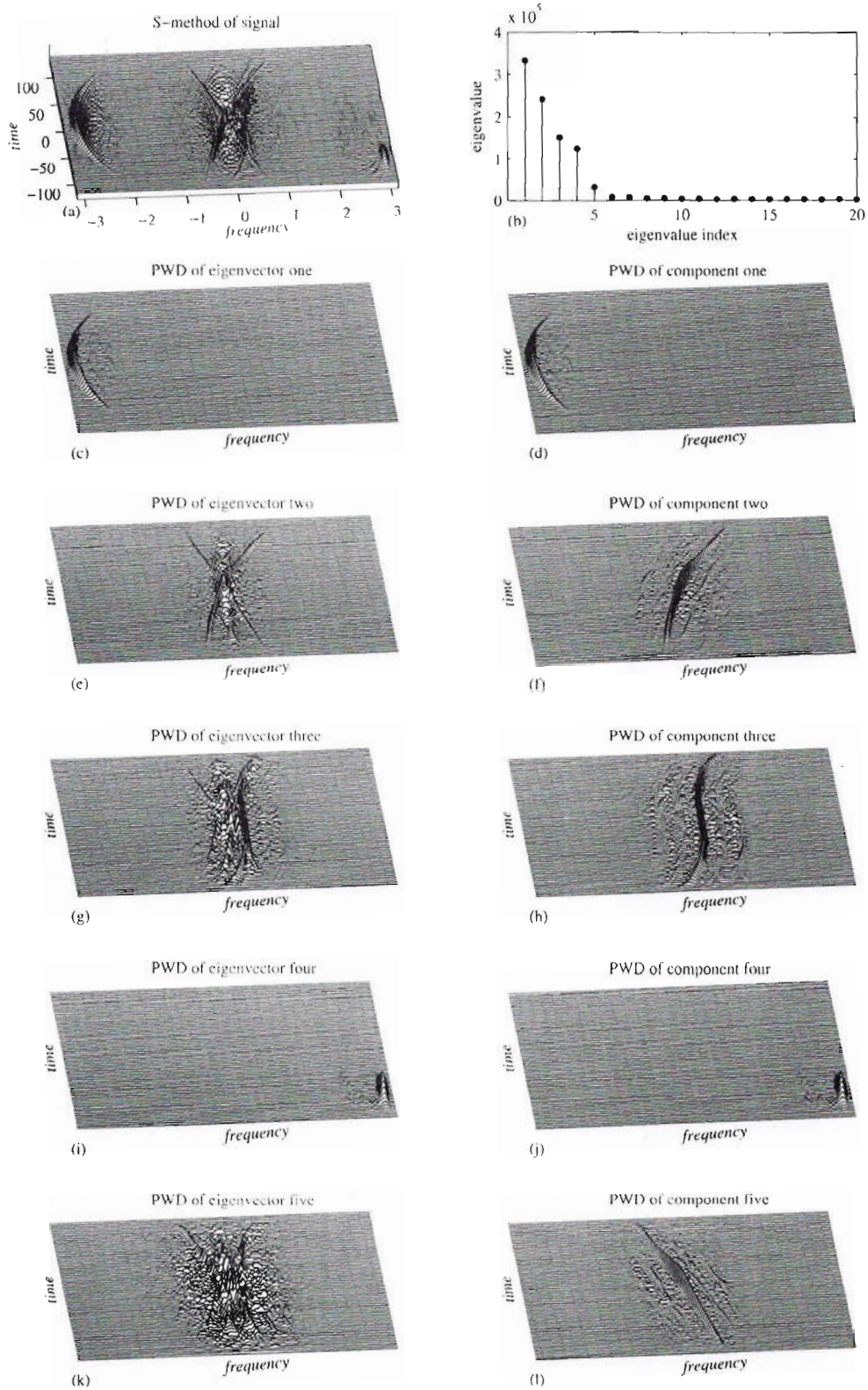
Fig. 7. Decomposition of the noisy multivariate five-component signal from Example 4 with $N = 3$, based on S-method as underlying TFR. (a) S-method of the analyzed signal. (b) eigenvalues of the autocorrelation matrix **R**. (c), (e), (g), (i), (k) PWDs of eigenvectors corresponding to the largest five eigenvalues. (d), (f), (h), (j) and (l) PWDs of extracted signal components.

$$x_{3i}(t) = 0.9e^{-(t/128)^2}e^{j(\pi(t/16)^4/200+\pi t/8+\varphi_{3i})} \qquad (28)$$

$$x_{4i}(t) = e^{-(t/16)^2}e^{j(3\pi t/4+\varphi_{4i})} \qquad (29)$$

$$x_{5i}(t) = e^{-(t/96)^2}e^{j(-6\pi(t/16)^2/25+\pi t/4+\varphi_{5i})} \qquad (30)$$

where $i = 1, 2, 3$ denotes the channel index. In this example the S-method is used as the initial TFR, as shown in Fig. 6 (a). Application of the S-method is crucial here since we have five components and a trivariate signal only. The S-method would be able to separate (decompose) all non-overlapping components from one realization. Then, the available realizations are used for the overlapped components only. The eigenvalue decomposition of the S-method inverse autocorrelation matrix **R** produced five eigenvectors, corresponding to the five largest eigenvalues shown in Fig. 6 (b).

As the two non-overlapping signal components are mutually orthogonal and with the rest of intersected components, according to the theory presented in [1], there are exactly two eigenvectors corresponding to these two components (one eigenvector for each component). The pseudo Wigner distribution for these two eigenvectors are shown in Fig. 6 (c) and (i). Therefore, these two components are easily extracted, as shown in Fig. 6 (d) and (j). The three remaining components are obtained based on the proper linear combination of the three corresponding eigenvectors using coefficients β_i obtained by the proposed minimization procedure. The pseudo Wigner distributions of these three remaining eigenvectors are shown in Fig. 6 (e), (g) and (k), whereas the separated components obtained based on their proper linear combination are shown in Fig. 6 (f), (h) and (l).

The same experiment was repeated for the noisy signal $\hat{\mathbf{x}}(t) = \mathbf{x}(t) + \epsilon(t)$. The signal from each channel corrupted by additive, white zero-mean complex-valued i.i.d. Gaussian noise $\epsilon_i(t)$ with the variance of real and imaginary parts $\sigma^2 = 0.15^2$. The SNR level for one (linear FM) component was 7.13 dB, that is, quite low. The results of the proposed decomposition approach are presented in Fig. 7, illustrating that the proposed algorithm is robust against the additive Gaussian noise influence.

7. Conclusion

Decomposition of non-stationary signals overlapping in the time-frequency plane is still an open problem. Exploiting the fact that the Wigner distribution of multivariate signals exhibits significant cross-term change due to their arbitrary phases whereas the auto-terms are added up in phase, we have revisited the time-frequency based signal components decomposition. In this paper, we have shown that even with a small number of signal channels, relative to the number of components, an accurate decomposition can be performed with an appropriate linear combination of the signal autocorrelation matrix eigenvectors. Next, the decomposition and eigenvector combination algorithms have been proposed. Their efficiency has been illustrated over several examples, which conclusively validate the capability of the proposed algorithm to perform a complete and accurate extraction of overlapped and non-overlapped components. The robustness of the proposed approach has been illustrated over an example on a noisy signal.

References

[1] L. Stanković, T. Thayaparan, M. Daković, Signal decomposition by using the S-method with application to the analysis of HF radar signals in sea-clutter, IEEE Trans. Signal Process. 54 (11) (2006) 4332–4342.

[2] Y. Wei, S. Tan, Signal decomposition by the S-method with general window functions, Signal Process. 92 (1) (2012) 288–293.

[3] Y. Yang, X. Dong, Z. Peng, W. Zhang, G. Meng, Component extraction for non-stationary multi-component signal using parameterized de-chirping and band-pass filter, IEEE SP Lett. 22 (9) (2015) 1373–1377.

[4] Y. Wang, Y. Jiang, ISAR imaging of maneuvering target based on the l-class of fourth-order complex-lag PWVD, in: IEEE Transactions on Geoscience and Remote Sensing, 48, 2010, pp. 1518–1527.

[5] I. Orović, S. Stanković, A. Draganić, Time-frequency analysis and singular value decomposition applied to the highly multicomponent musical signals, Acta Acustica United With Acustica 100 (2014) 1.

[6] L. Stanković, M. Daković, T. Thayaparan, Time-Frequency Signal Analysis with Applications, Artech House, 2013.

[7] V. Katkovnik, L. Stanković, Instantaneous frequency estimation using the Wigner distribution with varying and data driven window length, IEEE Trans. Signal Process. 46 (9) (1998) 2315–2325.

[8] V.N. Ivanović, M. Daković, L. Stanković, Performance of quadratic time-frequency distributions as instantaneous frequency estimators, IEEE Trans. Signal Process. 51 (1) (2003) 77–89.

[9] A. Ahrabian, D. Looney, L. Stanković, D. Mandic, Synchrosqueezing-based time-frequency analysis of multivariate data, Signal Process. 106 (2015) 331–341.

[10] J.M. Lilly, S.C. Olhede, Analysis of modulated multivariate oscillations, IEEE Trans. Signal Process. 60 (2) (2012) 600–612.

[11] A. Omidvarnia, B. Boashash, G. Azemi, P. Colditz, S. Vanhatalo, Generalised phase synchrony within multivariate signals: an emerging concept in time-frequency analysis, in: IEEE International Conference on Acoustics, Speech and Signal Processing (ICASSP), Kyoto, 2012, pp. 3417–3420.

[12] J.M. Lilly, S.C. Olhede, Bivariate instantaneous frequency and bandwidth, IEEE Trans. Signal Process. 58 (2) (2010) 591–603.

[13] B. Boashash, Estimating and interpreting the instantaneous frequency of a signal. I. fundamentals, Proc. IEEE 80 (4) (1992) 520–538, doi:10.1109/5.135376.

[14] J.C. Wood, D.T. Barry, Radon transformation of time-frequency distributions for analysis of multicomponent signals, IEEE Trans. Signal Process. 42 (11) (1994) 3166–3177.

[15] G. Lopez-Risueno, J. Grajal, O. Yeste-Ojeda, Atomic decomposition-based radar complex signal interception, IEE Proc. Radar, Sonar Navig. 150 (4) (2003) 323–331.

[16] L. Stanković, M. Daković, T. Thayaparan, V. Popović-Bugarin, Inverse radon transform based micro-Doppler analysis from a reduced set of observations, IEEE Trans. AES 51 (2) (2015) 1155–1169.

[17] M. Daković, L. Stanković, Estimation of sinusoidally modulated signal parameters based on the inverse radon transform, in: ISPA 2013, Trieste, Italy, 2013, pp. 302–307.

[18] D.P. Mandic, N.u. Rehman, Z. Wu, N.E. Huang, Empirical mode decomposition-based time-frequency analysis of multivariate signals: the power of adaptive data analysis, IEEE Signal Process. Mag. 30 (2013) 74–86.

[19] S.M.U. Abdullah, N.u. Rehman, M.M. Khan, D.P. Mandic, A multivariate empirical mode decomposition based approach to pansharpening, IEEE Trans. Geosci. Remote Sens. 53 (7) (2015) 3974–3984.

[20] A. Hemakom, A. Ahrabian, D. Looney, N.u. Rehman, D.P. Mandic, Nonuniformly sampled trivariate empirical mode decomposition, in: IEEE International Conference on Acoustics, Speech and Signal Processing (ICASSP 2015), South Brisbane, QLD, 2015, pp. 3691–3695.

[21] G. Wang, C. Teng, K. Li, Z. Zhang, X. Yan, The removal of EOG artifacts from EEG signals using independent component analysis and multivariate empirical mode decomposition, IEEE J. Biomed. Health Inf. 20 (5) (2016) 1301–1308.

[22] S. Tavildar, A. Ashrafi, Application of multivariate empirical mode decomposition and canonical correlation analysis for EEG motion artifact removal, in: 2016 Conference on Advances in Signal Processing (CASP), Pune, 2016, pp. 150–154.

[23] Y. Zhang, M.G. Amin, B.A. Obeidat, Polarimetric array processing for nonstationary signals, in: Adaptive Antenna Arrays: Trends and Applications, Springer, 2004, pp. 205–218.

[24] L. Stanković, A measure of some time-frequency distributions concentration, Signal Process. 81 (2001) 621–631.

[25] J.C. Spall, Introduction to Stochastic Search and Optimization, Wiley, ISBN 0-471-33052-3.

[26] J. Larson, S.M. Wild, A batch, derivative-free algorithm for finding multiple local minima, Optim. Eng. 17 (1) (2016) 205228, doi:10.1007/s11081-015-9289-7.

[27] A. Neumaier, Complete search in continuous global optimization and constraint satisfaction, Acta Numerica 13 (1) (2004).

[28] W. Hu, K. Wu, P.P. Shum, N.I. Zheludev, C. Soci, All-optical implementation of the ant colony optimization algorithm, Sci. Rep. 6 (2016), doi:10.1038/srep26283.

[29] S. Kirkpatrick, C.D. Gelatt, M.P. Vecchi, Optimization by simulated annealing, Science 220 (4598) (1983) 671–680, doi:10.1126/science.220.4598.671.

[30] R. Chelouah, P. Siarry, Genetic and nelder-mead algorithms hybridized for a more accurate global optimization of continuous multiminima functions, Eur. J. Oper. Res. 148 (2) (2003) 335–348.

[31] A. Cichocki, S. Amari, Adaptive Blind Signal and Image Processing: Learning Algorithms and Applications, 1, John Wiley and Sons, 2002, pp. 191–193.

Gradient-based signal reconstruction algorithm in Hermite transform domain

M. Brajović, I. Orović>◁, M. Daković and S. Stanković

An algorithm for compressive sensing reconstruction of signals in the Hermite expansion domain is proposed. The compressive sensing problem is formulated in the Hermite framework, allowing fast and efficient reconstruction of missing data by exploiting the concentration of signal's representation in the Hermite basis.

Introduction: The Hermite expansion approach has drawn significant attention in certain signal processing applications where classical tools, including also the Fourier transform, are not suitable for analysis. Namely, the Hermite expansion is an orthogonal transform used in image processing, tomography, analysis of protein structure, biomedicine [1–3]. The Hermite functions have been used as a suitable basis for representation and compression of QRS complexes of ECG signals, important for diagnosis and medical treatment. Particularly, the application in compression algorithms shows that the reconstruction of ECG signals can be done using a few Hermite coefficients [1].

Compressive sensing (CS) as an alternative sampling theory assumes signal sparsity in a certain transform domain to achieve successful reconstruction of missing data. A reduced set of observations in CS may appear as a consequence of a sampling strategy, or by omitting samples highly corrupted by noise. The reconstructed signal can be obtained by using the ℓ_1-norm minimisation via convex optimisation algorithms [4–6], which could be complex in terms of the realisation and the number of iterations. Here, we provide an iterative reconstruction approach based on a steepest descent method using ℓ_1-norm minimisation in the Hermite transform domain. Namely, the CS framework is defined in the context of the Hermite expansion, while the achieved results demonstrate successful reconstruction using the gradient-based solution [7]. The proposed approach provides faster performance compared with the other convex algorithms such as the commonly used primal-dual method within the ℓ_1-magic toolbox [8].

Hermite expansion: The pth order Hermite function can be related with the pth order Hermite polynomial:

$$\psi_p(t, \sigma) = \left(\sigma 2^n n! \sqrt{\pi}\right)^{-1/2} e^{-t^2/2} H_p\left(\frac{t}{\sigma}\right). \tag{1}$$

where the parameter σ can be used to stretch or compress Hermite functions, to match the analysed signal [1].

A signal representation using the Hermite basis is referenced as Hermite expansion [1–3]:

$$f(t) = \sum_{p=0}^{\infty} c_p \psi_p(t, \sigma). \tag{2}$$

For a continuous signal $f(t)$, an infinite number $N \rightarrow \infty$ of Hermite functions is needed for an accurate expansion. However, in practice, a finite number of N Hermite functions is used, as an approximation of the signal. The pth order Hermite coefficient c_p is defined as:

$$c_p = \int_{-\infty}^{\infty} f(t) \psi_p(t) dt. \tag{3}$$

If Hermite functions are sampled at zeros of the Nth order Hermite polynomial, then the summation (2) becomes a finite orthonormal representation for the case of discrete signals [1]. In numerical calculation, the quadrature approximations (as a discrete form of the Hermite expansion) are used to obtain integral in (3). For instance, the Gauss–Hermite quadrature is defined as:

$$c_p \approx \frac{1}{N} \sum_{n=1}^{N} \frac{\psi_p(x_n)}{\left[\psi_{N-1}(x_n)\right]^2} f(x_n), \tag{4}$$

where x_n denotes zero of the Nth Hermite polynomial. For a signal of length N, the complete set of discrete Hermite functions consists of exactly N functions [1]. In some applications, a smaller number of Hermite functions (compared with signal length) can be used [·]. To simplify the notation, in the sequel the argument x_n will be replaced with the order n (of the Hermite polynomial zeros). The expansion using N Hermite functions can be written in matrix form. First, we

define the Hermite transform matrix W_H (of size $N \times N$):

$$W_H = \frac{1}{N} \begin{bmatrix} \dfrac{\psi_0(1)}{(\psi_{N-1}(1))^2} & \dfrac{\psi_0(2)}{(\psi_{N-1}(2))^2} & \cdots & \dfrac{\psi_0(N)}{(\psi_{N-1}(N))^2} \\[2mm] \dfrac{\psi_1(1)}{(\psi_{N-1}(1))^2} & \dfrac{\psi_1(2)}{(\psi_{N-1}(2))^2} & \cdots & \dfrac{\psi_1(N)}{(\psi_{N-1}(N))^2} \\[2mm] \vdots & \vdots & \ddots & \vdots \\[2mm] \dfrac{\psi_{N-1}(1)}{(\psi_{N-1}(1))^2} & \dfrac{\psi_{N-1}(2)}{(\psi_{N-1}(2))^2} & \cdots & \dfrac{\psi_{N-1}(N)}{(\psi_{N-1}(N))^2} \end{bmatrix} \tag{5}$$

If the vector of Hermite coefficients is: $c = [c_0, c_1, ..., c_{N-1}]^T$, and vector of M signal samples is: $f = [f(1), f(2), ..., f(N)]^T$, then we have:

$$c = W_H f. \tag{6}$$

Having in mind the Gauss–Hermite approximation (4), the inverse matrix W_{H-1} contains N Hermite functions is given by:

$$\Psi = \begin{bmatrix} \psi_0(1) & \psi_0(2) & \cdots & \psi_0(N) \\ \psi_1(1) & \psi_1(2) & \cdots & \psi_1(N) \\ \vdots & \vdots & \ddots & \vdots \\ \psi_{N-1}(1) & \psi_{N-1}(2) & \cdots & \psi_{N-1}(N) \end{bmatrix} = W_H^{-1}. \tag{7}$$

Now, the Hermite expansion can be defined as follows:

$$f = W_H^{-1} c = \Psi c. \tag{8}$$

CS problem formulation: Let us assume that the CS is done using a random selection of M_A signal values modelled by a random measurement matrix Φ:

$$y_{cs} = \Phi f = \Phi \Psi c = A_{cs} c. \tag{9}$$

Here, y_{cs} denotes the vector of available samples, matrix A_{cs} is obtained from the inverse Hermite transform matrix Ψ by omitting the rows corresponding to the missing samples. Hence, we deal with undetermined system of M_A linear equations and N unknowns. Although this system may have infinitely many solutions, the idea is to search for the sparsest one. Thus, the reconstruction problem can be defined as:

$$\min \|c\|_{\ell_1} \text{ subject to } y_{cs} = A_{cs} c. \tag{10}$$

Gradient based reconstruction algorithm: A previous minimisation problem can be solved by adapting the use of gradient descent [7] in the Hermite transform domain. The idea of the proposed method is to iteratively recover the values of missing samples, by a small appropriately estimated gradient-based step. The ℓ_1 norm behaviour is examined in the Hermite expansion domain acting as a sparsity measure.

Assume that the positions of available samples are defined by the set Θ, where Θ consists of $M_A \ll N$ elements and $\Theta \subset N = \{1, 2,..., N\}$. Denote by n_i indices defined by:

$$n_i = \begin{cases} i, & i \in \Theta \\ 0, & i \notin \Theta \end{cases}.$$

The missing samples positions form the set $\bar{\Theta}$, such that $\Theta \cup \bar{\Theta} = N$. The assumed signal sparsity is $K \ll N$.

The algorithm starts from the column vector y which contains available samples y_{cs} and zero values at the positions of missing samples. Hence, y can be defined as: $y(n) = f(n)$, for $n \in \Theta$, otherwise $y(n) = 0$ (with $f(n)$ being the original signal samples). Assume that the initial value of the step is $\Delta = \max(|y|)$. Each iteration (denoted by k) consists of the following steps.

(i) Form a matrix Y with N repeated vectors y:

$$Y^{(k)} = y^{(k)} 1_{1 \times N} = \begin{bmatrix} y^{(k)} & y^{(k)} & \cdots & y^{(k)} \end{bmatrix},$$

where the notation $1_{1 \times N}$ is used for all-ones matrix of dimensions $1 \times N$.

(ii) Calculate two test matrices as follows:

$$Y_{\Delta+}^{(k)} = \begin{bmatrix} y_{1\Delta+}^{(k)} & y_{2\Delta+}^{(k)} & \cdots & y_{N\Delta+}^{(k)} \end{bmatrix} = Y^{(k)} + \Delta \tag{11}$$

$$Y_{\Delta-}^{(k)} = \begin{bmatrix} y_{1\Delta-}^{(k)} & y_{2\Delta-}^{(k)} & \cdots & y_{N\Delta-}^{(k)} \end{bmatrix} = Y^{(k)} - \Delta \tag{12}$$

For better understanding, the previous matrices can be written in an expanded form given by:

$$Y_{\Delta\pm}^{(k)} = Y^{(k)} \pm \Delta = y^{(k)}1_{1\times N} \pm \Delta = \begin{bmatrix} y^{(k)}(1) & & y^{(k)}(1) \\ y^{(k)}(2) & & y^{(k)}(2) \\ \vdots & \cdots & \vdots \\ y^{(k)}(N) & & y^{(k)}(N) \end{bmatrix}$$

$$\pm \Delta \begin{bmatrix} \delta(1-n_1) & 0 & \cdots & 0 \\ 0 & \delta(2-n_2) & \cdots & 0 \\ \vdots & \vdots & \ddots & \vdots \\ 0 & 0 & \cdots & \delta(N-n_N) \end{bmatrix}_{N\times N}$$

where Δ is obtained by multiplying constant Δ by a diagonal matrix with elements $\delta(n-n_i)$, for $n, i = \{1, 2, \ldots, N\}$.

(iii) Based on calculated test matrices $Y_{\Delta+}^{(k)}$ and $Y_{\Delta-}^{(k)}$, the gradient vector G is calculated as:

$$G^{(k)} = \frac{1}{2\Delta}\left[\left\|\mathcal{H}^{(c)}\left\{Y_{\Delta+}^{(k)}\right\}\right\|_{\ell_1}^{(c)} - \left\|\mathcal{H}^{(c)}\left\{Y_{\Delta-}^{(k)}\right\}\right\|_{\ell_1}^{(c)}\right]$$

$$= \frac{1}{2\Delta}\left[\left[\left\|W_H y_{1\Delta+}^{(k)}\right\|_{\ell_1} \quad \left\|W_H y_{1\Delta+}^{(k)}\right\|_{\ell_1} \quad \cdots \quad \left\|W_H y_{1\Delta+}^{(k)}\right\|_{\ell_1}\right]\right.$$

$$\left. -\left[\left\|W_H y_{1\Delta-}^{(k)}\right\|_{\ell_1} \quad \left\|W_H y_{1\Delta-}^{(k)}\right\|_{\ell_1} \quad \cdots \quad \left\|W_H y_{1\Delta-}^{(k)}\right\|_{\ell_1}\right]\right] \tag{13}$$

with $\mathcal{H}^{(c)}\{\cdot\}$ being the operator that calculates the Hermite coefficients along the matrix columns, and operator $\|\cdot\|_{\ell_1}^{(c)}$ calculates ℓ_1 norm for each column separately. Note that gradient vector has zero values for signal samples at available samples positions.

(iv) Finally, the signal vector y is adjusted as follows:

$$y^{(k+1)} = y^{(k)} + G^{(k)}/(2\Delta) \tag{14}$$

As G is proportional to the error $y - f$, the missing values will converge to the true signal values. To obtain a high reconstruction precision, the step Δ should be reduced when adjustments in (14) does not improve precision. This can be detected either by measuring reconstructed signal sparsity or by detecting oscillatory nature of the adjustments [7].
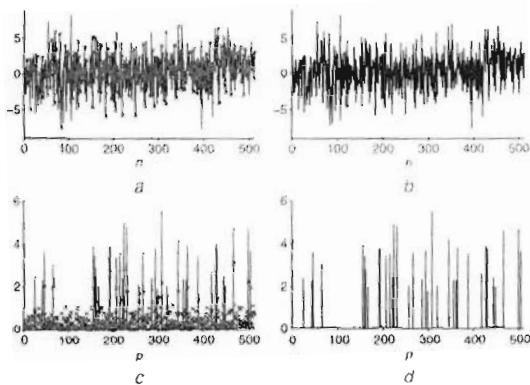

Fig. 1 *Reconstruction results*

a Desired signal (solid line) and available samples (crosses)
b Reconstructed signal
c Desired Hermite coefficients (solid line) and coefficients of signal with missing samples (crosses)
d Hermite coefficients of reconstructed signal

Experimental evaluation: Let us observe the signal in the form:

$$y_s(n) = \sum_{i=1}^{K} A_i \psi_{p_i}(n) \tag{15}$$

which is sparse in the Hermite transform domain with $K = 35$ components. The signal is corrupted by white Gaussian noise, with SNR = 30 dB, and only 50% of samples are available. The amplitudes A_i of components and the orders of Hermite functions p_i are randomly chosen. The reconstruction is done using the proposed approach (Fig. 1), with MSE $\sim 10^{-5}$. We may observe that, although the signal is not strictly sparse, the exact reconstruction is achieved. Compared

with the ℓ_1-magic algorithm [8] which belongs to the group of convex optimisations as well, the processing time (in Matlab) for the proposed algorithm is 2 to 4 times lower (depending on the random measurements and amplitudes). Moreover, the proposed algorithm will progressively accelerate as the number of available samples increases.

The algorithm is examined also on a real QRS complex of the ECG signals [9], shown in Fig. 2. To achieve sparsity, QRS complex needs to be sampled at the points proportional to the roots of Hermite polynomial. The sparsification is done according to the procedure in [1] to obtain signal values at adequate position. The error due to sparsification is 5.23%, which is medically acceptable as long as it is less than 10% [1]. The reconstruction MSE is 1.262×10^{-7} obtained after 18 iterations of the proposed algorithm. The reconstructed results are compared with original signal in Fig. 2.
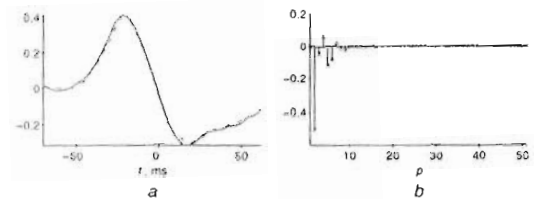

Fig. 2 *Reconstruction results for ECG signal (QRS complex)*

a Desired (solid line) and reconstructed signal (dashed line)
b Hermite coefficients of desired (solid line) and reconstructed signal (crosses)

Conclusion: A gradient descent algorithm based on the Hermite transform domain solves the problem of CS reconstruction for signals that exhibit sparsity in the Hermite basis domain. The highly accurate algorithm performance is proven on both synthetic and real data.

One or more of the Figures in this Letter are available in colour online.

M. Brajović, I. Orović, M. Daković and S. Stanković (*University of Montenegro, Faculty of Electrical Engineering, Podgorica 81000, Montenegro*)

✉ E-mail: irenao@ac.me

References

1 Sandryhaila, A., Saba, S., Puschel, M., *et al.*: 'Efficient compression of QRS complexes using hermite expansion', *IEEE Trans. Signal Process.*, 2012, **60**, (2), pp. 947–955, doi: 10.1109/TSP.2011.2173336
2 Leibon, G., Rockmore, D.N.W., Park Taintor, R., *et al.*: 'A fast hermite transform', *Theor. Comput. Sci.*, 2008, **409**, (2), pp. 211–228, doi: 10.1016/j.tcs.2008.09.010
3 Stankovic, S., Orovic, I., and Krylov, A.: 'The two-dimensional hermite s-method for high resolution inverse synthetic aperture radar imaging applications', *IET Signal Proc.*, 2010, 4, (4), pp. 352–362, doi: 10.1049/iet-spr.2009.0060
4 Candes, E., Romberg, J., and Tao, T.: 'Robust uncertainty principles: exact recovery from highly incomplete Fourier information', *IEEE Trans. Inf. Theory*, 2006, **52**, (2), pp. 489–509, doi: 10.1109/TIT.2005.862083
5 Wright, S.J.: 'Primal-dual interior-point methods' (SIAM Publications, Boston, 1997)
6 Davenport, M., Duarte, M., Eldar, Y., *et al.*: 'Introduction to compressed sensing', 'Compressed sensing: theory and applications' (Cambridge University Press, Cambridge, 2012)
7 Stankovic, L., Dakovic, M., and Vujovic, S.: 'Adaptive variable step algorithm for missing samples recovery in sparse signals', *IET Signal Process.*, 2014, 8, (3), pp. 246–256, doi: 10.1049/iet-spr.2013.0385
8 Candes, E., and Romberg, J.: 'ℓ_1-magic: recovery of sparse signals via Convex programming', 2005, available at www.acm.caltech.edu/l1magic/downloads/l1magic.pdf
9 PhysioNet: MIT-BIH ECG Compression Test Database, http://www.physionet.org/physiobank/database/edb, accessed February 2015

Hindawi

Research Article

Error in the Reconstruction of Nonsparse Images

Miloš Brajović [iD],[1] **Isidora Stanković** [iD],[1,2] **Miloš Daković** [iD],[1]
Cornel Ioana [iD],[2] and **Ljubiša Stanković** [iD] [1]

[1]Faculty of Electrical Engineering, University of Montenegro, 81000 Podgorica, Montenegro
[2]GIPSA Lab, INP, University Grenoble Alpes, 38400 Saint-Martin-d'Hères, France

Correspondence should be addressed to Miloš Daković; milos@ac.me

Sparse signals, assuming a small number of nonzero coefficients in a transformation domain, can be reconstructed from a reduced set of measurements. In practical applications, signals are only approximately sparse. Images are a representative example of such approximately sparse signals in the two-dimensional (2D) discrete cosine transform (DCT) domain. Although a significant amount of image energy is well concentrated in a small number of transform coefficients, other nonzero coefficients appearing in the 2D-DCT domain make the images be only approximately sparse or nonsparse. In the compressive sensing theory, strict sparsity should be assumed. It means that the reconstruction algorithms will not be able to recover small valued coefficients (above the assumed sparsity) of nonsparse signals. In the literature, this kind of reconstruction error is described by appropriate error bound relations. In this paper, an exact relation for the expected reconstruction error is derived and presented in the form of a theorem. In addition to the theoretical proof, the presented theory is validated through numerical simulations.

1. Introduction

Signals that can be characterized by a small number of nonzero coefficients are referred to as sparse signals [1–11]. These signals can be reconstructed from a reduced set of measurements [1–25]. The measurements represent linear combination of the sparsity (transform) domain coefficients [1, 7, 24]. Signal samples can be considered as measurements (observations) in the case when a linear signal transform is the sparsity domain. Signal sparsity in a transformation domain can be observed in a number of important applications. For example, ISAR images are commonly sparse in the two-dimensional Fourier transform domain, whereas digital images are well known for their good concentration in the domain of two-dimensional (2D) discrete cosine transform (DCT) [8, 21–24].

The idea of reduced number of observations is studied within the compressed sensing (CS) theory and the sparse signal processing framework. The reduced number of measurements may appear due to different causes. In the CS applications, it arises as a consequence of intentional sampling strategy, aiming to reduce the signal acquisition time, equipment load, and subject exposure to potentially dangerous radiation during the acquisition in biomedical applications, or, simply, there is a particular interest to reduce the amount of acquired samples while preserving the complete information (compression) [1–15]. In certain cases, physical unavailability can be a cause of a reduced number of measurements. In many applications, strong disturbances (noise) can significantly corrupt the signal samples. Such signals are processed by detecting and intentionally neglecting the corrupted measurements [7, 9, 23]. Regardless of their unavailability reasons, under certain reasonable conditions, missing samples can be reconstructed using well developed CS methods and algorithms [1, 2].

The DCT is an important and frequently used tool in signal processing [21–27]. Many signal classes can be more compactly represented in the DCT domain than in the Fourier domain. Due to its superior compressibility, the 2D-DCT is one of the most exploited transforms in the compression of digital images [24]. Moreover, this transform domain has been convenient for the reconstruction of digital images with missing pixels and/or noise corruption using the sparsity assumption [21–23]. Measuring the

2D-DCT coefficients concentration (using the ℓ_1-norm based measure) and varying missing samples values to obtain the sparsest possible solution leads to the prominent compressive sensing reconstruction results [20, 23]. In the orthogonal matching pursuit (OMP) framework, successful reconstruction is easily obtained if the coefficients corresponding to signal component positions are successfully identified [12, 28–30]. In that case, the true coefficient values can be calculated using the identified component positions and the 2D-DCT measurement matrix [9, 24]. However, it is important to note that, in practice, digital images are usually only approximately sparse or nonsparse in the 2D-DCT domain [21–24]. It means that besides the coefficients with significant values, carrying most of the signal energy, small valued coefficients may appear instead of zero-valued ones. As sparse recovery algorithms assume certain sparsity level, these coefficients will remain unreconstructed [8, 24]. This leads to inevitable reconstruction errors. The reduction of the amount of available samples manifests as a transform domain noise [7, 9]. During the reconstruction, this noise is completely cancelled out, if the sparsity assumption is strictly satisfied. However, if weak signal coefficients of a nonsparse signal remain unreconstructed, their contribution to the noise in the reconstructed coefficients remains. If a nonsparse signal is reconstructed with a reduced set of available samples, then the noise due to the missing samples in unreconstructed coefficients will be considered as an additive input noise in the reconstructed signal [8].

The existing compressive sensing literature provides only the general bounds for the reconstruction error for nonsparse signals (reconstructed with the sparsity assumption) [1, 2, 4, 5, 28]. The error bounds for the DFT and DCT are considered in [6] within the reconstruction uniqueness framework. In this paper, we present an exact relation for the expected squared error in approximately sparse or nonsparse signals in the 2D-DCT domain. It is assumed that these signals are reconstructed from a reduced set of observations, under the sparsity constraint. Missing measurements influence on the transform domain is modelled by an additive noise [7]. The noise originating from missing samples in each signal component is statistically modelled as a Gaussian stochastic process, and its mean-value and variance are determined. The results are further exploited in the derivation of the relation for the error in the reconstructed signal if the sparsity assumption is used for the reconstruction of nonsparse signals. The theory is illustrated and verified by numerical results.

The paper is organized as follows. Basic definitions regarding the 2D-DCT domain are provided in Section 2. In Section 3, the main result is presented in the form of a theorem which will be examined and proved in the next sections. In Section 4, the 2D-DCT transform is put into the framework of the reduced number of observations and the error of nonsparse images reconstruction is analyzed. In Section 5, the theory is validated with several numerical examples, while the concluding remarks are given at the end of the paper, along with Appendix with special cases.

2. Basic Definitions

Consider a 2D discrete signal (digital image) of size $M \times N$ denoted by $s(m, n)$. The 2D-DCT of this signal is defined by [24]

$$C(p, q) = \sum_{m=0}^{M-1} \sum_{n=0}^{N-1} s(m, n)\, \varphi_M(m, p)\, \varphi_N(n, q), \qquad (1)$$

where $p = 0, \ldots, M-1$ and $q = 0, \ldots, N-1$ are the transform coefficient indices, and

$$\varphi_M(m, p) = \sqrt{\frac{2}{M}} \cos\left(\frac{\pi(2m+1)p}{2M}\right), \quad p \neq 0$$
$$\varphi_N(n, q) = \sqrt{\frac{2}{N}} \cos\left(\frac{\pi(2n+1)q}{2N}\right), \quad q \neq 0 \qquad (2)$$

are the normalized basis functions. For $p = 0$ or $q = 0$ these functions are of the form $\varphi_M(m, 0) = \sqrt{1/M}$ and $\varphi_N(n, 0) = \sqrt{1/N}$, respectively. The corresponding inverse transform is given by

$$s(m, n) = \sum_{p=0}^{M-1} \sum_{q=0}^{N-1} C(p, q)\, \varphi_M(m, p)\, \varphi_N(n, q) \qquad (3)$$

with $m = 0, \ldots, M-1$, $n = 0, \ldots, N-1$. The 2D-DCT transform can be written in a matrix form as [24]

$$\mathbf{C} = \mathbf{\Phi s}, \qquad (4)$$

where $\mathbf{C}$ is the 2D-DCT coefficients matrix, $\mathbf{\Phi}$ is 2D-DCT transformation matrix, and s is the matrix containing pixel values of a digital image. For the inverse 2D-DCT the relation $s = \mathbf{\Psi C}$ holds, with $\mathbf{\Psi} = \mathbf{\Phi}^{-1}$.

An image of the form

$$s(m, n) = \sum_{l=1}^{K} A_l\, \varphi_M(m, p_l)\, \varphi_N(n, q_l) \qquad (5)$$

is sparse in the 2D-DCT domain if the number of nonzero 2D-DCT coefficients K is much smaller than the number of image pixels; that is, $K \ll MN$. The components are located at the DCT indices (p_l, q_l) with amplitudes A_l, $l = 1, 2, \ldots, K$.

Assume that only $N_A \leq MN$ randomly positioned pixels at $(m_i, n_i) \in \{(m_1, n_1), (m_2, n_2), \ldots, (m_{N_A}, n_{N_A})\} = \mathbf{N_A} \subseteq \mathbf{N} = \{(0, 0), (0, 1), \ldots, (M-1, N-1)\}$ are available. If we rearrange the available pixels $\mathbf{y}$ into a vector with elements

$$y(i) = s(m_i, n_i)$$
$$= \sum_{p=0}^{M-1} \sum_{q=0}^{N-1} C(p, q)\, \varphi_M(m_i, p)\, \varphi_N(n_i, q), \qquad (6)$$

where $i = 0, 1, \ldots, N_A$, we can write it in the matrix form as

$$\mathbf{y} = \mathbf{AC} \qquad (7)$$

representing the mathematical model for the compressive sampling procedure, where $\mathbf{A}$ is an $N_A \times MN$ measurement

matrix. It is defined as the partial inverse 2D-DCT matrix, containing rows of Ψ that correspond to the available pixel positions.

Compressive sensing reconstruction inherently assumes the signal sparsity. An image $s(m, n)$ is K-sparse in the 2D-DCT domain if only K of its 2D-DCT coefficients assume nonzero values. The nonzero coefficients at the positions $(p, q) \in \Pi_K = \{(p_1, q_1), (p_2, q_2), \ldots, (p_K, q_K)\}$ will be defined as $\mathbf{C}_K$.

The 2D-DCT of an image reconstructed under the K-sparsity assumption will be denoted by $\mathbf{C}_R$. This is a vector with K reconstructed nonzero coefficients at $(p, q) \in \Pi_K$.

An image is approximately sparse or nonsparse if the coefficients $C(p, q), (p, k) \notin \Pi_K$ are small or of the same order as the coefficients $C(p, q), (p, k) \in \Pi_K$, respectively. In that case, the vector $\mathbf{C}_K$ contains K largest values of $\mathbf{C}$. The vector $\mathbf{C}_K$ zero-padded up to the size of the original $\mathbf{C}$ and written in the same format as $\mathbf{C}$ will be denoted by $\mathbf{C}_{K0}$.

3. Reconstruction Error Energy

The main result of the paper providing the exact formulation of the expected squared reconstruction error in the case of nonsparse images will be given in the form of a theorem.

Theorem 1. *Assume an image nonsparse in the 2D-DCT domain, with largest amplitudes A_l, $l = 1, 2, \ldots, K$. Assume that only N_A out of total MN samples are available, where $1 \ll N_A < MN$. Also assume that the image is reconstructed under the assumption as it was K-sparse. The energy of error in the K reconstructed coefficients $\|\mathbf{C}_K - \mathbf{C}_R\|_2^2$ is related to the energy of unreconstructed components $\|\mathbf{C}_{K0} - \mathbf{C}\|_2^2$ coefficients as follows:*

$$\|\mathbf{C}_K - \mathbf{C}_R\|_2^2 = \frac{K(MN - N_A)}{N_A(MN - 1)} \|\mathbf{C}_{K0} - \mathbf{C}\|_2^2, \quad (8)$$

where

$$\|\mathbf{C}_K - \mathbf{C}_R\|_2^2 = \frac{K(MN - N_A)}{N_A(MN - 1)} \sum_{l=K+1}^{MN} A_l^2,$$

$$\|\mathbf{C}_{K0} - \mathbf{C}\|_2^2 = \sum_{l=K+1}^{MN} A_l^2. \quad (9)$$

The theorem will be proved in the next section.

4. The Reconstruction Process and the Proof

The proof will be presented through four subsections. In the first subsection, we will define the 2D-DCT transform put into the framework of the reduced number of observations. Then, we will describe how the missing pixels affect other components in mono- and multicomponent cases, respectively. Finally, the reconstruction under the assumption that the signal is K-sparse is considered.

4.1. Initial Estimate. The initial (norm-two based) 2D-DCT estimation uses the available pixels only

$$C_0(p, q) = \sum_{(m,n)\in\mathbf{N}_A} s(m, n)\, \varphi_M(m, p)\, \varphi_N(n, q), \quad (10)$$

where $p = 0, 1, \ldots, M-1$, $q = 0, 1, \ldots, N-1$. The same results are obtained if the missing (unavailable) pixels assume zero values [7]. In a matrix form we can write

$$\mathbf{C}_0 = \mathbf{A}^T \mathbf{y}. \quad (11)$$

The coefficients in (10) act as random variables, with different statistical properties at positions of the image components, $(p, q) = (p_l, q_l)$, and positions not corresponding to image components, $(p, q) \neq (p_l, q_l)$.

4.2. Noise-Only Coefficients in Monocomponent Signals. We will first observe the monocomponent signal case, that is, when $K = 1$, and then generalize the result for multicomponent signals. Without loss of generality, we will assume that the amplitude is $A_1 = 1$. From (5) and (10) we get

$$C_0(p, q)$$
$$= \sum_{(m,n)\in\mathbf{N}_A} \varphi_M(m, p_1)\, \varphi_N(n, q_1)\, \varphi_M(m, p)\, \varphi_N(n, q). \quad (12)$$

The variable

$$x_{p_1 q_1}(m, n, p, q)$$
$$= \varphi_M(m, p_1)\, \varphi_N(n, q_1)\, \varphi_M(m, p)\, \varphi_N(n, q) \quad (13)$$

is random for random values of (m, n). Its statistical properties for $(p, q) \neq (p_1, q_1)$ are studied next. Special cases are considered in Appendix. The initial 2D-DCT estimate can be written in the form

$$C_0(p, q) = \sum_{(m,n)\in\mathbf{N}_A} x_{p_1 q_1}(m, n, p, q). \quad (14)$$

When $(p, q) \neq (p_1, q_1)$, the 2D-DCT coefficients correspond to nonsignal (noise) position and $C_0(p, q)$ behaves as a random Gaussian variable [7]. Using the basis functions orthogonality

$$\sum_{m=0}^{M-1}\sum_{n=0}^{N-1} x_{p_1 q_1}(m, n, p, q) = \delta(p - p_1, q - q_1) \quad (15)$$

and the fact that values of $x_{p_1 q_1}(m, n, p, q)$ are equally distributed, it can be concluded that the mean-value of $C_0(p, q)$ is equal to zero:

$$\mu_{C_0(p,q)} = E\{C_0(p, q)\} = 0, \quad (p, q) \neq (p_1, q_1). \quad (16)$$

In the case of the coefficient corresponding to the image component, using the same orthogonality property and the assumption of equal distribution of values $x_{p_1 q_1}(m, n, p, q)$, it follows that

$$\mu_{C_0(p,q)} = E\{C_0(p, q)\} = \frac{N_A}{MN}, \quad (p, q) = (p_1, q_1). \quad (17)$$

For the zero-mean random variable, the variance definition is

$$\sigma^2_{C_0(p,q)} = E\left\{ \sum_{(m,n)\in N_A} x^2_{p_1 q_1}(m,n,p,q) \right.$$
$$+ \sum_{(m,n)\in N_A} \sum_{\substack{(i,j)\in N_A \\ (i,j)\neq(m,n)}} x_{p_1 q_1}(m,n,p,q) \tag{18}$$
$$\left. \cdot x_{p_1 q_1}(i,j,p,q) \right\}.$$

As in the case when $(p,q) \neq (p_1,q_1)$ is observed, it can be concluded that

$$\sum_{m=0}^{M-1}\sum_{n=0}^{N-1} x_{p_1 q_1}(m,n,p,q) = 0. \tag{19}$$

Multiplying the left and right side of (19) by $x_{p_1 q_1}(i,j,p,q)$ and taking the expectation of both sides we get

$$E\left\{ \sum_{m=0}^{M-1}\sum_{n=0}^{N-1} x_{p_1 q_1}(m,n,p,q)\, x_{p_1 q_1}(i,j,p,q) \right\} = 0, \tag{20}$$

with $(i,j) \in N$. Values $x_{p_1 q_1}(m,n,p,q)$ are equally distributed. Therefore, terms $E\{x_{p_1 q_1}(m,n,p,q)x_{p_1 q_1}(i,j,p,q)\}$ for $(m,n) \neq (i,j)$ are the same and equal to a constant D. The total number of these terms is $MN-1$. Further, based on (20) we get

$$(MN-1)D + E\left\{ x^2_{p_1 q_1}(m,n,p,q) \right\} = 0. \tag{21}$$

The initial variance definition can be written as

$$\sigma^2_{C_0(p,q)} = N_A E\left\{ x^2_{p_1 q_1}(m,n,p,q) \right\} + \left(N_A^2 - N_A \right)D, \tag{22}$$

as there are exactly N_A expectations with quadratic terms in the first summation and $N_A(N_A - 1)$ terms in the second variance summation equal to D. In order to determine the unknown term $E\{x^2_{p_1 q_1}(m,n,p,q)\}$, several special cases should be taken into account. Special cases of the 2D-DCT indices are considered in Appendix.

Consider the general case when $p \neq p_1$, $p \neq M - p_1$, $q \neq q_1$, $q \neq N - q_1$ are satisfied. Then

$$E\left\{ x^2_{p_1 q_1}(m,n,p,q) \right\} = E\left\{ \varphi^2_M(m,p_1)\varphi^2_N(n,q_1) \right\}$$
$$\times E\left\{ \varphi^2_M(m,p)\varphi^2_N(n,q) \right\} \tag{23}$$
$$= \frac{1}{M^2 N^2}.$$

holds. Incorporating this result into (21) we get that

$$D = -\frac{1}{M^2 N^2}\frac{1}{MN-1}. \tag{24}$$

Further, based on (22) the variance can be written as

$$\sigma^2_{C_0(p,q)} = \frac{N_A(MN - N_A)}{M^2 N^2(MN-1)}. \tag{25}$$

This result also holds when $(p_1,q_1) = (0,0)$. Note that when $A_1 \neq 1$, the result is multiplied by A_1^2.

It can be easily concluded that the average value of the variance (A.12) when all special cases from Appendix are included is constant and equal to

$$\sigma^2_C = A_1^2 \frac{N_A(MN - N_A)}{M^2 N^2(MN-1)^2}\left(MN - \frac{21}{4} \right). \tag{26}$$

As $MN \gg 1$, an accurate approximation for the average variance of noise-only coefficients follows

$$\sigma^2_N = \bar{\sigma}^2_{C_0} \approx A_1^2 \frac{N_A(MN - N_A)}{M^2 N^2(MN-1)}. \tag{27}$$

4.3. Noise-Only Coefficients in Multicomponent Signals.

In the multicomponent signal case, the observed random variable becomes

$$C_0(p,q) = \sum_{(m,n)\in N_A}\sum_{l=1}^{K} A_l \varphi_M(m,p_l)\varphi_N(n,q_l) \tag{28}$$
$$\times \varphi_M(m,p)\varphi_N(n,q).$$

In this case, the coefficients at noise-only positions $(p,q) \neq (p_l,q_l)$ are random variables Gaussian in nature and zero-mean, as they are formed as the summation of independent zero-mean Gaussian variables over l. Namely, now the missing pixels in each image component contribute to the noise, and the noise originating from each component is proportional to the squared amplitude of that component, following (27) with A_l, $l = 1, \ldots, K$. Therefore, 2D-DCT coefficients mean-value for a multicomponent signal (image) can be written as

$$\mu_{C_0(p,q)} = \frac{N_A}{MN}\sum_{l=1}^{K} A_l \delta(p - p_l, q - q_l). \tag{29}$$

The average variance of noise-only coefficients in this case easily follows

$$\bar{\sigma}^2_{C_0} = \sum_{l=1}^{K} A_l^2 \frac{N_A(MN - N_A)}{M^2 N^2(MN-1)}. \tag{30}$$

However, it is important to mention that components of the image multiplied with basis functions may cause a coupling effect if they are placed at positions satisfying certain conditions. Consequently, this effect may cause the increase of the previously derived variance at these positions. However, if it appears, for example, at the position (p_1,q_1) then the variance will be decreased for the same amount at the position $(M - p_1, N - q_1)$. Therefore, we can further neglect this effect and assume that the variance expression in (30) holds in mean, which is crucial for the following derivation of the error in the nonsparse image reconstruction.

4.4. *Nonsparse Signal Reconstruction.* We consider that an image is reconstructed under the assumption that it is K-sparse and that it satisfies the condition for unique reconstruction in the compressive sensing theory. The number of reconstructed components is K. According to (30), each unreconstructed component in the image behaves as a Gaussian input noise with variance

$$\sigma_N^2 = A_l^2 \frac{N_A (MN - N_A)}{M^2 N^2 (MN - 1)}. \tag{31}$$

Therefore, all $MN - K$ unreconstructed components will behave as a noise with variance

$$\sigma_T^2 = \sum_{l=K+1}^{MN} A_l^2 \frac{N_A (MN - N_A)}{M^2 N^2 (MN - 1)}. \tag{32}$$

After reconstruction, the total noise energy from the unreconstructed components (in K reconstructed components) will be

$$\|C_K - C_R\|_2^2 = K \frac{M^2 N^2}{N_A^2} \sigma_T^2 = \frac{K (MN - N_A)}{N_A (MN - 1)} \sum_{l=K+1}^{MN} A_l^2. \tag{33}$$

The noise of unreconstructed components can easily be related to the energy of the unreconstructed components

$$\|C_K - C\|_2^2 = \sum_{l=K+1}^{MN} A_l^2. \tag{34}$$

That is, the total error in the reconstructed components is

$$\|C_K - C_R\|_2^2 = \frac{K (MN - N_A)}{N_A (MN - 1)} \|C_K - C\|_2^2. \tag{35}$$

This completes the proof of the theorem.

5. Numerical Results

In this section, the theoretical result from (35) is numerically checked on a number of test images. The images are used for the numerical calculation of the expected squared error with various sparsity K per block. The block size is assumed to be $B \times B$. The squared errors in one block are calculated as

$$E_{stat} = 10 \log \left(\|C_K - C_R\|_2^2 \right) \tag{36}$$

to obtain the numerical result, whereas the theoretical curves are calculated using the right side of (35), that is,

$$E_{theor} = 10 \log \left(K \frac{B^2 - N_A}{N_A (B^2 - 1)} \|C_K - C\|_2^2 \right). \tag{37}$$

These errors are calculated for each block separately and then the results are averaged over all blocks in an image. The statistical peak signal-to-noise ratio ($PSNR_{stat}$) is defined as

$$PSNR_{stat} = 10 \log \left(\frac{255^2}{\|C_K - C_R\|_2^2} \right) \tag{38}$$

TABLE 1: Error and PSNR for 8 test images.

Test image	Error		PSNR	
	Statistics	Theory	Statistics	Theory
Boat	−19.13	−19.20	81.97	82.13
Pout	−27.32	−27.38	80.35	80.42
Pirate	−10.10	−10.23	70.97	71.10
Lifting Body	−24.78	−24.86	82.97	83.11
Pears	−25.60	−25.67	78.77	78.86
Autumn	−15.80	−15.88	90.81	90.92
Peppers	−22.16	−22.22	79.16	79.23
Football	−18.72	−18.87	68.69	68.83

and the theoretical one is calculated according to

$$PSNR_{teor} = 10 \cdot \log \left(\frac{255^2}{K \left((B^2 - N_A) / (N_A (B^2 - 1)) \right) \|C_K - C\|_2^2} \right), \tag{39}$$

where 255 is considered as the maximal pixel value of an image. They are used to additionally validate the results. In all following examples the reconstruction is performed using the OMP algorithm.

Example 1. The considered image is the grayscale image "Barbara" of size 512×512. The image is first split into blocks $B \times B = 16 \times 16$. It is assumed that 60% of pixels are available. In the reconstruction, the sparsity is assumed to be $K = 16$ per each block. The original image is shown in Figure 1(a), the image with the available pixels is shown in Figure 1(b), and the reconstructed image from reduced set of pixels, with assumed sparsity, is shown in Figure 1(c).

The statistical error and the theoretical one are shown in Figure 2. We considered various sparsity levels K per each block, changing between 1 and 16. The red asterisk represents the statistical values and the theoretical result is presented with the black line.

Example 2. Let us consider the RGB image "Lena" of size 512×512. We will again split the image into blocks of size $B \times B = 16 \times 16$. It is assumed that 60% of pixels are available. The sparsity is assumed to be $K = 16$ per each block. The original image, image with the available pixels, and the reconstructed image are shown in Figure 3.

The statistical error and the theoretical one are shown in Figure 4. The results are obtained by averaging errors from each block and each channel. Sparsity K per each block was varied between 1 and 16. The red asterisk represents the statistical values and the black line represents the theoretical result.

Example 3. A test image set with standard MATLAB images, shown in Figure 5, is used for this example. Each image is split into $B \times B = 16 \times 16$ blocks. The reconstruction is performed under the sparsity assumption $K = 16$, with 60% of randomly positioned available pixels. The statistical and the theoretical errors are calculated according to (36) and (37), whereas the PSNR is calculated using (38) and (39). The results are presented in Table 1, confirming a high agreement between the theory and statistics.
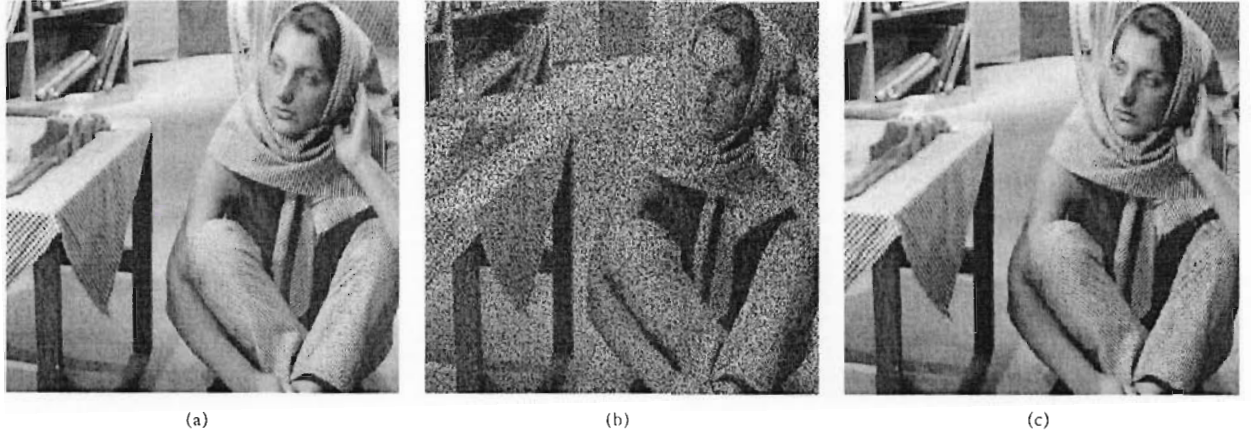
(a)   (b)   (c)

FIGURE 1: Reconstruction of image "Barbara" with 60% available pixels and sparsity $K = 16$ per each block of size 16×16: original image (a); noisy image (b); reconstructed image (c).
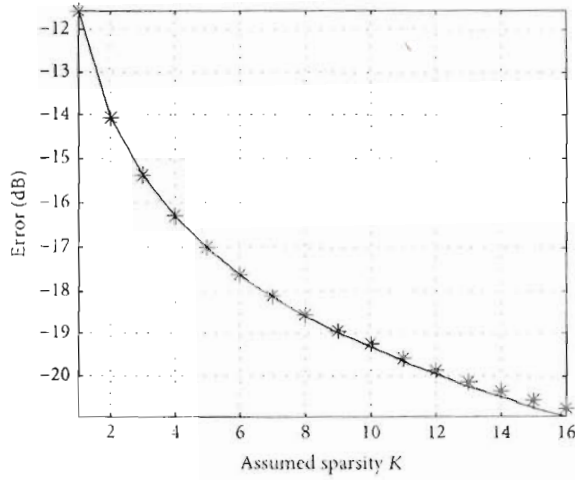

FIGURE 2: Error caused by the unreconstructed components with various sparsity per block in image "Barbara"; red asterisk: statistics, black line: theory.

6. Conclusions

In this paper, we considered the influence of nonsparsity in the reconstruction of images. Images are originally sparse or approximately sparse in the two-dimensional discrete cosine transform domain. The reconstruction error relation is presented in the form of a theorem. The reconstruction results are checked on a number of images, both grayscale and color. It is confirmed that the statistical results are close to the derived theoretical results.

Appendix

Special Cases of Indices

The values of 2D-DCT coefficients variance, for $(p, q) \neq (p_1, q_1)$, are considered in Section 4.2. Other special cases of indices are considered in this Appendix.

Case 1. When nonsignal (noise-only) positions satisfy $p = p_1$, $q \neq q_1$, $q \neq N - q_1$ we have

$$
\begin{aligned}
&E\left\{x^2_{p_1 q_1}(m, n, p_1, q)\right\} \\
&= E\left\{\varphi^4_M(m, p_1)\right\} \times E\left\{\varphi^2_N(n, q_1)\right\} E\left\{\varphi^2_N(n, q)\right\}.
\end{aligned}
\tag{A.1}
$$

Using the property $E\{\varphi^2_N(n, q_1)\}E\{\varphi^2_N(n, q)\} = 1/N^2$, we can further write

$$
\begin{aligned}
&E\left\{x^2_{p_1 q_1}(m, n, p_1, q)\right\} \\
&= \frac{1}{N^2}\left[\frac{1}{M^2} + \frac{1}{2M} E\left\{\varphi^2_M(m, 2p_1)\right\}\right].
\end{aligned}
\tag{A.2}
$$

This holds for $p_1 \neq 0$. In the previous derivation, we used the fact that the function $\varphi_M(m, 2p_1)$ has a zero mean-value for random m. Using the cosine function periodicity, we may write $E\{\varphi^2_M(m, 2p)\} = 1/M$. Finally, we get

$$
E\left\{x^2_{p_1 q_1}(m, n, p_1, q)\right\} = \frac{3}{2M^2 N^2}.
\tag{A.3}
$$

Incorporating this into (21) and (22) leads to

$$
\sigma^2_{C_0(p,q)} = \frac{3N_A(MN - N_A)}{2M^2 N^2(MN - 1)},
\tag{A.4}
$$

for $p_1 \neq 0$. When additional condition $p = p_1 = 0$ holds, then

$$
E\left\{x^2_{p_1 q_1}(m, n, p, q)\right\} = \frac{1}{M^2 N^2}
\tag{A.5}
$$

is obtained, which leads to the same result as (25).

Case 2. Using same derivations as for Case 1, it is easily shown that the result (A.4) is obtained for $p \neq p_1$, $p \neq M - p_1$, $q = q_1 \neq 0$. Condition $q = q_1 = 0$ also leads to (25).
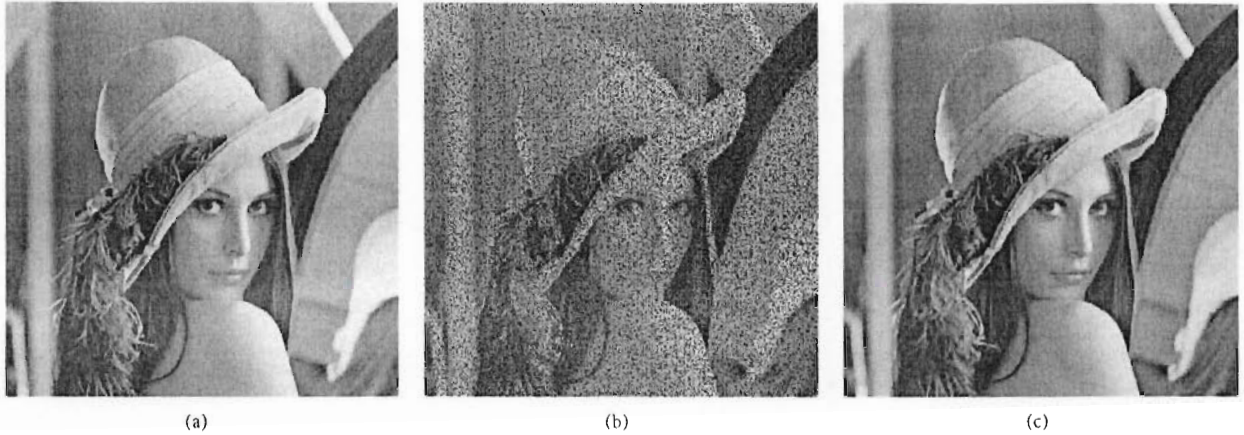
FIGURE 3: Reconstruction of image "Lena" with 60% available pixels and sparsity $K = 16$ per each block of size 16×16: original image (a); noisy image (b); reconstructed image (c).
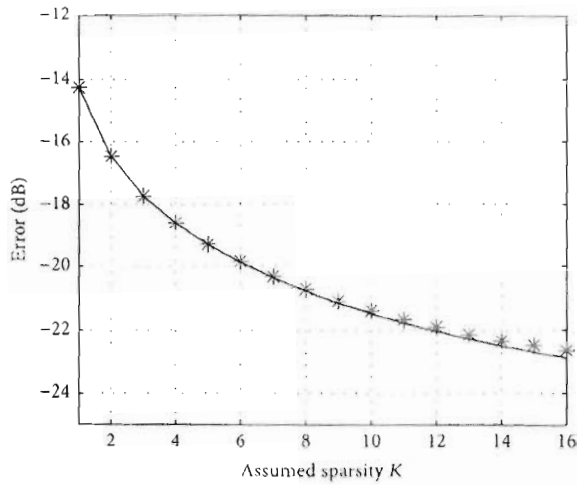

FIGURE 4: Error caused by the unreconstructed components with various sparsity per block in image "Lena"; red asterisk: statistics, black line: theory.

FIGURE 5: The test image set used for the analysis in Example 3.

Case 3. Observe now the case $p = M - p_1, q \neq q_1, q \neq N - q_1$. Also assume that $p_1 \neq 0$. The unknown quadratic term becomes

$$
\begin{aligned}
E &\left\{ x_{p_1 q_1}^2 (m, n, M - p_1, q) \right\} \\
&= E \left\{ \varphi_M^2 (m, p_1) \times \varphi_M^2 (m, M - p_1) \right\} \\
&\cdot E \left\{ \varphi_N^2 (m, q) \varphi_N^2 (m, q_1) \right\} = \frac{1}{N^2} \\
&\cdot E \left\{ \varphi_M^2 (m, p_1) \psi_M^2 (m, p_1) \right\},
\end{aligned}
\tag{A.6}
$$

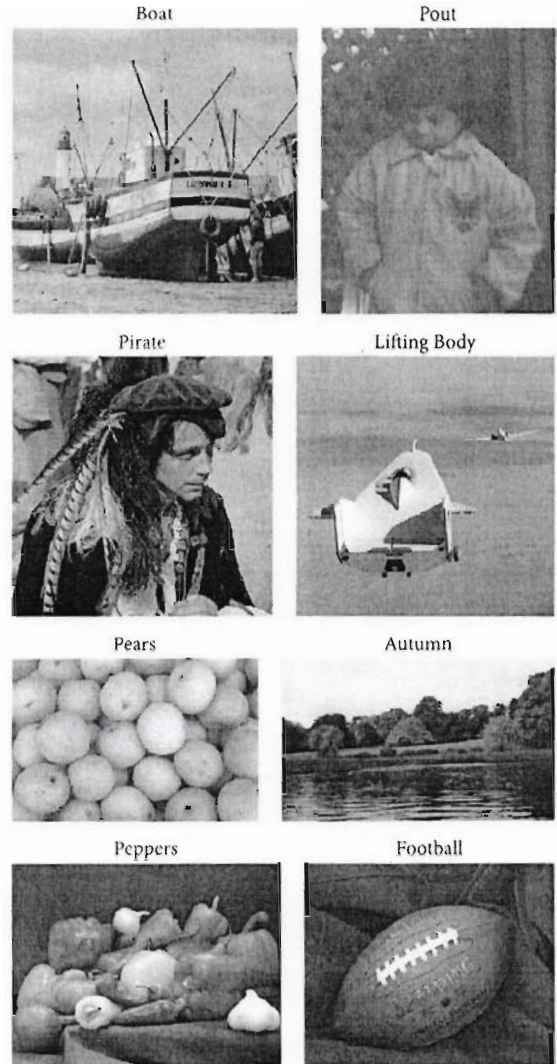where $\psi_M(m, p_1) = \sqrt{2/M} \sin(\pi(2m + 1)p_1/(2M))$ for $p_1 \neq 0$ and $\psi_M(m, 0) = \sqrt{1/M}$.

Note that we used identities $\psi_M^2(m, M) = 2/M$ and $\varphi_M(m, M) = 0$ that appear in $\varphi_M^2(m, M - p_1)$ when it is expressed as $\varphi_M(m, M)\varphi_M(m, p_1) + \psi_M(m, M)\psi_M(m, p_1)$. Using the trigonometric identity for the sine of double angle and expectation $E\{\psi_M^2(m, 2p_1)\} = 1/M$, analogous to the quadratic cosine expectation case, we get

$$E\left\{x_{p_1 q_1}^2(m, n, M - p_1, q)\right\} = \frac{1}{2M^2 N^2}. \qquad (A.7)$$

Putting this into (22) leads to

$$\sigma_{C_0(p,q)}^2 = \frac{N_A(MN - N_A)}{2M^2 N^2(MN - 1)}. \qquad (A.8)$$

which holds when $p_1 \neq 0$. When $p_1 = 0$ it is easily shown that (25) holds.

Case 4. In the equivalent case when $p \neq p_1$, $p \neq M - p_1$, $q = N - q_1$ results are the same as in Case 3. When $q_1 = 0$, result (25) holds.

Case 5. Observe the condition set $p = p_1$, $q = N - q_1$. Combining the derivations for Cases 1 and 3, it is easily shown that variance becomes

$$\sigma_{C_0(p,q)}^2 = \frac{3N_A(MN - N_A)}{4M^2 N^2(MN - 1)}. \qquad (A.9)$$

Otherwise, when $p_1 \neq 0$ or $q_1 \neq 0$ (25) holds as shown in previously analyzed cases. When $(p_1, q_1) = (0, 0)$ is assumed, result (25) also holds.

Case 6. In the analogous case when conditions $p = M - p_1$, $q = q_1$ are satisfied result (A.9) holds, whereas under additional conditions that $p_1 \neq 0$ or $q_1 \neq 0$ or $(p_1, q_1) = (0, 0)$ the variance becomes (25).

Case 7. When $p = M - p_1$ and $q = N - q_1$, unknown expectation becomes

$$E\left\{x_{p_1 q_1}^2(m, n, M - p_1, N - q_1)\right\} = \frac{1}{4M^2 N^2} \qquad (A.10)$$

for $(p_1, q_1) \neq (0, 0)$, leading to

$$\sigma_{C_0(p,q)}^2 = \frac{N_A(MN - N_A)}{4M^2 N^2(MN - 1)}. \qquad (A.11)$$

For $(p_1, q_1) = (0, 0)$ we have $E\{x_{00}^2(m, n, M, N)\} = 1/(M^2 N^2)$. Therefore, in the case of noisy coefficient $(M - p_1, N - q_1)$, the variance becomes (25). It can be shown that for either $p_1 = 0$ or $q_1 = 0$ this variance is equal to (A.8).

Note that the variance expressions obtained in all considered cases are multiplied with A_1^2 when $A_1 \neq 1$. Previous results can be unified as follows:

$$\begin{aligned}
\sigma_{C_0(p,q)}^2 = A_1^2 \frac{N_A(MN - N_A)}{M^2 N^2(MN - 1)} \times \Bigg[1 + \Big(1 \\
- \delta(p_1, q_1)\Big)\left(\frac{1}{2}\sum_{i=0}^{N-1}(1 - \delta(p_1, 0))\right. \\
\cdot \delta(p - p_1, q - i) + \frac{1}{2}\sum_{i=0}^{M-1}(1 - \delta(0, q_1)) \\
\cdot \delta(p - i, q - q_1) - \frac{1}{2}\sum_{i=0}^{N-1}(1 - \delta(M - p_1, 0)) \\
\cdot \delta(p - (M - p_1), q - i) - \frac{1}{2} \\
\cdot \sum_{i=0}^{M-1}(1 - \delta(0, N - q_1))\delta(p - i, q - (N - q_1)) \\
+ \frac{1}{4}(1 - \delta(p_1, 0) - \delta(0, q_1)) \\
\cdot \delta(p - (M - p_1), q - (N - q_1)) \\
- \frac{1}{4}(1 - \delta(p_1, 0) - \delta(0, q_1)) \\
\cdot \delta(p - p_1, q - (N - q_1)) \\
- \frac{1}{4}(1 - \delta(p_1, 0) - \delta(0, q_1)) \\
\left.\cdot \delta(p - (M - p_1), q_1)\right)\Bigg],
\end{aligned} \qquad (A.12)$$

where $\delta(p, q) = 1$ if $p = 0$ and $q = 0$ and $\delta(p, q) = 0$ otherwise.

The variances are statistically checked in the next example.

Example A.1. Assume a monocomponent signal in the 2D-DCT domain, defined as

$$s(m, n) = A_1 \varphi_{p_1}(m, M)\varphi_{q_1}(n, N), \qquad (A.13)$$

where $M = 16$, $N = 20$, $A_1 = 1$, $p_1 = 9$, and $q_1 = 16$. Only $N_A = 128$ randomly positioned samples of the signal are available and 20,000 independent random realizations of the signal are observed. Based on the initial estimates (10), the variance of 2D-DCT coefficients is calculated numerically, averaging initial estimates over all realizations. The results are shown in Figure 6, scaled with constant term (25). Special cases considered in Appendix are denoted in Figure 6.
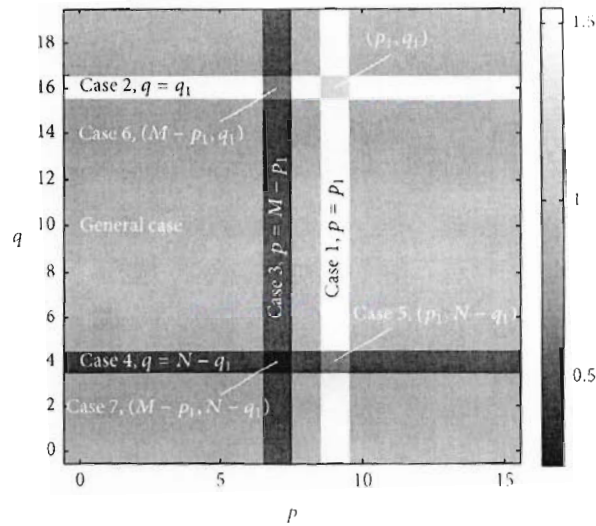
FIGURE 6: Variance of the initial 2D-DCT estimate. It is obtained numerically based on 20,000 independent realizations of a $M \times N = 16 \times 20$ monocomponent signal sparse in 2D-DCT domain, with $N_A = 128$ randomly positioned available samples.

Conflicts of Interest

The authors declare that they have no conflicts of interest.

References

[1] D. L. Donoho, "Compressed sensing," *Institute of Electrical and Electronics Engineers Transactions on Information Theory*, vol. 52, no. 4, pp. 1289–1306, 2006.

[2] E. J. Candès, "The restricted isometry property and its implications for compressed sensing," *Comptes Rendus Mathematique*, vol. 346, no. 9-10, pp. 589–592, 2008.

[3] R. G. Baraniuk, "Compressive sensing," *IEEE Signal Processing Magazine*, vol. 24, no. 4, pp. 118–121, 2007.

[4] E. J. Candès, J. Romberg, and T. Tao, "Robust uncertainty principles: Exact signal reconstruction from highly incomplete frequency information," *Institute of Electrical and Electronics Engineers Transactions on Information Theory*, vol. 52, no. 2, pp. 489–509, 2006.

[5] E. J. Candès and M. B. Wakin, "An introduction to compressive sampling: a sensing/sampling paradigm that goes against the common knowledge in data acquisition," *IEEE Signal Processing Magazine*, vol. 25, no. 2, pp. 21–30, 2008.

[6] B. Wohlberg, "Noise sensitivity of sparse signal representations: reconstruction error bounds for the inverse problem," *IEEE Transactions on Signal Processing*, vol. 51, no. 12, pp. 3053–3060, 2003.

[7] L. Stanković, S. Stanković, and M. Amin, "Missing samples analysis in signals for applications to L-estimation and compressive sensing," *Signal Processing*, vol. 94, no. 1, pp. 401–408, 2014.

[8] L. Stanković, I. Stanković, and M. Daković, "Nonsparsity influence on the ISAR recovery from reduced data," *IEEE Transactions on Aerospace and Electronic Systems*, vol. 52, no. 6, pp. 3065–3070, 2016.

[9] S. Stanković, I. Orović, and L. Stanković, "An automated signal reconstruction method based on analysis of compressive sensed

[10] M. Elad, *Sparse and Redundant Representations: From Theory to Applications in Signal and Image Processing*, Springer, Berlin, Germany, 2010.

[11] M. A. Davenport, M. F. Duarte, Y. C. Eldar, and G. Kutyniok, "Compressed sensing: Theory and applications," in *Introduction to compressed sensing*, Cambridge University Press, Cambridge, UK, 2012.

[12] D. Needell and J. A. Tropp, "CoSaMP: Iterative signal recovery from incomplete and inaccurate samples," *Applied and Computational Harmonic Analysis*, vol. 26, no. 3, pp. 301–321, 2009.

[13] E. Sejdić, M. A. Rothfuss, M. L. Gimbel, and M. H. Micklel, "Comparative analysis of compressive sensing approaches for recovery of missing samples in implantable wireless Doppler device," *IET Signal Processing*, vol. 8, no. 3, pp. 230–238, 2014.

[14] E. Sejdić, A. Can, L. F. Chaparro, C. M. Steele, and T. Chau, "Compressive sampling of swallowing accelerometry signals using time-frequency dictionaries based on modulated discrete prolate spheroidal sequences," *EURASIP Journal on Advances in Signal Processing*, vol. 2012, article 101, 2012.

[15] E. Sejdić, "Time-frequency compressive sensing," in *Time-Frequency Signal Analysis and Processing*, B. Boashash, Ed., pp. 424–429, Academic Press, Mass, USA.

[16] B. Jokanović, M. G. Amin, Y. D. Zhang, and F. Ahmad, "Multi-window time-frequency signature reconstruction from undersampled continuous-wave radar measurements for fall detection," *IET Radar, Sonar & Navigation*, vol. 9, no. 2, pp. 173–183, 2015.

[17] Z. Zhang, Y. Xu, J. Yang, X. Li, and D. Zhang, "A survey of sparse representation: algorithms and applications," *IEEE Access*, vol. 3, pp. 490–530, 2015.

[18] I. Volaric and V. Sucic, "On the noise impact in the L1 based reconstruction of the sparse time-frequency distributions," in *Proceedings of the 1st International Conference on Broadband Communications for Next Generation Networks and Multimedia Applications, (CoBCom '16)*, Graz, Austria, September 2016.

[19] L. Stanković, I. Orović, S. Stanković, and M. G. Amin, "Robust time frequency analysis based on the L-estimation and compressive sensing," *IEEE Signal Processing Letters*, vol. 20, no. 5, pp. 499–502, 2013.

[20] L. Stanković, M. Daković, and S. Vujović, "Reconstruction of sparse signals in impulsive disturbance environments," *Circuits, Systems and Signal Processing*, vol. 36, no. 2, pp. 767–794, 2017.

[21] X. Li and G. Bi, "Image reconstruction based on the improved compressive sensing algorithm," in *Proceedings of the IEEE International Conference on Digital Signal Processing, (DSP '15)*, pp. 357–360, Singapore, July 2015.

[22] J. Music, T. Marasović, V. Papić, I. Orović, and S. Stanković, "Performance of compressive sensing image reconstruction for search and rescue," *IEEE Geoscience and Remote Sensing Letters*, vol. 13, no. 11, pp. 1739–1743, 2016.

[23] I. Stanković, I. Orović, M. Daković, and S. Stanković, "Denoising of sparse images in impulsive disturbance environment," *Multimedia Tools and Applications*.

[24] L. Stanković, "Digital Signal Processing with Selected Topics, CreateSpace Independent Publishing Platform, An Amazon.com Company".

[25] P. Maechler, C. Studer, D. E. Bellasi et al., "VLSI design of approximate message passing for signal restoration and compressive sensing," *IEEE Journal on Emerging and Selected Topics in Circuits and Systems*, vol. 2, no. 3, pp. 579–590, 2012.

[26] G. Bi, S. K. Mitra, and S. Li, "Sampling rate conversion based on DFT and DCT," *Signal Processing*, vol. 93, no. 2, pp. 476–486, 2013.

[27] V. Britanak and K. R. Rao, "Efficient implementation of the forward and inverse MDCT in MPEG audio coding," *IEEE Signal Processing Letters*, vol. 8, no. 2, pp. 48–51, 2001.

[28] J. J. More and G. Toraldo, "On the solution of large quadratic programming problems with bound constraints," *SIAM Journal on Optimization*, vol. 1, no. 1, pp. 93–113, 1991.

[29] G. Davis, S. Mallat, and M. Avellaneda, "Adaptive greedy approximations," *Constructive Approximation. An International Journal for Approximations and Expansions*, vol. 13, no. 1, pp. 57–98, 1997.

[30] R. Tibshirani, "Regression shrinkage and selection via the lasso: a retrospective," *Journal of the Royal Statistical Society: Series B (Statistical Methodology)*, vol. 73, no. 3, pp. 273–282, 2011.

KRATKA BIOGRAFIJA

Miloš Brajović je rođen 24.05.1988. godine u Podgorici, Republika Crna Gora. Nakon završene osnovne škole „Njegoš" u Spužu, 2003. godine upisao je opšti smjer gimnazije „Petar I Petrović Njegoš" u Danilovgradu. Dobitnik je diploma „Luča", za ostvarene rezultate u osnovnoj i srednjoj školi. Od strane Nastavničkog vijeća gimnazije proglašen je za učenika generacije.

Elektrotehnički fakultet u Podgorici, na odsjeku Elektronika, telekomunikacije i računari, upisuje septembra 2007. godine. Specijalističke studije, na smjeru Računari, upisuje odmah nakon završenih osnovnih studija, i završava ih u junu 2011. godine, odbranom specijalističkog rada **„Vremensko-frekvencijska analiza i predstavljanje trenutne frekvencije"**, čime je stekao stepen Specijaliste (Spec.Sci) za oblast Elektronike, telekomunikacija i računara.

Od septembra 2011. godine angažovan je kao saradnik u nastavi na Elektrotehničkom fakultetu u Podgorici, gdje iste godine upisuje i magistarske studije, na smjeru Računari, pod mentorstvom prof. dr Miloša Dakovića. Magistarsku tezu sa temom: **„Rekurzivno izračunavanje vremensko-frekvencijskih reprezentacija"** odbranio je u oktobru 2013. godine. Počevši od 2012. godine, kandidat je bio ili je još uvijek angažovan na 8 naučno-istraživačkih i stručnih projekata.

Kandidat je trenutno u završnoj fazi izrade doktorske disertacije sa radnim naslovom: **"Analiza algoritama za rekonstrukciju signala rijetkih u Hermitskom i Furijeovom transformacionom domenu"**. Mentor za izradu doktorske disertacije je prof. dr Miloš Daković.

Miloš Brajović obavlja dužnost recezenta u više od renomiranih međunarodnih časopisa sa SCI/SCIE liste, za koje je do sada recenzirao preko 50 naučnih radova. Obavljao je dužnost recezenta i u domaćim časopisima, zatim za veći broj međunarodnih i domaćih konferencija. Do sada je publikovao 8 radova u međunarodnim časopisima sa SCI/SCIE liste, 3 rada u ostalim časopisima, 25 radova na međunarodnim konferencijama (indeksiranim u SCOPUS-u i IEEE Xplore bazama) i 11 radova na regionalnim i lokalnim konferencijama. Više radova, na kojima je jedan od autora, nalazi se u postupku recenziranja. Kompletan spisak referenci dostupan je na sajtu http://www.tfsa.ac.me/milosb_papers.html.

CURRICULUM VITAE

Lični podaci:

Ime i prezime:	**Miloš Brajović**
Adresa:	Spuž bb, Danilovgrad
Telefon:	+38269-486-639
Email:	milosb@ac.me
Datum rođenja:	24.05.1988.
Institucija:	Elektrotehnički fakultet, Univerzitet Crne Gore

Obrazovanje:

2013.-sada.: Student doktorskih studija elektrotehnike na Univerzitetu Crne Gore, Elektrotehnički fakultet u Podgorici; radni naslov doktorske teze - "**Analiza algoritama za rekonstrukciju signala rijetkih u Hermitskom i Furijeovom transformacionom domenu**"

2011.-2013.: Magistar elektrotehnike u oblasti Elektronika telekomunikacije i računari – smjer Računari (MSc) na Univerzitetu Crne Gore, Elektrotehnički fakultet u Podgorici; naslov magistarske teze - „**Rekurzivno izračunavanje vremensko-frekvencijskih reprezentacija**"

2007.-2011.: Stepen bečelor (BSc) Elektronika, telekomunikacije, računari i stepen specijaliste (Spec Sci), Elektronika, telekomunikacije i računari – Računari na Univerzitetu Crne Gore, Elektrotehnički fakultet u Podgorici; specijalistički rad - „**Vremensko-frekvencijska analiza i predstavljanje trenutne frekvencije**"

Radno iskustvo:

2011.– sada: Saradnik u nastavi na Elektrotehničkom fakultetu u Podgorici, Univerzitet Crne Gore

Kandidat je učestvovao u izvođenju časova računskih i laboratorijskih vježbi na više predmeta sa Elektrotehničkog fakulteta i Fakulteta za sport i fizičko vaspitanje. Predmeti sa Elektrotehničkog fakulteta na kojima je učestvovao u izvođenju vježbi su:

1. Digitalna obrada signala – računske i laboratorijske vježbe, 3. godina osnovnih akademskih studija, studijski program ETR
2. Osnovi računarstva II - laboratorijske vježbe, 1. godina osnovnih akademskih studija, studijski program ETR
3. Adaptivni diskretni sistemi i neuralne mreže – računske vježbe, 1. godina specijalističkih akademskih studija, smjer Računari, studijski program ETR
4. Baze podataka – računske i laboratorijske vježbe, 1. godina specijalističkih akademskih studija, smjer Računari, studijski program ETR
5. Ekspertni sistemi – računske vježbe. 1. godina specijalističkih akademskih studija, smjer Računari, studijski program ETR
6. Osnovi računarstva II – računske i laboratorijske vježbe, 1. godina osnovnih akademskih studija, studijski program EA
7. Signali i sistemi – računske i laboratorijske vježbe, 2. godina osnovnih akademskih studija, studijski program EA
8. Operativni sistemi - laboratorijske vježbe, 1. godina osnovnih primijenjenih studija, studijski program SPR
9. Administriranje računarskih sistema - laboratorijske vježbe, 2. godina osnovnih primijenjenih studija, studijski program SPR
10. Internet tehnologije - laboratorijske vježbe, 3. godina osnovnih primijenjenih studija, studijski program SPR
11. Matematika u računarstvu (napredni kurs) - računske vježbe, 1. godina specijalističkih primijenjenih studija, studijski program SPR

Predmeti sa Fakulteta za sport i fizičko vaspitanje na kojima je kandidat učestvovao u izvođenju vježbi su:

12. Uvod u informatiku i računarstvo – laboratorijske vježbe, 1. godina osnovnih akademskih studija, studijski program Fizička kultura
13. Informatika i računarstvo – laboratorijske vježbe, 2. godina osnovnih primijenjenih studija, studijski program Obrazovanje sportskih trenera
14. Primijenjena informatika – laboratorijske vježbe, 2. godina osnovnih akademskih studija, studijski program Obrazovanje sportskih novinara
15. Informacione tehnologije u sportu (od 2017. godine) – laboratorijske vježbe, 1. godina osnovnih akademskih studija, studijski programi Fizička kultura i zdravi stilovi života i studijski program Sportski novinari i treneri

Predmeti sa Pomorskog fakulteta - Kotor na kojima je kandidat učestvovao u izvođenju vježbi su:

16. Elektronski navigacioni uređaji – laboratorijske vježbe, 2. godina , studijski program Brodska elektrotehnika

Angažovanje na projektima

Tokom dosadašnjeg rada kandidat je učestvovao ili učestvuje u realizaciji više naučno-istraživačkih i stručnih projekata:

1. Radarski sistemi sa stohastičkim talasnim oblicima - NOISERADAR (Radar systems with stochastic waveforms - NOISERADAR), national research project, Montenegrin Ministry of Science, 2012-2015 (milos@ac.me)
2. New ICT Compressive sensing-based trends applied to: multimedia, biomedicine and communications - CS-ICT, Montenegrin Ministry of Science, project grant funded by the World Bank loan, 2014-2017 (Grant no. 01-1002)
3. BIO-ICT Centre of Excellence in Montenegro, project for establishing the first center of excellence in Montenegro, Montenegrin Ministry of Science, project grant funded by the World Bank loan, 2014-2015 (Contract No. 01-1001)
4. Compressive Sensing and Super-resolution in the application of surveillance systems based on optical sensors (Compressive Sensing i Superrezolucija u primjenama sistema za nadzor zasnovanih na optičkim senzorima) – bilateral project between Montenegro and Croatia, project leaders Irena Orović (irena@ac.me) and Josip Musić, 2016-2017
5. An Adriatic Network for Advancing Research Development and Innovation towards the Creation of new Policies for Sustainable Competiveness and Technological Capacity of SMEs, "ADRIATinn" IPA Adriatic Cross-Border Cooperation, 2014-2016, http://www.adriawealth.eu/project/adriatinn/
6. Modelovanje analognog sistema obrade signala frakcionog reda (Modeling of analog fractional order signal processing system), bilateral research project between Montenegro and Croatia, Montenegrin leader Budimir Lutovac (budo@ac.me), 2017-2018
7. Kompresivno očitavanje i vremensko-frekvencijska analiza sa primjenama (Compressed sensing and time-frequency analysis with applications), bilateral research project, Montenegro-China, Montenegrin project leader Srdjan Stankovic (srdjan@ac.me)
8. Digitalizacija u Crnoj Gori, Istorijat, stanje i perspective (Digitalization in Montenegro: History, Current State and Perspectives), research project, Montenegrin Academy of Sciences and Arts, 2018-2019, project leader Ljubiša Stanković, (ljubisa@ac.me)

Strani jezici:

- Engleski jezik
- Ruski jezik

Rad na računaru:

- Operativni sistemi Windows i prateće aplikacije, Active Directory, operativni sistem Linux
- Pogramski paket Microsoft Office, LaTeX
- MATLAB/Octave, C, MySQL, Oracle, PHP, HTML, C++, C#, CLIPS

BIBLIOGRAFIJA KANDIDATA

Master thesis:

[1] M. Brajović, "Rekurzivno izračunavanje vremensko-frekvencijskih reprezentacija" ("Recursive calculation of time-frequency representations") MSc Thesis, University of Montenegro, Podgorica, November 2013

Leading International Journals (SCI/SCIE list)

[2] LJ. Stanković, and M. Brajović, "Analysis of the Reconstruction of Sparse Signals in the DCT Domain Applied to Audio Signals," IEEE/ACM Transactions on Audio, Speech, and Language Processing, vol. 26, no.7, July 2018, pp.1216-1231, DOI: 10.1109/TASLP.2018.2819819

[3] M. Brajović, I. Orović, M. Daković, and S. Stanković, "Compressive Sensing of Sparse Signals in the Hermite Transform Basis," IEEE Transactions on Aerospace and Electronic Systems, Volume: 54, Issue: 2, April 2018, pp. 950 - 967, DOI: 10.1109/TAES.2017.2768938

[4] M. Brajović, S. Stanković, and I. Orović, "Analysis of noisy coefficients in the discrete Hermite transform domain with application in signal denoising and sparse signal reconstruction," Signal Processing, vol. 150, September 2018, https://doi.org/10.1016/j.sigpro.2018.04.007

[5] M. Brajović, I. Stanković, M. Daković, C. Ioana, and LJ. Stanković, "Error in the Reconstruction of Nonsparse Images," Mathematical Problems in Engineering, Volume 2018 (2018), Article ID 4314527, 10 pages https://doi.org/10.1155/2018/4314527

[6] LJ. Stanković, D. Mandic, M. Daković, and M. Brajović, "Time-frequency decomposition of multivariate multicomponent signals," Signal Processing, Volume 142, January 2018, pp. 468-479, http://dx.doi.org/10.1016/j.sigpro.2017.08.001

[7] M. Brajović, V. Popović-Bugarin, I. Djurović, and S. Djukanović, "Post-processing of Time-Frequency Representations in Instantaneous Frequency Estimation Based on Ant Colony Optimization," Signal Processing, Vol. 138, September 2017, pp. 195–210, http://dx.doi.org/10.1016/j.sigpro.2017.03.022.

[8] M. Brajović, I. Orović, M. Daković, and S. Stanković, "On the Parameterization of Hermite Transform with Application to the Compression of QRS Complexes," Signal Processing, in print, vol. 131, pp. 113-119, February 2017.

[9] M. Brajović, I. Orović, M. Daković, and S. Stanković, "Gradient-based signal reconstruction algorithm in the Hermite transform domain," Electronics Letters, Volume 52, Issue 1, pp.41-43, 2016

Other International, Regional, and National Journals:

[10] M. Brajović, A. Draganić, I. Orović, and S. Stanković, "Sparse Representation of FHSS Signals in the Hermite Transform Domain," Telfor Journal, Vol. 9, No. 2, 2017.

[11] S. Vujović, M. Brajović, V. Popović-Bugarin, N. Latinović, J. Latinović, and M. Bajčeta, "A web service for grapevine monitoring and forecasting a disease," ETF Journal of Electrical Engineering, Vol. 22, No. 1, 2016

[12] M. Brajović, LJ. Stanković, and M. Daković, "Reconstruction of non-stationary signals with missing samples using S-method and a gradient-based reconstruction algorithm," ETF Journal of Electrical Engineering, Vol. 21, No. 1, 2015.

International conferences (Indexed in SCOPUS):

[13] M. Brajović, I. Stanković, C. Ioana, M. Daković, and LJ. Stanković, "Reconstruction of Rigid Body with Noncompensated Acceleration After Micro-Doppler Removal," *5th International Workshop on Compressed Sensing applied to Radar, Multimodal Sensing, and Imaging (CoSeRa)*, Siegen, Germany, September 2018.

[14] LJ. Stanković, M. Brajović, I. Stanković, C. Ioana, and M. Daković, "Analysis of Initial Estimate Noise in the Sparse Randomly Sampled ISAR Signals," *5th International Workshop on Compressed Sensing applied to Radar, Multimodal Sensing, and Imaging (CoSeRa)*, Siegen, Germany, September 2018.

[15] I. Stanković, M. Brajović, M. Daković, and C. Ioana, "Effect of Random Sampling on Noisy Nonsparse Signals in Time-Frequency Analysis," *26th European Signal Processing Conference EUSIPCO 2018*, Rome, Italy, September 2018.

[16] M. Brajović, LJ. Stanković, M. Daković, and D. Mandic, "Additive Noise Influence on the Bivariate Two-Component Signal Decomposition," 7th Mediterranean Conference on Embedded Computing, MECO 2018, Budva, Montenegro, June 2018.

[17] M. Brajović, LJ. Stanković, and M. Daković, "Micro-Doppler removal in radar imaging in the case of non-compensated rigid body acceleration," 2018 23rd International Scientific-Professional Conference on Information Technology (IT), Zabljak, Montenegro, 2018, pp. 1-4, February 19-24, doi: 10.1109/SPIT.2018.8350451

[18] M. Brajović, S. Vujović, I. Orović, and S. Stanković, "Coefficient Tresholding in the Gradient Reconstruction Algorithm for Signals Sparse in the Hermite Transform Basis," Applications of Intelligent Systems 2018 (APPIS 2018), Las Palmas De Gran Canaria, 8-12 January 2018

[19] Z. Vulaj, M. Brajović, A. Draganić, and I. Orović, "Detection of Irregular QRS Complexes using Hermite Transform and Support Vector Machine," 59th International Symposium ELMAR-2017, Zadar, Croatia, 2017

[20] LJ. Stanković, M. Brajović, M. Daković, and D. Mandic, "Two-component Bivariate Signal Decomposition Based on Time-Frequency Analysis," 22nd International Conference on Digital Signal Processing IEEE DSP 2017, August 23-25, London, United Kingdom

[21] M. Brajović, I. Orović, M. Daković, and S. Stanković, "The Reconstruction of 2D Sparse Signals by Exploiting Transform Coefficients Variances," 17th IEEE Int. Conference on Smart Technologies, IEEE EUROCON 2017

[22] Z. Vulaj, A. Draganić, M. Brajović, and I. Orović, "A tool for ECG signal analysis using standard and optimized Hermite transform," 6th Mediterranean Conference on Embedded Computing, MECO 2017, Bar, Montenegro

[23] M. Daković, I. Stanković, M. Brajović, and LJ. Stanković, "Sparse Signal Reconstruction Based on Random Search Procedure," 40th International Convention on Information and Communication Technology, Electronics and Microelectronics MIPRO, Opatija, Croatia, May 2017

[24] M. Daković, T. Ružić, T. Rogač, M. Brajović, and B. Lutovac, "Neural Networks Application to Neretva Basin Hydro-meteorological Data," 13th Symposium on Neural Networks and Applications NEUREL 2016, November 2016, Belgrade, Serbia

[25] M. Brajović, I. Orović, and S. Stanković, "The Optimization of the Hermite transform: Application Perspectives and 2D Generalization," 24th Telecommunications Forum TELFOR 2016, November 2016, Belgrade, Serbia.

[26] M. Brajović, B. Lutovac, I. Orović, M. Daković, and S. Stanković, "Sparse Signal Recovery Based on Concentration Measures and Genetic Algorithm," 13th Symposium on Neural Networks and Applications NEUREL 2016, Belgrade, Serbia, November 2016

[27] M. Brajović, A. Draganić, I. Orović, and S. Stanković, "FHSS signal sparsification in the Hermite transform domain," 24th Telecommunications Forum TELFOR 2016, November 2016, Belgrade, Serbia

[28] I. Stančić, M. Brajović, I. Orović, and J. Musić, "Compressive sensing for reconstruction of 3D point clouds in smart systems," 24th International Conference on Software, Telecommunications and Computer Networks (SoftCOM 2016), Split, Croatia, September 2016

[29] M. Brajović, I. Orović, M. Daković, and S. Stanković, "Representation of Uniformly Sampled Signals in the Hermite Transform Domain," 58th International Symposium ELMAR-2016, Zadar, Croatia, Sept. 2016.

[30] M. Brajović, I. Orović, M. Daković, and S. Stanković, "Compressive Sensing of Signals Sparse in 2D Hermite Transform Domain," 58th International Symposium ELMAR-2016, Zadar, Croatia, Sept. 2016

[31] M. Brajović, M. Daković, and LJ. Stanković, "Convexity of the l1-norm based Sparsity Measure with Respect to the Missing Samples as Variables," 5th Mediterranean Conference on Embedded Computing, MECO 2016, Bar, June 2016

[32] M. Brajović, I. Orović, M. Daković, and S. Stanković, "The Analysis of Missing Samples in Signals Sparse in the Hermite Transform Domain," 23rd Telecommunications Forum TELFOR, Belgrade, 2015

[33] Draganić, M. Brajović, I. Orović, and S. Stanković, "A Software Tool for Compressive Sensing based Time-Frequency Analysis," 57th International Symposium ELMAR-2015, Zadar, Croatia

[34] M. Brajović, S. Vujović, and S. Djukanović, "An Overview of Smart Irrigation Software," Mediterranean Conference on Embedded Computing (MECO) 2015, Budva, Montenegro, June 2015.

[35] M. Brajović, and V. Popović-Bugarin, "Instantaneous Frequency Estimation Using Ant Colony Optimization and Wigner Distribution," 4th Mediterranean Conference on Embedded Computing, MECO 2015, Budva, Montenegro, June 2015.

[36] Drašković, M. Brajović, M. Daković, and LJ. Stanković, "Time- Frequency Plane Splitting for the First Order Local Polynomial Fourier Transform," 21st Telecommunications Forum TELFOR 2013, Beograd, Nov. 26-28, 2013

[37] M. Daković, M. Brajović, T. Thayaparan, and LJ. Stanković, "An algorithm for micro-Doppler period estimation," 20th Telecommunications Forum TELFOR 2012, Belgrade Nov. 20-22, 2012

Regional and National Conferences

[38] M. Brajović, M. Daković, and LJ. Stanković, "A Higher Order Time-Frequency Representation with Reduced Cross-Terms," 22nd International Scientific-Professional Conference Information Technology 2017, Žabljak, February 2017.

[39] T. Ružić, T. Rogač, M. Brajović, and M. Daković, "Digitalna obrada hidrometeoroloških podataka sa sliva rijeka Neretve i Trebišnjice," ETRAN 2016, Zlatibor, Serbia, June 2016

[40] Ž. Zečević, M. Brajović, and B. Krstajić, "An Adaptive Approach for Delay Estimation of Sinusoidal Signals," ETRAN 2016, Zlatibor, Serbia, June 2016

[41] S. Vujović, M. Brajović, V. Popović-Bugarin, N. Latinović, J. Latinović, and M. Bajčeta, "WEB servis za monitoring vinograda i predviđanje oboljenja vinove loze," Informacione Tehnologije - IT 2016, Žabljak, Montenegro Mar. 2016.

[42] M. Brajović, S. Vujović, V. Popović-Bugarin, S. Djukanović, M. Knežević, and A. Topalović, "Soil analysis database and the expert system for recommendations of fertilization in agriculture," Informacione Tehnologije - IT 2016, Žabljak, Montenegro, February 2016

[43] S. Vujović, M. Brajović, and S. Djukanović, "Web and mobile applications in agriculture," Informacione Tehnologije - IT 2015, Žabljak, Montenegro, February 2015

[44] M. Brajović, LJ. Stanković, and M. Daković, "Reconstruction of non-stationary signals with missing samples using S-method and a gradient-based reconstruction algorithm," Informacione Tehnologije - IT 2015, Žabljak, Montenegro, February 2015

[45] Žarić, M. Daković, and M. Brajović, "Radarski sistem baziran na analizi signala emitovanih iz postojećih izvora," ETRAN 2013, Zlatibor, Serbia, Juny 2013

[46] M. Brajović, A. Drašković, M. Daković, and LJ. Stanković, "Razmatranje numeričke implementacije nekih vremensko-frekvencijskih reprezentacija," Informacione Tehnologije - IT 2013, Žabljak, Montenegro, February 2013

[47] M. Brajović, M. Daković, and LJ. Stanković, "Vremensko-frekvencijska transformacija višeg reda zasnovana na aproksimaciji prvog izvoda faze," ETRAN 2012, Zlatibor, Serbia, July 2012

[48] M. Daković, M. Brajović, and LJ. Stanković, "Rekurzivni metod za računanje kratkotrajne Fourier-ove transformacije," Informacione tehnologije - IT 2012, Žabljak, Montenegro, February 2012

Prof. dr Ljubiša Stanković

BIOGRAFIJA

Ljubiša Stanković je rodjen 1. juna 1960. godine. Osnovnu školu je učio u Murini i Ivangradu. U Ivangradu je završio Gimnaziju, kao najbolji učenik u generaciji. Kao srednjoškolac je bio prvi na republičkom takmičenju iz matematike i osvojio zlatnu medalju na smotri omladine tehničkih stvaralaca Jugoslavije.

Elektrotehnički fakultet Univerziteta Crne Gore je upisao 1978. i diplomirao nakon 3 godine i 9 mjeseci sa prosjekom 9,98. Kao student dva puta je učestvovao na Susretima studenata elektrotehnike Jugoslavije (1980. i 1982.) i oba puta osvojio prvo mjesto na takmičenju iz matematike. Dobitnik je zlatne plakete Univerziteta kao najbolji diplomirani student za 1982. godinu, a te iste godine je bio proglašen i za najboljeg studenta u Crnoj Gori.

Stanković je magistrirao 1984. godine na Elektrotehničkom fakultetu u Beogradu, na smjeru Telekomunikacije sa prosjekom 10. Kao dobitnik Fulbrightove stipendije, boravio je školske 1984/85 na Worcester Polytechnic Institutu, SAD, gdje je položio sve ispite na doktorskim studijama sa najvišom ocjenom A i bio izabran za predavača. Doktorirao je 1988. godine na Elektrotehničkom fakultetu u Podgorici u oblasti prostiranja i zračenja elektromagnetnih talasa.

Stanković od diplomiranja 1982. radi na Elektrotehničkom fakultetu Univerziteta Crne Gore. U zvanje redovnog profesora univerziteta je izabran 1995. godine. Stanković je bio član Jugoslovenske inženjerske akademije, član je Inženjerske akademije Crne Gore, čiji je bio i prvi predsjednik. Od 1996. Stanković je član Crnogorske akademije nauka i umjestnosti (CANU). Član je Evropske akademije nauka i umjetnosti (European Academy of Scineces and Arts) od 2011. Godine. Član je Academia Europaea od 2013. Stanković je u dva mandata bio izabran na funkciju rektora Univerziteta Crne Gore za period 2003.-2005. i 2005.-2008. godine. Stanković je član International Advisory Boarda Alexander von Humboldtove fondacije od 2016. godine.

Uz podršku Alexander von Humboldtove fondacije, Stanković je u periodu 1997/98, 1999 i 2002 boravio na Rurskom Univerzitetu u Bochumu, u Njemačkoj. Pocetkom 2001. godine je boravio na Tehničkom Univerzitetu u Eindhovenu, Holandija, kao visiting profesor. Više puta je boravio na univerzitetima u Brestu i Grenoblu, Francuska, radeći na zajedničkim projektima. Stanković je bio mentor i član brojnih komisija za odbranu doktorata uključujući i doktorate u Holandiji, Australiji, Francuskoj i Indiji, a tokom 2012/2013 godine je bio visiting akademik na Imperial Collegeu u Londonu, UK. U periodu 2001-2003 naučno-istraživacki rad grupe na Univerzitetu Crne Gore, kojom rukovodi Stanković, je podržan od strane Volkswagenove fondacije, SR Njemacka. U periodu od 2003-2013 naučni rad Stankovića, u oblasti obrade radarskih signala, je finansiran i od strane Ministarstva odbrane, odjel za istraživanje i razvoj, Vlade Kanade. Intenzivno saradjuje na istraživanju sa kolegama iz mnogih zemalja širom svijeta.

Stanković je bio član IEEE Komiteta za teoriju i metode u obradi signala od 2002. do 2008. godine, kao i član Komiteta za Visoko obrazovanje Savjeta Evrope. Stanković je bio jedan od urednika i u časopisima IEEE Signal Processing Letters, IEEE Transactions on Image Processing i IEEE Transactions on Signal Processing. Sada je član redakcija časopisa IEEE Transactions on Image Processing (u zvanju senior area editor), Signal Processing (u izdanju Elseviera) i IET Signal Processsing.

Stanković je 1997. godine dobio najvišu nacionalnu nagradu "13. jul".

Stanković je bio aktivan i u političkom životu Crne Gore. Bio je profesionalni član Predsjedništva Crne Gore (1989-1991). predsjednik Socijalističke partije Crne Gore (1990-1993), predsjedavajući Demokratskog foruma, kao prvog stalnog višestranačkog tijela formiranog 10. januara 1990. uz učešće svih partija i drugih političkih organizacija i udruženja, koji je imao zadatak da stvori zakonske i adaminstartivne pretpostavke za održavanje prvih višestranačkih izbora u Crnoj Gori. Stanković je bio predsjednik Saveza reformskih snaga za

Crnu Goru (1990-1992) i kandidat za predsjednika Crne Gore ovog Saveza na prvim višestranačkim izborima odražanim 9. decembra 1990. godine, poslanik u Skupštini Crne Gore (1991-1992) i poslanik u Skupštini Jugoslavije (1992-1996). Stanković je u periodu od 2011. do 2015. godine obavljao dužnost ambsadora Crne Gore u Ujedninjenom Kraljevstvu Velike Britanije i Sjeverne Irske, kao i ambasadora Crne Gore na Islandu i u Republici Irskoj.

U jednom periodu, sredinom osamdesetih, se bavio umjetničkom fotografijom, gdje je takodje imao zapažena ostvarenja na izložbama u Crnoj Gori i širom bivše Jugoslavije.

Stanković je objavio veliki broj naučnih radova, od kojih preko 150 u vodećim svjetskim časopisima. Radovi su mu citirani oko 7500 puta, sa h indeksom citiranosti 46. Primjena i razrada metoda koje je on definisao je bila tema mnogih radova objavljenih u najrenomiranijim svjetskim časopisima od strane vodećih naučnika u oblasti obrade signala iz Evrope, Amerike, Australije i Azije. Poznati profesori iz SAD su u svom radu o estimacijama spektra diskretnih signala sve estimatore podijelili u dvije klase od koji su jednu imenovali po tvorcima algoritama za brzu Fourierovu transformaciju, a drugu su predstavili kao varijacije na Stankovićevu klasu estimatora. U dva teksta koje je vodeće svjetsko udruzenje u oblasti obrade signala, IEEE Signal Processing Society, objavilo povodom 50 godina postojanja citirani su doprinosi Stankovića po imenu. Za doprinose u nauci najveće svetsko udruženje u oblasti elektrotehnike IEEE sa sjedištem u New Yorku mu je dodijelilo najviše zvanje Fellow IEEE.

Pored brojnih naučnih radova objavljenih u vodećim časopisima i poglavlja u referentnim knjigama svjetskih izdavača, Stanković je, izmedju ostalog, u SAD objavio udžbenik "Time-Frequency Signal Analysis with Applications" (668 strana) u izdanju jedne od vodećih izdavačkih kuća u svijetu, Artech House, Boston, SAD, 2013. Objavio je poglavlje od 120 strana u referentnoj monografiji Academic Press Library in Signal Processing, objavljenoj 2013. od strane Academic Pressa. Po pozivu je napisao poglavlje "Sparse Signal Processing - An Introduction" za Wiley Encyclopedia of Electrical and Electronics Engineering, John Wiley and Sons, izdanje od 2017. godine. Stanković po pozivu upravo piše knjigu na temu grafova i frekvencijske analize za izdavačku kuću Springer. Knjiga će se pojaviti do kraja 2018. godine.

Za rad objavljen u časopisu Signal Processing, u izdanju Elseviera, Stanković je 2017. dobio godišnju naradu Evropske Asocijacije za Obradu Signala (EURASIP) za najbolji rad objavljen u časopisu u oblasti obrade signala.

Od 2016. godine Stanković je potpredsjednik Crnogorske akademije nauka i umjetnosti.

Više detalja i kompletan spisak referenci se mogu naći na adresi:

http://www.tfsa.ac.me/ljubisa_papers.html

DESET REFERENCI

[1] LJ. Stanković, E. Sejdić, and M. Daković, "Vertex-Frequency Energy Distributions," *IEEE Signal Processing Letters*, Vol: 25, Issue: 3, March 2018, pp. 358 - 362 , (ISSN: 1070-9908, DOI: 10.1109/LSP.2017.2764884)
Link na rad:
https://ieeexplore.ieee.org/document/8078234
SCI lista:
http://mjl.clarivate.com/cgi-bin/jrnlst/jlresults.cgi?PC=MASTER&Word=*IEEE%20Signal%20Processing%20Letters

[2] LJ. Stanković, M. Daković, I. Stanković, and S. Vujović, "On the Errors in Randomly Sampled Nonsparse Signals Reconstructed with a Sparsity Assumption," *IEEE Geoscience and Remote Sensing Letters*, Vol: 14, Issue: 12, Dec. 2017, pp. 2453 - 2456, (ISSN: 1545-598X, DOI: 10.1109/LGRS.2017.2768664)

Link na rad:
https://ieeexplore.ieee.org/document/8110831
SCI lista:
http://mjl.clarivate.com/cgi-
bin/jrnlst/jlresults.cgi?PC=MASTER&Full=*IEEE%20Geoscience%20and%20Remote%
20Sensing%20Letters

[3] LJ. Stanković, M. Daković, and E. Sejdić, "Vertex-Frequency Analysis: A Way to Localize Graph Spectral Components," *IEEE Signal Processing Magazine*, Vol.34, No. 4, July 2017, pp. 176-182 (Print ISSN: 1053-5888, Electronic ISSN: 1558-0792, DOI: 10.1109/MSP.2017.2696572)
Link na rad:
https://ieeexplore.ieee.org/document/7974871
SCI lista:
http://mjl.clarivate.com/cgi-
bin/jrnlst/jlresults.cgi?PC=MASTER&Word=*IEEE%20Signal%20Processing%20Maga
zine

[4] LJ. Stanković, "On the STFT Inversion Redundancy," *IEEE Transactions on Circuits and Systems II*, 10.1109/TCSII.2015.2482438, Vo.63, No.3, March 2016, pp.284-288. (Print ISSN: 1549-7747, Electronic ISSN: 1558-3791, DOI: 10.1109/TCSII.2015.2482438)
Link na rad:
https://ieeexplore.ieee.org/document/7277057
SCI lista:
http://mjl.clarivate.com/cgi-bin/jrnlst/jlresults.cgi?PC=MASTER&ISSN=*1549-7747

[5] Djurović, and LJ. Stanković, "XWD-algorithm for the instantaneous frequency estimation revisited: Statistical analysis," *Signal Processing*, vol. 94, 2014, pp. 642-649. (ISSN: 0165-1684, DOI: https://doi.org/10.1016/j.sigpro.2013.07.030)
Link na rad:
https://www.sciencedirect.com/science/article/pii/S0165168413003095
SCI lista:
http://mjl.clarivate.com/cgi-
bin/jrnlst/jlresults.cgi?PC=MASTER&Full=*Signal%20Processing

[6] LJ. Stanković, S. Stanković, I. Orović, and M. Amin, "Robust Time-Frequency Analysis based on the L-estimation and Compressive Sensing," *IEEE Signal Processing Letters*, Vol. 20, No. 5, pp. 499-502, (ISSN: 1070-9908, DOI: 10.1109/LSP.2013.2252899)
Link na rad:
https://ieeexplore.ieee.org/document/6479684
SCI lista:
http://mjl.clarivate.com/cgi-
bin/jrnlst/jlresults.cgi?PC=MASTER&Word=*IEEE%20Signal%20Processing%20Letter
s

[7] LJ. Stanković, T. Thayaparan, and I. Djurović, "Separation of Target Rigid Body and Micro-Doppler Effects in ISAR Imaging," *IEEE Transactions on Aerospace and Electronic Systems*, Vol 42,No. 7, Oct. 2006, pp. 1496-1506 (Print ISSN: 0018-9251, Electronic ISSN: 1557-9603, CD-ROM ISSN: 2371-9877, DOI: 10.1109/TAES.2006.314590)
Link na rad:
https://ieeexplore.ieee.org/document/4108000
SCI lista:
http://mjl.clarivate.com/cgi-bin/jrnlst/jlresults.cgi?PC=MASTER&Word=*Aerospace
(rezultat sa rednim brojem 8)

[8] LJ. Stanković, T. Thayaparan, and M. Daković, "Signal Decomposition by Using the S-Method with Application to the Analysis of HF Radar Signals in Sea-Clutter," *IEEE Transactions on Signal Processing*, Vol.54, No.11, Nov. 2006, pp.4332- 4342 (Print ISSN: 1053-587X, Electronic ISSN: 1941-0476, DOI: 10.1109/TSP.2006.880248)
Link na rad:
https://ieeexplore.ieee.org/document/1710379
SCI lista:
http://mjl.clarivate.com/cgi-bin/jrnlst/jlresults.cgi?PC=MASTER&Word=*%20IEEE%20Transactions%20on%20Signal%20Processing

[9] Djurović, and LJ. Stanković, "Modification of the ICI rule based IF estimator for high noise environments," *IEEE Transactions on Signal Processing*, Vol. 52, No.9, 2004, pp. 2655-2661(Print ISSN: 1053-587X, Electronic ISSN: 1941-0476, DOI: 10.1109/TSP.2004.832030)
Link na rad:
https://ieeexplore.ieee.org/document/1323271
SCI lista:
http://mjl.clarivate.com/cgi-bin/jrnlst/jlresults.cgi?PC=MASTER&Word=*%20IEEE%20Transactions%20on%20Signal%20Processing

[10]   LJ. Stanković, T. Alieva, and M. J. Bastiaans, "Time-frequency signal analysis based on the windowed fractional Fourier transform," *Signal Processing*, Vol.83, No.11, Nov.2003, pp.2459-2468 (ISSN: 0165-1684, DOI: https://doi.org/10.1016/S0165-1684(03)00197-X)
Link na rad:
https://www.sciencedirect.com/science/article/pii/S016516840300197X
SCI lista:
http://mjl.clarivate.com/cgi-bin/jrnlst/jlresults.cgi?PC=MASTER&Full=*Signal%20Processing

UNIVERZITET CRNE GORE

Broj: _01-437_

Podgorica, 16.06.1995.

Na osnovu člana 97. Zakona o Univerzitetu ("Sl. list RCG" br. 37/92) i člana 94. Statuta Univerziteta Crne Gore, Naučno-nastavno vijeće Univerziteta Crne Gore na sjednici održanoj 8.06.1995. donijelo je

ODLUKU
o izboru u zvanje

Dr LJUBIŠA STANKOVIĆ bira se u zvanje

redovnog profesora Univerziteta Crne

Gore za predmet Digitalna obrada signala

za rad na neodredjeno vrijeme sa   punim radnim vremenom na

Elektrotehničkom fakultetu u Podgorici .

PRAVNA POUKA: *Protiv ove Odluke lica koja smatraju da su im povrijedjena prava imaju pravo žalbe Naučno- nastavnom vijeću Univerziteta Crne Gore u roku od 15. dana.*

R E K T O R,

Prof. dr Ratko Djukanović

Prof. dr Miloš Daković

BIOGRAFIJA

Miloš Daković je rođen 1970. godine u Nikšiću, Crna Gora. Diplomirao je 1996., magistrirao 2001. i doktorirao 2005. godine, na Elektrotehničkom fakultetu Univerziteta Crne Gore. Vanredni je profesor na Univerzitetu Crne Gore od 2011. godine.

Učestvovao je u više od 10 naučno-istraživačkih projekata finansiranih od strane Volkswagen fondacije, crnogorskog Ministarstva nauke i kanadske vlade (DRDC). Recenzent je u više međunarodnih časopisa, među kojima su: IEEE Transactions on Signal Processing, IEEE Signal Processing Letters, IEEE Transactions on Image Processing, IET Signal Processing, Signal processing i Geoscience and Remote Sensing Letters.

Dosadašnji naučno-istraživački rad profesora Dakovića rezultovao je objavljivanjem blizu 150 radova, od čega je oko 50 u vodećim međunarodnim časopisima, uključujući i poglavlja u knjigama renomiranih izdavača. Koautor je knjige *Time-Frequency Signal Analysis with Applications* čiji je izdavač Artech House, Boston.

Oblasti njegovog naučno-istraživačkog interesovanja su: obrada signala, vremensko-frekvencijska analiza signala, obrada radarskih signala i compressive sensing.

Dr Daković je dobitnik Godišnje nagrade za naučna dostignića u 2015. godini, u kategoriji pronalazač – inovator za najuspješnije inovativno rješenje, koju uručuje Vlada Crne Gore.

Više detalja i kompletan spisak referenci može se pronaći na sajtu http://www.tfsa.ac.me/milos_papers.html.

DESET REFERENCI

1. LJ. Stanković, E. Sejdić, and M. Daković, "Reduced Interference Vertex-Frequency Distributions," *IEEE Signal Processing Letters*, vol 25, no.9, Sept., 2018, pp. 1393-1397. (**ISSN:** 1070-9908 DOI 10.1109/LSP.2018.2860250)

    Link na rad:
    https://ieeexplore.ieee.org/document/8421033

    SCI lista:
    http://mjl.clarivate.com/cgi-bin/jrnlst/jlresults.cgi?PC=MASTER&Word=*Signal%20Processing%20letters

2. I. Stanković, C. Ioana, and M. Daković, "On the reconstruction of nonsparse time-frequency signals with sparsity constraint from a reduced set of samples," *Signal Processing*, vol. 142, January 2018, pp. 480-484, (ISSN: 0165-1684, DOI: http://dx.doi.org/10.1016/j.sigpro.2017.07.036)

    Link na rad:
    https://www.sciencedirect.com/science/article/pii/S0165168417302827?via%3Dihub

    SCI lista:
    http://mjl.clarivate.com/cgi-bin/jrnlst/jlresults.cgi?PC=MASTER&Full=*Signal%20Processing

3. LJ. Stanković, S. Stanković, and **M. Daković**, "From the STFT to the Wigner distribution," *IEEE Signal Processing Magazine*, Vol. 31, No. 3, May 2014, pp. 163-174 (ISSN: 1053-5888, DOI: 10.1109/MSP.2014.2301791)
Link na rad:
http://ieeexplore.ieee.org/xpl/articleDetails.jsp?arnumber=6784080&queryText=From%20the%20STFT%20to%20the%20Wigner%20distribution&newsearch=true

SCI lista:
http://mjl.clarivate.com/cgi-bin/jrnlst/jlresults.cgi?PC=MASTER&Word=*IEEE%20Signal%20Processing%20Magazine

4. LJ. Stanković, **M. Daković**, and S. Vujović, "Adaptive Variable Step Algorithm for Missing Samples Recovery in Sparse Signals," *IET Signal Processing*, vol. 8, no. 3, pp. 246 -256, 2014. (ISSN: 1751-9675, DOI: 10.1049/iet-spr.2013.0385)
Link na rad:
http://ieeexplore.ieee.org/xpl/login.jsp?tp=&arnumber=6817404&url=http%3A%2F%2Fieeexplore.ieee.org%2Fiel7%2F4159607%2F6816971%2F06817404.pdf%3Farnumber%3D6817404

SCI lista:
http://mjl.clarivate.com/cgi-bin/jrnlst/jlresults.cgi?PC=MASTER&Word=*IET%20Signal%20Processing

5. LJ. Stanković, **M. Daković**, T. Thayaparan, and V. Popović-Bugarin, "Inverse Radon Transform Based Micro-Doppler Analysis from a Reduced Set of Observations," *IEEE Transactions on Aerospace and Electronic Systems*, Vol. 51, No. 2, April 2015. (ISSN: 0018-9251, DOI: 10.1109/TAES.2014.140098)
Link na rad:
http://ieeexplore.ieee.org/xpl/articleDetails.jsp?arnumber=7126172&newsearch=true&queryText=Inverse%20Radon%20Transform%20Based%20Micro-Doppler%20Analysis%20from%20a%20Reduced%20Set%20of%20Observations

SCI lista:
http://mjl.clarivate.com/cgi-bin/jrnlst/jlresults.cgi?PC=MASTER&Word=*Aerospace
(rezultat sa rednim brojem 8)

6. LJ. Stanković, **M. Daković**, and T. Thayaparan, "A Real-Time Time-Frequency Based Instantaneous Frequency Estimator," *Signal Processing*, Volume 93, Issue 5, May 2013, pp.1392-1397 (ISSN: 0165-1684, DOI: 10.1016/j.sigpro.2012.11.005)
Link na rad:
http://www.sciencedirect.com/science/article/pii/S0165168412004008

SCI lista:
http://mjl.clarivate.com/cgi-bin/jrnlst/jlresults.cgi?PC=MASTER&Full=*Signal%20Processing

7. LJ. Stanković, **M. Daković**, T. Thayaparan, and V. Popović-Bugarin, "Micro-Doppler Removal in the Radar Imaging Analysis," *IEEE Transactions on Aerospace and Electronic Systems*, Vol. 49, No. 2, April 2013, pp.1234-1250 (ISSN: 0018-9251, DOI: 10.1109/TAES.2013.6494410)

Link na rad:
http://ieeexplore.iece.org/xpl/login.jsp?tp=&arnumber=6494410&url=http%3A%2F%2Fi
eeexplore.ieee.org%2Fiel7%2F7%2F6494371%2F06494410.pdf%3Farnumber%3D6494
410

SCI lista:
http://mjl.clarivate.com/cgi-bin/jrnlst/jlresults.cgi?PC=MASTER&Word=*Aerospace
(rezultat sa rednim brojem 8)

8. **M. Daković**, T. Thayaparan, and LJ. Stanković, "Time-frequency based detection of fast manoeuvring targets," *IET Signal Processing*, Vol. 4, No. 3, June 2010, pp. 287-297. (ISSN: 1751-9675, DOI: 10.1049/iet-spr.2009.0078)
Link na rad:
http://ieeexplore.ieee.org/xpl/articleDetails.jsp?arnumber=5485216&newsearch=true&qu
eryText=Time-
frequency%20based%20detection%20of%20fast%20manoeuvring%20targets

SCI lista:
http://mjl.clarivate.com/cgi-
bin/jrnlst/jlresults.cgi?PC=MASTER&Word=*IET%20Signal%20Processing

9. T. Thayaparan, **M. Daković**, and LJ. Stanković, "Mutual interference and low probability of interception capabilities of noise radar," *IET Radar, Sonar & Navigation*, Vol. 2, No. 4, Aug. 2008, pp. 294-305 (ISSN: 1751-8784, DOI: 10.1049/iet-rsn:20070146)
Link na rad:
http://ieeexplore.iece.org/xpl/articleDetails.jsp?arnumber=4607173&newsearch=true&qu
eryText=Mutual%20interference%20and%20low%20probability%20of%20interception
%20capabilities%20of%20noise%20radar

SCI lista:
http://mjl.clarivate.com/cgi-
bin/jrnlst/jlresults.cgi?PC=MASTER&Word=*%20IET%20Radar

10. LJ. Stanković, T. Thayaparan, and **M. Daković**, "Signal Decomposition by Using the S-Method with Application to the Analysis of HF Radar Signals in Sea-Clutter," *IEEE Transactions on Signal Processing*, Vol.54, No.11, Nov. 2006, pp.4332- 4342 (ISSN: 1053-587X, DOI: 10.1109/TSP.2006.880248)
Link na rad:
http://ieeexplore.ieee.org/xpl/articleDetails.jsp?arnumber=1710379&newsearch=true&qu
eryText=Signal%20Decomposition%20by%20Using%20the%20S-
Method%20with%20Application%20to%20the%20Analysis%20of%20HF%20Radar%2
0Signals%20in%20Sea-Clutter

SCI lista:
http://mjl.clarivate.com/cgi-
bin/jrnlst/jlresults.cgi?PC=MASTER&Word=*%20IEEE%20Transactions%20on%20Sig
nal%20Processing

Univerzitet Crne Gore
adresa: address Cetinska br 2
81000 Podgorica, Crna Gora
telefon phone 00382 20 414 255
fax 00382 20 414 230
mail rektorat@ac.me
url www.ucg.ac.me

University of Montenegro

Broj / Ref 03-79
Datum / Date 12.01.20 17

Na osnovu člana 72 stav 2 Zakona o visokom obrazovanju („Službeni list Crne Gore" br. 44/14, 47/15,40/16) i člana 32 stav 1 tačka 9 Statuta Univerziteta Crne Gore, Senat Univerziteta Crne Gore na sjednici održanoj 12.januara 2017.godine, donio je

O D L U K U
O IZBORU U ZVANJE

Dr Miloš Daković bira se u akademsko zvanje **redovni profesor Univerziteta Crne Gore** za oblast **Digitalna obrada signala i adaptivni sistemi na Elektrotehničkom fakultetu** i na nematičnim fakultetima, na neodređeno vrijeme.

R E K T O R
Prof. Radmila Vojvodić

Crna Gora
UNIVERZITET CRNE GORE
ELEKTROTEHNIČKI FAKULTET

Primljeno:	17.01.2017		
Org. jed.	Broj	Prilog	Vrijednost
02/1	55		

Prof. dr Danilo Mandić

BIOGRAPHY

Danilo P. Mandic is a Professor in signal processing with Imperial College London, UK, and has been working in the areas of adaptive signal processing and bioengineering. He is a Fellow of the IEEE, member of the Board of Governors of International Neural Networks Society (INNS), member of the Big Data Chapter within INNS and member of the IEEE SPS Technical Committee on Signal Processing Theory and Methods. He has received five best paper awards in Brain Computer Interface, runs the Smart Environments Lab at Imperial, and has more than 300 publications in journals and conferences. He has authored/coauthored research monographs: Recurrent Neural Networks for Prediction (Wiley, 2001), Complex Valued Nonlinear Adaptive Filters: Nonlinearity, Widely Linear and Neural Models (Wiley, 2009), and a two volume monograph Tensor Networks for Dimensionality Reduction and Large Scale Optimisation (Now Publishers, 2016, 2017). Prof Mandic has received the President Award for Excellence in Postgraduate Supervision at Imperial. He is a pioneer of Ear-EEG, a radically new in-the-ear-canal EEG recording system, and has extended this work to in-ear monitoring of vital signs. This work appeared in IEEE Spectrum, MIT Technology Review and has won several awards.

More information and a complete list of references can be found on the official web presentation of the Imperial College London:

https://www.imperial.ac.uk/people/d.mandic,

https://www.imperial.ac.uk/people/d.mandic/publications.html

LIST OF TEN REFERENCES

[1] Cheng H, Xia Y, Huang Y, Yang L, Mandic DP et al., 2018, A Normalized Complex LMS Based Blind I/Q Imbalance Compensator for GFDM Receivers and Its Full Second-Order Performance Analysis, *IEEE TRANSACTIONS ON SIGNAL PROCESSING*, Vol: 66, Pages: 4701-4712, (ISSN: 1053-587X, DOI: http://dx.doi.org/10.1109/TSP.2018.2860556)
Link:
https://ieeexplore.ieee.org/document/8423196
SCI/SCIE list:
http://mjl.clarivate.com/cgi-bin/jrnlst/jlresults.cgi?PC=MASTER&Word=*%20IEEE%20Transactions%20on%20Signal%20Processing

[2] Nakamura T, Goverdovsky V, Mandic DP, 2018, In-Ear EEG Biometrics for Feasible and Readily Collectable Real-World Person Authentication, *IEEE TRANSACTIONS ON INFORMATION FORENSICS AND SECURITY*, Vol: 13, Pages: 648-661, (ISSN: 1556-6013, DOI: http://dx.doi.org/10.1109/TIFS.2017.2763124)
Link:
https://ieeexplore.ieee.org/document/8067531
SCI/SCIE list:
http://mjl.clarivate.com/cgi-bin/jrnlst/jlresults.cgi?PC=MASTER&ISSN=*1556-6013

[3] Talebi SP, Werner S, Mandic DP, 2018, Distributed Adaptive Filtering of alpha-Stable Signals, *IEEE SIGNAL PROCESSING LETTERS*, Vol: 25, Pages: 1450-1454, (ISSN: 1070-9908, DOI: http://dx.doi.org/10.1109/LSP.2018.2862639)
Link:
https://ieeexplore.ieee.org/document/8424469
SCI/SCIE list:
http://mjl.clarivate.com/cgi-bin/jrnlst/jlresults.cgi?PC=MASTER&Word=*%20IEEE%20Signal%20Processing%20Letters

[4] Xia Y, Douglas SC, Mandic DP, 2018, Performance analysis of the deficient length augmented CLMS algorithm for second order noncircular complex signals, *SIGNAL PROCESSING*, Vol: 144, Pages: 214-225, (ISSN: 0165-1684, DOI: http://dx.doi.org/10.1016/j.sigpro.2017.10.021)
Link:
https://www.sciencedirect.com/science/article/pii/S0165168417303808
SCI/SCIE list:
http://mjl.clarivate.com/cgi-bin/jrnlst/jlresults.cgi?PC=MASTER&ISSN=*0165-1684

[5] Xia Y, Douglas SC, Mandic DP, 2018, A perspective on CLMS as a deficient length augmented CLMS: Dealing with second order noncircularity, *SIGNAL PROCESSING*, Vol: 149, Pages: 236-245, (ISSN: 0165-1684, DOI: http://dx.doi.org/10.1016/j.slgpro.2018.03.009)
Link:
https://www.sciencedirect.com/science/article/pii/S0165168418301075
SCI/SCIE list:
http://mjl.clarivate.com/cgi-bin/jrnlst/jlresults.cgi?PC=MASTER&ISSN=*0165-1684

[6] Xia Y, Kanna S, Mandic DP, 2018, Maximum Likelihood Parameter Estimation of Unbalanced Three-Phase Power Signals, *IEEE TRANSACTIONS ON INSTRUMENTATION AND MEASUREMENT*, Vol: 67, Pages: 569-581, (ISSN: 0018-9456, DOI: http://dx.doi.org/10.1109/TIM.2017.2782980)
Link:
https://ieeexplore.ieee.org/document/8263203
SCI/SCIE list:
http://mjl.clarivate.com/cgi-bin/jrnlst/jlresults.cgi?PC=MASTER&ISSN=*0018-9456

[7] Xia Y, Mandic DP, 2018, Augmented Performance Bounds on Strictly Linear and Widely Linear Estimators With Complex Data, *IEEE TRANSACTIONS ON SIGNAL PROCESSING*, Vol: 66, Pages: 507-514, (ISSN: 1053-587X; DOI: http://dx.doi.org/10.1109/TSP.2017.2773428)
Link:
https://ieeexplore.ieee.org/document/8106751
SCI/SCIE list:
http://mjl.clarivate.com/cgi-bin/jrnlst/jlresults.cgi?PC=MASTER&Word=*%20IEEE%20Transactions%20on%20Signal%20Processing

[8] Xiang M, Kanna S, Mandic DP, 2018, Performance Analysis of Quaternion-Valued Adaptive Filters in Nonstationary Environments, *IEEE TRANSACTIONS ON SIGNAL*

PROCESSING, Vol: 66, Pages: 1566-1579, (ISSN: 1053-587X, DOI:http://dx.doi.org/10.1109/TSP.2017.2787102)
Link:
https://ieeexplore.ieee.org/document/8239856
SCI/SCIE list:
http://mjl.clarivate.com/cgi-
bin/jrnlst/jlresults.cgi?PC=MASTER&Word=*%20IEEE%20Transactions%20on%20Sig
nal%20Processing

[9] Talebi SP, Mandic DP, 2017, Distributed Particle Filtering of alpha-Stable Signals, *IEEE
SIGNAL PROCESSING LETTERS*, Vol: 24, Pages: 1862-1866, (ISSN: 1070-9908, DOI:
http://dx.doi.org/10.1109/LSP.2017.2761182)
Link:
https://ieeexplore.ieee.org/document/8062802
SCI/SCIE list:
http://mjl.clarivate.com/cgi-
bin/jrnlst/jlresults.cgi?PC=MASTER&Word=*%20IEEE%20Signal%20Processing%20L
etters

[10]   Xia Y, Mandic DP, 2017, Complementary Mean Square Analysis of Augmented
CLMS for Second-Order Noncircular Gaussian Signals, *IEEE SIGNAL PROCESSING
LETTERS*, Vol: 24, Pages: 1413-1417, (ISSN: 1070-9908, DOI:
http://dx.doi.org/10.1109/LSP.2017.2717945)
Link:
https://ieeexplore.ieee.org/document/7954619
SCI/SCIE list:
http://mjl.clarivate.com/cgi-
bin/jrnlst/jlresults.cgi?PC=MASTER&Word=*%20IEEE%20Signal%20Processing%20L
etters

Imperial College

London

Imperial College London
Level 4 Faculty Building
South Kensington Campus, London, SW7 2AZ, UK
Telephone: +44 (0)20 7594 5001/2 Fax: +44 (0)20 7594 5004

Email: k.onions@imperial.ac.uk
www.imperial.ac.uk

Sir Keith O'Nions FRS
President and Rector

22 May 2014

Professor Danilo Mandic
Professor of Electrical Engineering
Department of Electrical and Electronic Engineering
Imperial College London
Electrical and Electronic Engineering Building
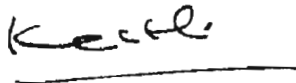South Kensington Campus
London SW7 2AZ

Dear Danilo

President's Award – Research Supervision 2014

I am writing to let you know that your department has nominated you for the President's Award for Excellence in Research Supervision 2014. It gives me enormous pleasure to tell you that you are a winner.

The Award celebrates and acknowledges staff who are considered to have made an outstanding contribution to the enhancement of research supervision. Providing world-class research supervision for our students is hugely important for the College and core to our mission, so I would like to express sincere thanks for your exceptional endeavours and dedication. In recognition of this, you will be presented with an award of £250 and a certificate as a lasting record of your achievement. The Education Office will contact you in due course with details of when the presentations will take place.

With very many congratulations

Sir Keith O'Nions
President

HOME   HONOURS AND MEMBERSHIPS   RESEARCH   PUBLICATIONS   TEACHING
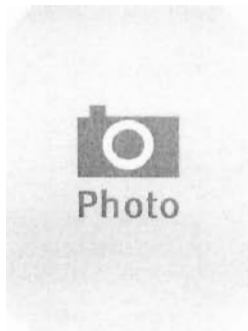
PROFESSOR DANILO MANDIC

/// Faculty of Engineering, Department of Electrical and Electronic Engineering
Professor of Signal Processing

SUMMARY

Dr. Mandic received the Ph.D. degree in nonlinear adaptive signal processing in 1999 from Imperial College, London, London, U.K. He is now a Senior Lecturer with the Department of Electrical and Electronic Engineering, Imperial College London, London, U.K. He has previously taught at the Universities of East Anglia, Norwich, Norfolk, U.K., and Banja Luka, Bosnia Herzegovina.

He has written over 100 publications on a variety of aspects of signal processing and a research monograph on recurrent neural networks. He has been a Guest Professor at the Catholic University Leuven, Leuven, Belgium, and Frontier Researcher at the Brain Science Institute RIKEN, Tokyo, Japan. Dr. Mandic is a Member of the IEEE Signal Processing Society Technical Committee on Neural Networks for Signal Processing, Associate Editor for IEEE TRANSACTIONS ON CIRCUITS AND SYSTEMS II, and Associate Editor for International Journal of Mathematical Modeling and Algorithms. He has won awards for his papers and for the products coming from his collaboration with industry.

SELECTED PUBLICATIONS

JOURNAL ARTICLES

Zhao Q, Caiafa CF, Mandic DP, et al., 2013, Higher Order Partial Least Squares (HOPLS): A Generalized Multilinear Regression Method, *IEEE Transactions on Pattern Analysis and Machine Intelligence*, Vol:35, ISSN:0162-8828, Pages:1660-1673
DOI   Author Web Link   Open Access Link

Looney D, Kidmose P, Park C, et al., 2012, The In-The-Ear recording concept, *Ieee Pulse Magazine*, Vol:3, Pages:34-42

Rehman N, Mandic DP, 2010, Multivariate empirical mode decomposition, *Proceedings of the Royal Society A: Mathematical, Physical & Engineering Sciences*, Vol:466, ISSN:1364-5021, Pages:1291-1302
DOI   Author Web Link

Xia Y, Douglas SC, Mandic DP, 2012, Adaptive Frequency Estimation in Smart Grid Applications, *IEEE Signal Processing Magazine*, Vol:29, ISSN:1053-5888, Pages:44-54
DOI   Open Access Link

Ahmed MU, Mandic DP, 2011, Multivariate multiscale entropy: A tool for complexity analysis of multichannel data, *Physical Review E*, Vol:84, ISSN:1539-3755

CONTACT

+44 (0)20 7594 6271
Email
Website

ASSISTANT

Ms Melanie Albright
+44 (0)20 7594 6267

LOCATION

813
Electrical Engineering
South Kensington Campus

AFFILIATIONS

> Centre for Neurotechnology
> Communication and Signal Processing
> Department of Electrical and Electronic Engineering
> Neuromuscular Rehabilitation Technology Network

LINKS

> College Directory
> Search College Directory
> Faculty of Engineering
> Department of Electrical and Electronic Engineering
> Expert Directory

More Publications

Main campus address:
Imperial College London, South Kensington Campus, London SW7 2AZ, tel: +44 (0)20 7589 5111

Campus maps and information   About this site   This site uses cookies   Log in